THE UNIVERSITY
of EDINBURGH

Smoke Management For Modern Infrastructure

Presented By

Ryan Robert Hilditch

For The Degree Of

Doctor Of Philosophy

The University Of Edinburgh

2017

Smoke Management for Modern Infrastructure

by

Ryan Robert Hilditch

This thesis has been supervised by

Professor José L. Torero
&
Professor Luke Bisby

The examining committee consisted of:

Dr Daniel Alvear
&
Dr Rory Hadden

To Fiona, and our family

Declaration

This thesis and the work described within have been completed solely by Ryan Robert Hilditch at the BRE Centre for Fire Safety Engineering at the University of Edinburgh, under the supervision of Prof. José Luis Torero and Prof Luke Bisby. Where others have contributed or other sources are quoted, references are given.

Ryan Robert Hilditch

September 2017

Abstract

Concerning management of smoke following an accidental fire within a building it is desirable to be able to estimate, within some understood, acceptable magnitude of error, the volume of smoke resulting from the combustion process of a predefined design fire scenario. Traditionally a range of first principle-based and empirically derived correlations are used to estimate the mass flow of smoke at a height of interest within the fire plume and are based upon the understanding that the mass flow of smoke at that height is a function only of the gravitational vector within the fire system, that is to say, that induced by the pressure differential between the naturally occurring hot plume gases and the surrounding quiescent bulk fluid. The statement that the fire plume is surrounded by a quiescent bulk fluid is in itself a significant simplification and is a key assumption required to facilitate the relative simplicity of the Froude-based entrainment correlations.

It is of course quite intuitive to imagine that in real accidental fire scenarios in the built environment and across an array modern infrastructure, rarely does a fire exist submerged in a passive, quiescent atmosphere. This disconnect between the natural mechanics of the buoyant fire mechanism and the surrounding fluid in which it exists was necessary when the problem of entrainment by the fire plume was first described in the mainstream engineering literature around the middle of the twentieth century. Some 25 years later as ideal entrainment mechanics were beginning to be discussed specifically for application by a field of engineering in its infancy, a few researchers in the field of *fire safety engineering* published data that suggested that the addition of a relatively weak cross flow to the fire plume could have a significant impact upon the rate of air entrained by the plume, and by extension, the resultant smoke mass flow rate. The data published appeared more as a brief comment on an observation made during testing. It would be easily missed, nuzzled away in the middle of a lengthy doctoral thesis. Said thesis however happens to be one of the primary pieces of work that may be cited in reference to the formulation of perhaps the best known form of the axis-symmetric fire plume entrainment correlation, that of the so-called *Zukoski correlation*. It is perhaps curious then that the mention of a *3-fold increase* in entrainment measurements following “small disturbances” in the atmosphere during the experimental work has seemingly been ignored by researchers, probably never-learned by students, and apparently forgotten by an industry.

In a fire situation smoke can limit way-finding ability, severely irritate critical soft tissue like the eyes, trachea and oesophagus, impair cognitive function, contribute to significant

property damage, facilitate the transfer of heat and carcinogens to locations remote to the fire source and it is well understood that most deaths due to fire are caused by asphyxiation following smoke inhalation. Significant portions of project budgets may be spent on designing, validating, installing and maintaining smoke management systems including the use of active systems such as extraction and pressurisation, passive curtains/reservoirs and detection such aspirating, video and beam detectors. Turbulent atmospheres may arise in any manner of situations such as modern buildings with large open spaces (airports, museums), hotel foyers and those with atriums spanning many floors, hangars and storage facilities/warehouses. Strong winds are normal on offshore oil platforms, outside the window on most floors of super-tall buildings or quite simply, anywhere on a blustery day. In specific cases the extraction systems designed to remove smoke and even normal HVAC systems can cause substantial air flow over large areas. In fact, a simple compartment with an uneven distribution of ventilation points (windows/doorways) has been shown to result in a directional fire flow that results in a significantly tilted flame, essentially inducing a cross flow scenario using the natural fire alone.

With the coming-of-age of computational fluid dynamics models which are now a standard tool in all commercial fire engineering design offices, and probably in every smoke modelling report, it might be argued that there is little need to revisit the hand calculations from the ground up. Accepting, however, that a cross flow may increase the rate of entrainment of a fire plume and that this challenges the fundamental principles that all previous entrainment correlation knowledge is based on, and demonstrating the outcome (in terms of plume mass flow rate) with the use of a computational model, is an entirely different thing to understanding *why* this happens.

Smoke management is one of the core design criteria, or questions at least, in practically all fire engineering design projects. In the literature there appears to be; no work quantitatively investigating cross flow fire plume entrainment rates; no work qualitatively describing the behaviour of the flame / fire plume under the influence of a cross flow (with respect to entrainment); and certainly no work framing this paradigm in the theoretical or practical context of the impact upon modern smoke control systems.

This work aims to venture into these areas in the hope of beginning to piece together the overarching story of entrainment in the cross flow fire plume. The fundamental paradigm here is the addition of cross flow inertia (a horizontal pressure differential) to the axis-symmetric case where buoyancy (a zero initial momentum, vertical pressure differential) is the sole driver of the fluid flow system. How these flows then interact in a *mixed convection*

sequence is investigated and described in terms that are useful for practical consideration by fire safety engineers. It is hoped that the concepts postulated and the questions raised will inspire further investigation into this poorly understood, but fundamental fire safety problem.

Lay Summary

When a fire burns air is entrained into the sides of the flame region and the hot smoke plume region immediately above. The air mixes with the gaseous unburnt fuel (soot) and the other gaseous products of combustion is then referred to as smoke.

The mass of smoke produced by a fire is commonly estimated using a range of empirical correlations – based upon the results of a set of experiments with controlled atmospheric conditions, primarily, a still environment (no wind currents). The ideal fire plume is considered to be driven by one main force, the upward buoyant force generated by the heating of air at the flame. The premise of the traditional approach to estimating smoke mass produced by the fire is to relate the velocity of air flowing into the sides of the fire plume (entrainment velocity) to the velocity of the upward flowing buoyant air at the centre of the fire plume (centreline velocity).

When an air current (such as a crossflow) is added to the traditional experiments, the correlations used to estimate entrainment no longer adequately describe the mass of smoke produced. The amount of smoke tends increase considerably, albeit, resulting in a more dilute concentration. Therefore the continued use of the traditional smoke mass (entrainment) correlations in industry do not well describe the problem of smoke quantity pertaining to smoke control systems.

This thesis uses experiments where a fire is subjected to a relatively strong crossflow driven by a fan pointed at the fire, tilting the fire plume and producing an environment where a horizontal crossflow inertial force interacts with the upward vertical buoyant force of the fire plume and the smoke production rate (the entrainment into the fire plume) is measured and compared to that anticipated by the use of the traditional correlations.

The impact of the crossflow is investigated and the fundamental changes in the behaviour of the fire plume due to the crossflow are identified, measured and discussed. A model is described whereby, with further work, a range of *crossflow magnitude* vs *fire size* ratios may be used to gain intuition as to the impact upon smoke production likely in a range of design fire scenarios for use as a reference point for industry.

Acknowledgements

First and foremost, I would like to thank José. From time first time I stepped into his office in Edinburgh, (trying to decided how I could sound a bit more intelligent), to the last time I visited his current office in Queensland to add some much needed direction to this thesis, he has been a fountain of knowledge, perspective and inspiration. I am so grateful to have had him as an academic mentor and as a dependable, generous friend. His insight, ideas and, often-challenging answers to my questions, have guided and influenced this work no end.

To Luke and all the academic leaders involved with the fire group, always available to help, and whose resources and expert knowledge I surely did not take enough advantage of. The BRE Centre for Fire Safety Engineering at University of Edinburgh certainly felt like the world-leading fire science research centre it is know it to be.

Close allies - Adam, Cecilia, Juanito, Agustín, Steffen, Cristian, Bittern, Martin & Michal. Exceptionally bright colleagues, even better friends. Four months in Watford serve as proof.

Thanks to Debbie Smith and the BRE Trust for the funding and support throughout.

To my family, for always being there.

Last but not least, to my awesome wife Fiona, whose unconditional love and support has been critical to all my (professional) endeavours over the last 5 years. Possibly, someone should give you an award.

Contents

List of Figures

Figure 4.3 - Purely buoyant flame over 2 second period captured in video stills at 30fps. Oscillation frequency of 3Hz, similarly to that presented in figure 2.5.

Figure 4.4 - Part **(a)** shows examples of the extremes cases - a straight flame where the relative balance between buoyancy and inertia are approximately equal over the full flame length and the case where a perturbed vortex structure acquires enough buoyant pressure to rise almost vertically despite the cross flow inertia, causing a sharp change in plume fluid propagation. Part **(b)** shows the evolution from one case to the other over a period of approximately 320ms.

Figure 4.5 - Part **(a)** highlights the typical flame shapes observed throughout the period of a vortex cycle under low cross flow conditions. Vortex ring generation, as depicted by Cetegen, is superimposed where appropriate to demonstrate the growth and upward transition during cross flow conditions that lead from the straight flame to the sharply angled flame shape.

Figure 4.6 - Tilted flame under weaker cross flow demonstrates fairly consistent flame tilt angle. Vortex shedding frequency is approximately 3/s in this one second sequence, of 24 frames.

Figure 4.7 - With an increased cross flow pressure the flame is observed to shorten in length and vortex shedding frequency equals roughly 3 where the second vortex is not well defined and tends to appear immediately in the wake of the second vortex.

Figure 4.8 - As per [previous figure 4.7] another one second sample shows the flame significantly shortened in length and very turbulent in nature rendering vortex birth and lifespan quite perturbed.

Figure 4.9 - 1.25 second sequence providing resolution of flame fluid contours.

Figure 4.10 - Fourier analysis performed on pressure probe data from test 3 for the fully buoyant flame and two iterations of cross flow strength for Q=10kW and Q=20kW.

Figure 4.11 - Shows the nature of the flame sheets at the base under strong cross flow conditions whereby the air inflow at the rear of the burner is significantly decreases compared to the axis-symmetric case.

Figure 4.12 - Under fully buoyant conditions with a quiescent bulk fluid **(a)** the inflow driven by the buoyancy of the fire is approximately equal from all directions. Under cross flow conditions **(b)** the inflow is severely perturbed and the flame sheet representing a combustion zone at the rear edge of the burner (LHS) appears to exist only below the rear edge lip where O2 is present. This is seen consistently under strong cross flow conditions.

Figure 4.13: 50% flame presence probability average images of 10kW flame with (a) no crossflow, (b) strong crossflow, approx. 2.4m/s, (c) low crossflow approx.. 2.4ms velocity and (d) as per part (c) but using only the 8 images when clear flame inflection occurred.

Figure 4.14 - The blue line represents the average flame velocity trend of the fully buoyant, axis-symmetric plume, and is reproduced from [41]. The red trend line represents the increase in plume velocities over the height of the plume following the addition of the cross flow. The shallow gradient section of the red trend line corresponds to the laminar portion of the tilted flame, as depicted in the following pages in figure 4.16. This shallow gradient shows that the local flame fluid velocity accelerates more steeply than the buoyant case, and does so with very little elevation increase since the cross flow pressure both increases overall fluid velocity tilts the fluid dramatically, to almost horizontal.

Figure 4.15 - The laminar portion of the flame acts as a wave under the inertial pressure and trails of buoyant fluid regularly escape, acquire toroidal momentum and contribute to the dominant vortex structure which rises up near the rear edge of the burner surface.

Figure 4.16 - Simplistic depiction of the pressure fields contributing to the turbulent but repetitive flame behaviour. Blue = buoyancy, red = inertia, green = toroidal momentum acting to create vortices and engulf fresh air into the flame domain.

Figure 5.1 - In the classical description buoyancy is the only force driving fluid flow.

Figure 5.2 - The ideal assumption is that the natural fire flow entrains air equally from all sides around 360° depicted here in **(a)** lateral view and **(b)** plan view.

Figure 5.3 - The addition of a cross flow to the classic system introduces the subsequent pressure differential perpendicular to the initial buoyant force.

Figure 5.4 - High negative pressure area (blue) created by the fan results in generation of fluid movement toward that area from all radial points, creating a decreasing dynamic pressure gradient with distance from the fan.

Figure 5.5 - (Top) An idealised cone of the flow field induced by the exhaust fan and (bottom) general trends of static pressure (P), pressure difference (ΔP), cone cross-sectional area (dA) and air flow velocity (v).

Figure 5.6 –Idealised buoyant and inertial flow fields.

Figure 5.7 - Test 1 location of probes relative to burner and fan. Probes 1, 3 and 5 are positioned horizontally to read the pressure differential invoked by the fan-induced flow. This image is not to scale and is provided to give context to the following pressure probe

data graphs. It is important to remember that as the extraction fan speed is increased probes 3 and 5 become fully involved with the flame for significant periods of time, which is not depicted here.

Figure 5.8 - Horizontal pressure probe data for Test 1 when fan speed is fixed at v1 and z is fixed at 0.6m. Note increasing data noise as Q is increased. Data colours are aligned with probe colours of figure PIC1 for clarity. Exponential regression analysis has been applied to the noisy raw data in order to better identify data trends corresponding to the variation in boundary conditions.

Figure 5.9 - As per figure 4.8 except in **(a)** fan speed has been increased (v2) and in **(b)** fan speed has been increased further (v3).

Figure 5.10 - Purely buoyant case has no cross flow and is assumed to be immersed in an ambient bulk fluid. Probes 1, 3 and 5 are identical to the previous case however probes 2, 4 and 6 have been added and are aligned to measure (buoyant) vertical flow (downward flow would be recorded as set of negative numbers).

Figure 5.11 - **(a)** Horizontal velocities and **(b)** buoyant (vertical) velocity readings from the purely buoyant axis-symmetric case, where Q = 10kW.

Figure 5.12 –Re-arranged probe locations to acquire further pressure data from critical locations within and around the flame. The buoyant case and a cross flow case are depicted. Again this figure is not to scale and is approximate only.

Figure 5.13 –Vertical pressure probe readings for test 3 where **(a)** is at the flame centreline and in **(b)** probes 2A and 6A are a few centimetres outside the front and rear flame edge.

Figure 5.14 - Horizontal pressure probe readings for test 3 where **(a)** is at the flame centreline and in **(b)** probes 1A and 5A are a few centimetres outside the front and rear flame edge.

Figure 5.15 - **(a)** Predicted flame velocities using equation 2-29 compared with **(b)** measured velocities by pressure probes. Predicted inflow velocities are based on the assumption v=0.15u (equation 2-6).

Figure 5.16 - ΔP Measurements at Probes (0.6m, 0.8m, 1.0m cases) with NO flame present.

Figure 5.17 - From analysing conservation of mass using velocity data from nine locations along the experimental area the flow field cross-sectional area may be approximated for 3 fan speeds where no fire is included. The fan is depicted at x=0 and is 0.3m in diameter.

Figure 5.18 - ΔP Measurements at Probes, z'=0.6m, Q=10kW (v1, v2, v3).

Figure 5.34 - Change in velocity (ΔU) at each probe across a scaled interpretation of the experiment extents, **(a)** v1, **(b)** v2 and **(c)** v3. Flame images are NTS.

Figure 5.35 - Progression from fully buoyant plume **(a)** to inertia dominated flame **(c)**. The mixed flow case **(b)** requires an assessment of the balance of buoyant and inertia forces.

Figure 5.36 - Length scales used in calculation of the Grashof number at each probe location are demonstrated. Probes 3 & 5 are measured from the leading edge of the burner, while probe 1 is measured laterally from the leading edge. Probes are located at same locations relative to the burner in each z case, where z is measured from flame centreline to the face of the fan.

Figure 5.37 - Examples of flames demonstrating **(a)** inertia and buoyant-dominated regions with an aspirated cross flow source, **(b)** inertia-dominated flame and **(c)** inertia/buoyant regions where the cross flow is blown rather than aspirated.

Figure 5.38 - Average flame tilt angles for all 27 cases.

Figure 5.39 - Standard deviation of averaged flame angles for each HRR at each distance z.

Figure 5.40 - Measured flame tilt angle normalised by predicted tilt angle (equation 5-10).

Figure 5.41 - Range of error in normalised tilt angle (z=0.6m) as a function of the maximum and minimum value for empirical constants in equation 5-10 (predicted flame correlation).

Figure 5.42 - Gr*/Re2 plotted against the inverse of the non-dimensional wind velocity.

Figure 5.43 - Demonstrates the range of Grashof numbers as calculated at various locations along the length of the flame.

Figure 5.44 - The data from figure 5.43 is displayed (blue) against the same data but when the reduction in the Grashof number *as a function of decrease in gravitational magnitude* (resulting from increasing flame tilt angles) is excluded (red) from the Grashof correlation.

Figure 5.45 - Increase in Re with increasing downstream distance (L along z') for z'=0.6/0.6/1.0m and 10/20/30kW (a-c respectively).

Figure 5.46 - Gr* v Re for all cases where **(a)** Gr*Log(10) demonstrates the full range of Gr development (v1, v2, v3) and **(b)** zooming in (to the region y= $1x10^6$ through $2.6x10^7$) depicts the variation in data gradient for the region that appears to plateau (v2, v3) in figure part **(a).**

Figure 5.47 - Gr* v Re for all cases (close up of figure 4.46) **(a)** separates the three Gr* plateaus for each fire size (10/20/30kW) and **(b)** includes logarithmic trend lines.

Figure 5.48 - Gr^*/Re^2 charts varying horizontally in fan-fire distance (z=0.6/0.8/1.0m) and varying vertically in fire size (Q=10/20/30kW).

Figure 5.49 - Close up of figure 5.47 (a) of the 10kW cases only. Data points that lie within dotted lines correspond to probe 5 for all 9 of the 10kW cases.

Figure 5.50 - Velocity data for all 10kW cases, recorded at probes located 0.02m, 0.375m and 0.495m downwind from the burner leading edge. Velocity readings increase from probe 1 through probe 5. The background flame image is purely an example for spatial context.

Figure 5.51 - Gr^*/Re^2 as a function of measured cross flow velocity for all 10kW cases.

Figure 5.52 - Gr^*/Re^2 as a function of flame tilt angle. Data points represent probe 3.

Figure 6.1 - Idealised interaction of buoyant plume and forced cross flow where **(a)** represents z' = 0.6m, **(b)** represents z' = 0.8m and **(c)** represents z' = 1.0m. Flow field vectors have been removed (as per figure 5.26) for clarity.

Figure 6.2 - Measured (experiment) mass flow rate and design mass flow rates for all 27 cases. z'= **(a)**0.6m, **(b)** 0.8m and **(c)** 1.0m.

Figure 6.3 - Change in mass flow rate between experimental rate and design mass flow rates, at **(a)** z=0.6m, **(b)** z=0.8m and **(c)** z=1.0m. The transition from positive to negative change on the mass flow rate can be seen across a-c whereby the increase in z affects the design mass flow correlations but not the experimental mass flow readings.

Figure 6.4 - Measured (experiment) mass flow normalised by design mass flow rates.

Figure 6.5 - This figure reproduces the Gr/Re^2 charts of figure 5.48, however the relationship between non-dimensionalised mass flow rates depicted in figure 6.4 and Gr/Re^2 characteristics of each case have been highlighted where for *red* charts: $\dot{m}e/\dot{m}a > 1$ and are typically forced-flow dominated and for *blue* charts: $\dot{m}e/\dot{m}a < 1$ and are typically buoyancy-dominated.

Figure 6.6 - Gr* v Re for all cases where **(a)** depicts the variation in data gradient for the region that appears to plateau (v2, v3) in figure part (a).

pressure where vortex streets may be generated as a result of the viscosity and horizontal flow magnitude.

Figure C1 - Overview of the decreasing ΔP_f magnitude with distance from the fan for each fan speed, each Q, and at each probe

Figure C2 - Break down of the data from figure C1 by distance z'=0.6, 0.8 and 1.0m. Probes 5, 3 and 1 are spaced accurately on the graphs relative to each other, as they would appear on the experiment set-up.

Figure C3 - Break down of the data of figure C2 by distance, z' (fan speed v1) in order to visualise the direct impact of increasing z' in each instance

Figure C4 - Break down of the data of figure C2 by distance, z' (fan speed v2) in order to visualise the direct impact of increasing z' in each instance

Figure C5 - Break down the data of figure C2 by distance, z' (fan speed v3) in order to visualise the direct impact of increasing z' in each instance

Figure C6 - Change in velocity (Δu) at probe 5 for 10/20/30kW cases at z'= (a)0.6m, (b) 0.8m and (c) 1.0m, for the three fan speeds versus the no flame case

Figure C7 - Change in velocity (Δu) at probe 3 (and probe 1 for context) for 10/20/30kW cases at z'= (a)0.6m, (b) 0.8m and (c) 1.0m, for the three fan speeds versus the no flame case

Figure C8 - Change in velocity (Δu) at probe 1 for 10/20/30kW cases at z'= (a)0.6m, (b) 0.8m and (c) 1.0m, for the three fan speeds versus the no flame case

Figure C9 - Rearranges the data of figures C6-C8 to appear with relevance to probe location relative to the burner and other probes

Figure C10 - breaks down data of figure C9 for velocity change data at each probe location relative to burner for fire sizes 10/20/30kW, z'=0.6/0.8/1,0m, for fan speed v1

Figure C11 - breaks down data of figure C9 for velocity change data at each probe location relative to burner for fire sizes 10/20/30kW, z'=0.6/0.8/1,0m, for fan speed v2

Figure C12 - breaks down data of figure C9 for velocity change data at each probe location relative to burner for fire sizes 10/20/30kW, z'=0.6/0.8/1,0m, for fan speed v3

Figure D1 - Fast Fourier Transform (FFT) of pressure probe data from test 1

List of Tables

List of Abbreviations

FFT	-	Fast Fourier Transform
HRR	-	Heat Release Rate
HVAC	-	Heating, Ventilation & Air Conditioning unit
IR	-	Infra-red **(**Thermal Imaging Camera**)**
kW	-	Kilowatt
LES	-	Large Eddy Simulation
LDV	-	Laser Doppler Velocimeter
LHS	-	Left Hand Side
MET	-	Meteorological Office
PIV	-	Particle Imaging Velocimeter
PMMA	-	Polymethylmethacrylate
PUA	-	Per Unit Area
RHS	-	Right Hand Side

Nomenclature

l	-	Characteristic length scale (typically downstream from burner) (m)
ΔP	-	Differential pressure (Pa) (experimental)
ΔP_1	-	Differential pressure (Pa) (design)
ΔP_F	-	Differential pressure, forced force (Pa)
ΔP_B	-	Differential pressure, buoyant force (Pa)
$\Delta P_{(avg)}$	-	Differential pressure, averaged across multiple probes (1,3,5) (Pa)
z	-	Length scale, plume centreline distance, strictly vertical (m)
z’	-	Length scale, plume centreline distance, strictly horizontal (m)
z’’	-	Length scale, plume centreline distance, angled (m)
Gr	-	Grashof number general, ratio of buoyant forces / fluid viscosity
Gr*	-	Grashof number, modified to describe change based on HRR
Re	-	Reynolds number, ratio of inertiall forces / fluid viscosity
Gr/Re^2	-	Richardson number, outside boundary layer
Gr^*/Re^2	-	Richardson number articulating modified Grashof number
$Gr/Re^{1/2}$	-	Richardson number, inside boundary layer
Hz	-	Hertz (frequency)
O_2	-	Oxygen
$\dot{Q}$	-	Heat release rate (kW) (Used interchangeably with *HRR*)
$\dot{Q}_c$	-	Heat release rate, convective portion (kW)
Q*	-	Non-dimensional Heat Release Rate
g	-	Gravitational acceleration ($9.81 ms^{-2}$)
D	-	Burner source diameter (m)

ρ	-	Density of fluid (kgm^{-3})
ρ_∞	-	Density, ambient (kgm^{-3})
c_p	-	Specific heat capacity (J/kg.K)
T	-	Temperature of fluid (°C, K)
T_∞	-	Temperature, ambient (°C, K)
ΔT	-	Temperature differential (°C, K)
u	-	Fluid velocity (ms^{-1})
u_0	-	Flame centreline velocity (ms^{-1})
v	-	Inflow fluid velocity, buoyant entrainment (ms^{-1})
α	-	Buoyant entrainment constant
b	-	Plume radius, ideal plume (m)
dz	-	Differential height, typically along plume
$\dot{m}_e$	-	Experiment mass flow rate [kgs^{-1}] (fan flow rate)
$\dot{m}_{e(z')}$	-	Experiment mass flow rate [kgs^{-1}] (emphasising tilted horizontal axis)
$\dot{m}_{a(B)}$	-	Design mass flow rate [kgs^{-1}] (general)
$\dot{m}_{a(Zuk)}$	-	Design mass flow rate [kgs^{-1}] (as per Zukoski specifically)
$\dot{m}_{a(Hesk)}$	-	Design mass flow rate [kgs^{-1}] (as per Heskestad specifically)
$\dot{m}_{a(z)}$	-	Design mass flow rate [kgs^{-1}] (emphasising the dependence on the strictly vertical axis)
$\dot{m}_T$	-	Total mass flow rate [kgs^{-1}]
$\emptyset_Q$	-	(Portion of) combustion product (as function of *Q*)
$\partial\emptyset_{Q(i)}$	-	(Portion of) combustion product retained in the inertial flow
$\partial\emptyset_{Q(B)}$	-	(Portion of) combustion product retained in the general buoyant flow
$\partial\emptyset_{a(i)}$	-	(Portion of) combustion product mixed with air entrained due to inertia-dominated flow

$\partial\emptyset_{a(B)}$	-	(Portion of) combustion product mixed with air entrained due to buoyancy-dominated flow
$\partial\emptyset_{a(B)z}$	-	(Portion of) combustion product mixed with air entrained due to *typically vertical* buoyancy-dominated flow
$\partial\emptyset_{a(B)z''}$	-	(Portion of) combustion product mixed with air entrained due to *strongly perturbed* buoyancy-dominated flow
$\dot{E}_{buoy(z)}$	-	(Portion of) air entrained, due to buoyant force (emphasising the dependence on the *strictly vertical* axis)
$\dot{E}_{buoy(\sim z)}$	-	(Portion of) air entrained, due to buoyant force (emphasising the dependence on the *typically vertical* axis)
$\dot{E}_{inertia(z')}$	-	(Portion of) air entrained into inertia-dominated flow (emphasising the dependence on the *essentially horizontal* axis)
$\dot{E}_{buoy(z'')}$	-	(Portion of) air entrained into buoyancy-dominated flow (emphasising the dependence on the *perturbed vertical* axis)
L	-	Flame length (m)
θ	-	Angle (of flame tilt), measured from horizontal
u^*	-	Non-dimensional wind velocity
$\dot{m}$	-	Fuel mass loss rate (g/s)
ΔH_{eff}	-	Effective heat of combustion (kJ/g)
Fr	-	Froude Number
H	-	Flame height
P1	-	Bi-directional pressure probe 1 – horizontal alignment
P2	-	Bi-directional pressure probe 2 – vertical alignment
P3	-	Bi-directional pressure probe 3 – horizontal alignment
P4	-	Bi-directional pressure probe 4 – vertical alignment
P5	-	Bi-directional pressure probe 5 – horizontal alignment
P6	-	Bi-directional pressure probe 6 – vertical alignment

1 Introductory Discussion

1.1 The (Secret) Background Story

The late 1970's and early 1980's represents a brief golden age in the study of fire plume entrainment mechanics, by some of the main contributors to the fire engineering theory literature, still referenced heavily by the ever-growing community of fire safety engineers and designers today. Research into reactive plume entrainment mechanisms continued through the 80's and 90's, focusing research on less well-defined areas, such as near-field entrainment and vortex engulfment in the continuous flame region of the fire plume. It appears, one must concede, that one particular area of concern that was highlighted consistently during this brief 'golden age' received very little attention. Frankly, a few short statements in the pertinent research papers were the initial instigation of the current work. The following works are discussed in detail in the review of literature in chapter 2, but a brief mention here seems the most appropriate place to begin.

In the late 70's and early 80's Edward Zukoski and Baki Cetegen were publishing numerous related works regarding entrainment of the free fire plume. The main entrainment correlation resulting from this period of research built upon theoretically-derived work from decades earlier, but became what is, typically, the first fire plume entrainment correlation that the fire engineering student of today learns. Importantly, following this series of research it was pointed out that:

> *"Early in our experimental program, we observed that disturbances in the room air could have a substantial effect on entrainment rates. For example, currents produced by an air conditioning system caused the plume mass flux to rise by about 20% above the value obtained when the system was blocked off…*
> *The disturbances in these experiments were largely due to the flow of air through the room which was produced by the entrainment process itself…*
> *The effects of ambient disturbances which may present in real fire situations are to enhance the entrainment of fire plumes up to 50% in some cases."*
>
> Cetegen, Zukoski & Kubota [6]

Around the same time Quintiere, Rinkinen & Jones [19] were investigating the effect of various enclosure opening configurations upon entrainment of a room fire plume with pressure data of the outflow of smoke from the upper hot layer of the compartment. There are nuances to the set-up of the experimental-rig, which will be discussed later in detail, however the headline of this work was that recorded smoke mass flow rates were as much as 2-3 fold that predicted by the free-plume literature entrainment calculations, specifically that provided by Zukoski et al..

In 1982, (closely related to work a few years earlier) in their well-renowned plume dynamics research McCaffrey & Cox, while investigating entrainment and heat flux combined with the conversation around inconsistencies of dependent variables across the various portions of the fully-buoyant fire plume noted:

"Although the present results are considerably higher than point source plume theory, further disagreements between measurements and plume theory calculations noted in the literature are possibly due to increased entrainment brought upon by disturbances to the free burn behaviour, for example, by the door jet when the fire is located in an enclosure. Preliminary estimates of this effect are being pursued by Zukoski…"

McCaffrey & Cox [12]

A theme was clear amongst the research of the main players during that period. Although these researchers have all produced further interesting and exciting work on entrainment fundamentals of fire plumes, this tantalising and tedious issue remains largely, a small collection of, more-or-less, simultaneous comments from 35 years ago. The responsibility of course, does not lie with the researchers referenced here, it lies with the fire engineering community as a whole, and it seems strange, and it is unfortunate, that these comments remain essentially unaddressed decades later. Focused fire safety education researchers recently discussed the issue of the need for prominent researchers in the fire safety engineering field in detail in [74].

In his definitive guide to fire engineering knowledge and principles "An Introduction to Fire Dynamics", the third edition - published in 2011, Drysdale notes that:

> "*Air movement tends to enhance the rate of entrainment of air into the fire plume. This is likely to promote combustion within the flame and thus reduce its length, although this remains to be quantified properly*".
>
> Drysdale [40]

Introduction to Fire Dynamics is essentially an informative text that translates decades of fire safety research into digestible and practical engineering direction. As it stands, the detail in the first sentence in the Drysdale quote above quite acutely reflects the amount of focused work which has been done and framed specifically around non-ambient fire plume entrainment since the aforementioned authors had highlighted the issue and kicked-off proceedings in the 1980's. This is basically the same sentence that could have been written 35 years ago.

1.2 Some General Discussion

The problem of fire plume entrainment in non-ambient environments is certainly a complex one. In the review of literature that follows in chapter 2 it will become apparent that fundamental flow characteristics of mixed-convection and mixed flow phenomena are available in the literature, and in fact constitute some well-researched first principle flow dynamics in heat and mass transfer. The application of these to the fire plume case is possible, with some overarching assumptions. The placing of that work in the context of typical fire scenarios for use by the fire safety practitioner is also required. The study of fire plume entrainment in ambient conditions was first required to gain an understanding of the fundamental principles, and the physical relationships within the fluid flow fields, so that general principles could be articulated and defined. It has been established by the authors

mentioned previously that deviations from a controlled, ambient atmosphere lead to plume mass flow rates greater than those postulated under the ambient assumption. We know that real life accidental fire scenarios are rarely likely to exist in calm, ambient environments. Modern infrastructure is pushing the limits of architectural and structural design and these new spaces test the limits of prescriptive safety codes and in fact, the traditional fire safety design approaches - especially when the engineering correlations outlined decades ago have not been revisited, despite acknowledgment by their authors that critical unanswered questions persist.

The impact of an increased fire plume entrainment rate is multi-faceted. In a fire situation *more* smoke is undesirable. More smoke potentially indicates *diluted* smoke. Diluted smoke behaves differently to the less dilute smoke that is anticipated from the design fire specified for a particular fire engineering design. Certainly, people are killed most often by smoke in fire situations, so it would appear that within the context of today's fire engineering discipline, smoke mass flow, and fire plume entrainment are woven into the fabric of most fire engineering design problems. Subsequently of interest, the authors previously quoted also alluded to the fact that a cross flow can of course come from a forced mechanism such as a fan, however in the case of a unusual, or even a traditional box compartment, in tandem with very normal ventilation opportunities such as doors and windows, the fire plume itself can induce a unidirectional cross flow which results in what we can consider to be a breakdown of the traditional, axis-symmetric fire plume entrainment model.

Concerning smoke management following an accidental fire within a building in modern infrastructure it is desirable to be able to estimate, within some understood magnitude of error, the volume of smoke resulting from the combustion process of a predefined design fire scenario. Traditionally a range of empirically derived correlations are used to estimate the mass flow of smoke at a height of interest within the fire plume and are based upon the understanding that the mass flow of

smoke at that height is a function of the gravitational vector within the fire system, and there is no other pressure system driving the flow fluid flow. The statement that the hot plume is surrounded by a quiescent bulk fluid is in itself a significant simplification and is the assumption which is required to facilitate the approach of Froude-based [40] entrainment correlations.

In reality we know that accidental fires are rarely likely to be surrounded by a calm, quiescent bulk fluid. Depending upon the circumstance and location any number of individual air currents may be present influencing the fire plume, and each other. Consideration of many interacting currents in any one scenario would be highly complex, however a realistic case of non-quiescent bulk fluid behaviour near a fire is that of the unidirectional inertial flow field, resulting essentially in a cross flow interacting with the fire plume and emanating from a distant point. This case may be of great worth since an appropriate experiment design offers the opportunity to control the size of the fire (the buoyant differential pressure force) and the velocity or strength of the cross flow (the inertia or forced-flow pressure differential) perpendicular to the propagation of the fire plume. Mechanisms to measure attributes of the mixed flow field and to quantify the overall mass flow rate of interest are also required.

1.3 Some Context – Where are we Now?

1.3.1 Problem Statement

The problem statement really deserves to be based upon the background story at the beginning of this chapter. Put as simply as possible we know that when experimental measurements of fire plume mass flow have been made, very often, the measurements are significantly larger than the mass flow rates predicted by the traditional mass flow correlations composed for such cases. The disparity arises because of the assumptions which were required for the derivation of the correlations that assume an ambient atmosphere and therefore an inflow into the

plume of fresh air equally from all directions. Coinciding each time with the larger-than-expected mass flow rate measures noticeable air currents which observed to perturb the symmetry of the fire plume meaning that the equal-from-all-directions-inflow was untrue.

Therefore the traditional fire plume mass flow correlations can be said to be inappropriate for purpose in many cases - both in the laboratory, and, it is reasonable to assume, also in industry settings.

1.3.2 Previous Work

Significant work exists to both underpin the traditional entrainment theory as well as to inform and provide intuition as to the current problem. Morton [1] furthered the ideal plume theory based upon a point source plume located within a quiescent environment which was adapted further by, Zukoski (with Cetegen) [6], McCaffrey [12], Thomas [10], Heskestad [7] and Quintiere et al. [19]. After discrepancies were noted [6, 12, 19] between the ideal plume theories and plume mass flow measurements we must move away from fire plume literature (or what could be considered typical *fire engineering literature*) in order to find intuition for the mixed flow entrainment problem.

That being said, numerous researchers considered flames in a cross wind (typically in wildland fire research) and flame tilt, flame length and fire spread rate are all relatively well-defined. Pitts [64] provides an in-depth review of these works. What is missing of course is the entrainment problem from this large body of fire/cross flow research.

Hoult & Weil [18] are responsible for some of the main theoretical works in the large body of non-reactive plumes in cross flow literature available. They essentially separated the crossflow into the parallel and normal components to give entrainment rates as a function of the velocity of the plume relative to its

surroundings. These works are of interest but are not ideal for the reactive fire plume case which is the focus here.

Lavid & Berlad [29] carried out a theoretical study of the chemically reacting boundary layer flow over a horizontal flat plate with gravitationally induced buoyant force. Here the concept of using the ratio of buoyancy to inertial forces by combining the Grashof and Reynolds number for a flow case was put forth. This is an important concept and will be discussed in detail later and will form a key component of this investigation.

Apte et al. [24] investigated flame spread over a horizontal surface of polymethylmethacrylate (PMMA) under cross flow conditions in a wind tunnel and described various modes that the flame and plume may adopt under cross flow conditions, depending upon the ratio introduced by [29].

Torero and various co-workers produced a number of related works [20-23] following theoretical and experimental investigations into the transport mechanisms controlling a diffusion flame while varying the buoyancy across a range of normal and microgravity regimes. These works added further intuition to the premises outlined in [24] and [29].

These works [20-23, 24, 29] are some of the most important for mixed-convection fluid flow dynamics as applied to the fire plume case and helped to deconstruct the mixed-convection flows, providing some practical context to the theoretical descriptions. The ideals put forward in these papers will provide much of the understanding of the components of the mixed-convection entrainment problem.

Nmira et al. [26] composed a 3-dimensional computational model to study wind affects the geometric properties of vegetation fires and provided some of the few visual representations of the fluid flow characteristics resulting from horizontal flows interacting with strongly buoyant plume sources.

Leal [39] investigated the premise where a boundary surface is strictly horizontal thus eliminating any buoyant contribution to a horizontal stream-wise flow and generating a significant body force cross-stream. The effect of a comparatively strong cross stream body force is a so-called *stretched boundary layer* where the contribution of the body force within the cross flow is appropriated. This concept is directly applicable to a tilted flame where the magnitude of the buoyant force is diminished as the gravitational gradient increases. Leal applies a treatment combining flow vectors within first principle descriptions of buoyant and inertial forces for x and y-momentum equations. This work is one of the most interesting and intuitive while searching for a fundamental description of mixed-convection fluid dynamics.

1.3.3 What We Will Address in this Research

In [6], [12] and [19] discrepancies between measured and predicted mass flow rates was partially quantified in the case of [6], generally described with reference to non-reactive plume in wind entrainment theory in the case of [19] and mainly discussed qualitatively in [12]. In each case the deviation from expected mass flow rate was measured of course, however data was generally not gathered pertaining to fluid flow velocities at and around the flame and plume under cross flow cases (or when "small disturbances" [6] were noted). The average tilted flame angle was recorded in [19] but not fully quantified elsewhere and specifically the increase in mass flow was described generally in each case as presumed to be the result of increased turbulence / enhanced mixing due to the air currents that occurred. In [19] the entrainment constants from non-reactive plumes in wind theory were investigated and it was concluded that these were inflexible and not able to provide adequate explanation for the entrainment rates recorded.

Perhaps most importantly in all three cases the total measured mass flow was not delineated with respect to which portion of the fire plume it could be attributed to. Depending upon the relative strength of the buoyant force and inertia cross flow

force the fire plume exhibits varying degrees of tilt and can be described as inertia or buoyancy-dominated at any point downstream from the source [24] depending upon which force is most important at that location. It is suspected, for this work, that just as the axis-symmetric fire plume entrains air at varying rates in the continuous/intermittent flame and plume regions [12] it is likely that a similar variation is applicable to the tilted fire plume case. It is also postulated however that the entrainment rates attributable to each portion of the tilted fire plume differ, by varying degrees, to those of the axis-symmetric case.

This work will therefore begin by describing the tilted fire plume with reference to the previous literature and in relation to the varying degree of importance of the inertia and buoyant differential pressures which combine in this case. We will characterise inertia, buoyant and transitional portions of the fire plume and investigate a range of cases across which inertia is most important, buoyancy is most important, and where inertia and buoyancy are generally comparable.

The inertia-dominant regime will be isolated in each case and the mass flow attributable to this regime will be quantified by way of an exhaust fan and oxygen calorimeter / collection hood. The rate of entrainment will be controlled and trends in entrainment velocity and flame behaviour will be compared with the mass flow rate and other variable boundary conditions. The fluid flow characteristics in and around the fire plume under cross flow conditions will be characterised and qualitative analyses of near-field flame behaviour will be offered. Finally a scale will be defined along which the relative importance of buoyancy and inertia can be used to describe each experimental fire case and a general relationship between this definition and increasing mass flow rate will be postulated.

The main aim of this work therefore is to break down the cross flow entrainment in fire plume problem into manageable portions, to define these quantitatively and qualitatively where appropriate and to relate these data back to the bigger picture, which is application to smoke control in modern infrastructure.

2 Literature Review

The following chapter begins with an overview of the general principles which are used as a basis for traditional fire plume entrainment theory. We will then discuss in detail from where the traditional engineering approaches are derived and consider the experimental approaches used. Work that considers the effect of wind on non-reacting plumes will be briefly discussed since it is related to the problem but as will be seen, is not appropriate for the fire plume entrainment discussion. Some mixed-convection literature exists and will be considered in detail since the fundamentals outlined in these works may be directly applicable to the room-scale fire plume system. To close out the literature review we will return to fundamentals and consider the well-defined first principle descriptions of free and forced convection, as well as some interesting literature which seeks to combine these in a mixed-convection study, the abstract theory of which is possibly one of the most pertinent pieces of literature that can be applied to the cross flow fire plume entrainment case. The combination of all of these areas should outline the important work which has been done so far in fire plume fluid mechanics for entrainment as well as the related work which at the very least, informs the current work, and the problem of cross flow fire plume entrainment.

2.1 General Principles

The plume model previously described is representative of a diffusion flame which is characterised by low momentum at the source, whereby it is typically the density gradient due to local temperature gradients that is responsible for the upward flow of flame and plume fluid. By contrast the jet flame typically has significant initial momentum at the source where the gaseous fuel is pressurised on release. The relative importance of buoyancy and momentum at the fire source will determine the resulting fire characteristics and can be evaluated with a Froude number

analysis [40]. The Froude number equates inertia force with buoyancy and can primarily be written as:

$$Fr = \frac{u^2}{gD}$$

Equation 2-1

where the numerator represents inertial velocity and the denominator is the acceleration due to gravity g, and a characteristic length, typically the source diameter, D. By approximating the initial fuel velocity by dimensional analysis it can be shown [42] that the Froude number is proportional to:

$$Fr \propto \frac{\dot{Q}_c^2}{D^5} \qquad \left[thus, \sqrt{Fr} \propto \frac{\dot{Q}_c}{D^{5/2}}\right]$$

Equation 2-2

where $\dot{Q}_c$ is convective heat release rate (focus on the convective portion of the HRR is text-dependant). Through vast amounts of experimentation over some decades it has repeatedly been found convenient to express relational plume data in terms of a non-dimensional heat release rate which is described as the square of Froude number expressed in terms of heat release rate of the fire:

$$\dot{Q}_c^* = \frac{\dot{Q}_c}{\rho_\infty c_p T_\infty \sqrt{gD} \cdot D^2}$$

Equation 2-3

Where ρ_∞, c_p and T_∞ are the density, specific heat capacity and temperature properties of ambient air. $\dot{Q}^*$ is used to classify fire types where the ratio of $\dot{Q}$ to the characteristic source diameter describes the nature of the flame in terms of flame length based upon a *power* per unit area (PPUA). This power says a lot about the structure of the flame and gives intuition as to parameters such as fluid velocity and

therefore the likely laminar/turbulent nature of the flame and subsequently the possible nature of the entrainment regime. McCaffrey [57] described that fire plume in three related but fundamentally distinct regimes. These are outlined in figure 2.1:

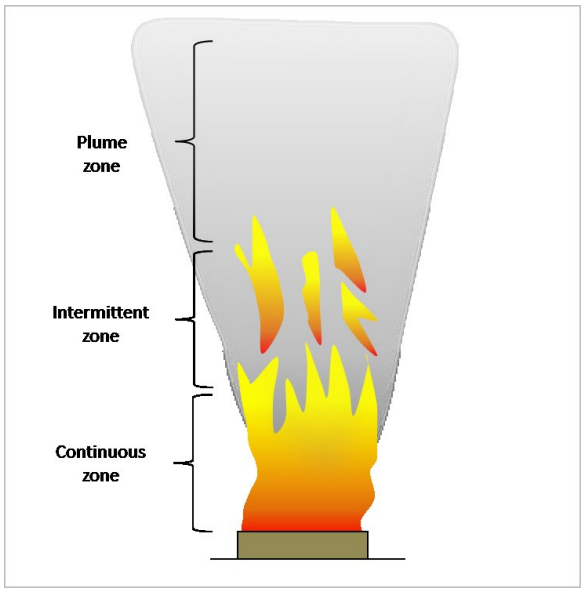

Figure 2.1: The continuous, intermittent and plume zones over a 0.3m diameter burner, as described by [57].

The three regimes may be outlined as follows:

- In the near-field a continuous flaming zone - exists with a practically constant flame presence and in which buoyant gas velocities accelerate upward.
- Intermittent zone - exists above the continuous zone where flame presence probability drops to around 0.5 [6] and gas velocities are considered to be roughly constant.
- Plume – within the buoyant plume there is no flame presence and gas velocity and temperature decrease with height.

Regarding entrainment, the physical differences outlined above have been found to have a significant impact upon the entrainment rate and entrainment mechanisms that dominate and best describe the processes in each separate zone. Following this, correlations which be conceived and altered to give best fit agreements for each zone separately. These will be discussed in greater detail throughout the chapter.

As a point of interest it should be noted at this stage that the structure of the fire plume as described above demonstrates a fundamental difference between the dynamics of the fire plume and a non-reacting plume in terms of entrainment rate and dominant entrainment mechanisms over the height of the plume. This will be important in later literature analysis.

2.2 Fundamental Beginnings: Morton et al.

The entrainment mechanism, due to the buoyant force of the fire plume, has been investigated by many researchers for free plumes in stability stratified, quiescent environments.

Morton et al. [1] developed theories of convection from maintained sources of buoyancy for a stratified body of fluid rising into a quiescent bulk fluid. This was expressed with non-dimensional forms of conservation equations for volume, momentum and density deficiency for a convective plume rising into a stably stratified atmosphere. Finding solutions to these and using dimensional analysis, coefficients could be arrived at to obtain a description of the functional relationships between upward flow velocity and temperature, source strength and height dependency. The three main assumptions employed here were:

1. Profiles of mean vertical velocity and mean buoyancy force were similar over the horizontal section at all heights
2. The rate of entrainment of fluid at the edge of the plume at any height were proportional to a characteristic velocity at that height, and

3. Fluids are incompressible and do not change volume on mixing and that the largest local variations in density throughout the field of motion were small compared to some reference density (taken from the bulk fluid, at the elevation of the source).

Subsequently, Yih [3] and Rouse, Yih & Humphreys [4] had published results of their measurements of (point source and line) plumes rising in an atmosphere of uniform temperature. In order to avoid the turbulence mixture length problem Morton et al. [1] applied the simpler transfer assumption of Taylor [5] in the hope of deriving a generally applicable description of the mechanics without requiring a detailed understanding of the turbulent eddy mixing of heated and ambient air. This assumption essentially relates the inflow of air into the edge of the plume over some height to be related to some typical velocity within the plume. The assumption of self-similarity of velocity and density deficit profiles allowed for any variation of temperature with height over a stably stratified atmosphere, which had not been accounted for previously.

The collective work of [1, 3-5] on convection currents in a plume above buoyant point and line sources can be described by the form:

$$\dot{m} = A\left(\frac{g\rho_\infty^2}{c_p T_\infty}\right)^{\frac{1}{3}} \dot{Q}^{\frac{1}{3}} z^{\frac{5}{3}}$$

Equation 2-4

where A has been suggested to be in the range of 0.153 ~ 0.20 across various literature papers and textbooks [1,3,4,8] depending on the value assigned to the empirical entrainment coefficient in each case. Equation 2-4 is applicable to the simplified plume model adopted within the fire engineering community to describe the fundamental processes of plume fluid behaviour – the so-called *Ideal plume*. This

theoretical derivations and empirical comparisons performed in [1-5] underlined the principle approach that the fire safety engineering community readily adopted and utilised in the characterisation of the simplified model for fire plumes and has been the theoretical basis for most of the subsequent entrainment work that followed. It is applicable to the weak plume as described by the assumptions made in the derivation, such as a top-hat profile across the plume diameter and that only small density differences exist locally, over the plume height and in relation to the ambient fluid.

As well as examining data from previous authors Morton et al. carried out a small-scale (tank = 1m tall and 0.3m diameter) water tank experiment to test their theoretical work where they released a lighter fluid into the bottom of the tank full of heavier fluid. The density of the lighter fluid could be manipulated by adding controlled amounts of salt solution. Care must be taken with such a procedure, not to give any initial vertical momentum to the injected fluid, and the physical constraints of the tank were witnessed as the plume edges impinged upon the side walls as the fluid at the top of the plume stratified and moved horizontally outward. The output of this experiment was in good agreement with the data of previous authors [2, 4] in the form of plume angle/horizontal length scale, despite there being a mixture of uniform and stably stratified ambient conditions utilised over the range of all data analysed. This was especially true, as would be expected, in the lower portion of the plumes where the total density deficit with height is less significant (though this would not be the case for a plume with a flaming source). Further, Morton et al. surmised that variation in results due to the output conditions (function of the physical parameters, source diameter for example) could be minimised further by taking measurement from a virtual source for each plume. The plume *virtual origin* will be discussed in more detail later.

2.3 The *Ideal Plume* Theory

The works discussed previously give rise to the theoretical approach described over the following pages. For the *ideal plume* we require to adopt a set of particular assumptions, as described in the work of [1] that allow a more general description of plume mechanics to be derived. As previously discussed, the work of [1] adopted the idea of an entrainment constant (sometimes referred to as the Taylor entrainment constant [5]), which removes the requirement to understand intrinsically the impact on entrainment of turbulent eddy mixing, following the birth and growth of vortex structures along the height of the flames and plume.

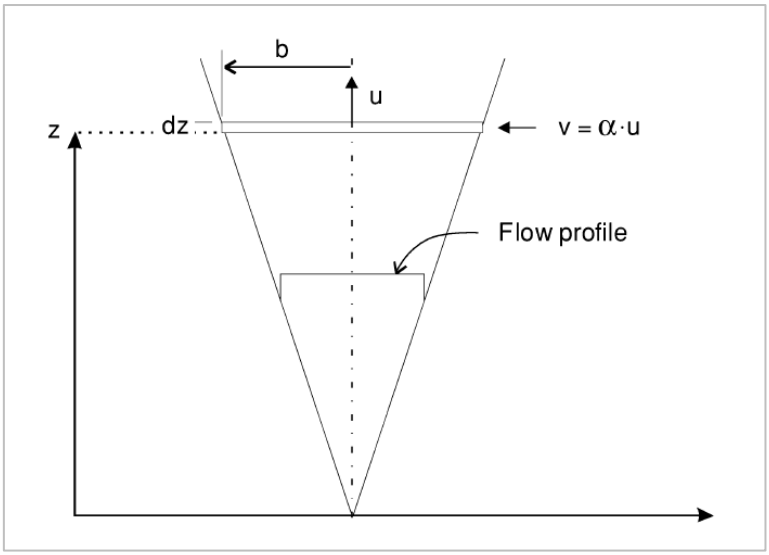

Figure 2.2: The standard representation of the Ideal Plume which introduces numerous simplifications in order to derive proportional flow characteristics. Image reproduced from [41]

Figure 2.2 depicts the ideal plume schematic where the point source and top hat profiles are definitive of this model. In this diagram u = buoyant plume fluid velocity, v = entrainment fluid velocity, b = plume radius at any height z on the vertical axis. Subsequently dz denotes any differential section of interest along the z (downstream plume) scale.

The assumptions required for this plume model can be outlined as follows:

1. All energy is assumed to be injected at the point source and all energy stays within the plume system. This assumptions disregards radiative energy loss which typically accounts for between 20-40% of the total energy released in combustion.
2. The Boussinesq approximation lets us consider the plume as a 'weak' plume, since, due to entrainment the density difference between the plume fluid and surrounding fluid is often small, allowing the assumption that plume density approximately equals bulk fluid density,

$$\rho_\infty = \rho$$

Equation 2-5

Subsequently, at heights close to the fire source, where a steep temperature gradient exists and buoyancy is strong this assumption and the equations that follow it are not valid.

3. The Taylor entrainment constant is invoked whereby entrainment at the edge of the plume is proportional to the buoyant gas velocity within the plume structure. [1-5] discuss the value of this constant however generally good agreement was found around 0.15, providing the understanding that horizontal entrainment velocity at any height is equal to approximately 15% of the vertical buoyant plume velocity at that height, whereby,

$$v = \alpha \cdot u$$

Equation 2-6

where v = horizontal entrainment velocity, u = vertical plume fluid velocity and the entrainment constant α = 0.15.

4. An entrainment constant of 0.15 is valid for when a top-hat flow profile is assumed over the plume height. We assume therefore that; temperature, velocity and force profiles are similar along the height of the plume regardless of elevation; velocity and temperature are constant over the entire horizontal section at any measure of z; and that outside the plume upward buoyant velocity is zero and temperature is that of ambient where,

$$u = 0, \quad T = T_{\infty}$$

Equation 2-7

With these restrictive conditions in place it is then possible to derive analytical expressions for the variables of interest whose proportionality can be approximated by beginning with general expressions for the process entities then refining the definitions, arriving at and solving the differential equations and inserting the relevant constants and balancing the resultant forms. This process is outlined in depth in [41] however an overview will be presented here since the ideal plume theory, despite the very generalising assumptions, articulates quite well the basis of most of the entrainment correlations in the literature and certainly represents the typical first order approximation performed by the practicing fire engineer. The following section therefore outlines the derivation of three plume relationships for plume gas velocity, mass flow rate and temperature difference which are available across a wide range of literature but are presented here in a manner similar to that outlined in [41] which provides a particularly intuitive description.

The related variables that are sought out in the process of deriving these analytical correlations include:

Temperature difference at height z, $\Delta T(z)$ given in [$°C$]

The radius of the plume at height z, b(z) given in [m]

Upward, buoyant, gas velocity at height z, u(z) given in [m/s]

The plume mass flow at height z, $\dot{m}_p(z)$ given in [kg/s]

General expressions for plume mass flow, momentum, buoyancy force and energy release rate can be set out as follows. The mass flow rate at some height z can be described by:

$$\dot{m}_p = \pi b^2 \rho u$$

Equation 2-8

where πb^2 equates to the plume cross-sectional area at some height z, ρ = plume density and u = upward plume fluid velocity. Within the small differential portion *dz* the differential buoyancy force acting on the mass (where g = acceleration due to gravity) is described by:

$$\Delta P_B = g(\rho_\infty - \rho) \cdot dz \cdot \pi b^2$$

Equation 2-9

Equation 1-5 can by multiplied by plume velocity to represent the time-rate momentum at some height z, as:

$$\dot{m}_p u = \pi b^2 \rho u^2$$

Equation 2-10

It is desirable to describe the density difference in terms of the heat release rate (HRR), $\dot{Q}$ and so a relationship between the two entities is sought. Assuming no radiative losses from the plume, the energy flow rate can be described by the mass

flow rate (Equation 1-5) multiplied by the product of heat of combustion, c_p, and temperature difference, ΔT:

$$\dot{Q} = \dot{m}_p \cdot c_p \Delta T = \pi b^2 \rho u \cdot c_p \Delta T$$

Equation 2-11

Substituting the ideal gas law description of temperature difference equation 1-8 can be expanded to:

$$\dot{Q} = \pi b^2 \rho u \cdot c_p \cdot \frac{\Delta \rho}{\rho} T_\infty$$

Equation 2-12

Dividing out ρ and rearranging for $\Delta \rho b^2$ then yields:

$$\Delta \rho b^2 = \frac{\dot{Q}}{\pi u c_p T_\infty}$$

Equation 2-13

The continuity equation then for mass states that the mass flowing upward through the plume, over some differential height *dz*, must be equal to the mass which enters the plume over that differential height through the sides. A balance can therefore be written equating these two flow components. Firstly then, adjusting equation 1-5 the rate of change of mass over the differential height *dz* (IE. the plume mass flowing upward over height *dz*) can be represented as:

$$\frac{d(\dot{m}_p)}{dz} = \frac{d(\pi b^2 \rho u)}{dz}$$

Equation 2-14

The mass of air then being entrained through the plume sides over the same height dz is equal to;

- the *area of the sides* (product of circumference 2πb, and differential height dz), multiplied by
- *density of ambient air* (ρ_∞), multiplied by
- *horizontal entrainment velocity* (where $v = \alpha \cdot u$, from equation 1-3).

By dividing this description by *dz* to attain the *rate* of entrained air *per unit height*, we arrive at:

$$(2\pi b \cdot dz \cdot \alpha \cdot u \cdot \rho)/dz$$

Equation 2-15

Equating the two flows therefore gives:

$$\frac{d(\pi b^2 \rho u)}{dz} = 2\pi b \cdot dz \cdot \alpha \cdot u \cdot \rho/dz$$

Equation 2-16

Invoking the weak plume assumption allows us to remove ρ and π from the relationship since this simplification assumes that density differences at height are small and therefore do not change over the height of interest *dz*, finally realising the differential equation:

$$\frac{d}{dz}(b^2 u) = 2\alpha u b$$

Equation 2-17

The equation therefore describes the fundamental, overarching assumption that the mass which is entrained into the plume through its sides is equal, over the same height of interest, to the mass flow rising upward through the plume. Turbulent,

vortex driven mixing and strong density differences near the flame are ignored at this point in order to arrive at this relatively simple mass balance approach to understanding the mass flow system of the fire plume. It is therefore an implicit assumption that the injected mass (gaseous fuel) is negligible compared with the entrained air mass, which is demonstrated in the analysis chapters.

For completeness in this discussion it is important to include the derivation of the momentum and buoyancy forces descriptions arising from the same principle of approach, which are intrinsic in describing the variation of the mass flow over the height of the plume and the force which essentially drives traditional plume mass flow.

The buoyancy force ΔP_B per unit height acting upon the differential height *dz* must equate to the rate of change of momentum over *dz*. The time-rate of momentum given by equation 2-10 can then be differentiated with respect to height to give the *rate of change of momentum per unit height* by:

$$\frac{d}{dz}\dot{(m_p u)} = \frac{d}{dz}(\pi b^2 \rho u^2)$$

Equation 2-17

The differential buoyancy force acting upon the mass within the differential height *dz* was given by equation 2-6. The buoyancy force acting upon *dz* per unit height is therefore:

$$\frac{\Delta P_B}{dz} = g(\rho_\infty - \rho) \cdot \pi b^2$$

Equation 2-18

Equations 2-17 and 2-18 can therefore be equated as:

$$\frac{d}{dz}(\pi b^2 \rho u^2) = g(\rho_\infty - \rho) \cdot \pi b^2$$

Equation 2-19

We can then return to the weak plume assumption so that ρ is considered constant with height (LHS), and by re-introducing equation 2-13 to represent the density difference in terms of Q, (and multiplying out ρ, π and b^2), equation 2-19 becomes as per 2-20. The residual density appearing on the RHS is then considered equal to ambient density (Boussinesq):

$$\frac{d}{dz}(b^2 u^2) = \frac{\dot{Q} g}{\pi u c_p T_\infty \rho_\infty}$$

Equation 2-20

The two differential equations (for mass continuity) equation 2-14 and (momentum-buoyancy) equation 2-18, may then be solved by assuming that the plume radius and plume fluid velocity change to some power of the height whereby, for example:

$$b = x_1 \cdot z^m$$

$$u = x_2 \cdot z^n$$

By a process of differentiation and then by dimensional analysis the constants x_1, x_2, m and n may be found, yielding analytical solutions. A full explanation of this solution will not be reproduced here but is available in detail in [41]. Combining the results for b and u, and assuming the entrainment coefficient α from equation 2-3 to be 0.15 the following relationship is achieved for plume gas velocity:

$$u = 1.94\left[\frac{g}{c_p T_\infty \rho_\infty}\right]^{\frac{1}{3}} \dot{Q}^{\frac{1}{3}} z^{-\frac{1}{3}}$$

Equation 2-21

Then, inserting the values for b and u into equation 2-5, and once more assuming that densities within the plume approximately equal those of the bulk fluid and taking α as 0.15, the plume mass flow correlation is achieved:

$$\dot{m}_p = 0.20\left[\frac{\rho_\infty^2\, g}{c_p T_\infty}\right]^{\frac{1}{3}} \dot{Q}^{\frac{1}{3}} z^{\frac{5}{3}}$$

Equation 2-22

This is possibly the most fundamental correlation in the entrainment discussion as the proportional arguments and dimensional analysis that were used to derive it, despite the simplifying assumptions required, still form the crux of the understanding of the basic entrainment process and many analytical analyses that came after this were used to modify and improve the suitability of this proportional relationship. It should be noted that the form is the same as that of equation 1-1 resulting from the analyses of the various works in [1-5].

Finally in this analysis, ΔT is acquired considering the energy content of the plume gases from equation 2-8 that $\dot{Q} = \dot{m}_p c_p \Delta T$, while assuming no radiative losses. Rearranging for ΔT and inserting the plume mass flow relationship of equation 1-20 results in a relationship for the temperature difference at height of interest z in the form of:

$$\Delta T = 5.0\left[\frac{T_\infty}{g c_p^2 \rho_\infty^2}\right]^{\frac{1}{3}} \dot{Q}^{\frac{2}{3}} z^{-\frac{5}{3}}$$

Equation 2-23

The previous analysis is a first principle argument which relies on proportional relationships in a stable system. [1] demonstrated applicability of their work through salt-water tank experiments and comparison with other literature and despite showing favourable results the buoyant plumes of interest in [1] were not the result of a (very) hot, flaming source. In this sense, the weak plume assumption is quite suitable. Years later further experimental and theoretical work would investigate the fire plume and would adopt a collection hood to capture and characterise the smoke resulting plume.

2.3.1 Zukoski & Cetegen

Other researchers have favoured a range of *collection hood* techniques for entrainment measurements. The hood is placed above the plume where the hot gases accumulate within and fill the volume. The hot gases are extracted from the top of the hood while maintaining a steady layer height within the hood, and a simple conservation argument suggests that the rate of extraction is equal to the mass flux rate.

The horizontal interface between the hot gases in the hood and the ambient air below poses several issues [9]. The presence of the interface itself limits the entrainment flow-field immediately beneath to the horizontal, where over the height of the plume this flow will generally gain increasing vertical velocity as it approaches the sides of the plume. Further, if one wants to estimate the mass flux over the height of the plume alone, then it is necessary to assume that no entrainment occurs over the area of the horizontal interface. For the purposes of smoke management of accidental fires, the total entrainment (over plume height and interface area) may in fact be the reading of interest due to the nature of hot gas layers to form in enclosure fire scenarios. Flow visualisation techniques have been used however to determine that entrainment due to the interface is very small [6, 9]

To measure entrainment in the flaming region alone, the hood may be positioned at the top of the flaming region and hot gases collected at this height. The gases are allowed to spill under the edges of the hood and gas composition within the hood is generally assumed to be uniform having been well mixed. Thus, an analysis of fuel flow rate to the burner and fuel-air ratio of gases within the hood may be used to estimate the entrainment rate.

Cetegen et al. [6] carried out a large number of tests using hoods ($1.2m^3$ and $1.8m^3$) to measure mass flux in both the plume and flaming region as a function of height. Natural gas burners of 10cm, 19cm and 50cm diameters were used with energy release rates in the range of 20-100kW.

The authors suggested that a Boussinesq treatment of density is an inadequate definition of the plume near the burner and removed dependency of density deficit by reducing the governing equations for conservation to incompressible forms. This was so since the flame width, being approximately equal to the burner (and theoretical plume width) does not promote a transitional fall-off in buoyant pressure-with-increasing-distance from the plume centreline (as is taken as the assumption further downstream, above the flaming region. Further they alter the entrainment assumption offered by Taylor [5] slightly and subsequently arrive at a prediction of entrainment equal to that reached by the use of the Boussinesq approximation. Thus it can be said that, by incorporating some small variances (to be discussed below), Cetegen et al. suggested that the weak plume derivation of Morton et al. might be applied to strongly buoyant plumes also. For better agreement with their experimental data (and to describe the plume in terms of having an area source) a virtual origin was introduced where height z should be taken from (dependent upon source diameter, and flame length as a function of the non-dimensional ERR). Subsequently to better fit their data, the empirical constant from [*A* from equation 2-4], was chosen as 0.21 from a potential range of 0.20 – 0.23. Thus Cetegen et al. essentially modified (1) to produce:

$$\dot{m} = 0.21\left(\frac{\rho^2 g}{c_p T_\infty}\right)^{\frac{1}{3}} \dot{Q}^{\frac{1}{3}} \left(z + z_0\right)^{\frac{5}{3}}$$

Equation 2-24

The authors discussed at length the variation in entrainment over the height of the plume noting abrupt changes in functional dependencies below and above the flaming region and subsequently defined 3 regions over the plume height where mass flux was not consistent; near field- where entrainment is essentially independent of HRR; far field where a simple modified point-source correlation (equation 2-24) adequately describes the mass entrained (as a function of height $z+z_0$ and HRR Q), and a region generally existing around the intermittent flaming zone where entrainment appears to follow that of the turbulent flame but with plume-like characteristics. This is of importance because in the plume region equation 2-24 holds well (under predicting by up to 30% that of experimental measurements) but becomes less adequate closer to the flaming region. Further investigation was carried out seeking an integral solution to describe entrainment in the near field, and a model was produced. The under prediction of entrainment was ever more apparent when near field model predictions were compared to the near field experimental data. This was probably due to three particular aspects. Firstly the integral model does not account for vortex structures produced near the burner surface which prevent flame contraction as would be seen in strongly laminar flames. Further, vorticity turbulence has the effect of increasing flame surface area by creating a wrinkled flame surface (and smaller and smaller vortices), which will increase entrainment further and is not accounted for by the model. Finally, model calculations are confined to the plume mass flux alone and cannot take account of any mass flux through the interface at the horizontal layer boundary, whereas the experimental technique measured this potentially larger flux.

Therefore rather than fully turbulent profiles, the flames produced by the gas burner design had an initial laminar profile near to the burner with transition to a

fully turbulent regime only occurring at a height, sometimes several diameters from the source. The fully turbulent flames of most accidental fires will likely entrain more air due to the physically larger turbulent surface area, suggesting that this experimental design requires modification for direct application to smoke management in industry. Considering combustion dynamics further, the burner used by Cetegen et al. required the fuel to pass through a bed of glass beads before reaching the burner surface. While this may have slowed the fuel velocity somewhat in an attempt to mimic the low initial velocity of pyrolised gases from a solid fuel, the effect of radiant feedback on this process is somewhat perturbed, and the glass beads that are directly affected by the radiant feedback, subsequently heat the gaseous fuel to several hundred degrees Celsius before it reaches the burner surface. The effect on initial buoyancy of the gaseous fuel and how this impacts upon the entrainment process when compared to solid or liquid fuels is not quantified.

2.4 Heskestad, Thomas and others

Heskestad, Thomas and McCaffrey have all made significant contributions to the discussion of entrainment across the height of the plume, and for different flame height/source diameter ratios. Heskestad [7] used the large body of entrainment data produced by Cetegen et al [6] to analyse the point-source model when derived by assuming self-preserving velocity and density-deficit profiles rather than velocity and temperature-rise, as in [6]. The author substituted a description of centreline temperature (suggested by Morton) into a mass flow formula based on self-preserving density deficiency and velocity profiles to give:

$$\dot{m} = 0.071 Q_c^{\frac{1}{3}} \left(z - z_v\right)^{\frac{5}{3}} \left[1 + 0.026 Q_c^{\frac{2}{3}} \left(z - z_v\right)^{\frac{-5}{3}}\right]$$

Equation 2-25

This correlation is essentially as that of equation 2-24 but with the addition of the bracketed term and a virtual origin calculated with a different approach. This approach includes several non-dimensional terms in the derivation, each relating changes in plume velocity, radius (and a density term), which were given values based on empirical data from the literature. The temperature change correlation used in the derivation (which was suggested by Morton [11] as an extension of the weak plume theory to strong plumes) is only valid down to the mean flame height, thus equation 2-25 is also only valid above this height. Direct comparison of equations 2-24 and 2-25 based on the large amount of measured data of [6] suggest that the mass flow correlation of Heskestad (assuming self-preserving profiles of velocity and density) shows a smaller amount of variation in results and fewer obscure data points. The Cetegen et al. correlation (2-24) generally returns results of between +10% and -30% of measured plume flow rates and the Heskestad correlation (2-25) gives a spread over +/- 20%. Cetegen et al. clearly under-predicts near the top of the flaming region, gives good agreement at around twice this height, and by 3 times the flame height begins to over-predict more systematically. Heskestad by contrast, gives a spread of +/- 20% prediction over the full range of heights described above, thus is slightly more accurate at the top of the flaming region, at 3 times this height, and gives a more varied spread than Cetegen et al. at twice flame height.

Using a relationship for mean-flame height and mass flow at this height, and assuming the validity of the linear relationship between mass flow rate and height (and a dependence on Q) as suggested by other researchers [12, 13, 14]. Heskestad also produced an expression for mass flow in the (fully turbulent) flaming region:

$$\dot{m} = \frac{0.0054 Q_c z}{0.166 Q_c^{\frac{2}{3}} z_v}$$

Equation 2-26

This is in contrast to previous work [6, 10, 15] that suggested entrainment in the near field to correlate height and perimeter or height and diameter, but not with Q. When compared to various data from literature a generally good agreement is achieved for burners of diameter 0.3-0.9m, suggesting entrainment increased linearly with height up to the mean-flame height, with average error of around +/- 20% and a tendency to under-predict as the mean-flame height is approached.

Thomas et al. [10] carried out work focusing essentially on the near-field region and predominantly, where mean flame height was significantly less that the diameter of the fuel source (L/D <1), otherwise described as large area fires.

For comparison, the correlation produced was:

$$\dot{m} = 0.096 \rho_\infty \left(\frac{g \rho_f}{\rho_\infty} \right)^{\frac{1}{2}} P z^{\frac{3}{2}}$$

Equation 2-27

Thus, entrainment in the near-field was concluded to be more-or-less independent of the HRR but rather was better described as a function of the perimeter of the fire, P, and again of the height of interest, z (by way of $z^{3/2}$) particularly for the dimensional ratio described above L/D < 1. The strong plume consideration is described, in part, by accounting for the large deficit between the ambient and flame fluid densities. Thomas et al. used a different design of the hood technique (around 15 years prior to Cetegen et al.) for their work on roof vent flows, and used both gas burners and wood cribs to produce room-scale fires. The roof structure comprised vents for smoke flow and short sidewalls, pertaining to a shallow hood design. At the layer interface the plume mass flux was estimated from data of hot layer depth and temperature. Due to the dimensions of the fire source and relation to hood height, flames regularly penetrated the horizontal layer interface and thus equation 2-27 pertinent to the near field of fire plumes was appropriated.

2.5 Near-field Entrainment

McCaffrey [12] recorded data on the vertical flow velocities within buoyant diffusion plumes using cross-correlation and pressure probe techniques using a natural gas burner of 0.3m square (range Q=150-600kWm^{-2}). McCaffrey derived a correlation which gave good agreement with the previous work of Thomas [10, 43] showing appropriate resemblance in data within the continuous zone however there was some over-prediction in plume mass flow other similar work [44]. In the intermittent zone strong over-prediction was shown against all data from other authors:

$$m/Q = 0.053\left(z/Q^{2/5}\right)^{1.3}$$

Equation 2-28

where m = mass flux and Q = total HRR . A correlation for centreline fluid flow velocity was also presented and can be adjusted for the continuous and intermittent flame regions as well as the plume region by varying the values of the two introduced constants:

$$u = K\left[\frac{z}{\dot{Q}^{2/5}}\right]^{\eta} \cdot \dot{Q}^{1/3}$$

Equation 2-29

where K and η are the variable constants assigned based upon fire plume region of interest. Describing the mass of air entrained in terms of the fuel flow rate [12] demonstrated that within the total flame region approximately 20 times the stoichiometric air requirement was entrained, which was noted to be roughly 30% higher than the equivalent data of [6]. Data from another study [45] had showed only ~5 times the stoichiometric requirement being entrained up to the flame tip in some momentum jet flames. McCaffrey showed that around ~5 times the stoichiometric requirement in had been entrained by approximately the top of the

continuous flame region and proposed that large-scale turbulent eddy mixing was the dominant entrainment mechanism below the flame tip [12]. Figure 2.3 gives a representation of McCaffrey's discussion. Finally it is suggested in the conclusions to [12] that the results were typically much higher than those for the point source model, and that this and a portion of the disagreement in entrainment correlations and recorded data in the literature may be connected to increased entrainment from disturbance to the ambient environment when a door to the lab, for example, is opened during experimentation.

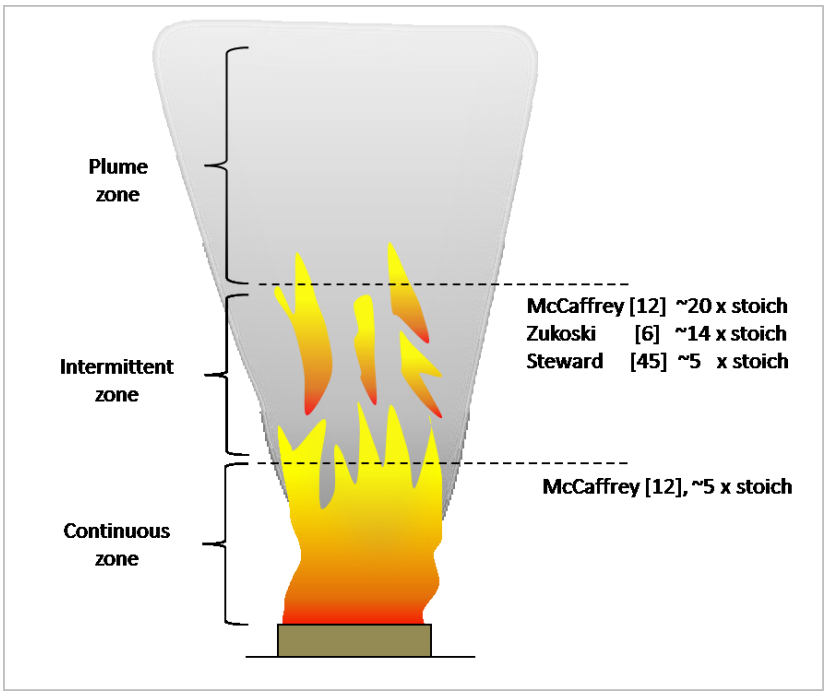

Figure 2.3: Entrainment magnitude as a function of stoichiometric air requirement. Data as reported in [12].

2.6 Vortex Generation, Flame Instability and Flicker

The literature on entrainment and vortex generation in flames is confined to a relatively small number of authors by comparison to that of the whole fire plume, or

non-reacting plumes. This is certainly the case concerning the *fire safety* literature. Pertinent examples include [47, 49-53].

Cetegen & Dong [46] proposed two modes of flame instability, namely *sinuous* and *varicose* forms. These are best described qualitatively as in figure 2.4:

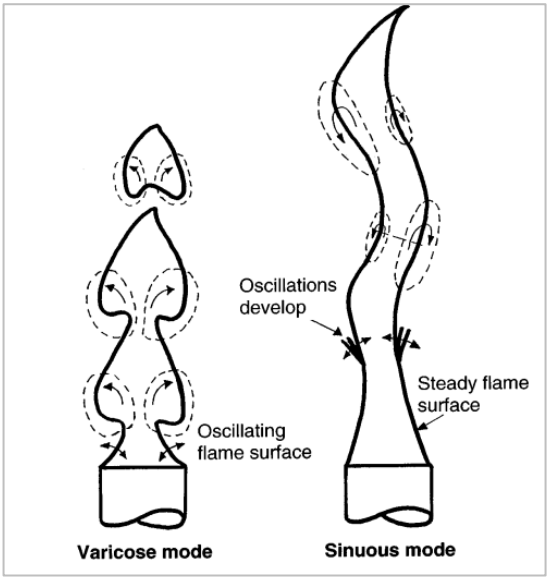

Figure 2.4: Varicose and sinuous flame instability modes as defined in [46]. Image reproduced from [46].

The motion of the flame during the sinuous mode is described as meandering and is said to be characteristic of flames with small diameter orifices. This mode was witnessed to originate dome distance downstream of the nozzle exit in the contracting regions of the flame. By contrast the varicose mode develops close to the orifice and manifests as (essentially) axis-symmetric perturbations of a contracting flame surface resulting in the generation of toroidal vortex structures that convect along the whole flame height, burning out at the self-imposed flame tip, causing periodic flame height fluctuations when viewed globally. Subsequently it was noted that the experimental flame would switch from one mode to the other however the

likelihood of generating the varicose mode improved with increasing Richardson number [46] where defined as:

$$Ri_0 = gD/V_F^2$$

Equation 2-30

Where g = gravitational acceleration, D = orifice diameter and V_F^2 = fuel exit velocity at the nozzle. The circular nozzle diameter was varied in this work from 2.5 to 7.6cm. It was previously demonstrated [49] that more buoyantly dominated flames (lower fuel velocity and/or larger source diameter) resulted in a flame front which would contract sharply at the nozzle centreline creating toroidal vortices that form near the burner exit and induce the varicose mode to dominate the instability mode in such cases. The sinuous mode can be described as a *convective* instability since the oscillation develops some way downstream of an otherwise stable flow [46] whereas there appears to be some debate about the appropriate definition of the varicose mode. An explanation was previously offered [49] that the varicose mode was linked to buoyant convective time scale and a strong coupling was argued between the unstable flame zone and vortex flow field behaviour. Subsequently the transition observed when a flame with an initial laminar region births toroidal vortex structures around the transition point to its comparatively downstream turbulent regime and the ability for flames to switch between the sinuous and varicose modes suggest that the varicose mode is its own type of convective instability rather than a global instability [46]. The argument for toroidal vortex generation to be considered as a global flame instability is put forward in [48] based on the premise that since no external disturbances are required to trigger or sustain vortex motion, buoyant instability should be considered as a global, absolute instability. The argument in [48] however does not appear to address the implications of the two modes defined in [46]. This debate can be found in the literature as recently as 2003 [48] and possibly more recently still, and is worth

consideration since depending upon the point of view, affecting the effective buoyant strength by altering the magnitude of the gravitational acceleration (anti-stream-wise component) with respect to the plume propagation and/or the velocity difference at the flame boundary (which has typically been confined to buoyant magnitude vs ambient bulk fluid) may take on varying significance.

The question of the frequency at which flicker of a flame occurs is regularly cited in the literature and a short evaluation is presented in [40]. The following relationship is given for the frequency f (Hz), where the product is proportional to $D^{-1/2}$ (where D is the diameter of the source) [55]:

$$f = (0.5 \pm 0.04)(g/D)^{1/2}$$

Equation 2-31

and visual estimates of the average flame height are around 10% greater than the 0.5 presence probability location [54]. Equation 2-31 gives good agreement [40] with [50], [52] and [56].

[50], [57] and [58] carried out flame flicker frequency analyses and compared results, which are visualised in [40]. Figure 2.5 shows 1.3 seconds of cine film showing oscillations of apparent varicose mode [46] vortex shedding:

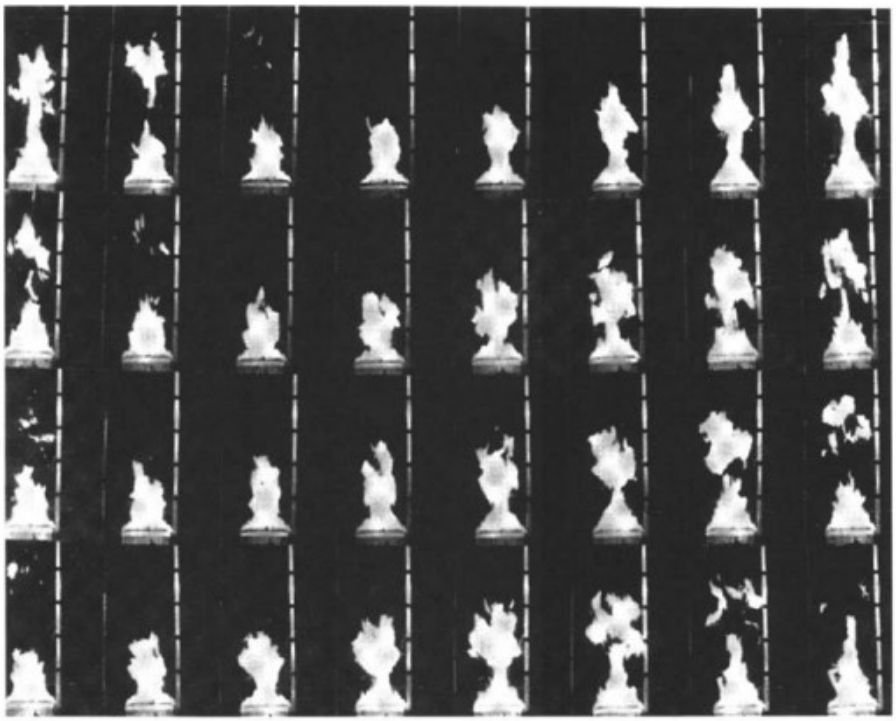

Figure 2.5: Vortex shedding of a flame from a 0.3m porous burner, showing approximately 3Hz oscillation (Image = 1.3sec period). Image reproduced from [40, 57]

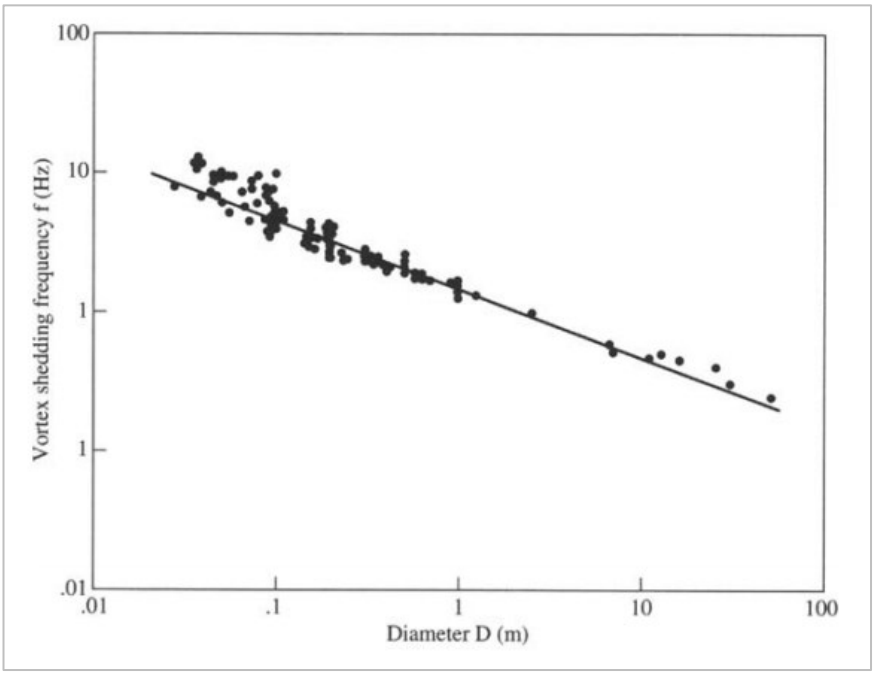

Figure 2.6: A general decrease in oscillation frequency with increasing burner diameter is demonstrated for the results of [50]. Image reproduced from [40, 58].

Such results as displayed in figure 2.6, when aligned with the assertion in [46] that varicose mode vortices are more probable with larger Richardson number, and therefore larger diameter source, underlines that the varicose mode average frequency is probably lesser than that for the sinuous mode, if the varicose mode is indeed more common with increasing diameter. This might be intuitive since the varicose vortex generation and shedding is more physically complex in its evolution that the smaller scale sinuous flicker.

2.7 Flame Dimensions

2.7.1 Flame Length

Many authors have published data on the flame length of a range of flames from varying source diameters, fuel types and diffusion/jet regimes. Two of the more commonly cited correlations in fire safety engineering include:

Zukoski [59] for values of $\dot{Q}_c^*$ greater than approximately 5:

$$l = 0.23\dot{Q}_c^{2/5} \text{ (m)}$$

Equation 2-32

Heskestad [60] adopted a modified Froude number to arrive at the correlation:

$$\text{L}=0.23\dot{Q}_c^{2/5} - 1.02D$$

Equation 2-33

The ratio of flame to characteristic source diameter D ($\pi D^2/4$ for non-circular sources), has been commonly demonstrated in the literature [45, 61, 62] to show proportionality with the arrangement:

$$\left(\frac{\dot{m}^2}{g\rho_0^2 D^5}\right)^x$$

Equation 2-34

where $\dot{m}$ is the mass burning rate, ρ_0 is a constant, ambient density and x is a variable exponent.

Of further interest are the attempts to qualitatively and quantitatively validate standard entrainment correlations using flow-visualisation apparatus. Zhou & Gore [16] used a laser Doppler Velocimeter (LDV) with a seeded ambient enclosure to study the mean and transient flow field induced by pool fires. Radial and axial mean velocity description is presented by vector plot to identify the flow pattern. The authors showed that in contrast to the inward flow-field, instantaneous outward mass motion from the fire plume, caused by local mass expansion occurred simultaneously, and labelled this process of "extrainment". This process is small however compared to the inward flow field and the usefulness of quantifying the extrainment mechanism further for the purposes of smoke control for fire engineering is debatable. Estimates of the entrainment flow rate based on various selections of radial position, R, are presented. There is significant discussion over the difficulties in defining R at any one time and at any height and the significant effect this will have on the estimated entrainment rate are alluded to. A cylindrical hood is also utilised and the technique of Cetegen et al. is adopted to acquire an independent entrainment estimate based on this technique. The complete set-up is of concern however, specifically regarding direct comparison with previous entrainment investigations. The 7.1cm pool fire is enclosed in a 1.0m x 1.0m cross-sectional enclosure with plexi-glass walls (3m in height) and a metal "floor" of radius of 0.51m located in the centre of the enclosure. Air flows into the chamber underneath the perimeter walls at a height significantly below the location of the pool fire and the authors suggested that the movement of air upward along the walls did not affect the fire flow near the plume. The bottom edge of the hot layer captured by the hood was located 0.64m above the pool source, and the "top" of the flame was described as being located 0.36m above the source. The height of the plume region, by definition then, was around 0.28m, or 4 times the diameter of the source. The results of the experiment were compared with various past authors but it is unclear as to whether, in the case of comparison with Cetegen et al. for example,

the near-field or far-field correlations were utilised. This is of interest since the accuracy of each correlation suggested by Cetegen et al. for near and far-field regimes are most ambiguous over the height measured in Zhou & Gore that is - over the transition from near field to far field, including the intermittent region of the plume. Further comparison between Cetegen (and other hood-based experiments) with both hood measurements and height/radius-based integration from Zhou & Gore are described as giving reasonable agreement, but do give a spread in results ranging approximately one order of magnitude. Certainly though, the qualitative flow vector plot can be very insightful in aiding visualisation of the transitional fire flow field. This would be particularly advantageous in a more complex flow field such as that of the crossflow case to be studied herein. Zhou, Gore & Baum subsequently conducted the first particle imaging velocimeter (PIV)-based measurements of the flow field around a pool fire [17]. This technique is similar to that of LDV but allows the necessary data set to be captured in a much shorter time. The authors suggested the usefulness of the fire Froude number (specifically, using approximations of velocity and length scales made by [15]) for correlating their pool fire entrainment data. Of most interest is the potential for the qualitative description of flow field dynamics offer by PIV.

2.8 Effect of Wind

2.8.1 Flame Tilt

Numerous correlations have been developed to estimate the angle of tilt of a flame following exposure to a forced cross flow. The following approach has been shown to give fair estimates for a range of fuel types [40]:

$$cos\theta = d'(u^*)^{e'} \qquad for\ u^* \geq 1$$

Equation 2-35

and

$$cos\theta = 1 \qquad for\ u^* < 1$$

Equation 2-36

Where

$$u^* = \frac{u_w}{u_c}\ if\ \ u_w \geq u_c$$

Equation 2-37

And

$$u^* = 1\ \ if\ \ u_w < u_c$$

Equation 2-38

In this explanation u^* is a dimensionless wind speed which is a ratio of wind speed (u_w, ms^{-1}) to a characteristic velocity which is a function of the fire source diameter:

$$u_c = (g\dot{m}''D/\rho_a)^{1/3}$$

Equation 2-39

Where $\dot{m}''$ is the mass burning rate ($gm^{-2}s$). For the constant d' and e' a range of values have been generated for various fuels (LNG and hydrocarbon pool fires and wood crib fires) [40] and figure 2.7 demonstrates calculated flame tilt against dimensionless wind speed u^*. It can be noticed that there is some significant scatter, especially at low comparative wind speeds, however the general trend of increasing tilt angle with increasing wind speed is abundantly clear. The graph uses the correlation set outlined above and uses values for the constants d' and e' from the American Gas Association (AGA) data [40]:

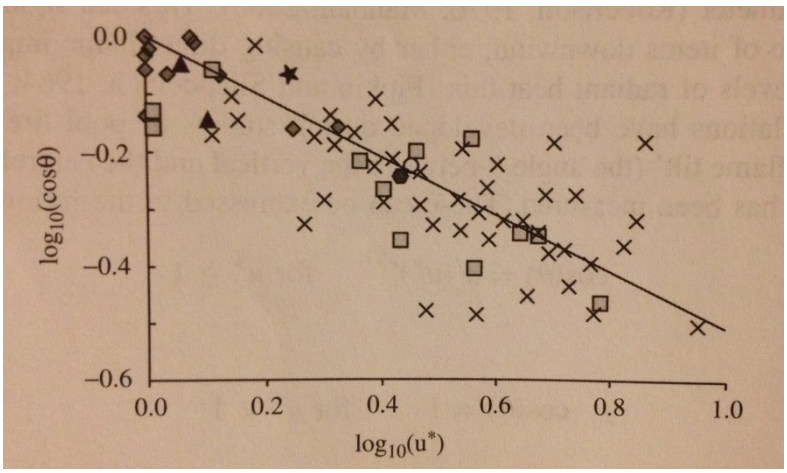

Figure 2.7: Typical relationship between flame tilt and non-dimensional wind velocity, using the AGA correlation data. Images reproduced from [40].

There are many approaches in the greater literature in general for correlating flame tilt angle with wind speed [64]. Nelson and Adkins [65] were able to demonstrate a log-log straight line (gradient 0.29) relationship between the tangent of the tilt angle and a Froude number, defined as Fr = U_w^2/gH (which requires the knowledge of H = flame height). A substantial work was carried out by Fang [66] in which flame angle was demonstrated as a function of a Froude number based on the flame depth, D:

$$\frac{tan\theta}{cos\theta} = C_D(U_w^2/gD)$$

Equation 2-40

Where $C_D = C_F/2\left(1 - \rho_0/\rho_a\right)$, in which C_F = a flame drag coefficient and ρ_0/ρ_a is the ratio of density at the fuel centreline/ambient air. Equations very similar to equation 2-40 were independently developed by a handful of different researchers [Pitts 64]. Quite contradictory findings are apparent in the literature. Rios [68] plotted flame drag coefficients against the product of Reynolds and Froude numbers for wood crib tunnel fires finding a strong link between drag coefficient

and wind velocity whereas Fang [66] and Welker & Sliepcevich [67] found this to the contrary. Rios [68] suggested that the variable depth of the flaming zone in cross flow conditions may explain the drag coefficient dependence. Such a model would not fit the constant flag drag coefficient of the other authors however.

2.8.2 Flame Length in Wind

Flame length is generally understood to shorten under cross flow conditions [63] and a large amount of data is available for many variations in boundary conditions [64]. It has been demonstrated that a non-dimensional flame length can be show proportionality with two non-dimensional groups – these include equation 2-34 and a modified Froude number, where the modified Froude is characteristic of the ratio of the inertial cross flow force to the buoyant force of the fire. Thomas demonstrated for line fires, cross flow flame height correlation with the following:

$$\frac{L}{D} = K(\dot{m}''^2/g\rho_0^2 D)^{0.43}\ (U_0^2/gD)^{-0.11}$$

Equation 2-41

where K is an empirical constant. More efficient plume entrainment (and therefore burning of the gaseous fuel over a shorter downstream distance from the base of the fire) in the cross flow case has been previously been suggested to explain the shortening flame length observed [68]. In the same paper a relationship was demonstrated between L/D and $\left(\dot{m}''^2/\rho_0(gD)\right)^{1/2}$. Similarity can of course be noticed here with equation 2-41 minus the modified Froude included in Thomas' work. Putnam [69] demonstrated proportionality of flame height with $(U_0/gL_0)^{-1/4}$ (where L_0 = no-wind flame length) and horizontal flame extension downwind with $(U_0/gL_0)^{-1/6}$ for strong wind cases.

2.9 Plumes in wind

Previous experiments attempted to achieve a quiescent atmosphere in order to study entrainment due to the fire-induced flow alone and to avoid the effects of a turbulent atmosphere, characterised for example, by a laminar crossflow, normal to the direction of the fire plume. While the rise and dispersion of non-reactive plumes (to replicate smoke from a tall factory chimney or discharge from a volcano for example) through the atmosphere have received considerable focus with similar approaches to that of [18]. The *entrainment rate* of fire plumes - representative of an accidental infrastructure fire event *subjected to some strength of crossflow*, have not. For the purposes of the this work, the term *non-reactive plume* is used to describe the smoke stack resulting from an industrial chimney or from a volcano, for example which is studied over a downwind length-scale orders of magnitude larger than the typical infrastructure fire size. The diminishing buoyancy of the smoke in these cases is studied compared to the atmospheric mixing with fresh air. The term *reactive plume* is used here to describe the infrastructure size fire for which the smoke plume is orders of magnitude smaller than the non-reactive examples, and a significant portion of the overall fire plume is composed of the flaming combustion zone and where there is a sharp temperature boundary between this combustion zone and the hot smoke it produces.

Indeed, wildland fires subjected to crossflows and some measure of turbulent atmosphere have received significant study regarding the consequential flame tilt angle and subsequent increased radiant heat flux transmitted to the forest fuel bed [64], but the question of the influence of a crossflow on the entrainment rate in the near-field to the fire source has received almost no focused research. The classical approach to non-reacting plumes in a cross wind has been in the decoupling of wind velocities, normal and parallel to plume direction, with a separate entrainment assumption parameter assigned to each. These correspond to two entrainment mechanisms; the first due to the difference in plume velocity u and wind velocity

component $v\ cos\theta$ in the direction of the plume; the second due to the wind velocity component $v\ sin\theta$ normal to the plume (figure 2.8).

Hoult & Weil [18] produced a simple entrainment model to explain the rise and growth of a turbulent plume in laminar crossflow. The conservation equations described in [1] (and therefore used as a basis in [6]) are extended to describe the velocity of the fire flow – or in this case *crossflow* – in terms of components both *normal and parallel* to the direction of the plume flow. This is necessary since previously where quiescent atmospheres were assumed for experiments and it was considered that there was no tilt, only the normal component was required to describe the entrainment flow field, since the plume remained vertical.

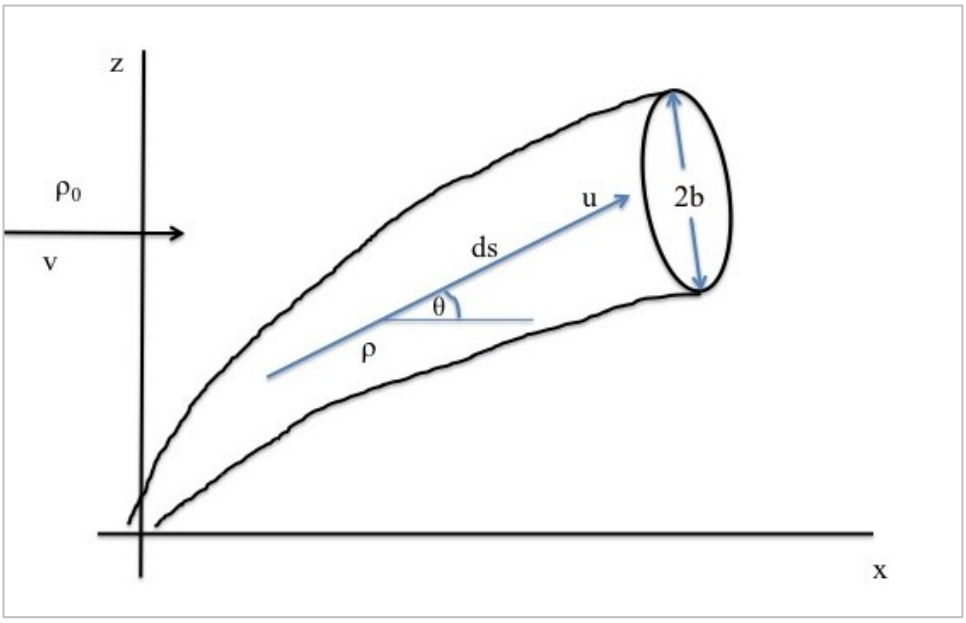

(a)

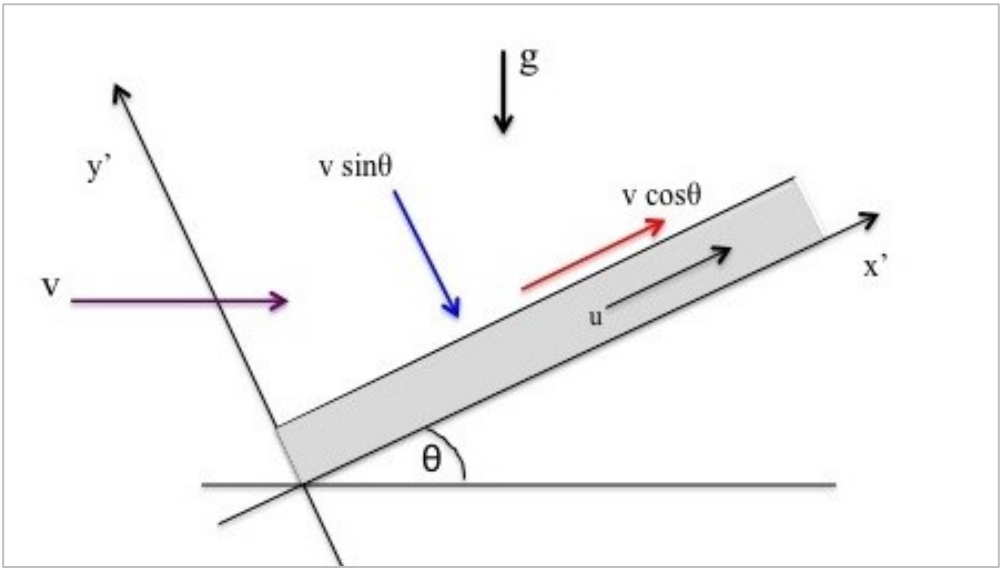

(b)

Figure 2.8: (a) Simple schematic for a plume in a crosswind (intermediate regime). Part (b) highlights the decoupling of wind components, a function of initial wind speed, plume velocity and tilt angle. It is then possible to incorporate such assumptions into conservation equations [18]. A c*onservation of mass* equation, for example, may be formed to include each specific component. Image adapted from [18].

Thus, the stronger the crossflow - the greater the flame tilt angle, and the greater the proportion of the cross flowing air mass that must be considered to be flowing parallel to the plume, rather than normal to it. Hoult & Weil explain this with a vector-based description of the crossflow relative to the plume and a simplified description of this can be seen as Figure 2.8.

Essentially, what is done is to extend the formulae and assumptions based on first principles defined in the previous entrainment papers to include descriptions of how each component of the crossflow impacts the intensity of the entrainment process. Although this process is controlled by many different physical attributes (such as turbulence, generated shear and specific boundary conditions along the flame/plume edge) a more achievable quantitative description at this stage can be described by considering the method of [18].

One of the basic but fundamental assumptions that underpins [1, 6] for example, is that the mass flowing upward through the plume cross-section over height z, must be equal to the mass entrained into the surface of the plume over that height. That is to say:

$$\frac{d}{dz}\pi r^2 u = 2\pi r \alpha u$$

Equation 2-42

where the density term has been omitted on each side by assuming only small density differences occur and crossflow velocity v is given as a function of plume velocity u.

Clearly this is a simplified analysis, but may be combined with empirical data (and combined with assumptions for momentum and buoyancy) to arrive at the "ideal plume" correlations. Hoult & Weil essentially separated the crossflow into the parallel and normal components to give entrainment rate as a function of the velocity of the plume relative to its surroundings:

$$\frac{d}{ds}\pi r^2 u = 2\pi r \alpha \left| u - v\cos\vartheta \right| + 2\pi r \beta \left| v\sin\vartheta \right|$$

Equation 2-43

where α and β are entrainment coefficients specific to each crossflow component and are assumed constant over the entire height of the plume. The authors also rely on descriptions of momentum and buoyancy length scales, measuring the scale of a pure jet (zero initial buoyancy) and a pure plume (zero initial momentum) accordingly. These are essentially ratios of appropriate functional parameters where the momentum length scale is suggested as: $l_m = r^*(u/v)$ and the buoyancy length scale is suggested as: $l_b = F/v^3$ where $F = ub^{2*}[(T_i-T_1)]^*g$. F then, is a non-dimensional expression of the relative buoyant force. These scales formed an important part of

the authors' analysis and predictions of plume angle and structure downwind of the source and have been used as measures of the curvature of the plume, but might also be helpful in analysing the dominant regime of the near field fire plume under strong crossflow conditions for the current study.

While the work of [18] gives good numerical agreement with a salt solution tow tank experiment conducted by the authors (plume height predicted to within 15% of observed data), the fundamental principles requiring to be addressed for the infrastructure fire plume are not applicable in the study. The salt solution tow tank experiment scales up to describe a (smoke stack) plume, mainly governed by momentum at the source, and reaching over 500ft vertically and up to 6000ft downwind. While the deconstruction of the crossflow into vector components gives an interesting and potentially viable approach to consider for the fire plume case, numerous pertinent concerns are not applicable in the study. Most notably:

1. Flaming region entrainment (the flaming region will account for a substantial proportion of the overall infrastructure fire plume)
2. Strongly buoyant source
3. Combustion process and energy release rate affected by increased oxygen flow
4. Simulation of gaseous fuel and oxidiser mixing at the source/flame boundary
5. Fully turbulent description of flaming region and plume
6. Impact of increasing crossflow strength on the usually symmetrical 360° fire wind flow field.

There is some discrepancy over the theoretical basis for a decoupled velocity component entrainment assumption to be additive with both parts carrying equal weighting as described above. [18] subsequently expressed this as in equation 2-43 where normal and parallel velocity components are simply additive. Devenish et al. [75] compared results for a LES model and Lagrangian stochastic model (developed by MET Office) finding that results correlated well for strong and weak crossflows, but diverged in the intermediate regime (moderate wind speed). It was thus

suggested that entrainment would be overestimated for the middle regime by a linearly additive approach. It was suggested quite simply, that there is no reason to presume a linear addition of the different components, and subsequently proposed:

$$\frac{dV}{ds} = \frac{2b|w|}{\hat{u}}\left(\alpha|w| + \beta U\right)$$

Equation 2-44

$$\frac{dV}{ds} = \frac{2b|w|}{\hat{u}}\sqrt[n]{\left(\alpha|w|\right)^n + \left(\beta U\right)^n}$$

Equation 2-45

A similar but more fundamental approach to including components of stream-wise and cross stream entrainment parameters will be reviewed in chapter 2.11.3.

2.10 Instances of Flames in Crossflows

Work by Schmidt [2] in 1941 appears to be one of the earliest accounts of consideration of the behaviour of convective currents at some height above their source in the literature - point and line sources with turbulent flows were described by Schmidt as *confined within a conical regions* as they rose through a uniform atmosphere. Schmidt supposed that a description of the temperature and velocity within this region could be achieved by balancing the horizontal turbulent transfer of heat and momentum against the vertical transfer by convection, allowing for the effect of buoyancy

Lavid & Berlad [29] carried out a theoretical study of the chemically reacting boundary layer flow over a horizontal flat plate with gravitationally induced

buoyant force. A diffusion flame sheet was model was developed to describe the combustion process and define the structure of the problem.

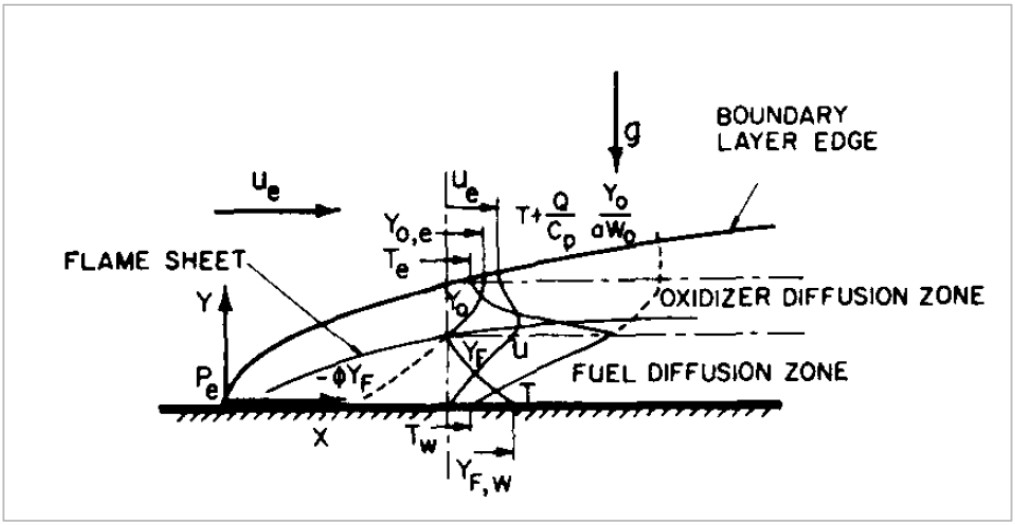

Figure 2.9: Physical model with flame sheet approximation over a horizontal flat plate. Image reproduced from [29].

The model depicts that gaseous fuel is transported from the burner surface to the boundary layer by convection and molecular diffusion where it reacts with the oxidiser, which is also transported to the flame/boundary layer by convection and molecular diffusion but from the main stream. This model was not new and had been considered previously by other authors [31-34] however the effects of gravity were not part of the paradigm of these works and the body force was consistently removed from the governing equations. Previously, [30] performed a general dimensionless analysis of the longitudinal and transverse momentum equations for boundary layer flows over a wedge and showed that the structure of the boundary layer is partially determined, for the mixed convection case, by a mixed convection dimensionless ratio between the interacting buoyant and inertial forces. Two distinct correlations were acquired to characterise the inertia-gravitational system:

$$\xi_x = \sin\theta \frac{Gr_x}{Re_x^2}$$

Equation 2-46

$$\xi_y = \cos\theta \frac{Gr_x}{Re_x^{5/2}}$$

Equation 2-47

where θ = tilt angle of interest, measured from horizontal. Typically then for the mixed convection regime when:

$\xi < 1$, inertia is increasingly dominant

$\xi > 1$, buoyancy is increasingly dominant, and

$\xi \approx 1$, inertial and buoyant forces are of comparable importance.

Equation 2-46 is derived from the longitudinal momentum equation and is said to be suitable for wedge and vertical wall scenarios whereas equation 2-47 is derived from the transverse momentum equation and is described as being characteristic of horizontal flat plate and very small inclination cases - which will be discussed in greater detail later. These quantities are not fixed and will vary at every point along the x (horizontal) axis since this length scale is contained in both the Grashof and Reynolds correlations, with Gr exhibiting greater dependence, as described previously. It is intuitive to consider then that further along the horizontal scale the buoyant force will acquire greater importance in the general Gr_x/Re_x ratio. Indeed the authors [29] suggested that at the leading edge boundary layer regime $\xi_y < 1$ and inertia was dominant and that moving down stream would result in a transition point $\xi \approx 1$, followed by a region where buoyancy and free convection would dominate over forced convection, $\xi > 1$. The focus of [29] however was specifically

on the inertia dominant boundary layer region where a representative value of $\xi = 0.003$. Other work has been produced however, which incorporates both the inertia and buoyant force-dominated regimes into the focus. Generally speaking, most of these works cite [29] and [30] as important preceding work.

Apte et al. [24] investigated flame spread over a horizontal surface of polymethylmethacrylate (PMMA) under cross flow conditions in a wind tunnel. Cross flow velocity ranged from 1m/s to 2.1m/s and the energy release rate of the fire was calculated to grow from several kW at ignition up to around 800kW as the flame spread along the 2.4m long / 0.65m wide PMMA sheet. In this test series the cross flow was induced using centrifugal exhaust fans located at the rear of the tunnel. The combustion products and hot gases were then transported directly to gas composition measurement system for analysis. Greater detail on the experimental design is available in related literature [25]. The most significant contribution from [24] for the current investigation was the observation and characterisation of two fire plume regimes as the ratio of cross flow strength (forced flow) and buoyant force were varied over time due to the lateral fire growth. Figure 2.10 depicts the two regimes.

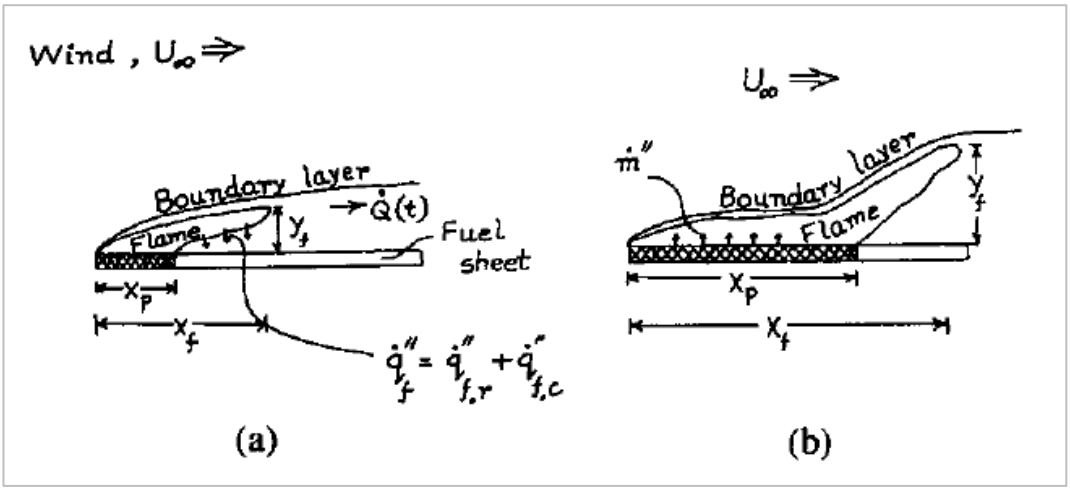

Figure 2.10: Describes the two regimes in the flame spread model (a) boundary layer mode and (b) plume mode. Image reproduced from [24].

Figure 2.10 part (a) shows the initial flame spread mode during which the flame was described as being confined within a *boundary layer*, and is comparable with figure 2.9. As the flame propagates further and the global buoyant force increases the flame begins to stand up, at an angle as depicted in (b) or closer to vertical later as the flame base footprint increases further. The system then increasingly resembles the traditional fire plume structure and (b) is referred to as the *plume* mode. This represents the scenario predicted in [29] where buoyancy becomes more important with increasing distance along the horizontal axis. The inertia of the cross flow runs left to right as the fans, located outside of this image to the extreme RHS draw the air in. The thickness of the boundary layer compared to the flame thickness was investigated in order to determine if the measured flame thickness (IE. flame tip height, denoted y_f in figure 2.10) aligned with the semi-empirical correlation for a turbulent boundary layer over a flat plate, given as:

$$\frac{y_f}{v/U_\infty} = 0.376\left(\frac{x_f}{v/U_\infty}\right)^{4/5}$$

Equation 2-48

where y_f = flame thickness (m), v = dynamic viscosity of gas (m^2s^{-1}), x_f = flame length (m) and U_∞ = average wind velocity in the tunnel (ms^{-1}). Rearranging for the flame thickness gives:

$$y_f = 0.04\frac{x_f^{4/5}}{U_\infty^{1/5}}$$

Equation 2-49

The experimental data was then graphed and a relationship between y_f and x_f was expressed (where $y_f = 0.3x_f$ in that case). The flame was calculated to be almost an order of magnitude larger than the non-burning turbulent boundary layer. The thickening of the boundary layer therefore is driven by buoyancy and pyrolysis mass flux. A comparison of the magnitude of the buoyant force and the inertial cross flow force was conceived by interrogating the normalised flame thickness and the Froude number and plotting the graph for:

$$\frac{v_f}{v/U_\infty} \quad vs \quad \frac{U_\infty}{\left(g\dot{Q}'/\rho_g\, c_g T_s\right)^{1/3}}$$

Equation 2-50

where g = gravitational acceleration (ms^{-2}), $\dot{Q}'$ = heat release rate per unit fuel sheet width (kW/m^{-2}), ρ_g = gas density, c_g = gas heat capacity ($kJ\ kg^{-1}\ K^{-1}$) and T_s = fuel surface temperature (K). It can be seen therefore that the Froude number is taken as the ratio of horizontal force and upward force in the mixed flow stream. It was determined that the flame thickness grows with a decrease in the Froude number. These two attributes correspond of course, to an increase in the buoyant force of the fire. The transition from the boundary layer to plume model regimes, as depicted in figure 2.10 is marked by a sharp increase in the angle of tilt (or of propagation of the flame) and the authors found that this occurred in each case at a Froude number proportional to the wind velocity (for instance at Fr = 0.6 for $U_\infty = 1ms^{-1}$, and Fr = 1.2 for $U_\infty = 2.1ms^{-1}$).

Of subsequent interest is the approach to estimating the rate of entrainment of oxygen adopted whereby the tilted flame height was considered as a turbulent forced convection boundary layer over a flat plate. Referring to work by [27] and [28], the authors suggested for the entrainment rate of oxygen (m'_{ox})($kg\ m^{-1}s^{-1}$) into the boundary layer model:

$$\dot{m'}_{ox}(x_f) = 0.313\rho_g Y_{ox,\infty} U_\infty \left(\frac{\nu}{U_\infty}\right)^{1/5} x_f^{4/5}$$

Equation 2-51

where $Y_{ox,\infty}$ = mass fraction of oxygen in ambient air.

Although the authors do not use the following description explicitly, it is being alluded to that flame thickness and tilt angle can therefore be characterised by a Richardson number - the ratio of the local Grashof and Reynolds numbers at any point along the length of the flame. This is true for locations within both the boundary layer and plume modes.

Torero and various co-workers produced a number of related works [20-23] following theoretical and experimental investigations into the transport mechanisms controlling a diffusion flame while varying the buoyancy across a range of normal and microgravity regimes. Laminar diffusion flames were established over a horizontal flat porous burner where fuel (ethane) was injected through the burner and the oxidiser (air) was delivered by forced flow parallel to the burner surface, therefore perpendicular to the natural buoyant force of the flame. The fuel injection velocity and forced air-flow velocities were varied and the effects studied. Data was recorded by video, gas analysis of combustion products and point temperature measurements with thermocouples.

The work of Torero et al. [20] is of particular interest to the current study since even though the premise of microgravity environment is not wholly applicable to the approach of introducing perpendicular pressure fields, the analysis of these flow parameters and the experimental set up point out details and considerations of interest that will inform the current experimental set up and analysis.

With the desire to study a buoyant diffusion flame [20] a porous burner was introduced since by substituting the combustible fuel of a pool fire, for example,

with the gas fuel of the burner the combustion problem was simplified since the fuel supply is no longer a function of heat transfer in the combustion process and the two variables can be manipulated independently, due to which this configuration allows for more effective study of phenomena such as entrainment due to thermal gradients. An observation pertinent to the current work was the characterisation of the flame structure, related to the balance of buoyant and perpendicular oxidiser pressure fields. At the leading edge of the burner the flame was found to present in a boundary layer regime, with the axis of propagation (angle of flame tilt) lying somewhere approximately between vertical and horizontal and further upstream the flame region ends and a plume region prevails, the plume region typically assumed more vertical, upward propagation. Figure 2.11 depicts the boundary layer region and the plume region described as the forced flow oxidiser (U_A) is introduced to the injected fuel flow (V_F). The boundary layer region forms near the leading edge of the burner. Approximate momentum and thermal boundary layers are outlined, as is the height of the tunnel compartment that housed the apparatus. The chamber functions similarly to a wind tunnel in that the forced flow is limited to the oxidiser flow field, IE. a unidirectional flow. Lateral inflow at the sides of the flame was minimised further since the burner width equalled the width of the chamber, and was flanked by solid walls (except for a window area further upstream). An important observation that is highlighted in figure 2.11 (upper image) is the impact of the chamber boundary upon the oxidiser flow field and flame shape.

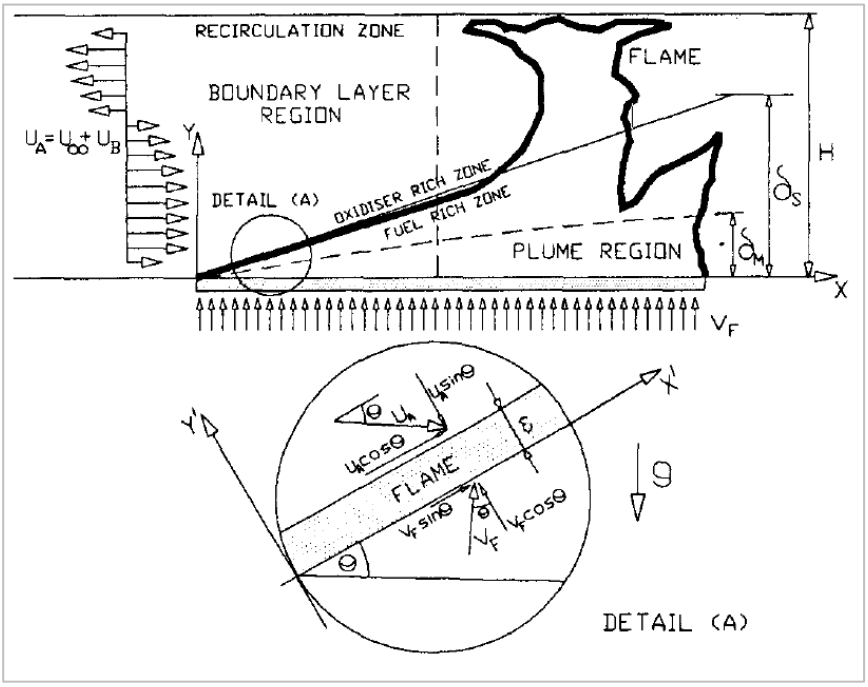

Figure 2.11: Boundary and plume regions and recirculation zone flow in the experiment by Torero et al [20]. Image reproduced from [20].

The flame/plume impinged upon the ceiling of the chamber at the more buoyant plume region. As with typical fire plumes in compartments this caused a lateral outward flow of plume gases upon meeting the ceiling boundary and a recirculation zone was established which flowed in opposition to the forced oxidiser flow. The vector arrows to the LHS of figure 2.11 describe this flow pattern. The focus of this work was primarily on the boundary layer region though and the recirculation effect was determined not to negatively influence the fluid behaviour at the area of interest. Concerning the dominant flow force across the boundary layer and plume regions it is highlighted the Richardson number is again cited and the controlling conditions are outlined where if the magnitude of the forced flow is large compared to V_f the flame is said to be inertia dominated (where the boundary layer regime is extensive and the plume region is small or barely noticeable) and when the forced flow is small and V_f is large, the flame is noted to be dominated by the buoyant force (characterised by a negligible or small boundary layer region and more or less

vertical plume region). Forced flow velocities were in the order of 0.03 to 0.3m/s and a characteristic U_B (buoyant force which contributes to the forced flow field) was found to be in the order of 0.1m/s, comparable with the forced flow velocity range. Finally the authors noted that since fuel injection velocity was approximately 50 times smaller than that of the forced flow velocity, a boundary layer region tied to the burner surface was previously expected. Instead a detached flame was regularly observed and the lower "detail" image in figure 2.11 was produced to describe the flow components that contributed to this phenomenon. A new coordinate system tied to the stoichiometric line was defined and the forced convection could then be characterised by the summation of the *y′ components* (the tilted y axis) of both the oxidiser and fuel velocities $U_A \sin\theta$ and $V_F \cos\theta$ respectively. Due to the newly defined "tilted" velocity planes (x', y') the Grashof number used in the Richardson number ratio was modified to accommodate the decreased gravity field that describes the relative buoyant force. In this instance the modified Grashof number was:

$$Gr = \left(\frac{2T_a}{T_a + T_g}\right)\left(\frac{g.tan\theta \cdot x^3}{v^2}\right)$$

Equation 2-52

Further detailed description of this study and subsequent overview are provided in [21] and [23] respectively. Audouin et al. [22] presented a novel technique to acquire average centreline temperature distribution and average flame height in simulated pool fires using images from a standard video camera and relationships with standard correlations. The process is described by which local mean luminous intensities of each video frame can be acquired by performing the arithmetic mean in each case. By quantifying the individual intensities on a suitable scale and assigning a corresponding grey scale, a time-step of grey levels can then be averaged to acquire the mean luminous intensity during the time period of interest. Thresholds can then be assigned concerning luminosity or presence probability for

example in order to acquire average flame temperature and flame height contours. The results can be acquired based on varying parameters that correspond to competing descriptions of flame characteristics such as time-dependent flame height descriptions or length-scale correspondence. In summary this paper contains an important overview of diffusion flame characterisation literature, a discussion on the impact of confinement upon entrainment and describes a still-image technique that can be utilised for dimensional analysis and fundamental characterisation of simulated pool fires with the use of gas burner diffusion flames.

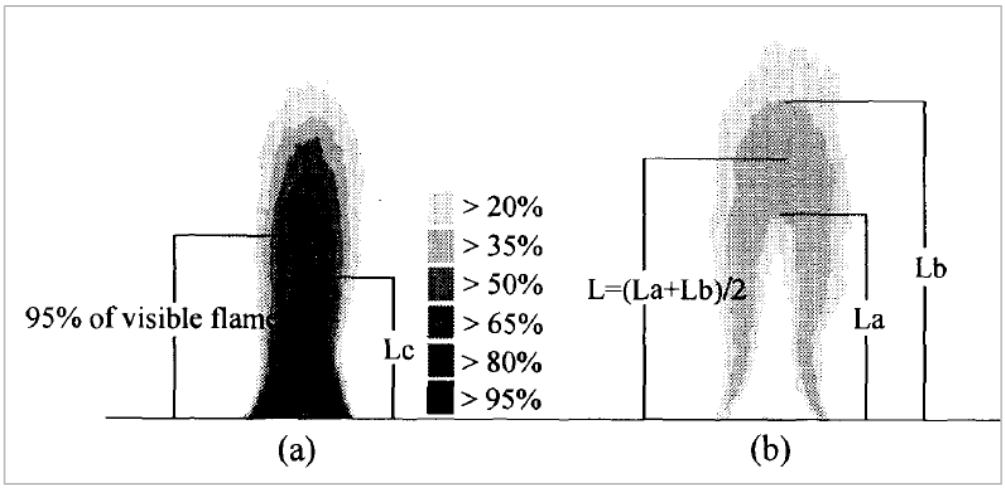

Figure 2.12: Part (a) shows flame presence probability contours and (b) demonstrates standard deviation of flame luminosity. Image reproduced from [22].

Nmira et al. [26] composed a 3-dimensional computational model to study wind affects the geometric properties of vegetation fires. Small and large aspect ratio line fires were investigated and specifically solved the Farve-averaged Navier-Stokes (FANS) equations for the gas phase including source terms to incorporate the contribution of the solid phase and included additional buoyancy production/destruction terms. The temperature of the solid phase and the pyrolysis rate were assumed constant, and unlike most of the wind-wildland fire literature the fire source area was also kept constant, where radiative feedback to the downstream fuel bed was the focus. Most interestingly results are presented for isotherms and

velocity streamlines of the flow around the flaming region for a baseline case of source area = 1.4 x 1.4m (H=1m to represent a stack of fine vegetation mass), heat release rate $\dot{Q}$ = 2.8MW and was subjected to a wind speed of 2ms^{-1}. Figure 2.13 present these streamline results for (i) the case described (source aspect ratio 1), and (ii) where the fire source width was increased to 10m (source aspect ratio 7.1) (H=1m) and the heat release rate $\dot{Q}$ = 2.0MW.

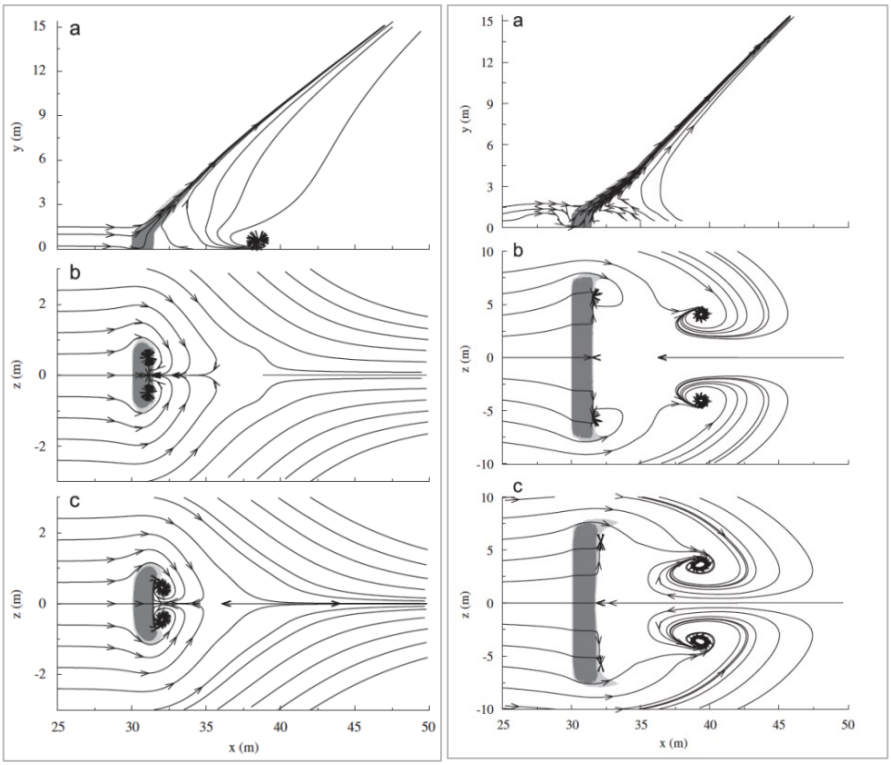

(i) (ii)

Figure 2.13: Isotherm contours (400/500 K) of gas temperature and velocity streamlines are presented for (i) 1.4m square source ($\dot{Q} = 2.8MW$) and (ii) 1.4m x 10m source ($\dot{Q} = 2.0MW$). In each case (a) shows the lateral view of the flaming region, (b) and (c) show horizontal planes at 0.5m and 1.0m of the source height, respectively. In ease case (b) and (c) are not to scale. Image reproduced from [26].

The temperature 500K represents the upper location of the intermittent flame and the corresponding isotherms can be seen to appear at the defined fire source and extend upward depicting an approximate flame height. There are many interesting facets to these data that greatly inform the current work. In both cases for the square source (i) and for the line source (ii) velocity streamlines are greatly deflected above

and around the flame showing that the flame effectively acts as an obstacle for the cross flow. In (i-b) it should be considered however that the fire source is modelled as a solid/porous structure so this is not directly comparable to the case of a flame on top of a porous burner (with solid walls) as will be the case in the current work. In (i-c) however the slice is taken at the source top edge which is more applicable since the "obstacle" is then genuinely the hot flaming region. The streamlines in (i-b) and (i-c) however show very similar results. It can perhaps be noticed therefore that in (i-c) a flow line to the RHS of the source propagating in the direction of the source (against the cross flow direction) is more prevalent that in (i-b). This could be attributed to greater fire inflow at this elevation due to the greater buoyant velocity field within the flaming region than would be present in the porous fuel stack however this detail is not discussed by the authors. As the streamlines are deflected around the combustion zone counter-rotating vortices develop at either side of the flame that appears to drive some entrainment flow at the rear of the flame. For better context the line source model has also been included here. Streamlines can be noticed to penetrate through the combustion zone in (ii) parts (b) and (c) more so than for the square source case of (i). Intuitively this makes sense since the HRR and therefore the buoyant force per unit area is spread over a greater area (which makes the inertia force of the cross flow comparatively greater against the buoyant force than in the square source case), and since the aspect ratio has increase approximately 7-fold it is unrealistic expect the cross flow to be diverted sufficiently to pass around the outer edges of such a wide flame source. This has the impact of tilting the flame further than in the square source case and subsequently moving the rear-side vortices further downstream of the source. Further, the authors presented data that showed that increasing the cross flow velocity increased cross flow penetration through the flame and in all cases had the effect of stretching the vortex structures and moving them even further downstream until they were effectively destroyed and replaced by relatively smooth flow lines in the cross flow direction. The question of inward fire flow of entrainment at the rear side of the source was not discussed explicitly further, suggesting that with line source in

particular, the cross flow propagation was generally constant over the leading edge and the area to the rear of the source once the inertia force of the cross flow was increased.

It is a little difficult to see due to the resolution of figure 2.13 concerning the flame region, however visual analysis of both cases for part (a) suggests that as the buoyant/inertia ratio changes in favour of inertia (cross flow) in (ii) by decreasing the total HRR (and the HRR PUA) the flame in (ii) begins to tend toward showing both boundary layer and plume modes as described in [24]. This is difficult to see however there is a noticeable change in gradient of the streamlines to the rear of the source in (ii-a), which would becomes more pronounced as the cross flow velocity was increased. By comparison (i-a) retains a more-or-less constant tilt angle due to the comparatively greater buoyant force near the source upper surface than in (ii).

Nmira [26] is an important work since there are very few papers discussing the flow field around and at the rear side of flames in cross flows in the literature, and since the computational modelling designed in this work showed good agreement with empirical wildfire flame geometry data from elsewhere. Again, without the authors describing it as so, the importance of the Gr/Re ratio in the buoyant flame/cross flow interaction is a core output of this work and produced a qualitative description that is quite rare in the literature.

In an unpublished PhD thesis [35] in which the cross flow flame experiment set-up was linked to that in the work by [20] and [22], visualisation of flame presence probability and of cross flow velocity fields around the flame within a wind tunnel chamber were produced. Firstly, an axis-symmetric and cross flow flame case were visualised using seeding techniques and plotting vector fields to describe the results.

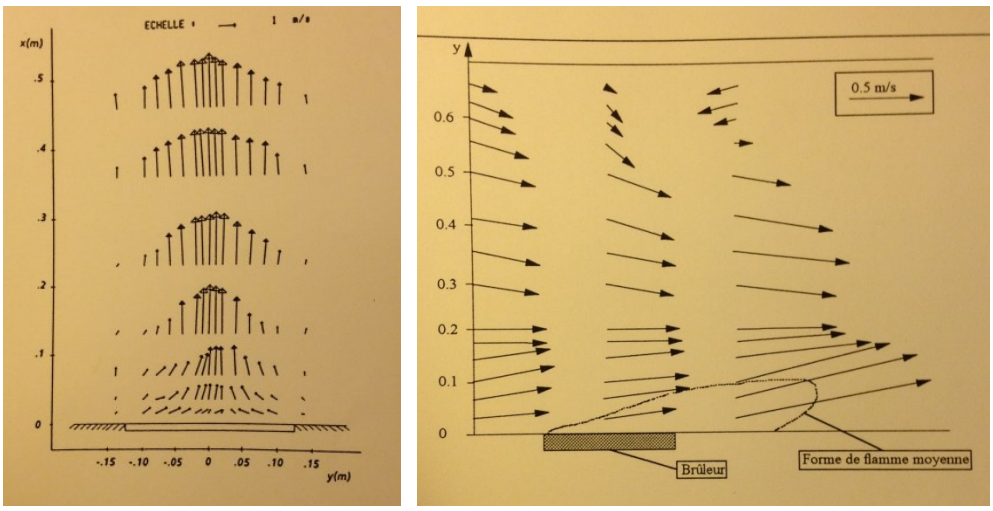

(a) (b)

Figure 2.14: Vectors for (a) axis-symmetric fire plume and (b) plume deflected by cross flow in seeded-air chamber. The gas burner was 0.25m^2 and HRR = 27kW. In (b) cross flow velocity was 0.5ms^{-1}.

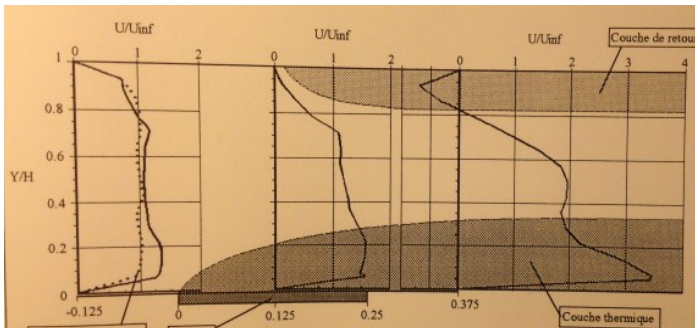

(a)

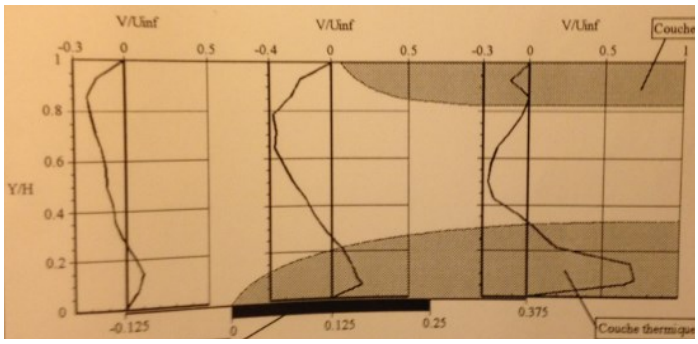

(b)

Figure 2.15: Shows vectors like those from figure 2.14 (b) plotted as velocity contours for the similar fire cases.

Figure 2.14 corroberates the traditional vector story for the axis-symmetric plume similar to those highlighted in [16] for example. Part (b) highlights the increase in

velocity of the forced flow as it mixes with the buoyant convection force of the flame and plume near the base of the chamber. This is characteristic of the asertions of [24] and many others, that the convection boundary layer serves to enhance the velocity of the cross flow when compared to a non-reacting boundary layer in the same location. The re-circulation zone at the top of the chamber due to the rise and lateral spread of the plume gases as described in [20] can also be noticed. Similarly in figure 2.15 the velocity contours mimic the trend of the mixed flow vectors in 2.14 where a stark velocity (and pressure field) is apparent within the boundary layer (flame) area (the dark boundary-layer type sections).

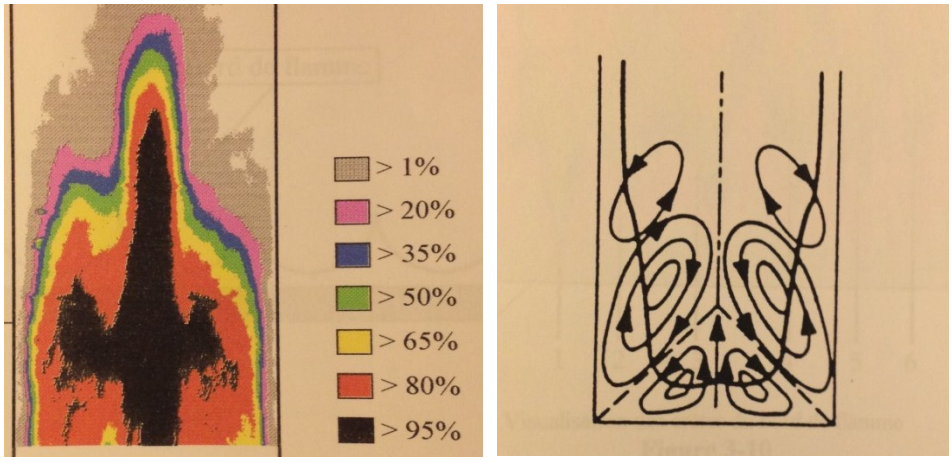

(a) (b)

Figure 2.16: Flame presence probability contours similar to those in [22] are depicted in (a) utilising the same principle technique as was described previously. Part (b) depicts the vortex generation of the cross flow subject to interaction with the flame insdie the seeded chamber. Images are reproduced from [35].

The flame presence data of figure 2.16 (a) highlights the shape of the flame looking into the chamber, along the direction of the cross flow. Considering the 95% contour for example lets us see that the cross flow air mass finds its way predominantly around the outside edges of the flame, as suggested by [26] for their square burner case, which was of course not bounded by lateral walls as is the case here in [35]. This flow field therefore facilitates the generation of large eddie currents at the rear

of the flame in the wake of the downstream air flow. This is highlighted in part (b) where vortices at the leading edge corners, laterally and to rear-laterally develop.

These results can be put into context by considering the principles of flow around a cylindrical obstruction whereby the flow boundary layer at the obstruction surface, at some point approaching the rear of the obstruction generates an adverse pressure gradient and separation of the flow from the surface occurs. A wake is formed downstream of this point and a highly irreguar flow pattern emerges, characterised by vortex generation and turbulent flow. This is depicted in figure 2.17 and figure 2.18. Even though the fire is not a solid object, the same principles of a negative pressure gradient in the wake of the fire source/flaming region exhibiting increased local velocities and turbulent on-set apply.

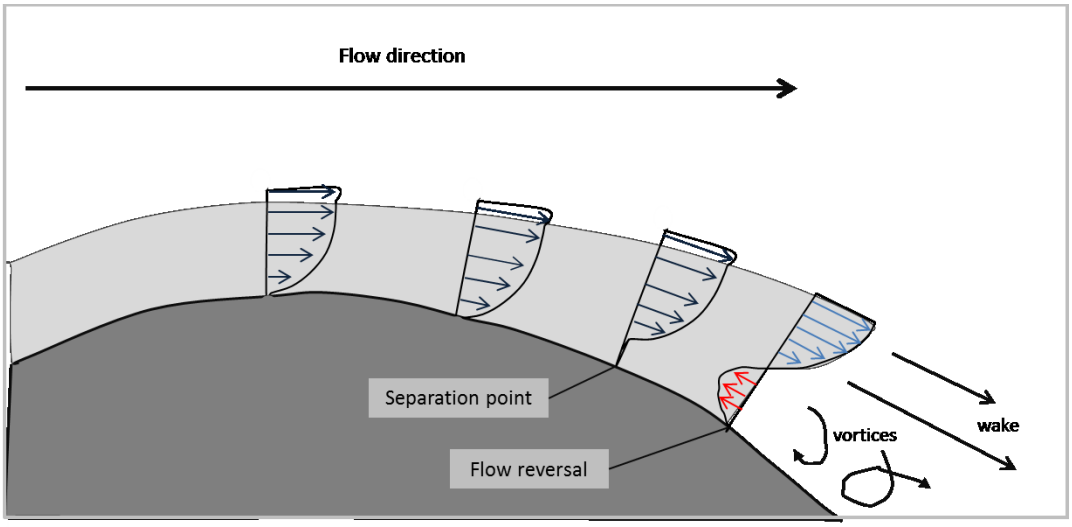

Figure 2.17: Velocity profile associated with separation around a circular cylinder in a cross flow. Image adapted from [36].

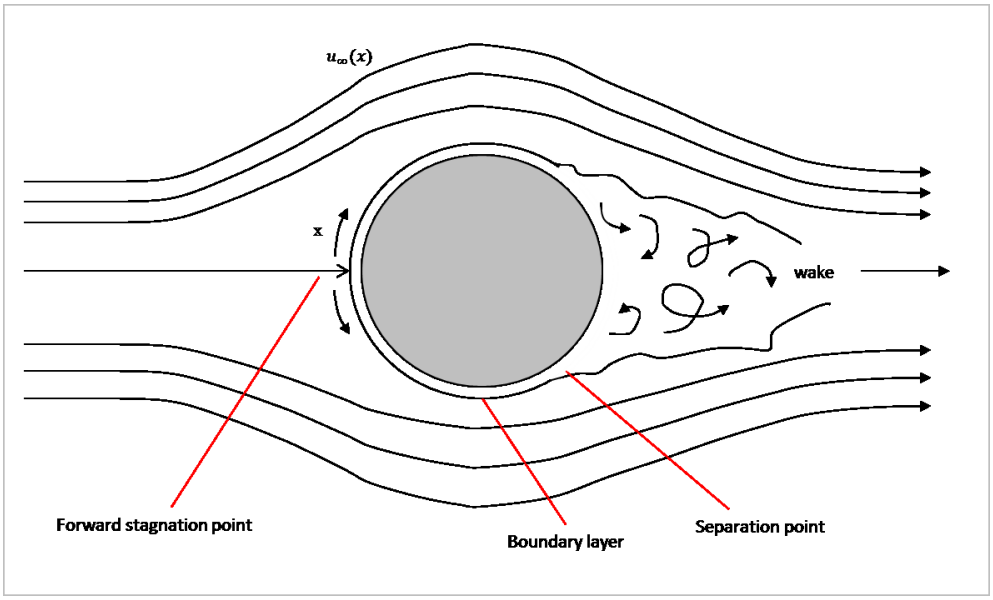

Figure 2.18: Boundary layer formation and separation on a circular cylinder in cross flow. Image adapted from [36].

2.11 Plume Flow Mechanics from First principles

The general phenomenon of interest in this thesis is that when the natural convection processes of the fire plume are perturbed by perpendicular forced flow. The term *mixed convection* is commonly used to describe instances where natural convection and forced convection flows are combined in a system. It is desirable therefore to consider the underlying principles of each of these flows and then to investigate instances where their combination has been studied in the literature. The following fundamental continuity principles of mass, momentum and energy are well described throughout the literature and in throughout heat transfer texts. This section takes some structural guidance includes nuance detail notes primarily from [36].

2.11.1 Free Convection

In free convection fluid motion is due to buoyancy forces within the fluid and the buoyant force is due to the combination of a *body force that is proportional to density*

and a *density gradient* within the fluid [36]. Most commonly, and certainly in the case of the fire plume, the density gradient is the result of a temperature gradient and subsequent fluid expansion. For this case the body force is due to the gravitational field. Free convection flows may be classified according to whether the flow is bounded by a surface [36] and in the case of a fire, the plume structure may be considered a free boundary flow. Figure 2.19 depicts a buoyancy-driven free convective plume flow:

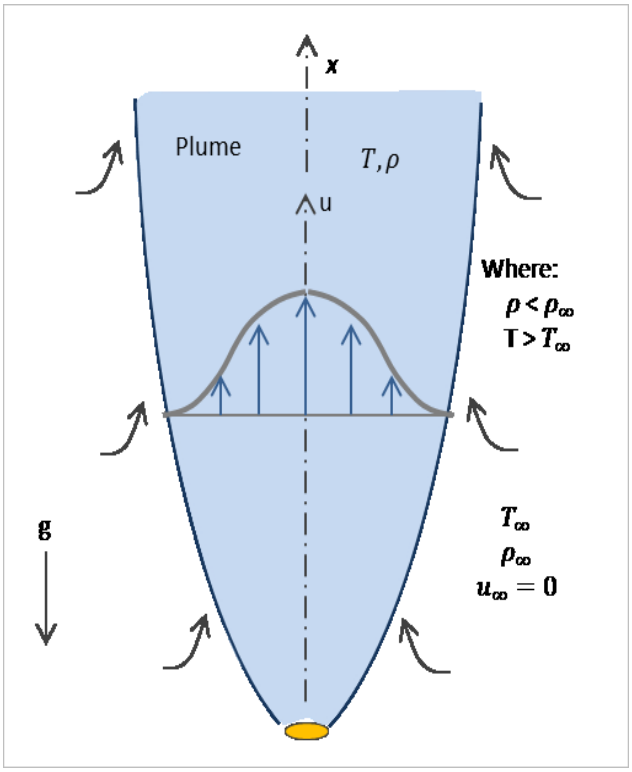

Figure 2.19: Free convection plume above a heated source. Image adapted from [36].

Figure 2.19 shows the formation of a plume of less dense fluid rising above a heated source immersed in a quiescent bulk fluid. The plume density is less than that of the quiescent environment due to the temperature gradient across the plume boundary. Air is entrained at the edges of the plume until such a height at which the plume structure will dissipate due to cooling from entrained air and viscous effects. It is

important to note that a defining parameter of a natural convection flow is that the initial velocity at the source is considered as zero. This is the principle distinction between a plume and buoyant jet which has a finite velocity at the source. The model in figure 2.19 fundamentally defines quite well the case of the axis-symmetric fire plume.

Turning to the example of a heated vertical plate in an adjacent quiescent environment demonstrates the establishment of a boundary layer when the convective flow field is bounded by a surface.

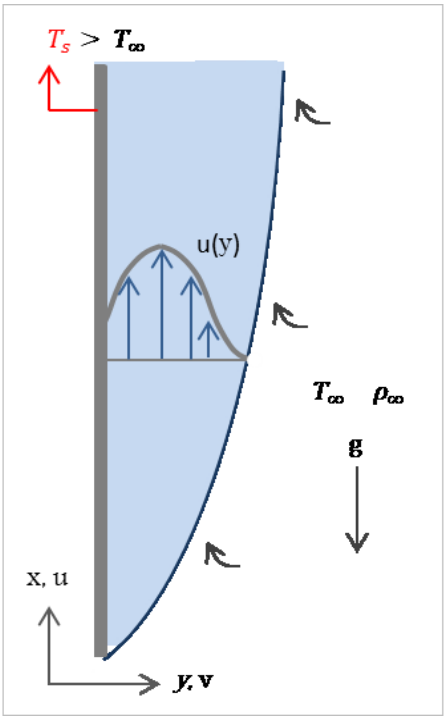

Figure 2.20: Boundary layer development on a hot vertical plate in a quiescent bulk fluid. Image adapted from [36].

Figure 2.20 shows a heated vertical plate immersed in a quiescent bulk fluid. Since the surface temperature is greater than that of the surrounding fluid, the fluid near to the plate becomes less dense than the fluid far from the plate and a buoyancy-

driven free convection boundary layer forms as the less dense fluid rises and entrains cooler fluid from the quiescent region. Upward velocity u, is zero at the y=0 as well as far from the surface, $y = \infty$.

In free convection buoyancy plays a major role and we can say that the buoyant force *sustains* the flow [36]. This can be described by considering the x-momentum equation for the case in figure 2.20:

$$u\frac{\partial u}{\partial x} + v\frac{\partial u}{\partial y} = -\frac{1}{\rho}\frac{\partial p}{\partial x} - g + v\frac{\partial^2 u}{\partial y^2}$$

Equation 2-53

in which the body force per unit volume is $-\rho g$, where of course g is local acceleration due to gravity. We must assume steady, 2-dimensional, constant property conditions and with the exception of the buoyancy force description (density difference in the Boussinseq approximation), assume an incompressible fluid.

The hydrostatic approximation allows one to define the important force for the heated vertical plate case. Since there is no body force in the horizontal (y-axis) we can say from an order of magnitude analysis that the force term is not a function of y ($P \neq f(y)$ and therefore in the y-momentum equation:

$$\frac{\partial P}{\partial y} = 0$$

Equation 2-54

It can be stated then that the x-pressure gradient at any point inside the boundary layer must equal the pressure gradient outside the boundary layer in the quiescent region. Outside the boundary layer in the quiescent region however u *and* v = 0.

Since the flow inside the boundary layer is buoyantly driven with no initial velocity, we can note that the only force in the vertical (x-axis) is the gravitation body force, hence:

$$\frac{\partial P}{\partial x} = -\rho_\infty g$$

Equation 2-55

Plugging equation 2-55 into equation 2-53 then gives:

$$u\frac{\partial u}{\partial x} + v\frac{\partial u}{\partial y} = \frac{g}{\rho}(\rho_\infty - \rho) + v\frac{\partial^2 u}{\partial y^2}$$

Equation 2-56

which is applicable at every point within the free convection boundary layer. The first term on the RHS of equation 2-56 describes the buoyancy force and this force derives from the variation in density within the region. The density difference can be stated and expanded as follows:

$$\Delta\rho = (\rho_\infty - \rho)$$

Equation 2-57

which gives the quantitative difference. The fractional description of the difference may be acquired by interrogation:

$$= \rho_\infty \left(1 - \frac{\rho}{\rho_\infty}\right)$$

Equation 2-58

which has the equivalency in terms of temperature variation:

$$= \rho_\infty \left(\frac{T - T_\infty}{T_\infty} \right)$$

Equation 2-59

The volumetric thermal expansion coefficient β, gives the order of density change following temperature variation at constant pressure. This thermodynamic property can be described by multiple means:

$$\beta = -\frac{1}{\rho}\left(\frac{\partial \rho}{\partial T}\right) = \frac{1}{\rho}\frac{p}{RT^2} = \frac{1}{T}$$

Equation 2-60

where for an ideal gas $\rho = p/RT$ (T in K). Therefore, combining $\beta = 1/T$ with equation 2-59 yields:

$$(\rho_\infty - \rho) \approx \rho\beta(T - T_\infty)$$

Equation 2-61

This can be inserted back into the x-momentum equation 2-56 whereby the buoyancy force as a function of the density difference subject to temperature variation is now well described:

$$u\frac{\partial u}{\partial x} + v\frac{\partial u}{\partial y} = g\beta(T - T_\infty) + v\frac{\partial^2 u}{\partial y^2}$$

Equation 2-62

We therefore acquire a set of governing equations as follows. Buoyancy effects are confined to the momentum equation so the mass and energy equations are the same as would be presented for a forced convection case:

Mass

$$\frac{\partial u}{\partial x} + \frac{\partial v}{\partial y} = 0$$

Equation 2-63

Momentum

$$u\frac{\partial u}{\partial x} + v\frac{\partial u}{\partial y} = g\beta(T - T_\infty) + v\frac{\partial^2 u}{\partial y^2}$$

Equation 2-64

Energy

$$u\frac{\partial T}{\partial x} + v\frac{\partial T}{\partial y} = \alpha\frac{\partial^2 T}{\partial y^2}$$

Equation 2-65

The thermal problem, previously confined to the energy equation is now incorporated into the hydrodynamic problem of the mass and momentum equations. The three equations are therefore now strongly coupled and must be solved simultaneously [36].

It is customary then to acquire the dimensionless functions that govern free convective flow and heat transfer. The governing equations are non-dimensionalised by assessing the constituents with the following appropriations:

$$x^* \equiv \frac{x}{L} \qquad y^* \equiv \frac{y}{L}$$

$$u^* \equiv \frac{u}{u_0} \qquad v^* \equiv \frac{v}{v_0}$$

$$T^* \equiv \frac{(T - T_\infty)}{(T_s - T_\infty)}$$

Equation 2-66

where L is a characteristic length of the problem and u_0 represents an arbitrary reference velocity, however since the quiescent region has zero effective velocity there is no practical or logical velocity suitable here. Non-dimensionalising for equations 2-64 and 2-65 yields:

$$u^* \frac{\partial u^*}{\partial x^*} + v^* \frac{\partial u^*}{\partial y^*} = \frac{g\beta(T_s - T_\infty)L}{u_0^2} T^* + \frac{1}{Re_L} v \frac{\partial^2 u^*}{\partial y^{*2}}$$

Equation 2-67

$$u^* \frac{\partial T^*}{\partial x^*} + v^* \frac{\partial T^*}{\partial y^*} = \frac{1}{Re_L Pr} \cdot \frac{\partial^2 T^*}{\partial y^{*2}}$$

Equation 2-68

The first term on the RHS of equation 2-67 is the direct result of the buoyancy force which drives and sustains the flow. In order to remove the undesirable u_o parameter it is traditional to multiply this term out by the Reynolds number to the second power. The result is the *Grashof number*, characterising the buoyancy force at any point within the system an equating with some local or reference viscosity:

$$\equiv \frac{g\beta(T_s - T_\infty)}{u_0^2} \left(\frac{u_0 L}{v}\right)^2$$

Equation 2-69

$$Gr = \frac{g\beta(T_s - T_\infty)L^3}{v_0^2}$$

Equation 2-70

The Grashof number then provides a measure of buoyant force to viscous forces and appears following a non-dimensional analysis, within the momentum equation for the vertical axis of the thermally-driven system. As discussed previously this approach describes well the case of the buoyantly driven fire plume, for the axis-symmetric, traditional model. Deconstruction of the mixed convection problem also requires consideration of the forced flow component, and specifically the case of a horizontal flow over a flat plate. Fundamentally the approach is very similar but the lack of the buoyancy force simplifies things somewhat since the momentum and energy equations are no longer intrinsically coupled by a temperature gradient.

2.11.2 Horizontal Forced Flow

Assuming steady, incompressible, laminar flow with constant fluid properties, and negligible viscous dissipation, as well as considering no change in pressure over the course of the flow field $dp/dx = 0$, the appropriate boundary layer equations can be written as:

Mass:

$$\frac{\partial u}{\partial x} + \frac{\partial v}{\partial y} = 0$$

Equation 2-63

Momentum

$$u\frac{\partial u}{\partial x} + v\frac{\partial u}{\partial y} = \nu\frac{\partial^2 u}{\partial y^2}$$

Equation 2-71

Energy

$$u\frac{\partial T}{\partial x} + v\frac{\partial T}{\partial y} = \alpha\frac{\partial^2 T}{\partial y^2}$$

Equation 2-65

The mass and energy equations are of the same form as for the free convection case and the buoyancy term is removed from the momentum equation. The flow schematic can be depicted as in figure 2.21:

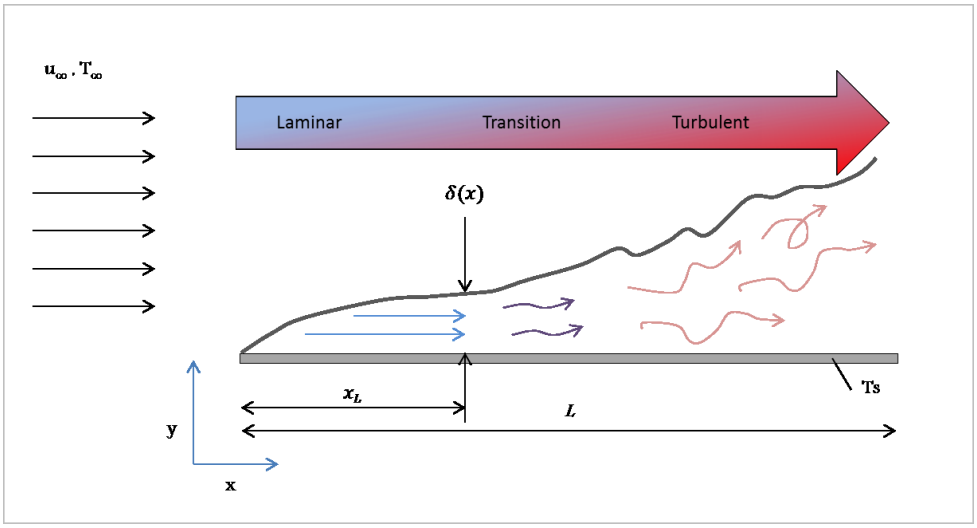

Figure 2.21: Forced flow across a flat plate where boundary layer thickness is a function of XL and the local Reynolds number and the laminar region is follow by transition to turbulence.

2.11.3 Mixed Convection

When the flat plate in the forced cross flow case is heated a buoyancy force is introduced into the forced flow system described above and a particular regime of mixed convective system is created where the initial vectors of each force in isolation are perpendicular. This theoretical system may be applied to the case of the fire plume in a cross flow and is directly related to the investigations presented in [20], [22], [24] and [26].

Raju et al. [37] studied a forced flow over uniformly heated horizontal and vertical plates where boundary layer development was aided by the buoyant force resulting from the plate surface. Transformed versions of the Gr/Re number were suggested to improve the solution procedure. Subsequently the divergence in velocity results between numerical models and theoretical solutions were found with increasing distance from the surface. The dominance of the forced flow near the leading edge of the plate and the importance of the body force far from the leading edge was demonstrated.

Sparrow and Minkowycz [38] showed that the body force acting perpendicular to a cross flow produces a stream-wise (with respect to the horizontal forced flow) pressure gradient and that the effects of buoyancy are more pronounced in low Prandtl number cases (where the ratio of viscous diffusivity to thermal diffusivity is low). The numerical results of [38] are commonly used for comparison by similar studies, including those discussed here.

Leal [39] adapted the premise of [38] whereby investigating the case where the boundary surface is strictly horizontal thus eliminating any buoyant contribution to the stream-wise flow and generating a significant body force cross-stream, ie. perpendicular to the direction of the horizontal cross flow. The effect of a comparatively strong cross stream body force is a so-called *stretched boundary layer* where the contribution of the body force within the cross flow is appropriated. This case is suitable for theoretical application to the case of the fire plume in a cross flow, since the burner surface is horizontal and the entire buoyant force provided by the fire can be considered, initially, to propagate cross-stream with reference to the forced flow.

The model is set up as shown in figure 2.22. A forced flow (incompressible Newtonian fluid, constant free stream velocity) is considered perpendicular to a heated, isothermal plate.

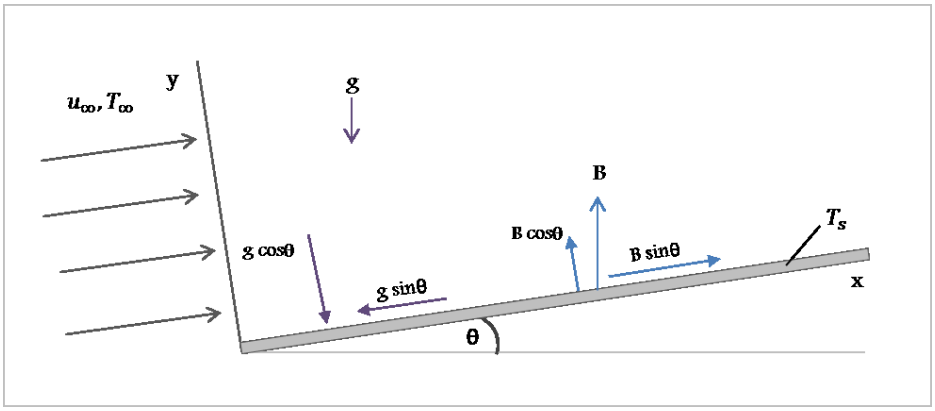

Figure 2.22: The physical model of [39]. The forced flow is parallel to the heated plate surface. The gravitational forces and buoyancy body force in their initial vector, stream-wise and cross stream components have been added for clarity. Image adapted from [39].

Following the manipulation of the governing equations as presented previously where the non-dimensional parameters are generated and inclusion of the relevant gravitational vector components (and therefore body force components) is implied, the suitable governing equations can be stated as:

Mass

$$\frac{\partial u}{\partial x}+\frac{\partial v}{\partial y}=0$$

Equation 2-72

Momentum

$$u\frac{\partial u}{\partial x}+v\frac{\partial u}{\partial y}=-\frac{\partial p}{\partial x}+\frac{Gr}{Re^2}T(cos\theta\vec{j}+sin\theta\,\vec{\imath})+\frac{1}{Re}\frac{\partial^2 u}{\partial y^2}$$

Equation 2-73

Energy

$$u\frac{\partial T}{\partial x}+v\frac{\partial T}{\partial y}=\frac{1}{\mathrm{Pr}\ Re}\frac{\partial^2 T}{\partial y^2}$$

Equation 2-74

where $\vec{j}$ and $\vec{\imath}$ represent unit vectors in the streamwise (x) and cross stream (y) directions. y and v are then non-dimensionalised by the transformations $Y = yRe^{1/2}$ and $V = vRe^{1/2}$. Following this [39] suggests the following expressions for the stretched boundary layer coordinates (x,Y) as:

Mass

$$\frac{\partial u}{\partial x}+\frac{\partial V}{\partial Y}=0$$

Equation 2-75

Momentum (Stream-wise)

$$u\frac{\partial u}{\partial x}+V\frac{\partial u}{\partial Y}=-\frac{\partial p}{\partial x}+\frac{Gr}{Re^2}T(sin\theta)+\frac{\partial^2 u}{\partial Y^2}+0\left(\frac{1}{Re}\right)$$

Equation 2-76

Momentum (Cross-stream)

$$\frac{\partial p}{\partial Y}=\frac{Gr}{Re^{5/2}}T(cos\theta)+0\left(\frac{1}{Re}\right)$$

Equation 2-77

Energy

$$u\frac{\partial T}{\partial x}+V\frac{\partial T}{\partial Y}=\frac{1}{\mathrm{Pr}\ \ Re}\frac{\partial^2 T}{\partial Y^2}+0\left(\frac{1}{\mathrm{Pr}\ \ Re}\right)$$

Equation 2-78

This then splits the momentum equation into separate entities for the stream-wise and cross-stream components. Upon integrating equation 2-77 with respect to Y and differentiating with respect to x, the equation can then be combined with equation 2-76 to yield a modified stream-wise momentum equation [39]:

$$u\frac{\partial u}{\partial x}+V\frac{\partial u}{\partial Y}=\frac{Gr}{Re^{5/2}}(cos\theta)\int_{Y}^{\infty}\frac{\partial T}{\partial x}dY+\frac{Gr}{Re^2}(sin\theta)T-\frac{\partial p_\infty}{\partial x}+\frac{\partial^2 u}{\partial Y^2}$$

Equation 2-79

Several limiting conditions, (well described by the particular *Pr* regime) are applicable here depending upon the nuances of the physical system modelled however this approach represents one of only a few literature examples that might be applied to the fundamental description of the processes attributable to the cross

flow fire plume case. Both of the buoyancy terms in equation 2-79 can be considered to contribute to the effective stream-wise pressure gradient.

2.12 Wind-blown Plume in the Context of Infrastructure

Papers furthering the findings of [6] - that small disturbances can cause a significant increase in entrainment rate are rare. Particularly for the infrastructure (enclosure) fire case. One such paper of course, is that of Quintiere et al. [19] where the impact of a notable crossflow was observed to have an greater magnitude of increase on entrainment rate as that described by [6]. The fire plume was this time put into the context of an actual enclosure but importantly, the crossflow was the result of the fire flow alone, impacted by the physical dynamics of entering the enclosure through various door/window openings and **not** due to any "wind" imposed by a fan or other mechanism.

A 30cm diameter porous plate diffusion flame burner (methane, constant flow, 62.9 and 158kW) was placed in the centre of a 2.8 x 2.8 x 2.13m enclosure and door/window sizes in the centre of one wall were varied over 14 experiment runs. One vertical tree of aspirated thermocouples measured temperatures in one corner and a tree of probes in the centre of the opening measured temperature and flow velocities. Flame tilt angle was recorded on a video camera and analysed frame by frame. The smoke layer interface was determined with temperature measurements to within +/- 30% accuracy. Clearly mixing/entrainment along the hot layer boundary was considered to be significantly more prominent than in [6] (where it was considered compared to "plume" entrainment alone), the enclosure surface area being around 3.5 times that of the hood used in [6]. When comparing the calculated results of the experiment with equation (2-24) the authors found good agreement with vertical flames (no/negligible crossflow) to around +/-10% but found that the same approach underestimated the entrainment rate of flames when significant tilt could be witnessed. The theory follows that of [18] and equation (2-

43) is referenced to explain the decoupling of crossflow components. There are large uncertainties in various measurements within this analysis, including velocity measurements and predictions an order of magnitude apart. Although a non-dimensional analysis of all the constituent components required for point-source entrainment predictions show a general trend of increased entrainment rate as flame tilt angle increases (normalised against equation (2-24)), practical knowledge is not really advanced other than to demonstrate that the theoretical approach of Hoult & Weil [18] is applicable, to a small extent, to the fire plume enclosure case.

2.13 Qualitative Descriptions of Entrainment

While most entrainment-focused papers in fire related literature are generally concerned, in the first instance at least, with testing resultant models and re-evaluating empirical assumptions based on test data, it seems appropriate that some consideration should be given to the physical description of the physics of entrainment. A qualitative description of entrainment physics may lead to a more thorough understanding of how complex fluid dynamics processes are affected for the fire plume subjected to a crossflow, and may offer additional quantitative methods to describe the fundamental dynamics.

Netterville [76] attempted to develop a quantitative description of air/plume mass transfer by considering closely the development of deterministic eddy structures that form within the turbulent boundary. Referencing early high-speed footage of shear layer mixing, it is suggested that entrainment is not a smooth process but rather occurs in short, sharp gulps via the quasi-regular formation of small vortices. Figure 2.23 shows a sketch of shear-induced vortex interleaving, fundamentally described by the Kelvin-Hemholtz instability. The term *extrainment* is used to describe, essentially, the reverse of entrainment. Just as parcels of air are entrained into the plume, smaller quantities of smoke/air parcels are entrained in the reverse

direction from the plume back into the surrounding fluid. Figure 2.24 simplifies the subsequent complicated entrainment/extrainment processes between plume and air.

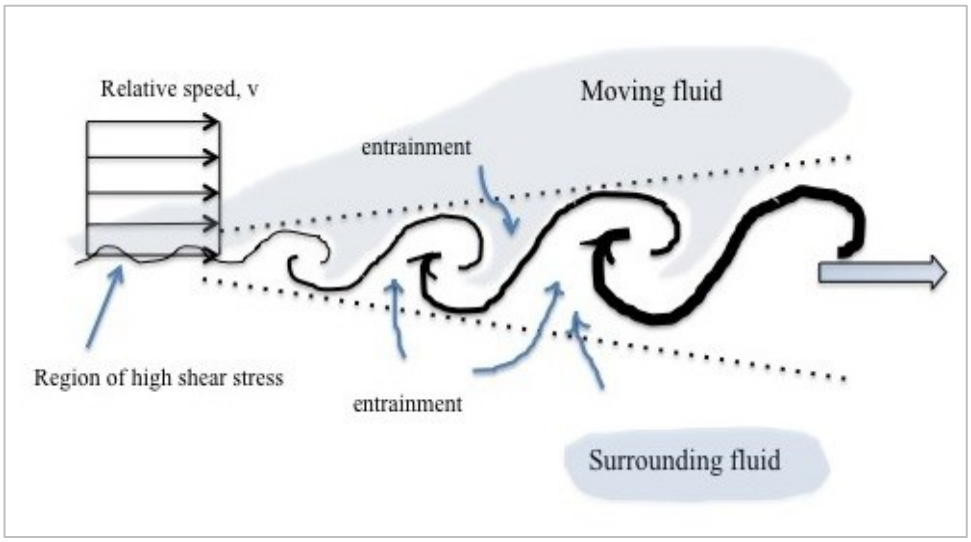

Figure 2.23: Shear-induced vortex roll-up. Image adapted from [76]

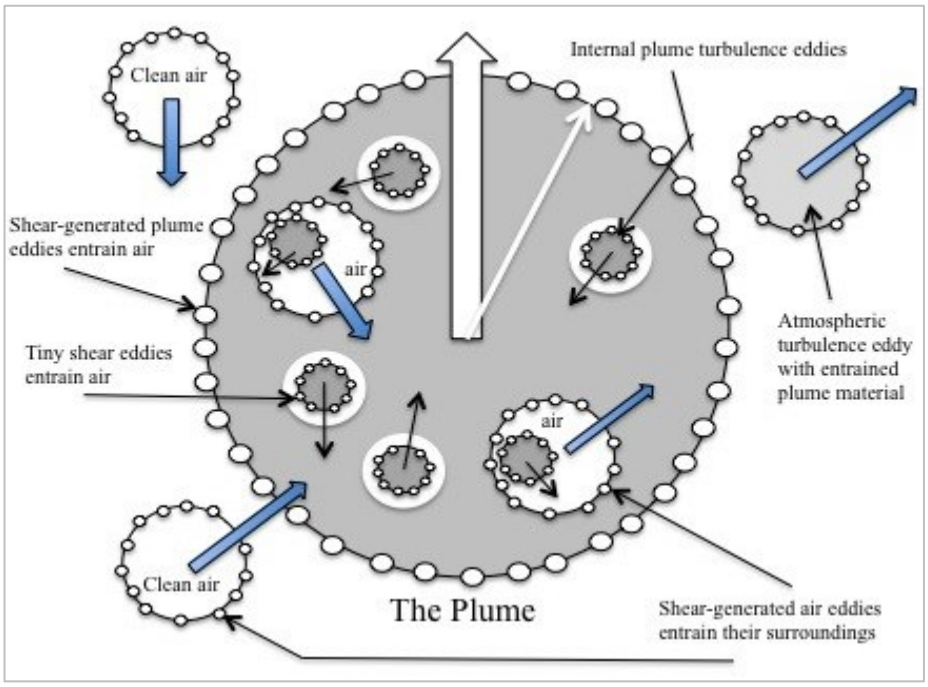

Figure 2.24: Plume/atmosphere interaction. Image adapted from [76]

Almost immediately after each eddy has formed, the interleaving process is irreversible and the author used this principle as a starting point to define a direct entrainment rate based upon shear eddy mass, birthrate, and number of shear eddy parcels per unit area. It is postulated by this author, that an understanding of, and ability to describe, the qualitative physics that govern the crossflow entrainment paradigm, will not only aid the investigation for quantitative output but will allow for a fundamental understanding of precisely *why* such quantitative output is so. This mirrors the hope behind this work that as well as acquiring quantitative data on mass flow rates, rich qualitative descriptions of the continuous flame region under cross flow conditions, which are apparently non-existent in the literature, can provide further intuition for the tilted flame entrainment processes.

3 Laboratory Experiment Methodology

Studying entrainment in an idealised environment was practical at the time of the authors throughout the literature (Morton, McCaffrey, Cetegen and etc), but was purely meant as a means to understand the fundamental principles and relationships between the plume system and its surrounding environment. Subsequently, studying fire plume dynamics in a compartment [19] was the next step in integrating the principle knowledge within practical and realistic scenarios in order to account for the effect of the surrounding environment upon smoke flow. It could be argued that there is an important step missing in this process. Free fire plume mass flow fundamentals are first understood and the impact upon the mass flow rate by bounding the fire plume in a compartment is then recorded, however qualitative and quantitative descriptions of how the fire plume flow fundamentals change under a cross flow regime appear to never have been discussed. Various mixed-convection descriptions [20, 24, 29] allude to the flow dynamics of a stream-wise and cross-stream scenario at small scale, but these are too abstract to apply directly to the fire plume case that the fire safety engineer is concerned with, in terms of describing the general flow dynamics of mixed flow entrainment. The reacting plume brings its own additional complexities of sharp temperature gradients across the flame boundary, flow dependencies which can be categorised by plume region (continuous/intermittent flame, plume), combustion chemistry which affects and is of course affected by the specifics of the plume and the environment itself and, as it will be seen, varying rates of entrainment depending upon the characterisation of each portion of the cross flow fire plume.

3.1 Experiment Aims and Goals

The overarching goal of the laboratory experimental work therefore, is to allow a qualitative description and to an extent, quantitative analysis of the changes in fluid flow, within and around the fire plume and to deconstruct the overall story of entrainment in the cross flow (mixed convection) fire plume. This shall include:

- Characterising the air flow velocity and behaviour around and within the fire plume for a range of cases where the buoyancy/cross flow inertia forces are varied, compared to the qualitative and quantitative descriptions in the literature
- Defining a scale by which to describe the inertia/buoyancy-dominated scenarios
- Observing how the boundary layer/transitional/plume modes structure, as defined for small scale in [20, 24, 29], manifests in the range of room-scale fire plumes
- Subsequently, isolate the inertia-dominant boundary layer mode region in cases where it exists as part of - or the entire - fire plume and quantify the smoke mass flow rate attributable to this section. Consideration of this portion alone is abstract in relation to the room fire plume for the engineer, however is necessary because it appears not to have been undertaken previously
- Understand the controlling mechanism(s) of entrainment in the boundary layer (inertia-dominated) region
- Understand, where, along the scale, buoyancy-dominated entrainment becomes important
- Use the range of buoyancy/inertia-dominant cases to approximately quantify the proportion of smoke (combustion product) which is attributable to the inertia and buoyancy-dominant entrainment regimes
- Consider the inertia-dominant mass flow and approximated buoyancy-dominated mass flow rates together for context of the engineering approach

- Determine whether the scale description of the range of cases might be used generally to inform the fire safety engineer in smoke management design

Subsequently,

- Characterise the flow behaviour at locations around and within the flame and plume so that future experiments can be refined further in terms of focus and design
- Highlight specifically potential focus areas for subsequent research
- Qualitatively, and quantitatively where possible, describe the behaviour of the mixed convection flame region in relation to that of the fully buoyant case in terms of the well-defined entrainment mechanisms at this region (vortex generation, large-scale eddies and turbulent engulfment).

3.2 Experimental Setup

3.2.1 General Schematic of Setup

The following schematic (figure 3.1) is a general description only. Section 3.3 contains concise details of positioning of the pressure probes and apparatus for each test case.

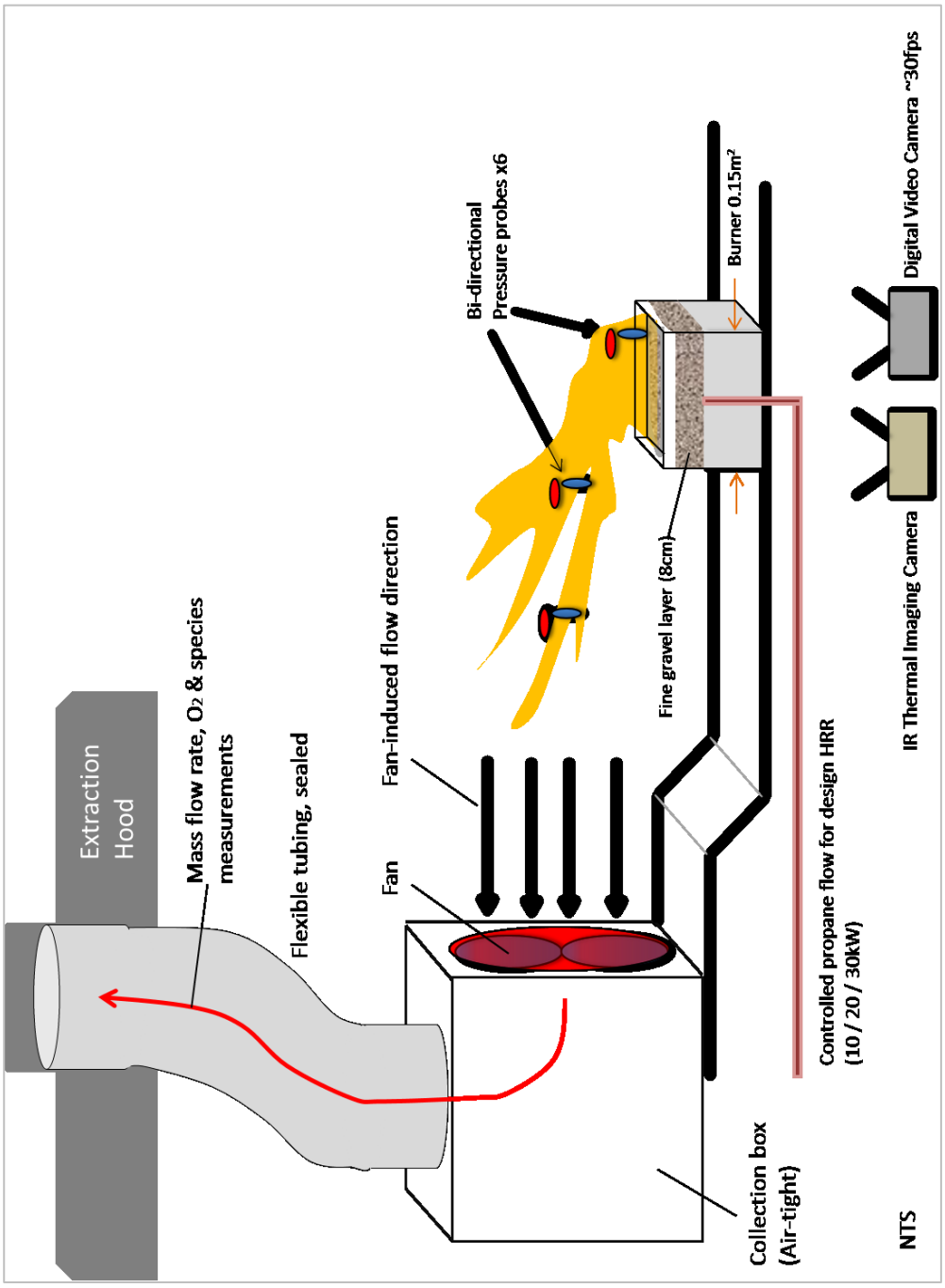

Figure 3.1: Schematic of typical components of the experimental setup

- Gas burner with 0.15 x 0.15m2 surface. The surface has a 1cm lip around the perimeter and is 0.28m above local grade. The burner body is filled with 8cm fine gravel to kill any momentum resulting from pressure at the fuel line orifice. The entire apparatus is built upon a series of tables (not shown) whose surface is 1m above the ground.
- 3 x horizontally and 3 x vertically orientated bi-directional pressure probes are located at various locations around and with the flame. Specific locations are discussed in the following section and in the results sections. All probes located along the centreline of the fan flow field, which corresponds with the centreline of the burner (figure 3.2).
- The fan used is a 0.28m diameter axial fan which is seated in a reinforced end-wall of a purpose built cube structure (collection box). The collection box is made from timber and is sealed along all edges with many layers of extra-wide electrical tape and metallic tape.
- Flexible metal tubing is used to connect the collection box to the extraction point at the top of the extraction hood, under which the apparatus is positioned. The connections at both ends of the flexible tubing are sealed in a similar manner to the collection box edges. Soot was cleaned extensively off of the extraction hood area and a very good connection was achieved with the electric and metallic tape. These connections were checked periodically throughout the experiment runs however no loss of integrity of connects was ever found. The metal tubing is approximately 24cm in diameter and so presents a slight narrowing of the passageway for smoke after it leaves the collection box and before reaching the extraction hood. The hood extraction duct was measured to be approximately 30cm x 30cm and after entering, the smoke must then travel several metres before reaching the calorimeter analysis instrumentation so it was considered that the slight narrowing of the flexible tubing would not influence flow rate measurement further downstream.

- An infra-red thermal imaging camera was positioned laterally to the rear edge (fan side) of the burner to capture thermal images of the flame. This allows analysis of flame tilt angle, flame shape, average flame height and temperature distribution under cross flow and still conditions. Time-step for recording images was approximately 4 seconds per image. FLIR thermal image processing software was used to capture, process and arrange images.
- The 'still condition' for the series of tests was achieved by setting forced-ventilation to the lab to minimum and by locating the test rig within the walls of the large hood. The walls (see figure 3.2) left a gap of 1.2m open to the bottom ensuring that air could freely be entrained equally from all side during the still condition cases, while eliminating random perturbations in air currents resulting from the ventilation system. Indeed, no random-but-significant fluctuations in flame shape were recorded during the still condition/ no wind cases. If real plume mass flow measurements were to be made during the still cases, the hood walls should perhaps be switched for a fine mesh to minimise air current perturbations while also minimising the impact upon natural entrainment across the entire height of the plume.
- A digital video camera was used to record motion footage of the flame from a number of angles and distances. This also allowed interpretation of the volume and within the combustion zone of the flame. Such detail is not achieved using thermal images alone. The frame rate is approximately 30fps, but can vary up to 24fps depending on light conditions. Digidesign ProTools [72] music and media processing software was used to sequence images, from which the frame rate could be confirmed for each sequence.

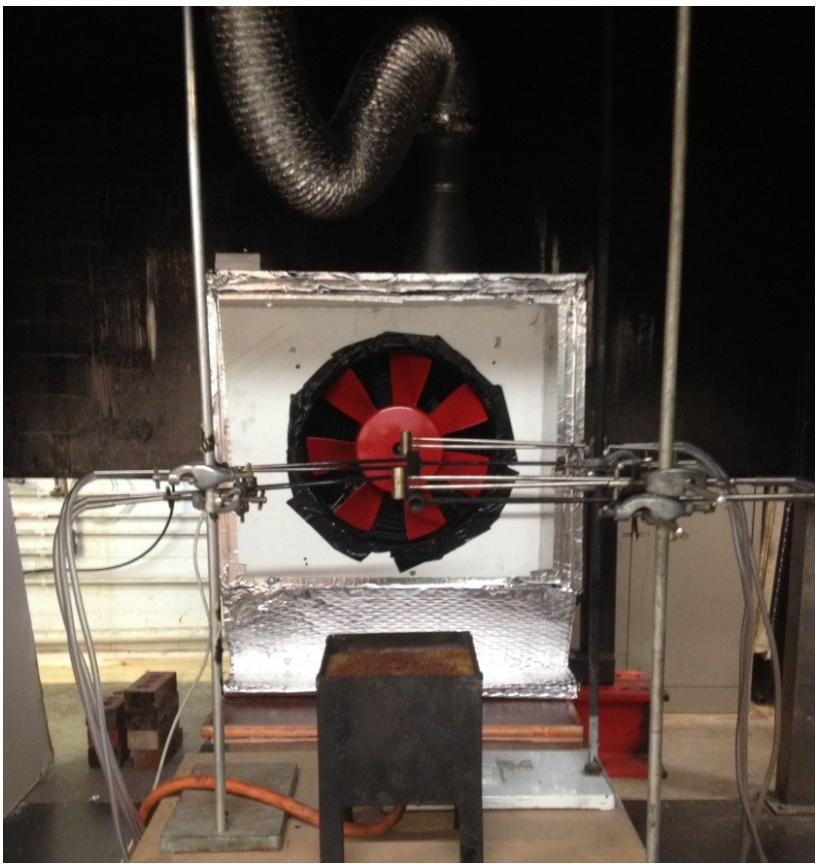

Figure 3.2: Image of apparatus setup looking along forced flow axis.

Figure 3.2 shows an image of the schematic outlined in figure 3.1 taken from the leading edge of the burner, looking along the forced flow centreline which will propagate away from the camera location and toward the fan. An example of probe location is shown and the clip-holder system used to position probes while trying to minimise the physical obstruction to the natural flame and forced cross flow fields. The 1cm deep lip around the burner surface perimeter can be seen as can the top surface of the fine gravel layer.

3.2.2 Elements of Design Influenced by Literature

3.2.2.1 Gaseous Fuel Source and Burner

The utilisation of a gaseous fuel source delivered via a gravel-filled burner affords a simplified analysis [24] since the fuel mass loss rate and therefore the HRR are independent of all other mechanisms with the flame such as heat flux to the source and oxygen delivery to the combustion zone, which is linked to the entrainment characteristics. In this way a range of non-variable heat release rates may be implemented so that the characteristic strength of the buoyant force may be controlled and studied. For these experiments definition of characteristic buoyant forces and characteristic inertial forces is important. This is significantly simplified by decoupling the fuel delivery rate from the complex fire processes.

3.2.2.1.1 Gaseous Fuel and Burner - Limitations

It is therefore not possible to study the potential impact upon the heat release rate by the variation in oxygen delivery rate to the combustion zone provided by the evolving entrainment characteristics of increasing cross flow forces. This phenomenon has not received a large amount of focus in the literature however is an interesting area since [6], [12] and [45] reported the axis-symmetric case for diffusion and jet flames that between 5-20 times the stoichiometric requirement for oxygen was met by entrainment in ambient conditions over the intermittent flame height.

3.2.2.2 Aspirating Fan

Audouin et al. [22] utilised aspirating fans whereby the cross flow was induced by a fan located downstream of the flame. Such a design is representative of the case in modern buildings where fans are installed to exhaust smoke from accidental fires as part of the smoke management system. No experimental cases have been uncovered in the literature for fires immersed in a cross flow generated by a fan upstream of the fire, where the cross flow inertia is generated by pushing. Further, such a design is not representative of a smoke control system in typical infrastructure. An upstream fan would further complicate matters since, concerning flame

characteristics, entrainment due to the boundary layer mode, plume mode and the transition section between these modes [24] must be studied together as highlighted in figure 3.3. For this work it is desirable to isolate the impact upon entrainment characteristics of the tilted portion of the fire plume since this has not explicitly been attempted previously with experimental work. To consider the tilted portion and any subsequent buoyant portion together is to consider the fire plume in the context of a compartment, as was the premise in [19]. In fact, the experiment design allows us to create a range of transitional cases using the set-up in part figure 3.3 part (b). As the relative buoyant force is increased and fire plume begins to overcome the forced flow. This is discussed in detail in the results sections.

3.2.2.2.1 Aspirating Fan - Limitations

It is desirable to study the impact of the cross flow entrainment within the context of a compartment since very few compartment fire analyses have explicitly tried to isolate the impact upon smoke mass flow resulting specifically from the generation of a unilateral cross flow. This is not the focus of this research however and findings from this work may be inferred within the context of the compartment scenario. The primary limitation of the chosen design setup is that any mass of smoke which escapes the fan flow cannot be captured and analysed.

3.2.2.3 Non-confined fire plume

[20] and [35] used a tunnel compartment to study their tilted flames and noted several physical influences that the compartment boundaries had upon the fluid flow therein. It is explained in [20] that when the fire plume reaches a plume mode whereby it overcomes the forced cross flow and propagates upward it is bounded by the ceiling of the tunnel compartment, an outward lateral flow of smoke was observed (as appreciated in typical roof jet theory) and a portion of the smoke was therefore directed upstream and subsequently, eventually reintroduced into the downstream flow. This was of course acceptable since the focus of the study was on the boundary layer portion and the smoke movement was judged not to negatively affect the goals of the work. In that work [20], the term 'boundary layer mode' was

used to describe the tilted laminar flame portion of the plume since the experiment was a small scale set up. The focus was on the impact of gravity upon a laminar diffusion flame, and the laminar manifestation of the flame under varying horizontal and vertical plane forces could be well described by that of boundary layer analogy. Such a boundary layer mode does occur in the present work near the base of the flame (and visually becomes more apparent, and comparable, to that described in [20] when stronger cross flow forces are applied) and can be visualised and is discussed in the experiment photos/characterisation that follow. In terms of entrainment however, the entrained mass within the small boundary layer portion of the flame cannot simply be decoupled from the total fire plume entrainment, due to the scale and measuring techniques of the current work. [35] presented images of the toroidal mixing which occurred at the downstream edges of the burner and flame, which were partially attributed to the presence of the lateral compartment walls which essentially bounded the flame. Lateral entrainment at the flame and along the plume length was therefore significantly inhibited by the presence of the compartment walls meaning that the smoke delivered for analysis with such a design would not have been diluted by the natural mixing that would occur in an unbounded space with a free fire plume. A tunnel compartment design was not chosen for this work so that lateral air entrainment at the flame and along the plume length was possible uninhibited. Subsequently, a qualitative analysis of the flame behaviour using photo evidence requires that entrainment from all directions is possible, as would likely be the base in an accidental fire in a building. Finally, it is desired for this work that when the plume mode region does occur, this can be realised and characterised. This would not be the case with a tunnel-compartment design.

3.2.2.3.1 Non-confined Free Fire Plume - Limitations

As was noted previously, any mass of smoke that escapes the exhaust fan forced flow field cannot be captured and analysed. This would have been possible with a tunnel compartment design, however as discussed above the entrainment

restrictions imposed by the bounding compartment walls are not conducive to the goals this work.

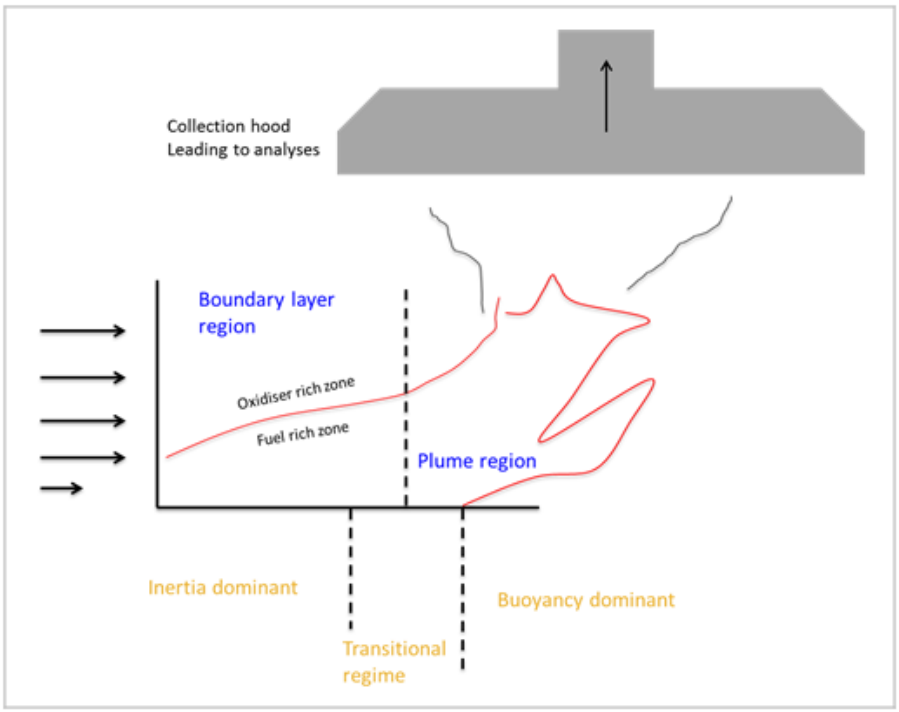

(a)

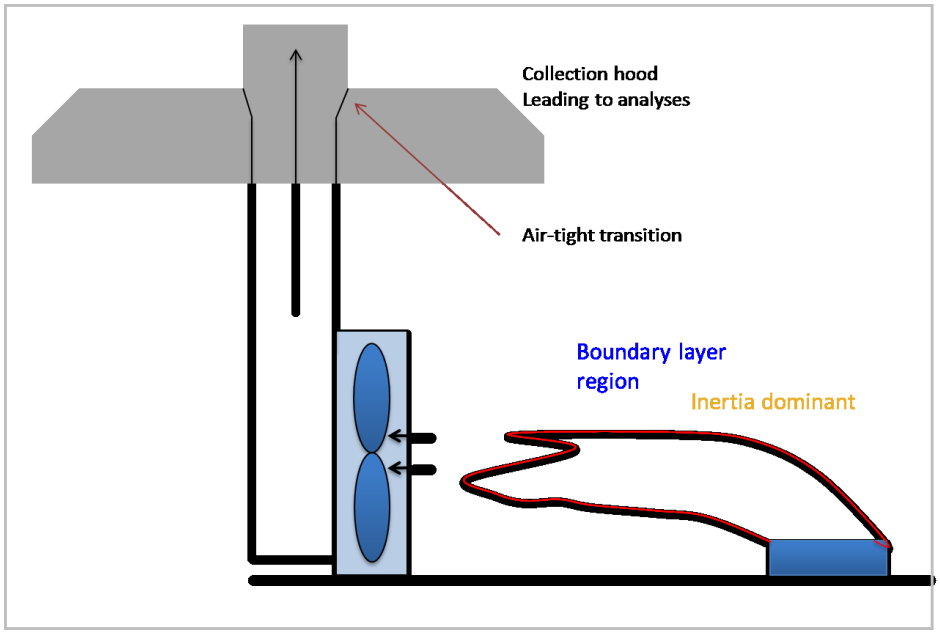

(b)

Figure 3.3: Part (a) depicts the various fire plume modes combined in the flow analysis when a pushed cross flow is generated. Part (b) shows the design intended to isolate the boundary layer mode with an aspirated flow.

3.3 Lab Experiment Outline

An initial test regime was designed in order to gain a sizeable group of data (test 1) and two variant tests (tests 2 & 3) were added in order to gain comparable flow field pressure data and a range of alternative flow field pressure data. An initial analysis of the three tests and what the data from each test reveals when compared is presented in Section 5.1. A deeper analysis mainly focusing on the data from test 1 is presented throughout chapter 5. The parameters of the three tests are outlined in figure 3.4. A mainly-qualitative introduction to the effects of the crossflow upon physical flame characteristics is provided by chapter 4. Much of the data presented in chapter 4 was acquired since some of the physical characteristics expected once a crossflow is applied to a buoyant flame were not observed during the formal cases outlined above (tests 1-3). Primarily this was driven by the lack of a reduction in mean flame length which is commonly cited in the literature. To this end, digital images were studied and have been presented comparing the buoyant flame, an intermediate case from the formal study and a further case where the entrainment fan was increased until such a point whereby the observable flame length was considerably reduced. Some quantitative data was recorded and some was acquired from analysing the images presented throughout chapter 4. This analysis is intended to give an introduction to the general tilted-flame characteristics before a thorough quantitative analysis is presented in chapter 5. It should be noted that when the entrainment fan rate was increased suitably to achieve a shortened flame length, the rate appeared to be so great that some smoke was noted to be exhausted back out of the fan box compartment and subsequently entrainment / mass flow readings during this approach were not deemed to be usable, and thus are not presented.

3.3.1 Test 1

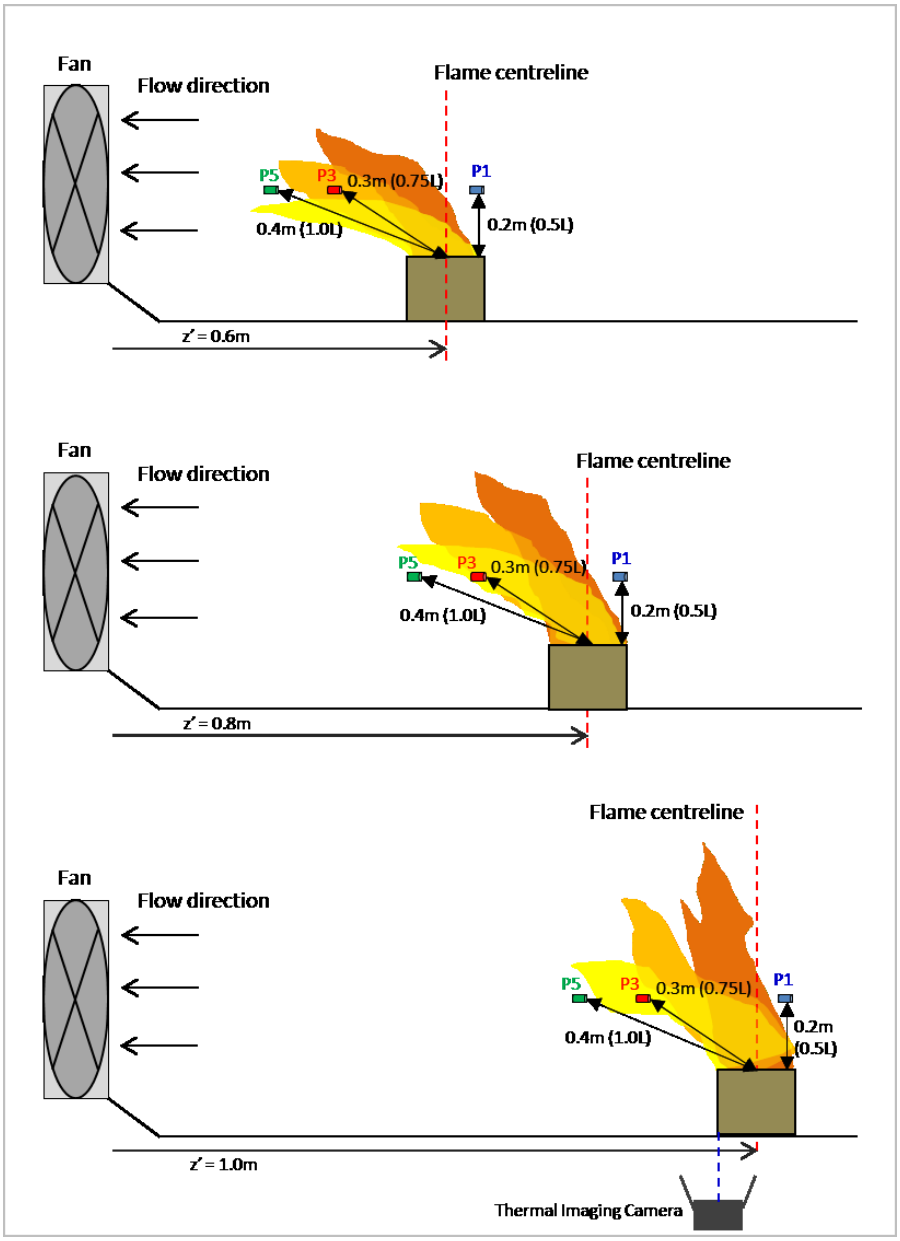

Figure 3.4: Highlights probe locations for Test 1

Test 1 is the primary test schedule with the most variables manipulated across the test run. Figure 3.4 depicts the three distances at which the flame is positioned with respect to the fan. The fan-to-flame distance is varied from 0.6m, 0.8m to 1.0m and the fan-to-flame distance is denoted z' and is akin to the buoyant case distance z, the elevation above the source chosen when evaluating the mass flow. This is so since the flame-to-fan distance is essentially the distance at which the mass flow rate is evaluated in the tilted plume cases.

Three fan speeds are selected and utilised for each of the three z′ cases. Fan speeds were chosen based upon trials with the smallest fire size/shortest z′ combination where the flame was practically tilted to horizontal (with the fastest fan speed, v3). This was so because all other cases after this extreme case are iterations moving toward the most buoyant case (largest fire size/greatest z′). The two slower fan speeds were then chosen by dividing equally the fan speed dial range between v3 and zero. Fan speeds are referred to as v1, v2 and v3 from here on. V0 is occasionally used in reference to cases where the fan is not engaged and a fully buoyant flame is studied. The mass flow rate that each fan speed corresponds with is detailed in section 3.4.3.1.

Test 1 includes a baseline case where the fan is engaged at v1, v2 and v3 but no flame is present. The primary fire size (10kW) was then introduced and the 9 variations described above (3 x fan speed and 3 x z′) carried out. The fire size is increased to 20kW and finally 30kW. In each case the 9 variations were again created producing a total of 30 variation cases, 27 with flame and three free cross flow cases (those baseline cases with no flame present). The thermal imaging camera recorded all 27 flame cases (although it is only depicted in the 1.0m in figure 3.4).

Horizontally orientated probes are denoted 1, 3 and 5 moving from the leading edge of the burner to the rear. This may seem odd however this was required to keep consistency across all tests once the vertically orientated probes were introduced in test 2.

3.3.2 Test 2

Test 2 was then carried out in order to gain data suitable for direct comparison between the cross flow iterations of test 1 and for the fully buoyant case where no cross flow is applied. Thus the horizontal probes 1, 3 and 5 are retained in their original locations relative to the flame and the three vertically orientated probes (2, 4 and 6) were introduced at locations corresponding to the horizontal probes. This test was carried out for comparison with the primary fire size (10kW) from test 1. Figure 3.5 shows the probe arrangement and presents a close-up image.

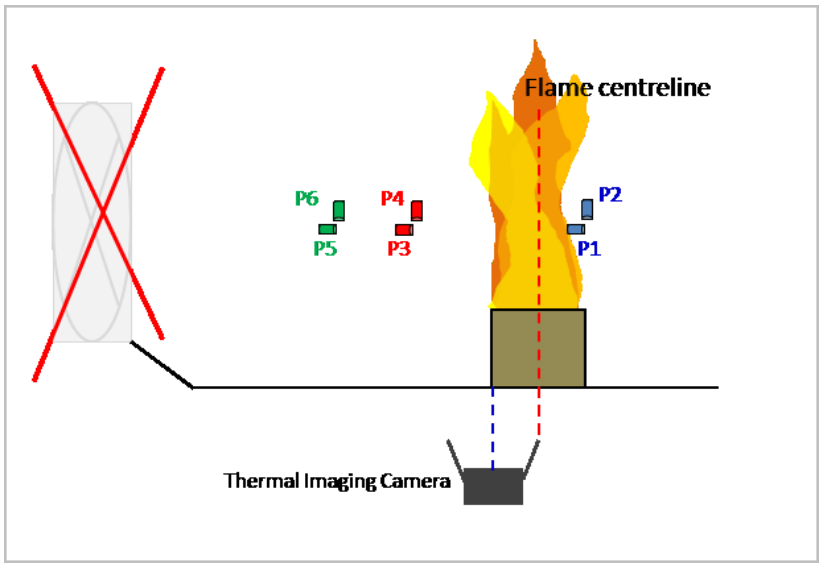

(a)

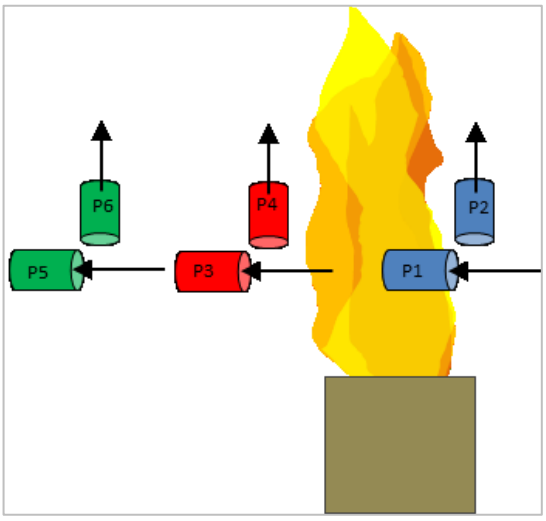

(b)

Figure 3.5: (a) Highlights probe locations for Test 2. Probe size has been exaggerated in part (b) and gives a close-up of probe orientation for clarity.

3.3.3 Test 3

Test 3 was then carried out to gain insight into the variation of velocities predominantly within the flaming region rather than around the flame as in tests 1 and 2. Figure 3.6 shows the probe arrangement which includes horizontal and vertical probes. In this case probes 1 and 2 were located very close to the leading edge just above a near-field laminar flame section that had been noticed during the cross flow cases of test 1. Probes 3 and 4 were located around at the centreline of the fully buoyant flame around 10cm from the base. Finally probes 5 and 6 were then located to the rear of the flame (20cm above the base) a few centimetres outside the fully buoyant flame edge, but typically fully immersed in the flame once a cross flow was applied. This case was performed at z'=0.6m for fire sizes 10 and 20kW and with fan speeds v0, v1 and v2.

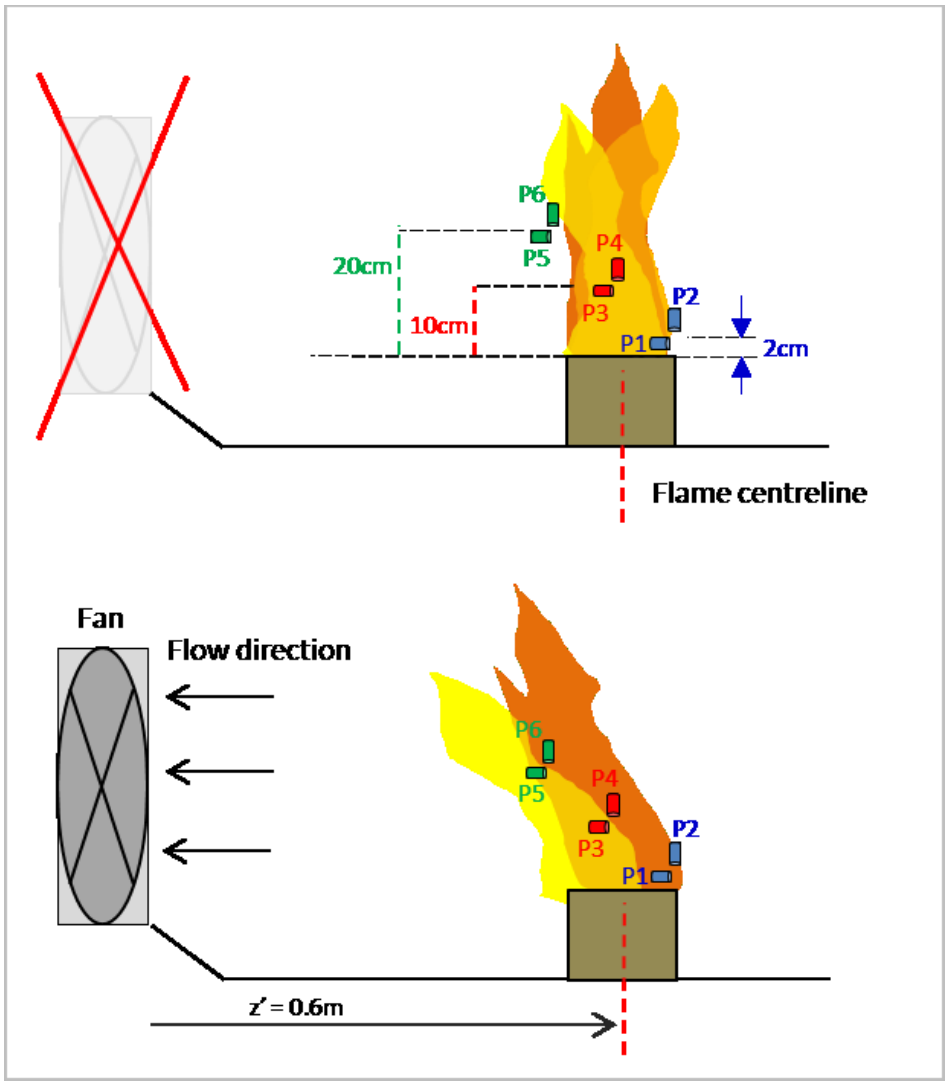

Figure 3.6: Highlights probe locations for Test 3

3.3.4 Experiment Schedule

The following three tables outline the test schedule for each of the three previously described test setups. The order in which the three primary variables are manipulated is outlined here and each iteration of the entire testing procedure is assigned a case number for reference throughout the results sections.

Test 1						
Case	Q (kW)	z' (m)	Fan speed	Probes	Thermal Imaging	Digital Video
0.1	N/A	0.6	v1	Probe Arrangement 1: 3 x Horiz Predominantly around flame	N/A	N/A
0.2		0.8	v2			
0.3		1.0	v3			
1	10	0.6	v1		IR Camera Lateral to burner (1.5m)	Where approriate
2			v2			
3			v3			
4		0.8	v1			
5			v2			
6			v3			
7		1.0	v1			
8			v2			
9			v3			
10	20	0.6	v1			
11			v2			
12			v3			
13		0.8	v1			
14			v2			
15			v3			
16		1.0	v1			
17			v2			
18			v3			
19	30	0.6	v1			
20			v2			
21			v3			
22		0.8	v1			
23			v2			
24			v3			
25		1.0	v1			
26			v2			
27			v3			

Table 1: Test schedule for Test 1

Test 2						
Case	Q (kW)	z' (m)	Fan speed	Probes	Thermal Imaging	Digital Video
28	10	0.6	v0	Pobe Arrangement 2: 3 x Horiz + 3 x vertical Location as per test 1	As test 1	As test 1
29		0.8				
30		1.0				

Table 2: Test schedule for Test 2

Test 3						
Case	Q (kW)	z' (m)	Fan speed	Probes	Thermal Imaging	Digital Video
31	10	N/A	v0	Probe Arrangement 3: 3 x Horiz + 3 x vertical Predominantly inside flame	As test 1	Near-field focus
32		0.6	v1			
33		0.8	v2			
34	20	N/A	v0			
35		0.6	v1			
36		0.8	v2			

Table 3: Test schedule for Test 3

3.4 Data Acquisition Techniques

3.4.1 Differential Pressure

Changes in the pressure and thus velocity profiles around and within the fire plume were measured using bi-directional pressure probes. Concerning probe dimensions – probe head outer diameter was 17.0 mm, head length 32.0 mm and pipe internal diameter 15.8 mm. Probes are shown in figure 3.7.

Figure 3.7: 24'' Probe head

These so-called *McCaffrey bi-directional probes* [70] were logged on pressure transducers which recorded the hydrodynamic pressure difference at each time step. The appropriate calibration method for the probes is outlined in Appendix A.

A range of locations were chosen at the leading edge of the flame, at the leeward edge of the flame and further downstream of the flame, toward the fan. Depending on the magnitude of the cross flow strength probes could effectively be located around the perimeter of the flame or immersed within it as a result of the varying flame tilt angle, length and volume during test 1. That is to say that throughout test 1, the probes were located in constant relation to the burner as the fan strength was increased and the flame was tilted further. Test 1 were designed this way so that a qualitative description could be garnered as to the changing pressure profiles at a range of points of interest as the cross flow flame evolved under increasingly strong cross flow. An additional arrangement with probes positioned inside the flame and along the centreline of the flame/plume was adopted in test 3. During the

preliminary trial runs it was discovered that the diffusion flame under cross flow conditions was quite moveable and the tilt angle and flame shape were far from constant. It was felt that, on initial observation, the concept of a true *centreline* was significantly lost downstream of the burner surface (relating to around 10cm from the burner surface along the flame "centreline") due to the turbulent conditions realised. The downstream probes (5/6) in test 3 were therefore positioned in a location that was largely involved with the flame over the various iterations of cross flow strengths giving an insight into the differential pressure within the flame fluid in each case. Choosing static locations in test 1 and 2 also allowed a picture of how the flow field around the entire flame perimeter was evolving as conditions were manipulated. The flow field at the leading edge of the flame, and to the rear of the flame in the wake of caused by the buoyant source immersed in the cross flow, are as important as the flow dynamics within the flame volume itself when entrainment in a non-ambient environment is the phenomenon of investigation. The evolution of local velocities in the region around the flame is discussed in detail in the results sections. What this combination of arrangements affords us is specific localised pressure data downstream within the flame region as well as an articulation of the characteristic velocities across the near and far-field of the fire plume system.

During calibration the units tested were mounted 140mm from the end of a wind tunnel with the head aligned perpendicular to the flow direction and was calibrated against a laser Doppler anemometer. In each experimental crossflow case increasing larger horizontal forces are pitted against the natural buoyant vertical flow field of the no wind case, creating a range of angled flow fields (combination of the vertical and horizontal forces). The probes were maintained on the vertical and horizontal planes throughout all tests so there may be some disparity between the design/ calibration configuration and that adopted in these tests. It is likely that angling the probes as such may create slightly more turbulence at the probe orifice under a laminar flow like that of the calibration process, resulting in pressure readings marginally lower than are actual present. The naturally turbulent flame flow fields however, especially when combined with the forced cross flow, presents a much

more generally turbulent flow field than in the calibration procedure, making the impact of angling the probe head much more difficult to address. For this reason the ratio between pressure readings at the different probe locations is of greater importance than specific pressure readings at any one location. Future tests will make use of a greater number of probes and the impact of probe head angle on turbulent flame flow readings will be better quantified.

3.4.2 Extraction Hood Calorimeter

3.4.2.1 Mass Flow Rate & Species Composition

The use of the hood calorimeter for the calculation of the HRR by oxygen calorimetry is problematic for the current experiment setup. As will be seen in the results sections the manipulation of the variables of cross flow strength, distance z' and HRR result in a range of progressively tilted fire plumes. In the more buoyantly-dominated cases not all the smoke is captured by the exhaust fan since the cross flow field is overcome by the buoyant force. It is therefore true that the O_2 measurements inside the hood system may not be measuring purely the reduction in oxygen fraction due to smoke but also in some cases the addition of the oxygen fraction due to clean air included in the cross flow field. A reliance on the calculation of HRR by the fuel flow rate and heat of combustion is therefore necessary. Figure 3.8 shows an example of O_2 measurement for a range of crossflow cases.

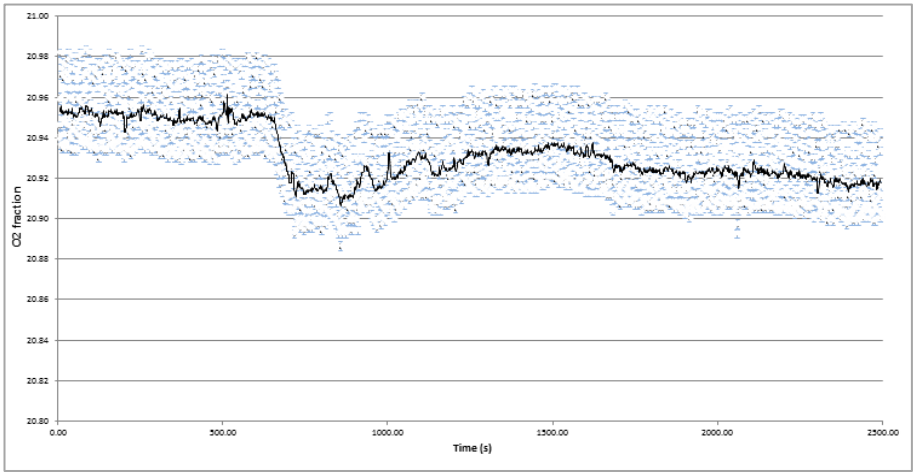

Figure 3.8: Baseline O_2 fraction with no fire source, associated data range in blue

This factor does however present the opportunity to estimate when the exhaust fan captures roughly all of the smoke and very little fresh air, since the HRR is predetermined. Once the O_2 readings from the calorimeter reach a level corresponding with the calculated HRR, it is reasonable to conclude that approximately all the smoke from the particular case is captured by the exhaust fan flow. For all cases where the O_2 reading is higher than expected (oxygen fraction not as low as expected for corresponding HRR) either of the following cases may be true. Either:

- The entire body of smoke produced by the fire is captured but due to the forced flow being greater than the purely-buoyant entrainment rate for the fire size in question, additional air is entrained along with the products of combustion (which are produced at a constant rate due to constant fuel injection rate) and the hood O_2 reading therefore appears higher than would typically be representative of the present HRR, or
- For cases where buoyancy is greater and some of the plume may manage to escape the exhaust fan flow field some of the combustion products are not transferred into the hood which has the same effect of producing a higher O_2 reading than expected for the current HRR.

Subsequently the additional clean air entrained as per point 1 may compound the result in the case of point 2. Species readings are therefore generally informative but only for applying general descriptive statements of the flow scenario. Referring to figure 3.8 - after 600s the fan is switched on with the fire located 0.6m away. At around 900s (the first data peak) the flame was moved further (0.8m) and at 1100s the flame was moved further again (1.0m). In each of these cases, even though the fire size remains constant the O_2 reading increases as more buoyant smoke escapes the fan-induced cross flow, demonstrating the nuance described above. Further O_2 data used in the analysis in the results sections.

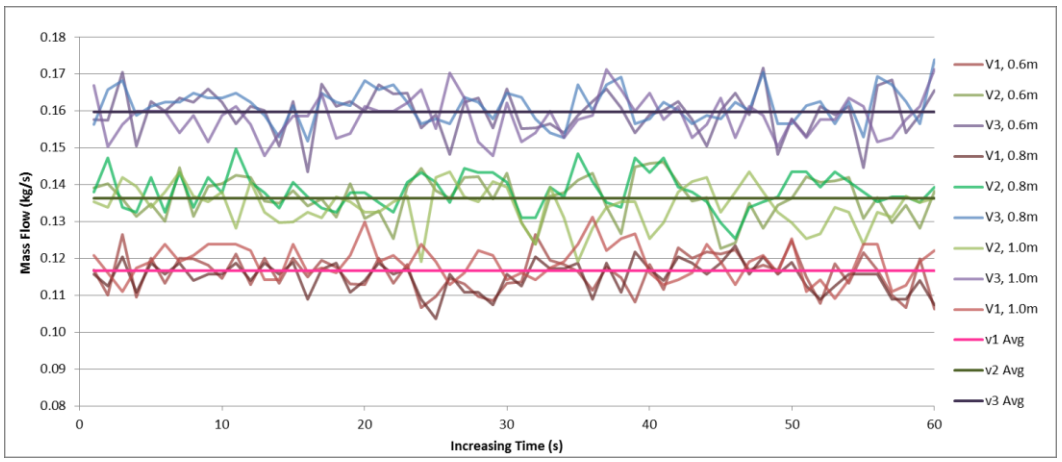

Figure 3.9: Average mass flow readings from extraction hood, where:
Red = v1, green = v2, blue = v3.

The mass flow rate is determined from a calculation of density utilising ideal gas assumptions and temperature measurements to derive the differential pressure within the instrumentation set. Flow velocity is then calculated with proportionality to the square root of the pressure differential and density and velocity are then combined. The hood mass flow rate readings for each set of experiments where the same 3 fan speed settings were implemented were recorded and compared to ensure no adverse error was introduced to the exhaust fan flow rate by the fan speed dial itself (figure 3.9). The extraction hood and measurement instrumentation was calibrated as per the University Fire Lab's standard and regular calibration schedule. [70] and [71] provide further information on technical considerations for extraction hood and oxygen calorimetry error potential and aspects of concern for the systems in typical usage scenarios. An error in the order of 10% for oxygen calorimetry results is detailed in [71] and additional causes for increased potential error magnitude are discussed.

3.4.3 Heat Release Rate

A digital flow meter was used to control the flow of propane gas (C_3H_8) to the burner. As noted previously the HRR was estimated based solely on this mechanism. For the fire sizes 10kW, 20kW and 30kW the propane flow rates were set at 0.216, 0.432 and 0.646 g/s respectively.

The settings were based on the relationship:

$$\dot{Q} = \dot{m}\Delta H_{eff}$$

Equation 3-1

Where $\dot{Q}$ = total HRR (kW), $\dot{m}$ = mass loss rate of fuel (g/s), or in this case fuel mass flow rate, and ΔH_{eff} is the effective heat of combustion of propane (46.45 kJ/g).

3.4.4 Thermal Imaging Camera

The IR thermal imaging camera provides the opportunity to acquire images of the flame and plume region based upon the thermal footprint which can differentiate regions of the flame, plume and surrounding gas or structures. This can be beneficial since only the flame and approximate smoke contours can be acquired approximately in the visual spectrum. The IR camera was positioned laterally to the rear edge of the burner in order to capture the flame at the burner and downwind in-so-far as possible. Positioning the camera further away in order to acquire a picture of a larger area surrounding the experiment apparatus was limited by the physical legs and walls of the hood structure and supporting members. The analyses undertook to acquire average flame tilt, flame length and flame temperature distributions is presented in section 3.5. Images were processed using a purpose-written Matlab (v. R2015a) script [72] for image analysis similar to that outlined in [73].

3.4.5 Digital Video Data

Physical flame characteristics including:

- Flame Volume
- Flame flattening
- Visual appreciation of wind effects on flame Shape
- Flame Oscillation - Visual Interrogation of:
    - Near-field laminar region
    - Transition to Turbulence
    - Boundary Layer Mode and Plume Mode Realisation

were analysed after recording the flame behaviour mainly during test 3 when pressure probe data was acquired close to the flame leading edge and within the flame region generally. These image data are discussed in section 6.

The video footage was shot at a variable frame rate of 24-30fps. The rate was automatically adjusted by the camera in reaction to the lighting at each specific camera location. This function is beneficial given the variation in available light to the lens between far-field shots where the flame is small within the camera field of view and close-up shots when the flame fills most of the field of view and is only a few inches from the lens. Close-up shots were only able to be filmed for a few seconds at a time in order to protect the camera lens.

Still shots were captured from the video reels using DigiDesign Pro-Tools multi-media processing software [77] which allows editing of video frame by frame.

3.5 Flame Angle and Length Measurement

3.5.1 Measurement Method

Figure 3.10 presents of (a) a colour contoured IR image, (b) grey scaled version of this image, and a range of binary images with varying cut-off threshold levels, relating to the black-white scale of the grey image. Problematic flame photographs with decaying luminosity at the flame edge are replaced by more well defined colour boundary between flame and background by using the IR image.

In figure 3.11 binary images from the total data set are combined and averaged using the range of cut-off thresholds presented in 3.10. When measured, the tilt angle appears constant across full threshold range. A higher threshold such as 0.8 gives an image of flame presence probability with higher confidence, essentially, the volume in which the flame fluid is present 80% of the time. Lower confidence intervals are also of interest so that deviation in flame shape (such as transition from boundary layer to plume mode) can be qualified. This level of detail can be missed if too high a confidence interval is selected. With these averaged images the true centreline is still obvious since the flame edges are not so well defined. The flame angle measurements specifically are attained by placing a protractor stencil across the resultant images and measuring the angle. The angle is measured from the centre of the burner. It could be argued to take the measurement from the front edge or rear edge in each case however the centre point seems to be an intuitive 'average' point from which to work. The flame length is measured using a calibrated measurement tool in an available CAD software package.

Due to uneven ground it was noticed during experiment trials that the camera could not be positioned exactly perpendicular to the ground, hence it can be seen in figure 3.11 that the vertical axis of the protractor example sketches are off-set from vertical. They run parallel with the probe clamp stand uprights, which were evaluated to stand essentially vertical, and perpendicular to the experiment rig local grade.

In figure 3.12 flame presence probabilities are demonstrated across the edge of the flame where 1 represents 100% chance of flame presence in that pixel and 0 equals zero occurrence of flame in that pixel across all images. Applying a threshold function to this data grid allows us to acquire a more well-defined flame shape where the presence probability gradient within and toward the edge of the flame is eliminated and the flame length and shape becomes a function of the presence threshold cut-off chosen to best represent the average flame shape.

This is demonstrated in figure 3.13 where a range of presence probability thresholds have been evaluated against the average flame image. This can be useful in

narrowing the flame width which can eliminate ambiguity when it exists around flame angle and perceived centreline. It can also however shorten the flame so that perturbations in flame shape further along the flame length may be lost. Any radical flame shapes however appear to be removed from the conversation by the process of averaging all 60 flame images. This process is repeated for every experimental case and the average flame shape in each instance again appears to demonstrate a well-defined average flame angle each time.

Figure 3.14 demonstrates the impact of decreasing the threshold on the apparent flame length (where varying flame lengths (y-axis) are presented as a fraction of the maximum flame length - where maximum flame length corresponds to cut-off threshold = 0.9). The flame length appears less sensitive to threshold variation between threshold values of 0.7 -0.4. This was found to be repeated across all cases. 0.5 therefore was selected since it exists within this range and since it also represents the average value of flame presence associated with intermittent flame length estimation, where the flame is therefore present at that point for precisely half of the experimental observation time period.

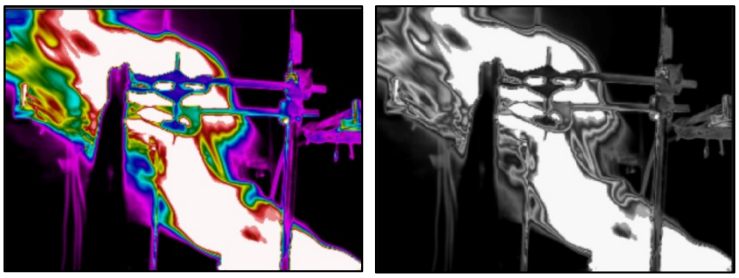

(a) Colour (b) Grey-scale

(c) Threshold = 0.1 (d) Threshold = 0.2

(e) Threshold = 0.3 (f) Threshold = 0.4

(g) Threshold = 0.5 (h) Threshold = 0.6

(i) Threshold = 0.7 (j) Threshold = 0.8

Figure 3.10: Colour, grey-scale and range of threshold-varied resultant binary images

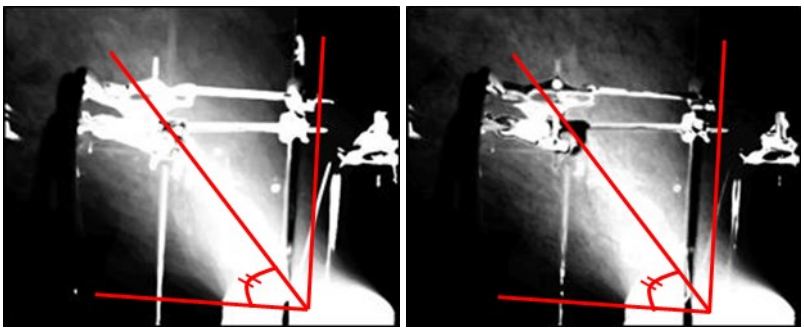

(a) Threshold = 0.1 (b) Threshold = 0.2

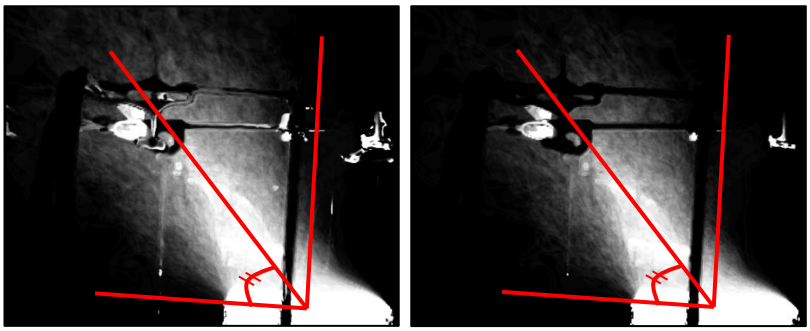

(c) Threshold = 0.3 (d) Threshold = 0.4

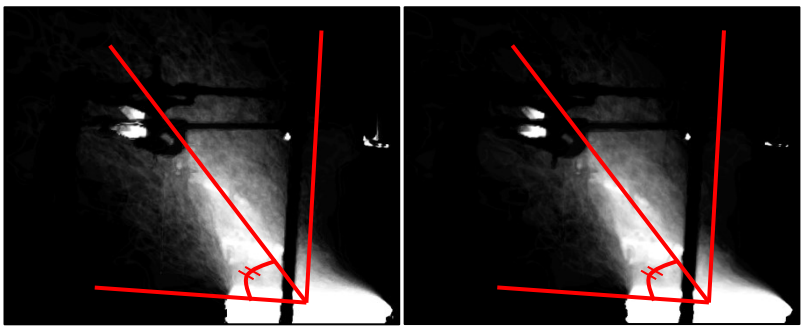

(e) Threshold = 0.5 (f) Threshold = 0.6

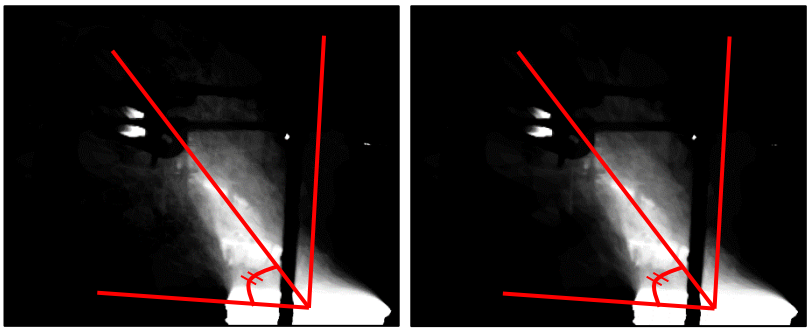

(g) Threshold = 0.7 (h) Threshold = 0.8

Figure 3.11: Range of average images as a function of chosen binary threshold

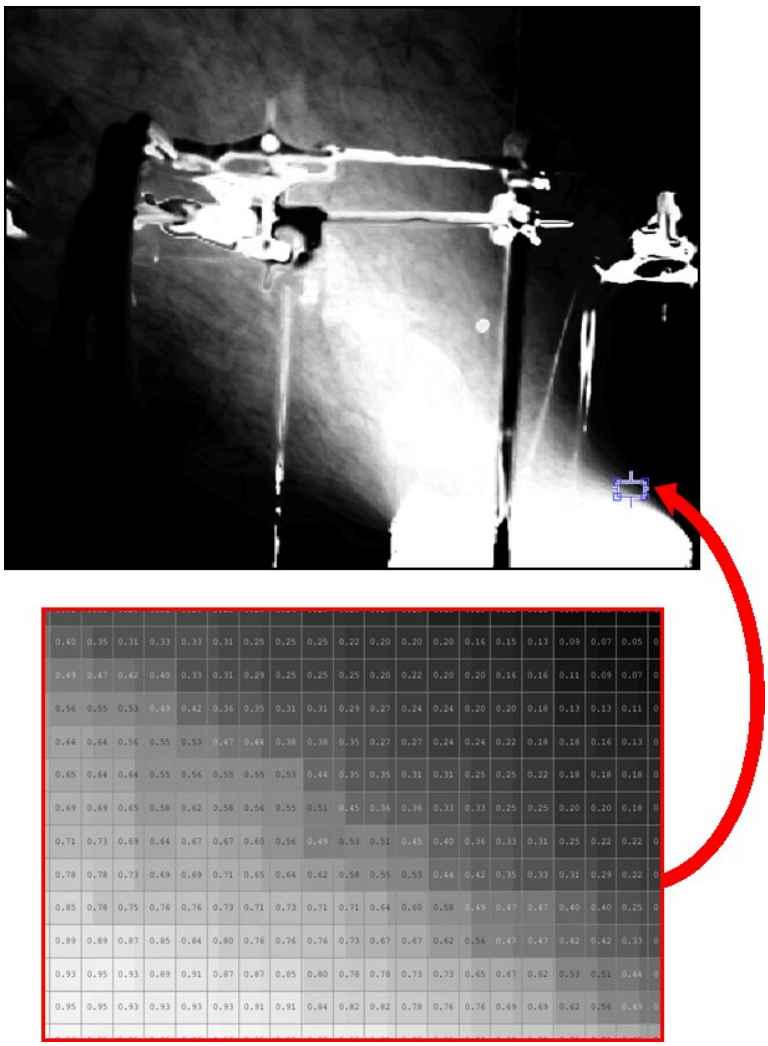

Figure 3.12: Average image with flame presence probabilities

3.5.2 Sensitivity to Flame Presence Threshold

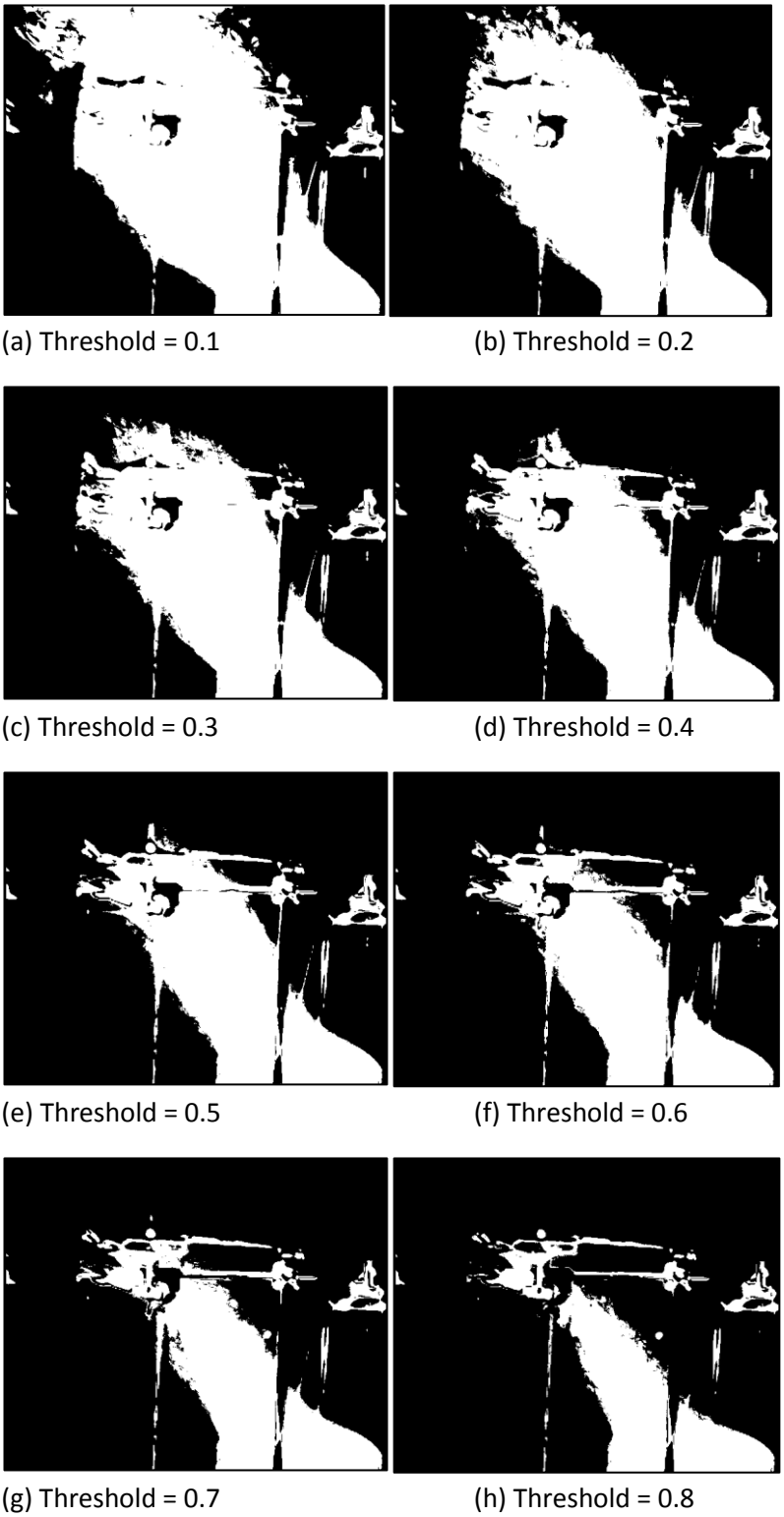

(a) Threshold = 0.1 (b) Threshold = 0.2

(c) Threshold = 0.3 (d) Threshold = 0.4

(e) Threshold = 0.5 (f) Threshold = 0.6

(g) Threshold = 0.7 (h) Threshold = 0.8

3.13: Final binary conversion allowing measurement of average flame angle and length relating to the 0.5 flame presence probability

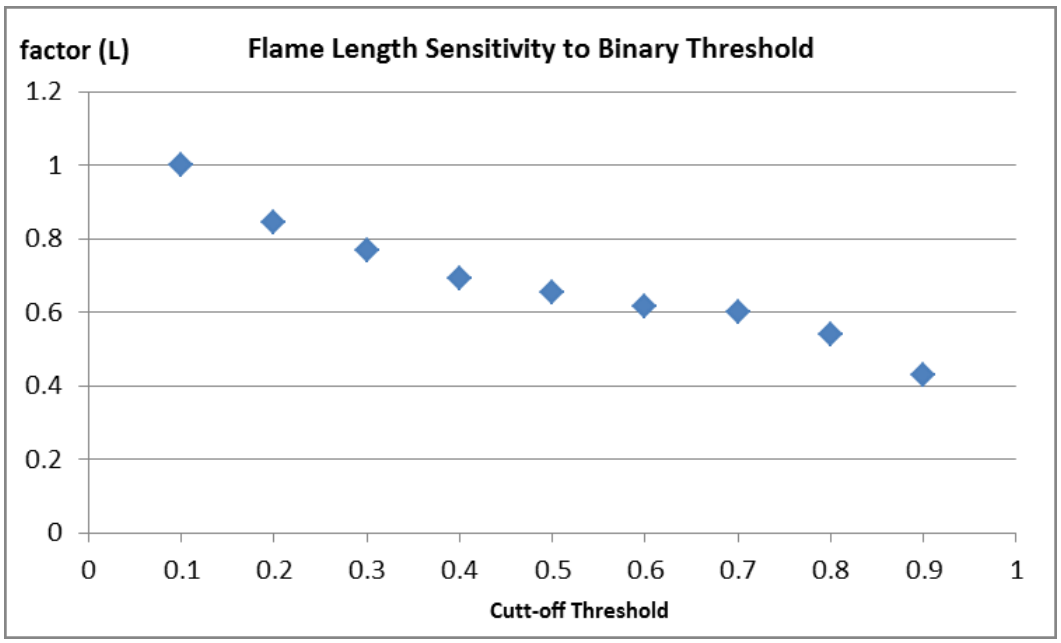

Figure 3.14: Sensitivity when varying the binary cut-off threshold on the flame length of *average flame angle* images. Length factor is a normalised value considering the 10kW flame for each fan speed setting.

4 Mixed-Convection Flame Characteristics

In chapter 5 consideration will be given to the impact that a cross flow has upon the entrainment of air into the fire plume as a whole, which is the context in which most of the discussion in literature for engineering purposes is focused. With this experimental set-up however it is desirable to consider the impact that the cross flow has upon the entrainment mechanisms specific to the flaming region of the fire, since this has rarely been discussed in the literature. This is the goal of chapter 4. Distinctions are made throughout the literature [12] between the flame (constant/intermittent) and plume region of the overall fire plume in terms of the defining physical attributes and fluid behavioural patterns, and the same is true for the entrainment mechanisms which apply to each portion of the fire plume, or more accurately, the entrainment mechanisms which share varying importance over the entire fire plume structure. The periodic generation, evolution and dissipation of convection-driven vortices is most prominent and apparent in the flaming region where a sharp temperature gradient exists at the flame and bulk fluid boundary and thus where the fluid motion pressure differential is greatest. The velocity difference across the flame boundary gives rise to a higher Reynold's number profile; a differential viscosity exists and results in substantial shear stress which all culminates in the formation of toroidal vortices around the circumference of the rising hot plume fluid. The impact upon this axis-symmetric fire plume system by the addition of a forced cross flow ΔP is lacking in the literature, certainly in the context of entrainment of fluid into the tilted plume and thus a qualitative and descriptive discussion is submitted herein. Some quantitative analysis will be included for context.

4.1 Vortex Generation

4.1.1 Buoyant Vortex Generation

A new near-field entrainment model was presented by Cetegen [47]. Motivations for this work stems from the acknowledgment that while the ideal plume model shows generally well-corellated entrainment rates for the fire plume above the flaming

region, Cetegen and McCaffery in particular [6, 12] noted the difference in dependence upon parameters for entrainment within the flaming region and for the plume region above. While the traditional plume equations find the mass entrained as a function of HRR (Q_c), source diameter and height of interest above the source (z), [46, 47] suggested dependence for entrainment in the flaming region on source diameter and height above the source only, excluding HRR. Subsequently Cetegen in [47] points out that the consideration alone of duffusive entrainament into the flame fluid sheet significantly underpredicts measured entrainment rates for the flaming region of the fire plume. Wrinkling and stretching of the flame sheet may offset this underprediction by a small amount but is not adequate to fully describe the entrainment rate at the flame in full. The main mechanism of entrainment is therefore the

"… large scale engulfment and turbulent mixing resulting from periodic, turbulent vortex generation."

(Cetegen, 1998).

Diffusive transport of air toward the flame sheet and fuel flow are therefore considered to be small when compared to the engulfment mechanism of the vorticy structure. As per the ideal plume theory, an axis-symmetric structure is assumed whereby the vortex rings which are produced (at the leading edge of the vortex structure generation) provide a periodic pumping mechanism for ambient air into the fire plume. Figure 4.1 demonstrates the idealised model schematics for this mechanism. Cetegen notes that the strength of the vortex circulation constitutes the strength of the pumping action, which alludes again to the consideration that the magnitude of air entrained is a function of the strength of the upward buoyant force (ΔP_B), and this is with repect to the relatively slow moving, (ambient), surrounding bluk fluid. By considering the volume of the vortex as a cylindrical length of diameter d and height z, and integrating for the time of the birth of the vortex until it rises to a height of interest z_c,Cetegen (1998) proposed the following equation for the volume of entrained fluid at a given instant during vortex convection:

$$Q_{ent} = \pi d \int_0^t \int_0^z U_{vortex}\, dz.dt. \qquad \left[where\ U_{vortex} = \frac{\tau(z_c)}{2\pi(z_c - z)}\right]$$

Equation 4-1

Here the *z*-integral accounts for the volume and the *t*-inegral the time of interest of vortex evolution. The vortex velocity field (U_{vortex}) is given for the outter edge of the ring where τ is the convection velocity and is the vortex strength. This approach essentially defines a volume of interest and applies an entrainment rate for the outter surface area of that volume at a rate governed by the velocity of the inward flow due to the vortex ring fluid velocity. The entrained air volume per vortex cycle can be multiplied by ambient air density and number of vortices (or the vortex shedding frequency) to find the mass of entrained air into the flame.

Figure 4.1 demonstrates this approach by visualising vortex formation at the edges of the flame fluid (a) and by considering the plane of motion of the subsequent toroidal flow field (b). It is important to note the axis-symmetry required for this approach and to appreciate how it is reminiscent of the axis-symmetric ideal plume approach in systematic structure. This approach has been shown to fit sufficiently with entrainment measurements but the perturbation of this system under the influence of an adjacent forced flow ΔP appears to be adbsent from fire safety literature, particularly in terms of entrainment of air into the flame/plume.

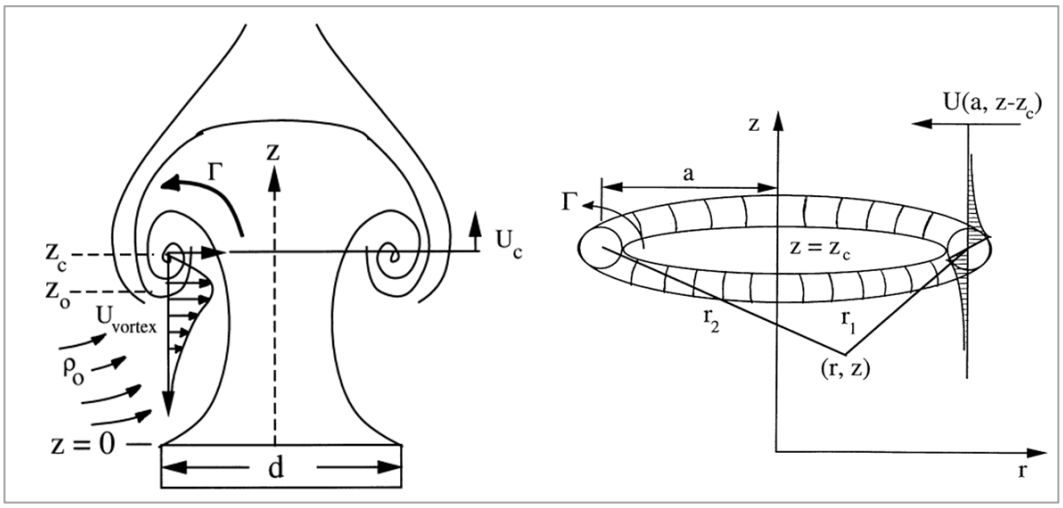

Figure 4.1: (a) Slice through the idealised vortex structure for the Cetegen near-field entrainment model. The mass of air englulfed by each vorticy is assumed to be far greater than the mass entrained by diffusion and (b) structure of a vortex ring with the whole circumference shown. Fluid flow is outward over the top of the ring and inward along the underside of the ring. As demonstrated by both views of the vortex an axis-symmetric plume structure is assumed in order to quantify the mass of air entrained. Images reproduced from [47].

4.1.2 Co-Flow Vortex Generation

Since the case of interest – the impact upon entrainment following the addition of a horizontal forced flow (ΔP_F) to the buoyant (ΔP_B) fire plume – is not present in the literature a partially representative regime can be considered. Some work exists in the fluid mechanics literature regarding buoyant plumes in a co-flow system, otherwise known as *assisted buoyancy*. Clearly this is not the same case as that of interest here however if we consider that the tilted fire plume cumulative vector is composed of some resultant combination of the buoyant and forced flow vectors then we can consider that the forced flow then contributes to the buoyant plume propagation. For intuition then we can consider the cases depicted in figure 4.2 of (a) assisted-buoyancy by co-flowing jet, and (b) buoyancy-assisted mixed convection between two walls.

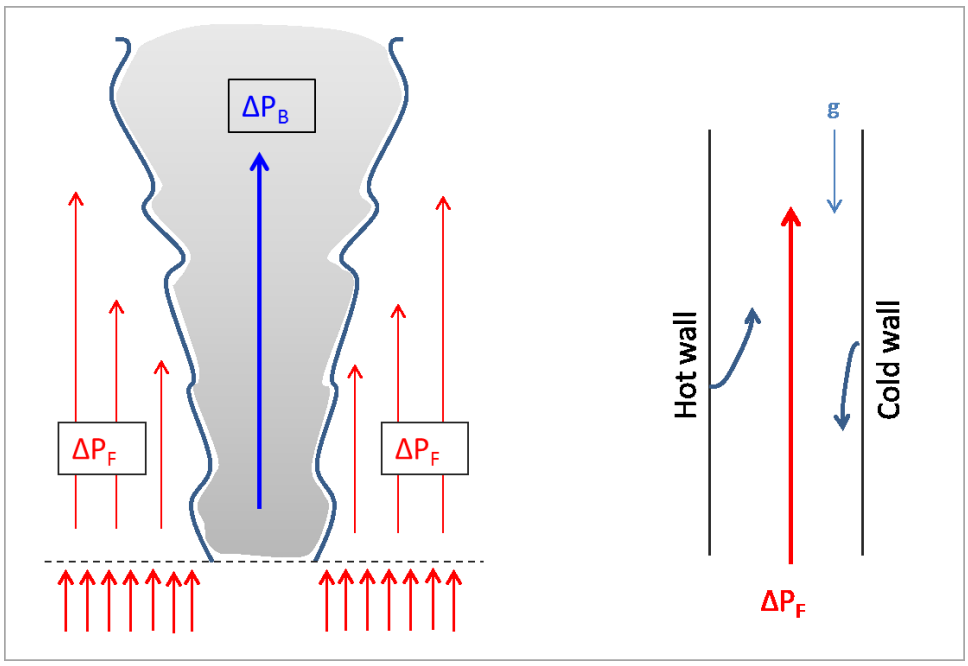

(a) (b)

Figure 4.2: (a) assisted-buoyancy by co-flowing jet and (b) buoyancy-assisted mixed convection between two walls

In the case of the co-flow jet, Subbarao & Cantwell [78] varied co-flow velocity to control the regularity of the vortex generation in a helium plume and demonstrated the impact of Reynolds number and Grashoff/Reynolds ratio upon the physical distance to the onset of turbulence with respect to the exit orifice. The buoyancy exhibited by the helium plume within the bulk fluid was described to approximately represent the case of the hot fire plume. It was demonstrated that increasing the Reynolds number (increasing ΔP_F) has the impact of bringing the onset of turbulence closer to the orifice, where vortex wavelengths appeared to stay approximately constant. When increasing the Richardson number (essentially increasing ΔP_B) and therefore the Grashof number) the laminar portion was again decreased however the wavelength of vortex structures was substantially increased. The acceleration at the plume centreline is understood to stretch this length while the structure is approximately maintained where the buoyant velocities outside of the centreline remain at some magnitude between that of the centreline and bulk fluid. In case (b) Dritselis et al. [8] investigated at low Reynolds/Grashof number

regimes the effect of parallel walls encasing an inertial flow where the left wall was heated and the wall to the right was cooled. This case is again, more abstract compared to the current investigation however the most basic findings are at least of simple relevance. The buoyant gradient produced by the hot wall was demonstrated to increase local velocity within the upward forced flow and the cold wall created a counter-flow due to the negative vertical velocities generated locally. Where these effects occur at the same level, the upward flow is substantially increased at the hot wall to maintain continuity of mass as the fluid at the cold wall sinks against the general upward flow direction. Of particular interest is the expansion of the fluid at the hot wall causing the generation of a buoyant ΔP_B. This pressure wave moves not only upward but also in the first instance outward, away from the wall, which briefly resembles the perpendicular vectors of buoyant and forced flow which are the initial boundary conditions in the design of the current fire plume investigation. The addition of the buoyant pressure wave to the [theoretically perpendicular] vertical inertial flow in [79] had the effect of enhancing the local velocity of the inertial flow. This is similar to this investigation where, in chapter 5, an increase in horizontal pressure probe readings is recorded when we add the 10kW fire to the free cross flow. In contrast to the current investigation the case in [79] was a low velocity, laminar regime however the basic function of the addition of the perpendicular pressure differentials - resulting in enhancement to the forced flow - is simply demonstrated and substantiates the current investigation data.

Returning to the question of vortex structure in the mixed convection fire plume, this has not been found in the literature search and a qualitative description, with the use of digit video stills can now be presented and compared to the existing theories and documented experimental work presented in this section.

4.1.3 Mixed Convection Vortex Generation

The important concept to appreciate here is that not only does the creation of an inertial ΔP *across* the flame alter the apparent angle of the flame but the naturally buoyant structure of the flame fluid flow process is also infracted and a new altered regime appears. The mechanisms that govern entrainment at the flame in the fully buoyant case are de-structured by the addition of the cross flow and this is rarely discussed in this context. Similarly to a jet flame the local Reynolds number is increased however unlike in a jet flame it is not the flame fluid itself which is the source of the inertia but rather the buoyant flame is now immersed in a forced flow so the difference in the velocities of the flame and the surrounding bulk fluid (in the direction of the flame) is reduced. The plume velocity and shear stress created by the instability at the flame / bulk fluid boundary contributes to the size, nature and frequency of each flame vortex as it evolves upward engulfing and entraining air inward. As the flame becomes ever more tilted by the forced cross flow the bulk fluid flow direction becomes further aligned with the flame fluid flow direction. When the difference in velocity between that of the bulk fluid and the flame fluid decreases and the magnitude of each becomes increasingly comparable the frequency of the vortex generation and the nature of the vortex evolution become directly affected.

The postulation then, based upon the pressure data that shall be presented in detail in chapter 5.3 and the video still images in the figures that follow, is that after a sufficiently large forced flow is added perpendicular to the plume propagation, a fundamental change occurs where the mass of air entrained due to diffusion becomes more important than that of the vortex engulfment process, in terms of the total mass entrained into the flame.

A series of video stills were captured and for the fully buoyant case, a low fan speed cross flow and a high speed cross flow. The slower fan speed is approximately equal to fan speed v2 (where velocity reading at probe 3 = approx.. 1.04m/s) from the main experiment and the higher fan speed, where the flow rate was increased until flame

length shortening was observed is produced a crossflow velocity reading of around 2.4m/s (significantly greater than the maximum crossflow reading of 1.8m/s attained during the formal experiment cases in chapter 5). The purpose here is not to focus on flow velocities but to acquire a qualitative description of the visual fire plume entrainment behaviour which has not previously been published as far as can be discerned. This initial observation and discussion is important because it highlights, arguably, a potential paradigm shift in the specific entrainment mechanics of the fire plume which have not previously been considered in quantitative entrainment models in the literature. Future research and experimental work may be designed to investigate and quantify further the impact of the attributes introduced here.

4.1.3.1 Buoyant Case

Figure 4.3 demonstrates a baseline case of video stills of the fully-buoyant flame (10kW) that the tilted flame images presented over the coming pages can be compared with. The sequence represents a one second time period and is displayed over 30 frames. The sequence is actually quite reminiscent of the cine film produced by McCaffrey [57] which was presented in figure 2.5 in the literature review. Figure 2.5 depicts a fully-buoyant gas flame of source diameter 0.3m and demonstrated quite well an oscillation rate (buoyant vortex shedding frequency) of 3Hz. Figure 4.3 also demonstrates quite clearly an oscillation rate of 3Hz despite the fact that our burner diameter in this case is half that of the case in [57]. This is interesting because, as discussed in chapter 2.6, equation 2.31 shows oscillation frequency to bear functionality with the inverse of the square root of the source diameter. With source diameters in the two cases being the same order of magnitude however this is realistic.

It can be observed that a small laminar region near the base is quite variable and appears surrounded by turbulent fluid each time a vortex structure is born near or at the base. In contrast, as the vortex ring rises upward a long, thin laminar region can be seen, momentarily, in its wake (certainly, in the top row). Overall the images collected in figure 4.3 present a consistent and well-defined vortex shedding system.

With each buoyant pulse eddy currents dance along the flame boundary engulfing fresh air consistently. This consistency will be challenged in the tilted cases that follow. What cannot be seen in the 30fps stills is the apparent flickering at the flame tip which is reminiscent of the motion of a small laminar candle flame.

Figure 4.3: Purely buoyant flame over 1 second period captured in video stills at 30fps. Vortex oscillation frequency of ~3Hz, similarly to that presented in figure 2.5.

4.1.3.2 Low Velocity Cross Flow

In this case the slower fan speed is applied and the case is best visualised in figure 4.7. The magnitude of the cross flow is enough to tilt the flame portion of the fire plume, but it is not the flame length is not noticeably decreased from the fully buoyant case. Two interesting structural phenomena are apparent here. Firstly, the flame is generally tilted more significantly near the base, where the buoyant pressure differential is not at its maximum and the cross flow inertia dominates, as demonstrated in [20, 24]. As the hot gases are pressed in the cross flow direction, buoyancy is built up within the plume boundary which is signified around the fan (rear) edge of the burner by a sharp directional change where the flame becomes buoyantly dominated, propagating upward and more closely to vertical experimental images of this process are presented in figure 4.4 and a diagrammatic interpretation of the vortex growth that drives this mechanism is presented in figure 4.5. This buoyant resurgence downstream in the flame is representative of the regime where more of the resultant smoke escapes the exhaust fan however these flame structure phenomena can last sometimes milliseconds before a second structural definition which occurs.

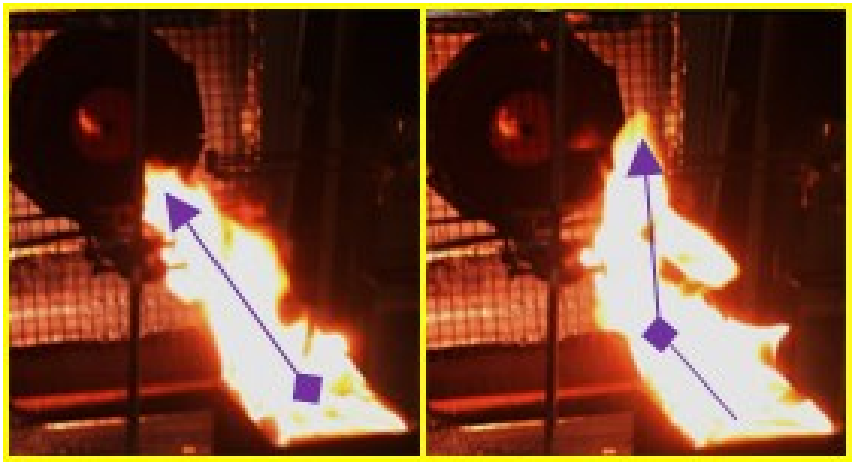

(a)

(b)

Figure 4.4: Part (a) shows examples of the extremes cases - a straight flame where the relative balance between buoyancy and inertia are approximately equal over the full flame length and the case where a perturbed vortex structure acquires enough buoyant pressure to rise almost vertically despite the cross flow inertia, causing a sharp change in plume fluid propagation. Part (b) shows the evolution from one case to the other over a period of approximately 320ms.

When the flame does not exhibit the buoyant upsurge described above it may be tilted and maintain a constant angle of tilt for the full flame length. This signals moments in time when the relative magnitude of the cross flow pressure differential impact upon the flame is approximately equal over the entire flame length. In these instances the downstream flame portion which usually exhibits the more buoyant, upward flow propagation is not strong and is either approximately equal to or slightly dominated by the inertia of the cross fan flow field, which increases as it approaches the fan. These two structural descriptions of the visual flame occur repetitively and consecutively with varying time periods and frequency of occurrence. Essentially, while vortex generation as understood in the axis-symmetric case can still be observed, albeit a slightly perturbed version, one of the

main observable actions that the addition of the cross flow inertia provides is the notion of a lateral motion, an intermittent swaying of the flame. Whereas in the axis-symmetric, fully buoyant case the periodic rising of vortex puffs was occurred along a vertical plane, now a lateral plane is introduced where the structure and shape of the flame will vary depending upon its location along that lateral position range

.

(a)

(b)

Figure 4.5: Part (a) highlights the typical flame shapes observed throughout the period of a vortex cycle under low cross flow conditions. Vortex ring generation, as depicted by Cetegen, is superimposed where appropriate to demonstrate the growth and upward transition during cross flow conditions that lead from the straight flame to the sharply angled flame shape.

It is important to understand that a portion of this momentum is a result of the fact that the buoyant pressure gradient, in calm conditions, is not constant, but due to the instability occurring at the plume boundary, is generated in waves and is of course signified by the periodic rising and dissipation of repetitive vortices. The cross flow inertia by comparison is essentially constant. Once the periodic buoyant pulsing of the fire plume is combined with the cross flow inertia, it is intuitive to

realise that the flame will assume either the more buoyantly-dominated or more inertia-dominated structure depending upon the stage of the vortex generation/shedding period which is applicable.

We may also like to say here that the vortex rings are no longer purely convectively self-propelled and may be somewhat influenced by the cross flow inertia. Within the frames studied however the only apparent influence that can be noticed visually is that the location of the vortex generation happens laterally to the axis-symmetric centreline and due to the tilt of the flame do not rise precisely vertically but rather at angle approximately between that of the tilted portion of the plume and vertical.

Therefore while the average flame angle and shape was previously important to acquire a description of flame behaviour over time, this analysis over a very short time period is also of great interest in understanding the processes which result in the averaged data.

The vortex shedding frequency is similar to that observed for the fully buoyant case and this will be further corroborated over the next few pages. The flame shape is certainly of interest and the new "multi-axis" journey of each vortex structure is fascinating. Whereas in the axis-symmetric case the buoyant force is unimpeded, in the cross flow (depending upon relative flow strengths) the buoyant force must grow in significance, which it does with distance, before overcoming the imposed cross flow. The impact of this qualitative observation upon entrainment, specifically by vortex/eddy engulfment will be difficult to quantify experimentally however the rest of this chapter will discuss the *potential* decrease in importance of entrainment by engulfment and the rise of importance of entrainment by diffusion in the near-field, across the increasingly forced flow-dominated cases.

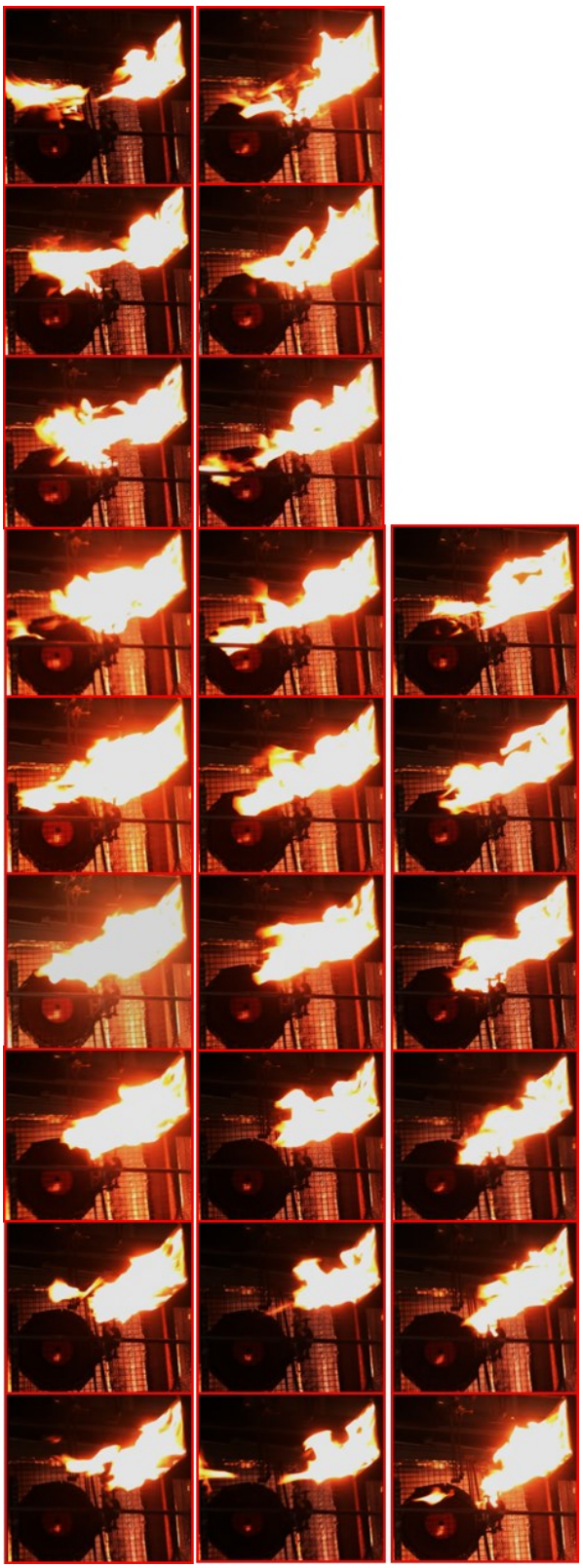

Figure 4.6: Tilted flame under weaker cross flow demonstrates fairly consistent flame tilt angle. Vortex shedding frequency is approximately 3/s in this one second sequence, of 24 frames.

4.1.3.3 High Velocity Cross Flow

The fan speed was then increased to the point that a different flame structure began to occur. A more turbulent and less periodic flame was achieved and figures 4.8 and 4.9 have been included to demonstrate some of the associated flame behaviour. As the cross flow ΔP is increased the average flame length decreases dramatically and a noticeable break-up in the periodic vortex cycle occurs. The lateral motion described previously when the flame fluctuates between buoyancy and inertia dominated regimes due to the intermittent nature of the buoyant pressure generation is at times even more noticeable and at times appears to cease for short periods. Row one, and to a lesser extent row two of figure 4.7 show the plume during a longer buoyancy-dominated phase. Although some tilting of the lower portion of the flame can be seen, the flame tends to be upright overall when compared to the previous case of the comparatively weaker cross flow. In row three a return to an inertia-dominated phase can be clearly observed where the flame is tilted and relatively straight for a short time. It can be said of this strong cross flow case that the lateral movement of the flame is particularly more random and more profound than when the cross flow was not so significant.

The dotted line after row three signifies 1 second from the first image. Row four is included out of interest since quite a different flame shape is observed compared to the same period one second earlier, where the flame is now quite tilted throughout but the average flame length is significantly shorter than before. Figure 4.8 is therefore included as an entire one second sequence can be observed wherein the flame length is maintained at this shorter stature throughout. The decreased flame length is likely due to a combination of two aspects. Firstly a sufficiently high inflow of air is typically understood to provide more oxygen to the combustion zone at the flame sheet boundaries whereby combustion of the available fuel is often completed over a shorter time and therefore over a shorter physical distance, the effect being that the visual representation of the flame surface appears shorter to the observer. Secondly and specifically in this case of the exhaust fan, during periods of inertia-dominance the intermittent region of the flame is accelerated away from the general

flaming zone due to the increasing exhaust flow pressure PUA. This section of the flame typically exhibits approximately the same (or slightly reduced) upward velocity in the fully-buoyant case as the buoyant pressure waves, characterised by the period rising vortex rings begin to dissipate vertically and laterally. The combination of these processes has the result of reducing the flame length most noticeably between buoyant periods as the flame fluctuates into an inertia-dominated phase. Figures 4.7 and 4.8 highlight that these momentary buoyancy and inertia-dominated phases can now extend for over a second, where before two to three fluctuations were generally noted per second in the weaker cross flow case.

It is difficult to comment therefore upon the true vortex shedding frequency in this strong cross flow case since even though the large vortex rolls which signify a buoyancy-dominated period are very easily noticed in this instance, multiple smaller vortex rings regularly begin to appear near the base but are quickly dissipated before travelling half way along the flame length. This could be due to the more turbulent conditions near the base of the flame as the Reynolds number increases due to the increases cross flow velocity and also due to the effect described above where exhaust fan pressure assists the propagation of the vortex structure rolling upward and essentially pulls the vortex fluid away at a great rate. This scenario sees the break-down of the periodic vortex shedding regime which is typically so well-defined in the purely-buoyant case. The vortex rings no longer purely self-propelled but now have momentum from cross flow and the velocity decay experienced by rising vortices with greater distance is no longer appropriate since the global velocity will increase or at least maintain as it approaches the fan.

The observed shortening of the flame suggests that the combustion processes complete more quickly and over a shorter physical distance (while moving away from the source) and that the vortex structures are dissipated sooner than in the fully buoyant case where they are self-propelled and die after a distance only since ΔP_B PUA decreases with height.

Since the consideration of the vortex structure as an ideal conical form is no longer realistic one must note at this point that the entrainment model offered in [47] for near-field entrainment, where vortex engulfment of air is most important, is no longer applicable. Further the simplified description of the negative pressure generation and angular buoyant pressure vector [20] leading to the flicker (at smaller scale) and ultimately vortex generation (at larger scale) is somewhat perturbed in practice. The fundamental principle is still applicable but is now important intermittently in a sequence of important entrainment mechanisms. Entrainment in the inertia-dominated flame phases in the strong cross flow case *appears* to be contributed to most by diffusion rather than by air engulfment as the periodic vortex shedding is hampered and dissipated quickly. This idea makes sense considering the increase in air velocity surrounding the flame as will be characterised in chapter 5, and demonstrated in chapter 6. Chapter 4.1.3.4 now compares the buoyant, low and high velocity crossflow cases discussed over the last few sub-chapters.

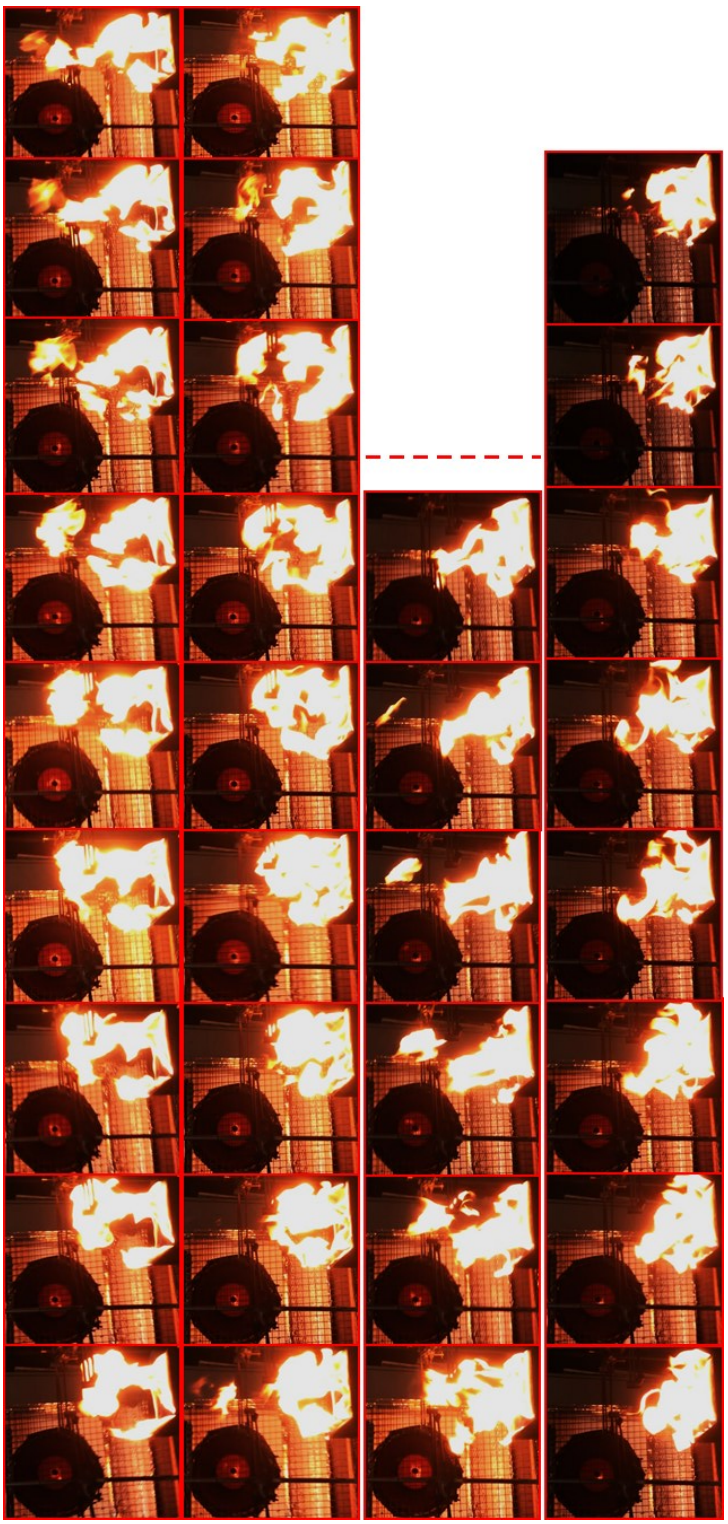

Figure 4.7: With an increased cross flow pressure the flame is observed to shorten in length and vortex shedding frequency equals roughly 3 where the second vortex is not well defined and tends to appear immediately in the wake of the second vortex.

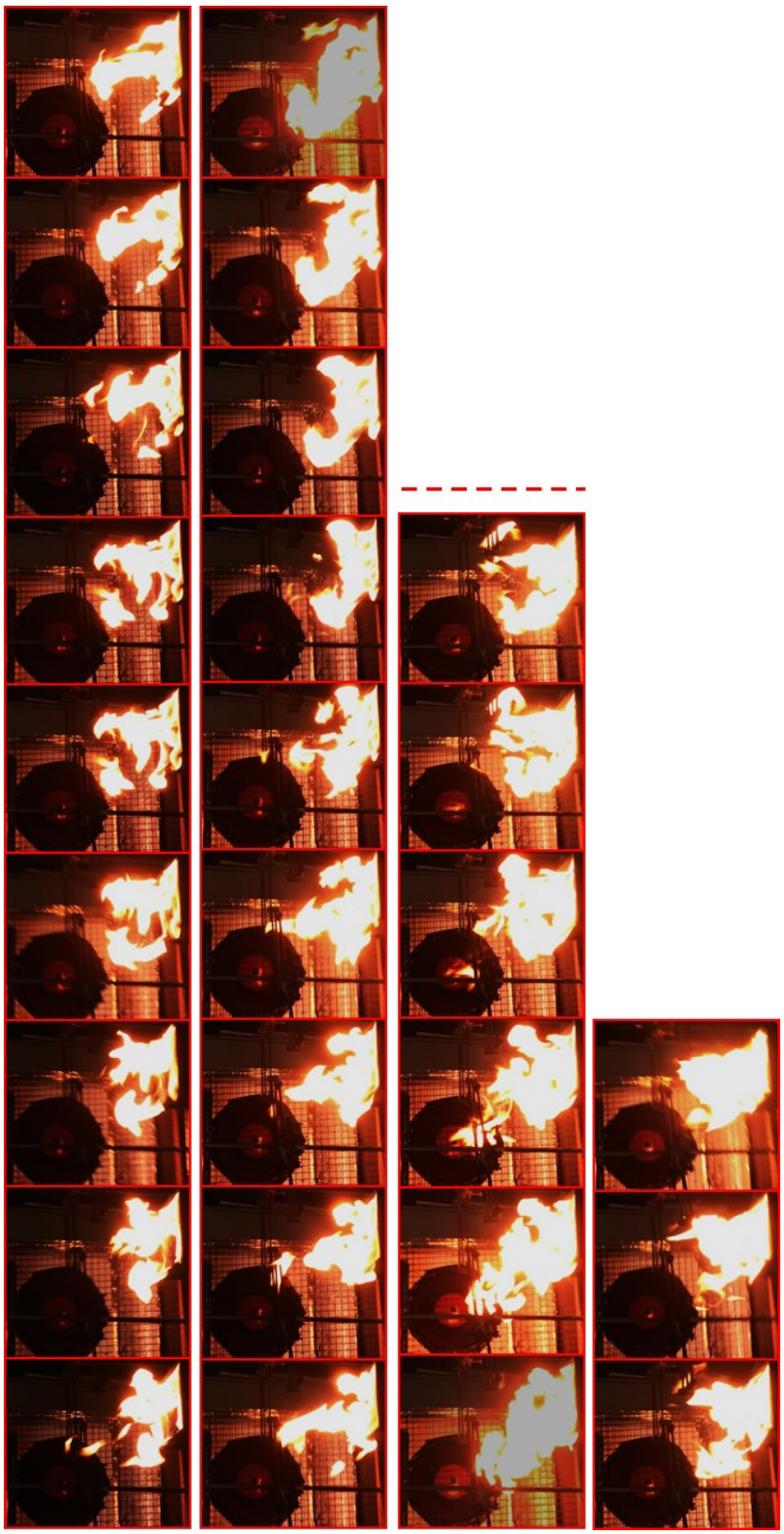

Figure 4.8: As per [previous 4.7] another one second sample shows the flame significantly shortened in length and very turbulent in nature rendering vortex birth and lifespan quite perturbed

4.1.3.4 Quantitative Comparison of Fully Buoyant, Low and High Velocity Cases

We now compare the buoyant, low and high velocity crossflow cases, present quantitative data on each case and demonstrate some of the qualitative imaging approaches that were used to acquire measurements

To quantify the effects somewhat that have been discussed above, measurements of the fully buoyant flame, a low flow velocity and high flow velocity cases have been taken for comparison. These cases are not part of the formal (27 case) review that will be outlined over the next two chapters, but are presented here to give a quantified example of the impact of varying crossflow strengths upon the physical characteristics of the flame. As discussed in chapter 4.1.3.1 – 4.1.3.3, the addition of a comparatively strong corssflow to the flame/plume has been witnessed to:

- Tilt the visible flame, to a fairly constant degree
- Shorten the visible flame region
- Decrease the length of the intermittnet flame region
- Decrease the apparent lifespan of rising vortices
- Change the propagation direction of rising vortices away from vertical
- Flatten the visible flame
- Decrease the theoretical volume of the flame fluid region, and
- Incerase the turbulence and broken nature of the visible flame region.

Subsequently, a comparatively low crossflow velocity was noticed to:

- Tilt the flame to a lesser degree than the strong corssflow
- Tilt the flame to a less constant degree, where by vertical buoyant puffs regularly negate the flame tilt angle.

Quantified data from the fully buoyant, low and high velocity crossflow cases discussed over the last few pages can be summarised as in the following table:

Case burner d = 0.15m	Cross Vel (m/s)	Mean L (m)	Mean Tilt (deg)	Surface Area (m^2)	Flame vol (m^3)	Vortex freq (Hz)	Inflection L (m)	Inflection angl deg
1. 10kW Fully buoyant	N/A	0.38	N/A	0.057	0.0067 (cylind) 0.0087 (Sq base)	~3 (vis obsv)	N/A	N/A
2. 10kW Dist z′ = 0.6m fan = v2	1.04 (probe 3)	0.36	40	0.054	0.0063 (cylind) 0.0081 (Sq base)	~3 (vis obsv)	18	82
3. 10kW Dist z = 0.6m Fan = full	~2.4 +/- 34% (probe 3)	18	29	0.027	< 0.0032 (cylind) < 0.0041 (Sq base)	~3 (vis obsv)	10	71
	Probe ΔP data process see chpt 5	Image measurement	Image measurement	Burner d by mean length L	Case 3 flame flattening not accounted for so these are upper limits	Image sequ measurement	Image measurement	

Table 4.1: Measured and observed flame length data

The three cases analysed here present a range of observable outcomes. The 27 cases comprising the formal entrainment investigation in chapter 5 did not produce the flame-shortening observed in much crossflow literature. For this reason additional data was sought and the fan flow rate was turned to full, which coincided with the visually observable shortening of the flame length.

As previously discussed the crossflow velocity (ΔP) in the 27 formal experiment cases did not appear to be of great enough magnitude to produce a visual shortening of the flame length. Case 2 presented above uses the experimental settings Q=10kW, z′=0.6m and fan speed = v2. The crossflow velocity for this case measured at probe 3 location (within the tilted flame) was approximately 1m/s and represents an intermediate case where significant flame tilt, but not length-shortening were observed. The maximum crossflow velocity attained in the formal

experiment was 1.8m/s (Q=10kW, z'=0.6m and fan speed = v3). When the fan was cranked to full a crossflow velocity of approximately 2.4m/s was achieved. At this point a clear reduction in mean flame length was observed at 0.18m, approximately 50% of the fully buoyant mean flame length. The other visual attributes such flame flattening and vortex frequency have been discussed previously. The general consensus in the literature is that the increased delivery of oxygen to the combustion zone, and particularly to the base of the flame results in more efficient combustion occurring over a shorter distance from the fuel bed. Observing these experiments however, and the stark reduction in visual flame length *and volume*, it also seems reasonable that pyrolised fuel that would otherwise (rise through) stay within the combustion zone until combustion occurs in the buoyant flame, may be delivered away from the combustion zone and quickly cooled so that the flame length is shortened due, in part, to a reduced mass of fuel vapour being present.

Figure 4-13 demonstrates the use of photographic and digital video still images to quantify the observational data presented in table 4-1.

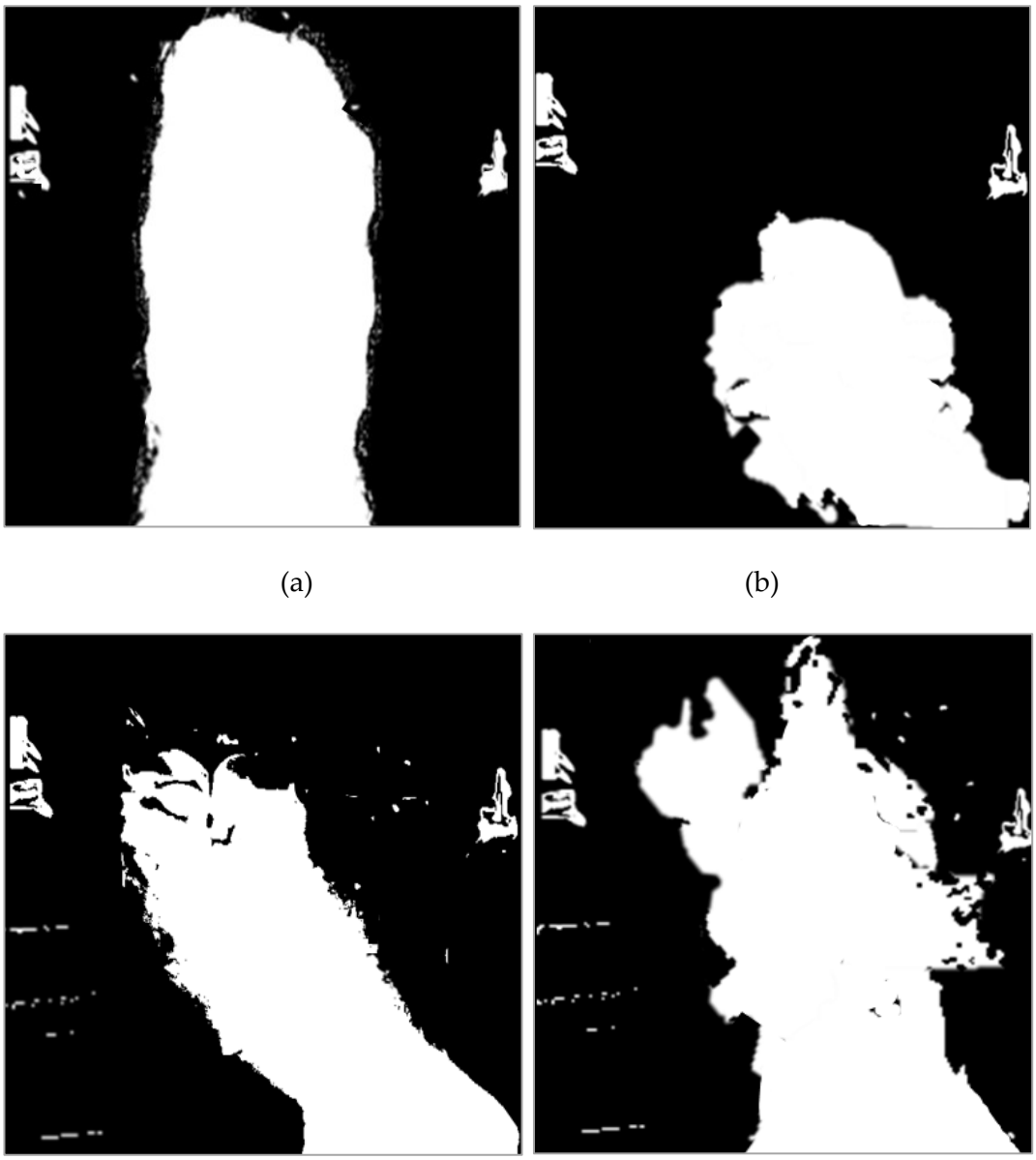

(a) (b)

(c) (d)

Figure 4.13: 50% flame presence probability average images of 10kW flame with (a) no crossflow, (b) strong crossflow, approx. 2.4m/s, (c) low crossflow approx.. 2.4ms velocity and (d) as per part (c) but using only the 8 images when clear flame inflection occurred.

Figure 4.13(a) demonstrates the almost symmetrical average flame image for the no crossflow case (60 images). By contrast, (b) demonstrates the clear extent of flame length reduction when the crossflow magnitude is increase suitably – these images correspond with those flames discussed so far in chapter 4. Part (c) is composed of 60 images and shows the average flame image for the lower crossflow (1.04m/s) (case 2 presented in table 4.1). Even though there is a clear tilt to the flame no flame

length reduction could be noticed during measurement. Part (d) is composed of the 8 images (from (c)) where a clear flame inflection occurred – as discussed in section 4.1.3.2. By contrast it looks like a completely different flame to that of (c) which demonstrates the lack of stability (at one particular angle) when the flame is exposed to a crossflow whereby the buoyant and momentum forces are comparable. Subsequently the technique of (d) was used to evaluate the flame inflection angle of the flame.

What these images, and the measurements that they make possible demonstrate is the range of physical manifestations that are possible by varying the boundary condition of horizontal pressure and the qualitative analyses and quantitative measurements from this chapter also suggest that the typical vortex generation and lifespan are altered beyond recognition once the crossflow strength becomes significant enough. This means that as the physical parameters of the flame change drastically, so too do the mechanisms that govern entrainment into the flame region of the fire plume. Chapter 5 will quantify in detail the nature of the changing pressure and fluid flow regimes in and around the fire plume that precede the flame manifestations discussed so far. Meanwhile, the effects of the crossflow at the laminar flame region near the base require consideration also.

4.1.3.5 Flame Detail

The stills in the previous figures highlight quite clearly the outline of the flame structure in each case however internal flame detail is absent, especially for the short flame length cases. Increasing resolution and contrast, and repositioning the camera allowed for visualisation of the flame internal contours. This was conducted in the hope of identifying the birth, growth and short lifespan of buoyant vortexes generated during the high velocity case described above, during which the flame length is significantly decreased and vortex rings were observed to dissipate abruptly and achieved much shorter lifespans than in the axis-symmetric case or even the low velocity fan speed case.

Figure 4.9 shows a one second period in 24 frames. The next 6 frames, constituting the following 250ms, are included for further context. The camera is positioned laterally to the flame (side on) and slightly behind with reference to the fan, which is located 0.6m metres to the left of the images. The one second time step is arranged in four rows of six images since the behaviour of the flame can approximately be divided into these four steps. In row one an approximately straight, tilted flame is apparent. By the fourth image a vortex structure is beginning to form which rolls upward and disconnects from the lower flame section over the first three images of row two. We can then notice an immediate return to the straight, tilted flame over the last three images of row two. Across row three the flame remains tilted but experiences more turbulence and loses its clean outline. After exhibiting the cleaner, tilted shape again by the last image of row three the next vortex structure is born and evolves upward across the row four images. This constitutes a one second period and two clear vortices have been shed in this time. The turbulent period during row two is most likely due to an upsurge in buoyancy, however due to the impact of the cross flow pressure wave a well-defined vortex cannot be observed. Similarly, in the first six images following the one second period, immediately after the vortex which rises up during row four the flame again exhibits a short period of poorly defined characteristic. It again appears more turbulent (and buoyant) but with no clear, dominant vortex ring.

Clearly the above description is not scientific and does not provide any quantitative data or small scale description of fluid mechanics, however the erratic process roughly described here are clearly substantially different to the periodic, convection driven mechanism that Cetegen [46, 47, 49] relied upon to approximate the near-field entrainment rate of the axis-symmetric case. The vortex shedding frequency is at best, perturbed, and indeed the ability of the fire to produce periodic, fully-developed vortices is severely hampered under cross flow conditions. The lateral swaying of the flame, described previously, can be observed here (by the straight-tilted and buoyant upright flame shapes) and roughly two full “sways” can be noticed during the one second period. Again this sway is characteristic of the switch

between the momentarily inertia-dominated flame and the bent or upright flame following a dominant vortex roll. The broken structure that persists makes estimation of flame surface area (and volume) quite difficult since the upper portion of the flame is now more erratic and turbulent than with the axis-symmetric case.

The next detail of interest is the tilted laminar portion of the flame which begins at the leading edge of the burner and reaches approximately one third to half way across the burner surface. This is of interest as it is comparable to the laminar portion at the base of the axis-symmetric flame, but again, appears in a perturbed state during weak and strong cross flow cases, and appears more constantly than in the buoyant case (figure 4.3). Given the increased velocities recorded parallel with the leading edge of the burner during the experimental cross flow cases it would be interesting to observe how the inertia/buoyancy pressures interact over the length scale provided by the laminar portion.

Figure 4.9: 1.25 second sequence providing resolution of flame fluid contours

4.1.4 Oscillation Frequency Estimation by Fourier Analysis

The following Fourier charts are composed of data from horizontal and vertical pressure probe readings from test 3 where probes are located typically within the flame fluid. Since turbulent flame motion, with and without a cross flow force imposed, is not confined to either a vertical or horizontal propagation the combination of horizontal and vertically aligned probes is suitable.

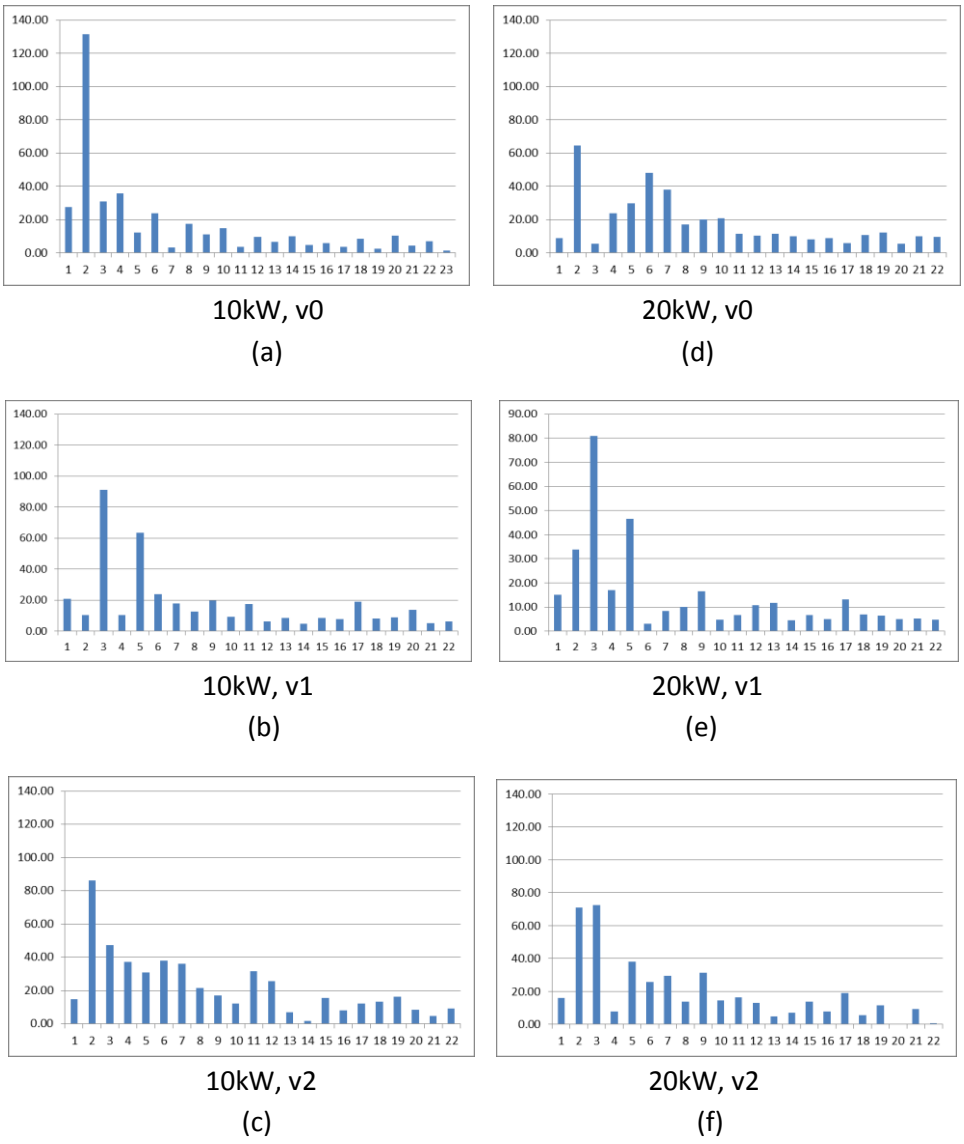

Figure 4.10: Fourier analysis performed on pressure probe data from test 3 for the fully buoyant flame and two iterations of cross flow strength for Q=10kW and Q=20kW. Across the x-axis the first 22 frequency components are plotted and the ratio of amplitudes in each case (amplitude = y-axis) demonstrates any recurrence of that frequency in the data.

In the 10kW case the fully buoyant flame returns a result which clearly suggests an oscillation frequency of around 2/sec with very little influence from elsewhere along frequency range. As the cross flow (v1) is introduced frequencies 3 and 5Hz appear more prominent. As the cross flow pressure is increased the frequency contribution becomes less-well defined. As discussed over the previous sections the increase in turbulence, and rapid lateral movement of the flame in the cross flow is likely to introduce a range of frequencies by fluid movement across the probe faces. Appendix D presents further Fourier analyses of cases from test 1 which demonstrates further this trend of increased turbulence in and around the flame under varying cross flow conditions. Combining the data from the previous image sequences and the data from the Fourier analysis would suggest that the mechanism for generation of buoyant vortex structures persists at more or less the same rate once the cross flow is added however the structure, velocity and lifespan of the buoyant vortex rings appears perturbed and diminished due to the change in velocity difference between the flame and surrounding fluid and the increased turbulence within the flame fluid. This means that the flame time portion for each increasing crossflow case, as depicted by the Fourier data, appears similar and a clear variation, cannot be determined from the depth of data available. Combining the Fourier data with the flame images presented above gives a combined quantitative and qualitative assessment that while the flame length appears diminished and the structure appears more broken, the frequency of vortex generation seems to be very similar across all cases. The engulfment of bulk fluid by the large eddy formation is certainly diminished and as suggested previously, the relative importance of vortex engulfment for near-field entrainment appears to be reduced in favour of entrainment by diffusion, resulting from an order of magnitude increase in bulk fluid velocity (as will be demonstrated in chapter 5.3). Chapter 4.1.5 now presents a qualitative discussion on the perturbed fluid dynamics at the base of the fire in the laminar region, the interesting region that typically precedes vortex generation.

4.1.5 Characteristics of the Laminar Flame Portion

4.1.5.1 Inflow and Burning region

Figure 4.11 shows a close-up series taken to highlight the shape of the flame sheet near the burner base where the inflow of air at each side of the flame meets and reacts with the fuel in the combustion zone. These images are a selection from a large number of very similar images taken during the higher velocity fan speed thus the flame length is particularly reduced and extends only marginally above the top boundary of the images. A direct comparison can be made between the cross flow case here and the fully-buoyant case presented earlier in chapter 4.1.1. It can be observed that a visual flame sheet is generally absent at the rear of the burner. At this location the air is generally being drawn away from the flame and toward the exhaust fan (which is located out of screen, outside the top left corner in each image).

Figure 4.11: shows the nature of the flame sheets at the base under strong cross flow conditions whereby the air inflow at the rear of the burner is significantly decreases compared to the axis-symmetric case

At the leading edge of the burner the cross flow pressure wave has the effect of drawing the flame sheet diagonally (almost horizontally in some previous cases presented) across the area of the burner base. Drawing fresh air into the fuel rich zone means that the flame fluid at the combustion zone is visible and demonstrates to the observer the nature of the fluid flow at that location. At the rear of the burner however the fresh air which would normally be drawn in at the same rate as from any other side of the burner appears to be significantly diminished. At the rear edge of the burner there is competition between the buoyant pressure of the flame which is diminished under tilted conditions to rise and draw fresh air in below and the inertial pressure provided by the exhaust fan which tries to draw air away from the rear edge of the burner.

We can see in each of the images in figure 4.11 that at the rear edge oxygen is present at the base of the burner, particularly up to the elevation of the burner lip, which is approximately 1cm in height and the luminous conditions following combustion are present locally. At this elevation any flame sheet, representing a thin layer of a combustion zone does not appear to be drawn over the rear edge of the burner as it typically does at greater elevation within the flaming region. A simplified depiction of the main flow behaviour and the impact upon flame sheet combustion regions is provided in figure 4.12. In the fully-buoyant case (a) flame sheets growing upward from the burner edges are of similar magnitude since fresh air is drawn inward at an approximately equal rate from all directions. When the cross flow is applied (b) the thin layers of the combustion regions are tilted toward the fan and the flame sheet at the rear edge is very small by comparison, barely growing above the burner lip at the rear edge. Although most likely a small amount of air is entrained at the rear edge due to the negative pressure differential created by the rising hot gases within the fire plume, the lack of presence of a luminous combustion region at the rear edge gives context to the strength and directional characteristics of the general fluid flow at the rear side of the burner, as a result of the exhaust fan flow.

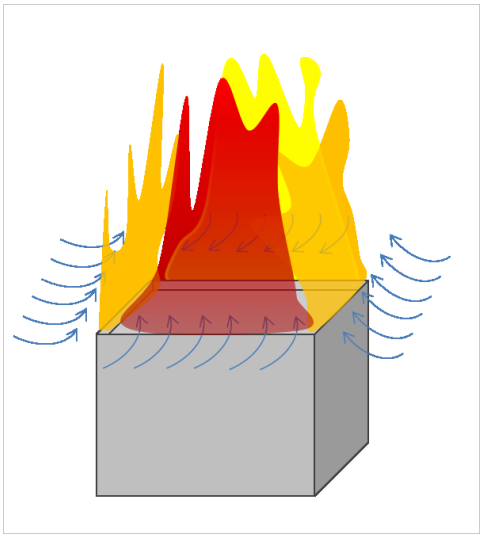

(a)

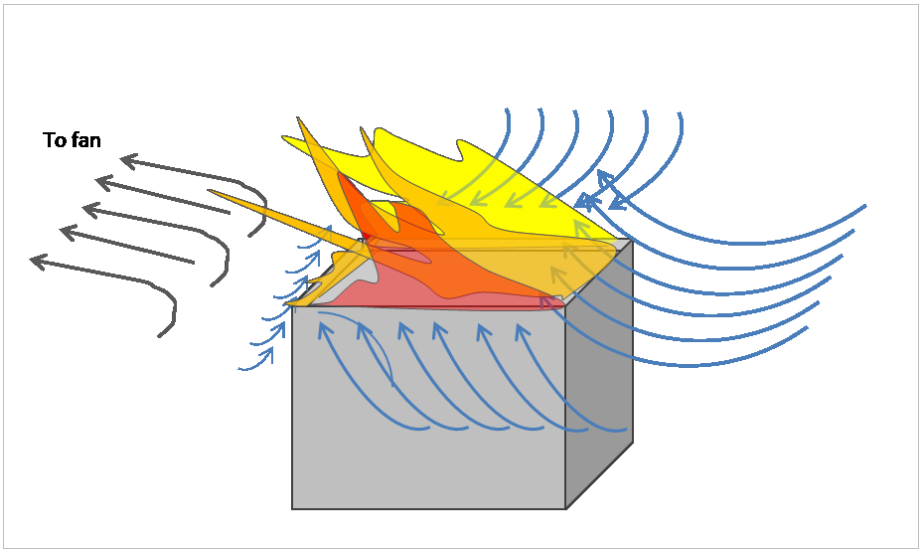

(b)

Figure 4.12: Under fully buoyant conditions with a quiescent bulk fluid (a) the inflow driven by the buoyancy of the fire is approximately equal from all directions. Under cross flow conditions (b) the inflow is severely perturbed and the flame sheet representing a combustion zone at the rear edge of the burner (LHS) appears to exist only below the rear edge lip where O2 is present. This is seen consistently under strong cross flow conditions.

4.1.5.2 Tilted Laminar portion

The laminar portion begins at leading edge of the burner and continues for around 0.1m, extending around half way across the burner surface on average. The laminar portion exists because the velocity difference across the flame/bulk fluid boundary is not great enough to invoke a turbulent regime. As the flame fluid velocities vary and the velocity of the bulk fluid significantly increases under cross flow conditions, the local Reynolds number at the now-tilted laminar region is substantially increased. Figure 4.13 depicts the velocity trend following the addition of the cross flow to the buoyant flame. A Reynolds number in the order of 10^5 [40] typically corresponds with the onset of turbulence in fluid flow. Figure 4.15 shows another close view of the base of the flame, this time a 0.5 second period is captured in fourteen frames. The overall story of this sequence is the appearance of a large vortex structure above the rear half of the burner surface in the latter half of the sequence which causes the sharp bend in the flame described previously as it rises almost vertically despite the persistent horizontal cross flow inertia. As discussed, the cross flow inertia and subsequent turbulent soup created has the effect of sporadically breaking the vortex rings up into many small vortices so they appear stretched and scattered compared to the relative control observed in the fully-buoyant case. The laminar portion can be seen to act in a wave motion where instability is present as a function of the pulsing buoyant force against the strong horizontal inertial flow. Enough stability at the flame boundary of the tilted laminar portion exists so that turbulence is generally staved off until further across the burner surface. Occasionally however momentary instability allows a single trail of buoyant fluid to break out of the laminar wave. The birth and evolution of this trail is discussed over the next pages with reference to the images in figure 4.15.

We know that the cross flow ΔP PUA is less at the leading edge than within the turbulent portion of the flame due to previous pressure measurements. Subsequently we can see this manifested in the behaviour of the flame fluid. In the buoyant case the laminar portion propagates in the same direction as the turbulent flame (upward, vertical) so that the lesser buoyant force near to the burner is not

apparent to the observer, however here the laminar portion is flattened and tilted (essentially) by the cross flow. As the buoyant force increases and becomes more comparable with the crossflow force, we can see the flame sharply beginning to point upward. The battle between the adjacent forces then ensues and results in the turbulent, unsteady tilted flame (and plume).

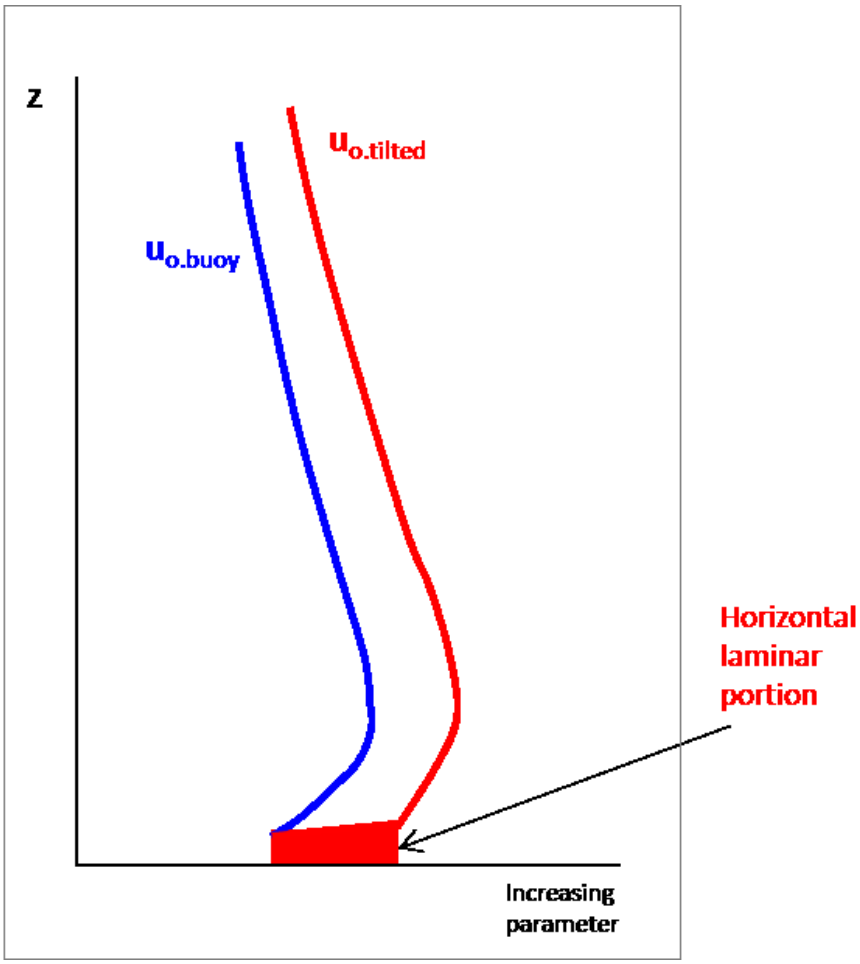

Figure 4.14: The blue line represents the average flame velocity trend of the fully-buoyant, axis-symmetric plume, and is reproduced from [41]. The red trend line represents the increase in plume velocities over the height of the plume following the addition of the cross flow. The shallow gradient section of the red trend line corresponds to the laminar portion of the tilted flame, as depicted in the following pages in figure 4.16. This shallow gradient shows that the local flame fluid velocity accelerates more steeply than the buoyant case, and does so with very little elevation increase since the cross flow pressure both increases overall fluid velocity tilts the fluid dramatically, to almost horizontal.

Figure 4.15: the laminar portion of the flame acts as a wave under the inertial pressure and trails of buoyant fluid regularly escape, acquire toroidal momentum and contribute to the dominant vortex structure which rises up near the rear edge of the burner surface.

It was noticed that occasionally the buoyant force in the laminar region could pulse due to the shear instability at the edge of the flame and vortices could begin to be generated out of the laminar portion. This is captured in the full sequence of figure 4.15. Figure 4.16 highlights the evolution of the structure of the horizontal laminar portion (a) as the vortex is initially generated (b), grows while moving along a horizontal path (c) and then maturing as it becomes part of the turbulent, buoyant portion of the flame finally propagating upward (figure 4.15). In the fully buoyant case the upward propagating vortex is witnessed alone (figure 4.3), and the strongly horizontal flow from which the early vortex was generated in figure 4.14, is not have been present.

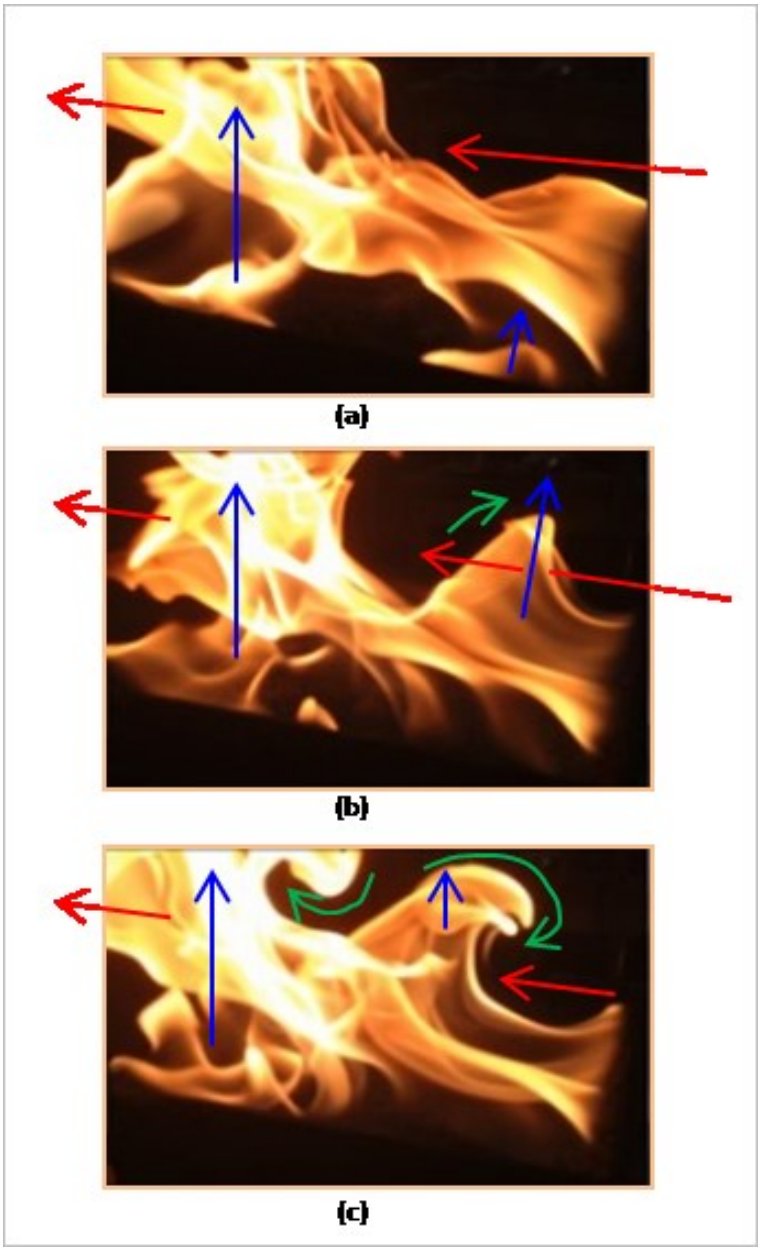

Figure 4.16: Simplistic depiction of the pressure fields contributing to the turbulent but repetitive flame behaviour. Blue = buoyancy, red = inertia, green = toroidal momentum acting to create vortices and engulf fresh air into the flame domain.

5 Characterisation of Fluid Flow Behaviour at the Flame

The aim of this section is to characterise the behaviour of the fluid flow at and around the fire when we introduce the fire into a fan-induced cross flow. The experimental set up is such that a fixed mass flow rate can be achieved by choosing one of a range of fan speed settings which, depending upon the fan speed, distance from fan to fire and fire size results in an altered fluid flow regime occurring at and around the fire. This regime is *altered* in the sense that it exhibits fundamentally different characteristics to those observed in the traditional entrainment experiments and theoretical derivations in which the fire plume is immersed in a large, quiescent fluid in a supposed ambient environment. In such cases the following fundamental is observed:

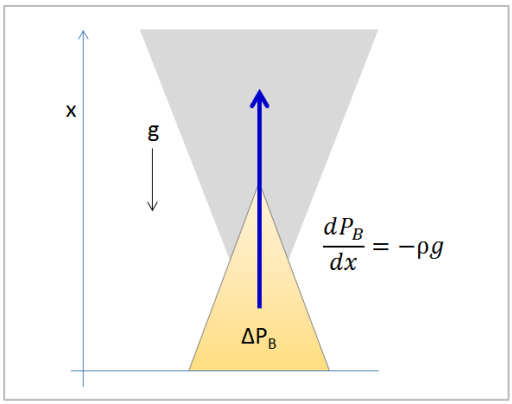

Figure 5.1: In the classical description buoyancy is the only force driving fluid flow

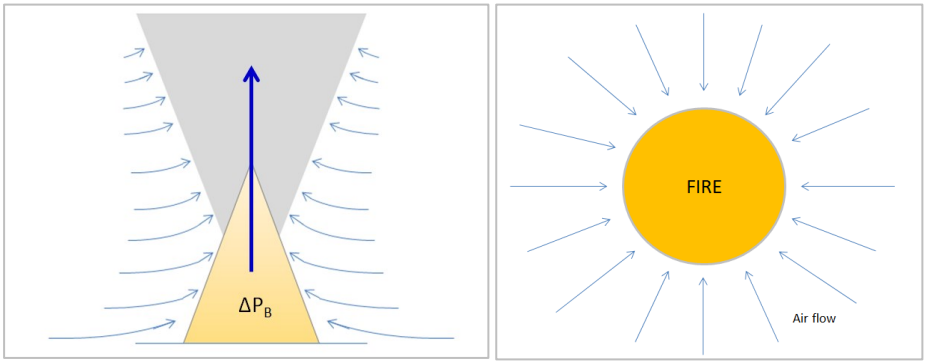

(a) (b)

Figure 5.2: The ideal assumption is that the natural fire flow entrains air equally from all sides around 360° depicted here in (a) lateral view and (b) plan view (from above)

Under the ideal model the density difference introduced by the exothermic combustion reactions is the only force driving the fire fluid flow. Considered to begin at the flame base with negligible initial velocity, the hot, less-dense gases rise due to buoyancy relative to the bulk fluid (figure 5.1) and the negative pressure gradient created in the wake of the rising fluid decreases with height as the volume that constitutes the rising plume increases radially and the heat dissipates. Subsequently the inward fire flow draws in air to be entrained approximately equally from all directions. This naturally occurring system functions quite effectively to maintain the entire plume structure through the delivery of oxygen to the combustion zone within the flame volume through the mixing of air with the hot combustion products to form a rising, expanding smoke plume. The apparent symmetry of this model reflects the effectiveness of the mechanism and facilitates the requirement for a simple correlation to describe its attributes.

The addition of the extraction fan perturbs the system significantly. In the simplest sense, figure 5.3 depicts the addition of a horizontal forced flow perpendicular to the initial buoyant flow. More specifically this is the introduction of a horizontal dynamic pressure field *across* what was previously a purely buoyant flow field, where the inward fire flow was small and equal from all directions which resulted in a net *cross flow* of zero.

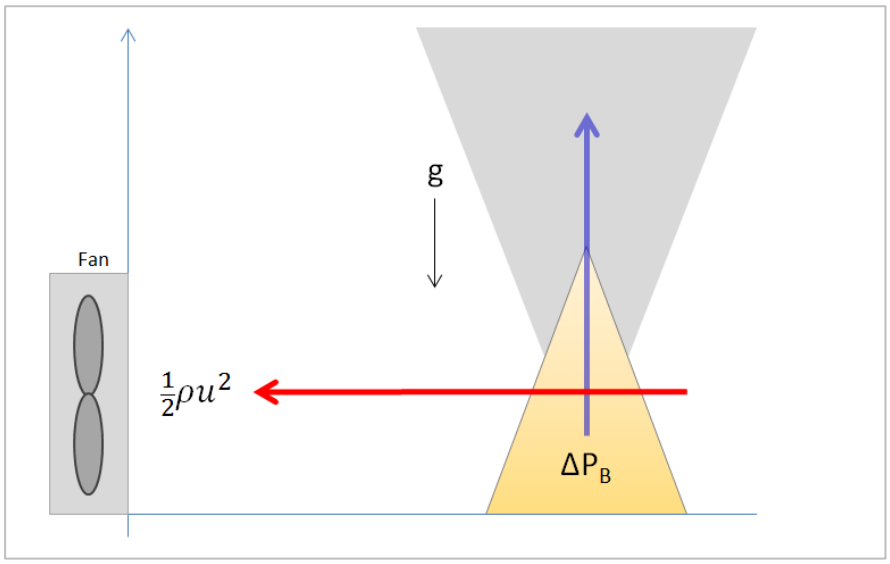

Figure 5.3: The addition of a cross flow to the classic system introduces the subsequent pressure differential perpendicular to the initial buoyant force

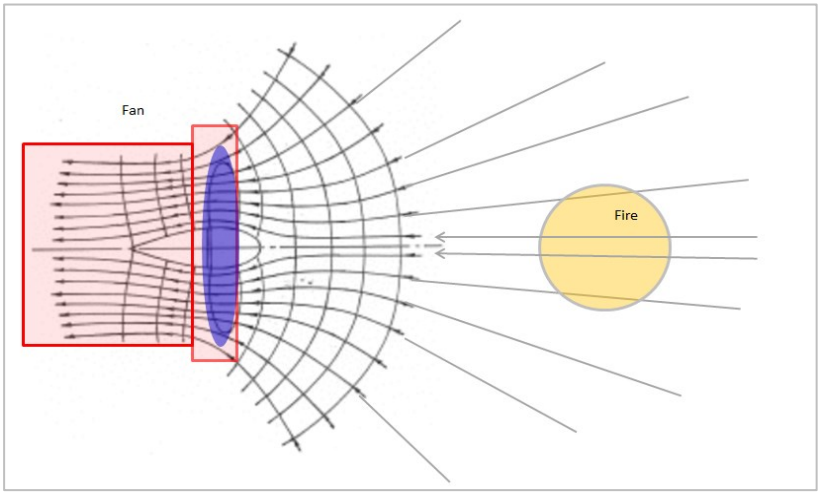

Figure 5.4: High negative pressure area (blue) created by the fan results in generation of fluid movement toward that area from all radial points, creating a decreasing dynamic pressure gradient with distance from the fan

The fan works by creating an area of low pressure at the leading edge of the rotating blades which in turn creates inertia in the bulk fluid toward and across the propeller. Figure 5.4 approximately demonstrates this flow propagating radially inward to the fan. The somewhat more idealised version of the inward flow depicted

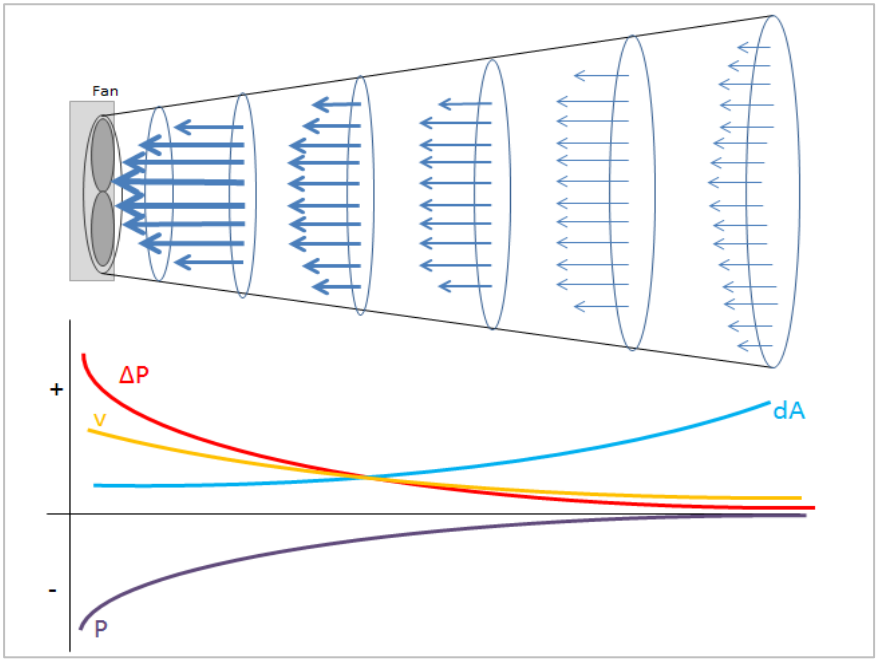

Figure 5.5: (Top) An idealised cone of the flow field induced by the exhaust fan and (bottom) general trends of static pressure (P), pressure difference (ΔP), cone cross-sectional area (dA) and air flow velocity (v).

in figure 5.5 attempts to demonstrate the decrease in dynamic pressure per unit area as the the cross-sectional area of the flow field increases with increasing distance from the fan. The thickness of the arrows in figure 5.5 represents increasing fluid flow velocity closer to the fan (and a growing negative pressure differential with reference to the general static pressure remote from the fan) as the theoretical fluid flow volume decreases as it approaches the fan. This is of course an expression of *conservation of mass* across the system. Given the idealisation of this model, the Bernoulli Principle allows us to describe the relationship between pressure and velocity along the length of interest of the forced flow field. The Bernoulli Principle states that with a decrease in local pressure an increase in fluid flow velocity will simultaneously occur and similarly an increase in local pressure is tied to a decrease in fluid velocity. If one assumes an inviscid, non-conducting, incompressible fluid where density is presumed constant along a streamline, then appropriate formulation of the Bernoulli equation may be written as:

$$\frac{v^2}{2} + gz + \frac{P}{\rho} = constant$$

Equation 5-1

where v is the velocity of the fluid, g is the gravitational force, z is some reference elevation, P is the pressure of the fluid at some point and ϱ is the density at all points in the fluid. The combined gz terms represent some form of potential energy which can change with elevation or a variable effective gravitation vector. To separate the pressure and density terms we can multiply by out by ϱ, and if considering each analysis to occur along a horizontal streamline, which we will now for now, equation Bern1 becomes:

$$\rho\frac{v^2}{2} + \rho g + P = constant$$

Equation 5-2

As outlined above, the Bernoulli equation in this form demonstrates the proportional relationship between pressure and velocity within a system where at any two points within that system the sum of the relative terms must be constant. The ρg term which was highlighted in figure 5.1 as the sole force of interest in the purely buoyant plume is realised here as a measure of the vertical pressure potential. Negating this component for the time being, as well as the constant static pressure P, for the purposes of evaluation of the forced flow, the dynamic pressure term which describes the magnitude of the inertia at any point within the 'cross flow volume' may be extracted:

$$\Delta P_f = \frac{1}{2}\rho v^2$$

Equation 5-3

As the dynamic pressure decreases with distance from the fan, the local velocity at any point in the horizontal flow field is a function not only of distance from the fan but also of the effective width of the flow field cross-sectional area (figure 5.5).

An inherent attribute of the test design therefore is that since the cross flow is generated by a fan on only one side of the fire plume, the magnitude of the resultant cross flow decreases with distance. While in principle, this complicates the global inertia description (as opposed to a wind-tunnel scenario with a constant inertia over the entire area of study) the current approach is by design a representation of the concept of an extraction system which might be found in the built environment.

It is therefore necessary to look at the local velocities (those measured at each probe) when the flame is immersed in the cross flow as a function of the velocity recorded at that probe when no flame is present. This has a further facet as it becomes apparent that the impact of the addition of the flame to the cross flow on local velocities varies depending upon the location of each probe *relative to the flame* over its length since the combination of the cross flow inertia and buoyant flame redefines the behaviour of the entrainment fluid flow around and into the fire plume in relation to that understood for the idealised axis-symmetric entrainment model. This facet will become very clear during the analysis of flow velocity and pressure data in the following sections and the relevance of these variations will be discussed at length.

To give fuller context to the problem of combining the purely buoyant plume flow to the inertia of the forced cross flow considering the experiment design, figure 5.6 depicts a simplified analogy of the similarity of the structure of these separate flows concerning the conservation of mass described above along the propagation of each responsible force.

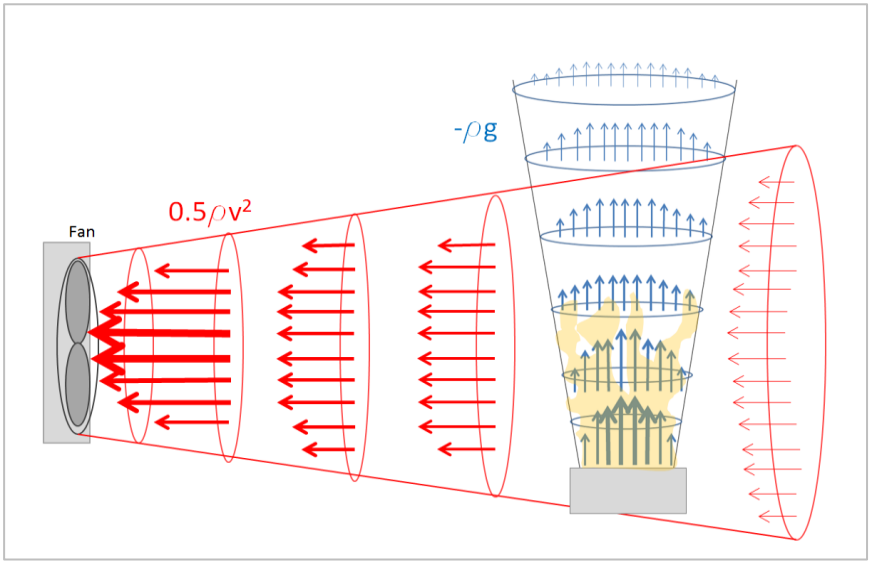

Figure 5.6: Idealised buoyant and inertial flow fields

Considered in isolation from one and other, the buoyant plume (blue) demonstrates essentially the same flow dynamics to that of the inertia of the cross flow (red). One essential difference is that in the fire plume the mass flow propagates away from the source due to buoyancy and in the forced cross flow the mass flow is toward the low pressure source. In the fire plume waves of hot, rising fluid leave low pressure regions in their wake which hot fluid from below and cooler adjacent fluid quickly replace. In both cases flow velocities decay with distance from the source as the overall fluid momentum is shared among fluid over an increasing larger surface area. Considering the mass flow for the axis-symmetric plume case, as represented by the blue cone above, the mass of smoke can be realised through the sum of a large number of discrete measures at ever greater elevations, representing increasing cross-sectional areas, up to an elevation of interest (ie. by defining a volume of interest). This can be described by:

$$(s)\int \dot{m}.dA$$

Equation 5-4

Similarly, for the mass flow of air in the forced horizontal flow:

$$(a) \int \dot{m}.dA$$

Equation 5-5

where $\dot{m}$ is the mass flow (kg) and A is the changing cross-sectional area at each point along the theoretically defined flow volume and where (s) denotes smoke and (a) denotes air.

Of course when the forced flow is applied across the naturally buoyant plume flow the theoretical flow volumes do not act in isolation as depicted above and instead a mixed convective regime is realised and a resultant angular flow occurs.

In the following sections we will evaluate this mixing of flows in terms of the impact that adding a hot buoyant fire plume to an initial cross flow has upon the characteristics of that cross flow. This will give a basic understanding of what happens when a hot source is added to a horizontal forced flow, since this can be thought of as a perturbation to the forced flow, and this concept is already well discussed in literature from a fundamental fluid mechanics point of view. Once informed by this, we can consider from the converse point of view - in the effect of applying the forced cross flow to the purely buoyant fire plume, since the entrainment paradigm is somewhat significantly redefined. This will be given practical context by consideration of the experiment fan as an extraction fan in the paradigm of smoke removal in modern infrastructure.

5.1 Consideration of the Data on Flow Velocities at the Flame

We will now consider the velocity data from each of the probe arrangements positioned around the flame and plume for tests 1, 2 and 3. There is a great deal that can be inferred from the trends and nuances of the pressure probe data that is of interest and will inform the subsequent discussion which seeks to analyse the tilted flame flow behaviour using pressure data as a key input. The scale of sensitivity of the pressure probes is also highlighted.

The first dataset example presented is the result of cases 1, 10 and 19 (see section 3.3.4). The flame is fixed at z = 0.6m from the extraction fan, which is fixed, in terms of figure 5.8, at the lowest of the 3 fan speeds (v1). Figure 5.8 shows velocity data for each horizontal probe (1, 3, 5) and demonstrates the impact on velocity at each of these locations as fire size is increased, where Q = 10/20/30kW. Case 0.1 (section 3.3.4) where no flame is present and the free cross flow is recorded is also included and thus the effect on the free cross flow of the addition of a buoyant heat source (the flame) can also be seen.

It will be seen across the following few figures that the noise of the probe data is variable and at times quite significant. This is discussed in relation to each figure specifically as a combination of knowledge and assumptions about the individual flow behaviour in each case are used to offer an explanation for the variation in data noise in each instance. The bi-directional pressure probes have been experienced to typically return quite noisy data results, depending upon the precise boundary conditions of the experiment however over sections 4.1.1 - 4.1.3 it should become apparent that relatively well-defined trends can be noticed as the boundary conditions are varied and these trends are of significant interest in terms of the results here. Since it is necessary to extract quantitative data for the non-dimension investigations in the following chapters an exponential regression analysis has been performed on the raw noisy data allowing for more concise data lines to be acquired and these have been superimposed over the raw data in the following figures.

5.1.1 Cross Flow Data (Test 1)

It can be seen from the "no flame" column to the extreme left of figures 5.8 and 5.9 that the location of each probe relative to the extraction fan dictates the magnitude of the forced-flow pressure differential experienced by each probe. Thus probe 5 being located the nearest to the fan experiences a higher velocity flow than probes 3 and 1. In figure 5.9 (a) and (b) it can be observed from the "no flame" column that as the fan speed is increased the relative decrease in cross flow pressure differential at each probe distance appears to change. Simply put, for example, as the fan speed is increased the difference in pressure differential (and air flow velocities) recorded at probes 1 and 3 becomes increasingly less. This is most probably as a result of the nature of the increase in negative pressure created close to the fan, and the range of directions from which the resultant air mass is draw from. It would be preferable for analysis if the cross flow pressure differential was constant over all probes for each fan speed, however as discussed in the Methodology section this is not possible based on the experimental set up. Nevertheless, of greater significance is the perturbation of the "no flame" cross flow once the flame is added, and subsequently as the flame size is increased. The addition of the buoyant flame to the free cross flow has a varying impact upon velocity readings at each probe depending on the location of each probe relative the flame. By considering figures 5.8 and 5.9 it can be observed that adding the 10kW flame to the free cross flow appears to increase velocity readings at probes 3 and 5 which are both located downwind of the flame, between the flame and fan. Further increase in velocities at these probes is achieved as the fire sizes are increased to 20kW and 30kW, and this becomes increasingly apparent for each case where the fan speed is increased. It is intuitive to imagine that the increase at probes 3 and 5 are as a result of the addition of the hot gases from the flame, having some initial velocity due to buoyancy, the propagation of some of which are pulled in the direction of the fan. Probe 1 by contrast appears to have no obvious increase in velocity once the flame is added in figure 5.8, and indeed in figure 5.9 (a) and increasingly so in (b) it can be observed that velocities at probe 1 tend to decrease once the flame is added, and decrease further, relatively

speaking, as the flame size is increased. Probe 1 is located upstream of the flame, at the leading edge, and it might be intuitive to imagine in this case that the buoyant gases of the flame shield the location of probe 1 somewhat from the fan-induced cross flow pressure differential. It is also quite clear that in this set of results that the magnitude of the probe reading *variation* (demonstrated with error bars) increases once the flame is added (from the "no flame" columns to the "10kW columns) and generally when Q is increased from 10kW to 30kW the data variation appears to increase further and become increasingly uniform. That is to say that the peak and trough magnitude specifically becomes more uniform. This suggests that in each case as the buoyant force is increased (increasing Q) the set cross flow force (v1, v2 and v3 in each case) has less of a chaotic impact upon the flame driven buoyant force and this is best appreciated by comparing the 10kW and 30kW data in figure 5.8, for example.

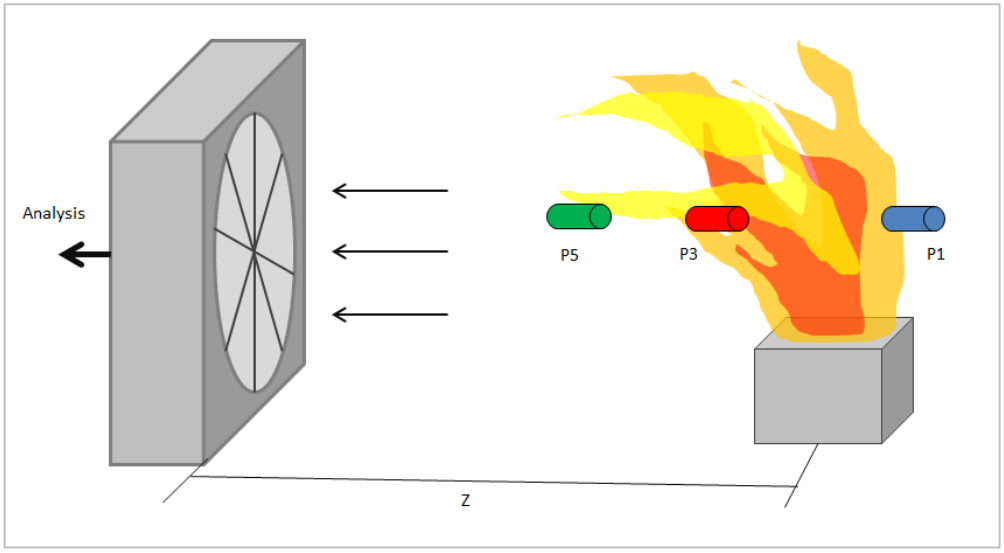

Figure 5.7: Test 1 location of probes relative to burner and fan. Probes 1, 3 and 5 are positioned horizontally to read the pressure differential invoked by the fan-induced flow. This image is not to scale and is provided to give context to the following pressure probe data graphs. It is important to remember that as the extraction fan speed is increased probes 3 and 5 become fully involved with the flame for significant periods of time, which is not depicted here.

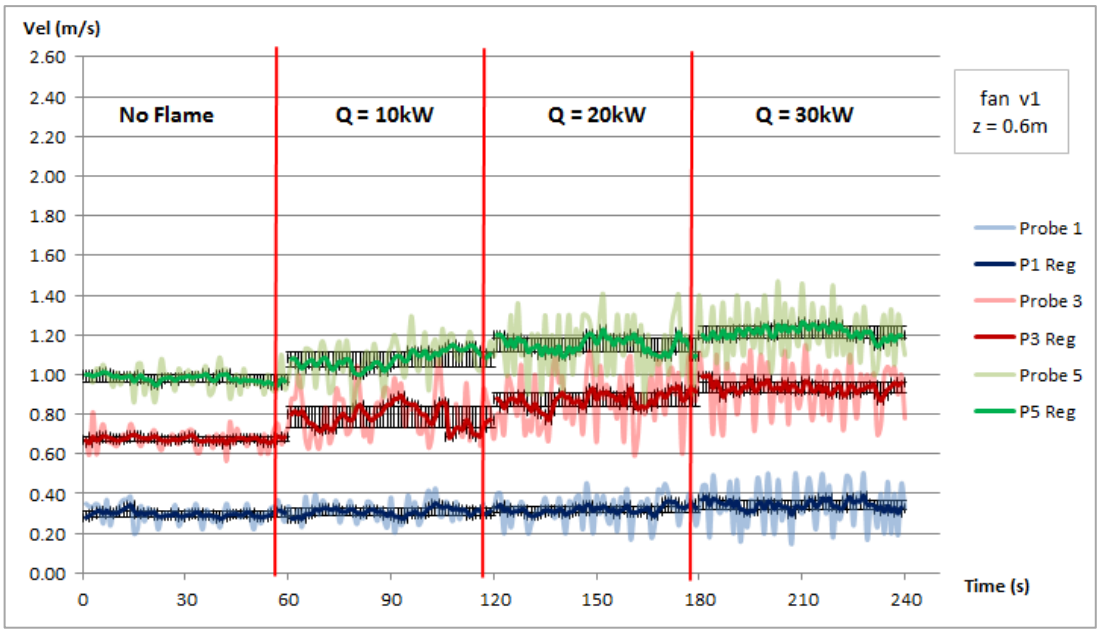

Figure 5.8: Horizontal pressure probe data for Test 1 when fan speed is fixed at v1 and z is fixed at 0.6m. Note that the velocity data point variation becomes increasingly consistent demonstrating that the buoyant force becomes more dominant as Q is increased. Data colours are aligned with probe colours of figure 5.7 for clarity. Exponential regression analysis has been applied to the raw data in order to better identify data trends corresponding to the variation in boundary conditions and standard deviation is marked.

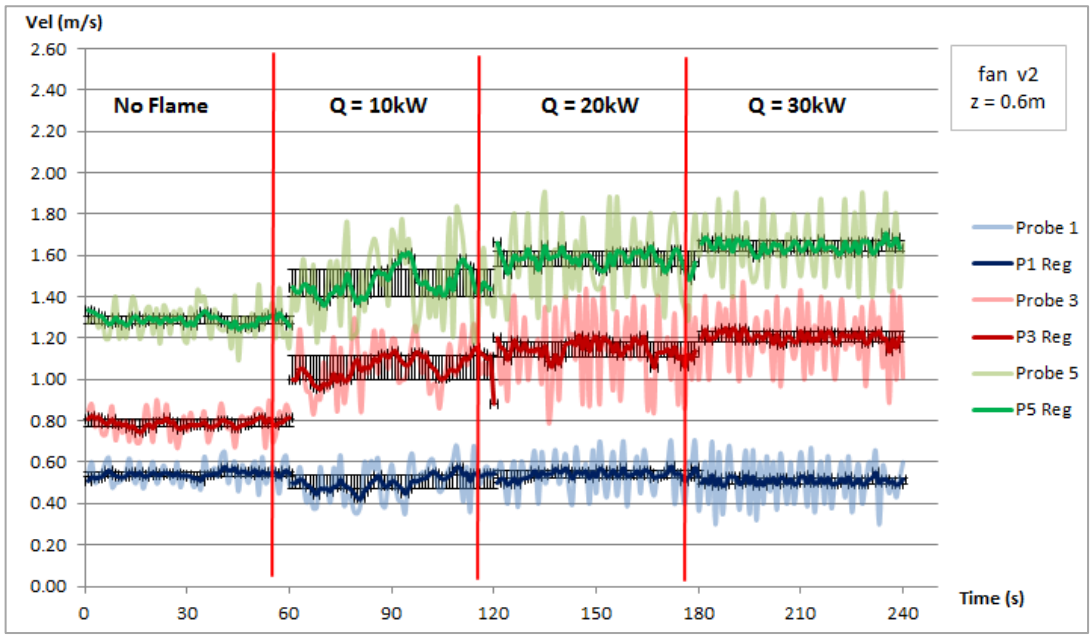

(a)

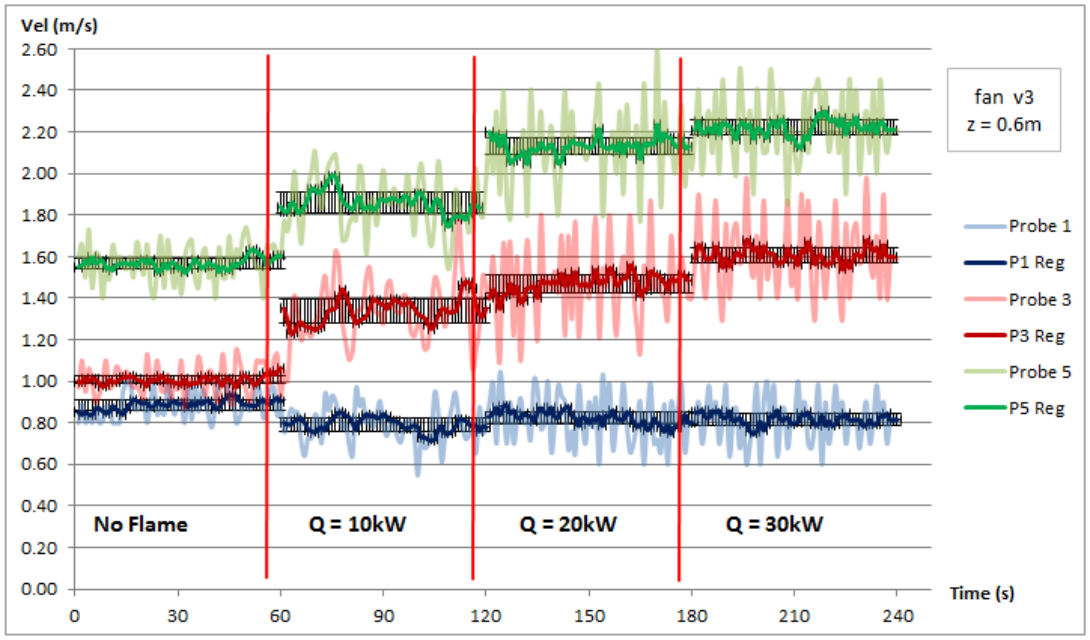

(b)

Figure 5.9: as per Figure 5.8 except in (a) fan speed has been increased (v2) and in (b) fan speed has been increased further (v3). The same trends are apparent but to a lesser extent under increasingly stronger cross flow pressure conditions. Standard deviation can be seen generally to decrease as Q is increased.

5.1.2 Introduction of Buoyancy Data (Test 2)

The subsequent case that is of interest of course is the purely buoyant, or axis-symmetric, case where no cross flow is introduced. A large body of work exists in the literature concerning this case, indeed, as discussed in the literature section essentially all empirical entrainment theories are based upon this controlled paradigm. The data gathered here is simply to offer a general comparison with all the various cross flow cases that are investigated in this work, and with the buoyant-case literature, in section 5.1.3.

Having observed the magnitude of the velocity fluctuations of the pressure probe readings and the subsequent general trends which emerge when the cross flow data from section 5.1.1 is regressed and viewed globally (each of the 12 cases considered in context with each other) it will be seen that the data acquired from the purely buoyant plume, while simplistic in design, uncovers interesting nuance and detail which are apparently lost when the cross flow pressure differential is added to the buoyant pressure differential.

In this purely buoyant (Q=10kW) case horizontal probe locations (probes 1, 3 and 5) are identical to those in section 4.1.1 so the data is directly comparable in terms of pressure/velocity reading and noise behaviour. For this case 3 vertically-aligned probes have been added (probes 2, 4 and 6) which are situated to acquire upward pressure readings as a result of the natural buoyant fire flow at approximately the same location as the 3 horizontal probes (figure 5.10).

Since there is now no fan-induced cross flow there are two primary mechanisms by which a horizontal flow field may be produced. Firstly the natural fire flow, which flows inward, toward the flame from all directions (around 360°) due to the negative pressure differential created, at any point over the height of the flame/plume, by the upward flowing hot gases. Secondly, the natural oscillation of the turbulent flaming region will produce pressure fluctuations in both horizontal directions manifested in large and small-scale vorticity generation [47]. Expansion

of the hot gases at the flame edge are one component of this complicated flow phenomenon

In figure 5.11 (a) the horizontal probes are still orientated so that pressure generated in the direction of the fan is read as positive on data the data graph and pressure generated in the opposite direction appears as negative data. With this in mind, where probes 3 and 5 read negative this is indicative of inward fire flow. This is the case over most of this dataset (a) where the inflow velocity at radial locations 0.1m (probe 3) and 0.3m (probe 5) at height z=0.2m range from around 0.1m/s to 0.3m/s. Large fluctuations are apparent however, most likely attributable to the turbulent oscillation of the flames and these are noticeably more pronounced at probe 3, which might be expected since probe 3 is in closer proximity to the flame boundary than probe 5. Probe 1 by contrast is orientated so that inward fire flow registers as positive data however it can be observed that the majority of the data from probe 1 resides in the negative suggesting a general pressure generation away from the flame for the majority of the data sequence. Probe 1 is of course located essentially just at the edge of the flame boundary, 0.02m from the burner edge. It is therefore realistic to assume that the hot flame fluid which is rising due to relative buoyancy with the surrounding bulk fluid creates pressure waves which are recorded by the probes due to the hot gases expanding in all directions, and specifically, with reference to probe 1, outward from the flame edge. In the case of probe 1 the sporadic peaks in graph data will be the result of air being pulled into the flaming area by rising vortices and gulping fluctuations as described in [47, 49].

Figure 5.11 (b) reveals some phenomena which we might well have expected. Probe 6, furthest from the flame, demonstrates little if any buoyant upward flow, as does probe 4, which generally follows the pattern of probe 6 relatively well with the exception of the large fluctuations which occur every few seconds. These fluctuations are likely to be exhibited in probe 4 since it is located closer to the flame than probe 6. Probe 2, located at the flame edge (with probe 1) appears to provide a more consistent reading by comparison for the first half of the data set and in the

second half of the data set two clearly defined, multi-peak, fluctuations can be observed. This highlights two points; firstly, despite proximity to the hot flame boundary (0.02m) no constant upward (buoyant) pressure wave is detected except when the turbulence of the flame causes sporadic pressure gradients to sweep upward from below the probe location (which are represented most extensively by the P2 peaks in (b)). We can infer therefore that since probes 4 and 6 return mainly negative data points (downward flow direction) that in fact the horizontal inflow is being read by the (top side) of these vertical probes (P4 and P6) and little or no upward buoyant flow is detected (excluding the large perturbations which can be witnessed in the data of the red and blue probes (particularly in P1 and P2, and to a lesser defined extent in P3 and P4 in figures 5.11 (a) and (b)). Secondly it may become apparent then that the results data for P4 and P6 mimics quite well the trends of P3 and P5 respectively, further evidence that the inflow is being read to some extent by both horizontal and vertical probes.

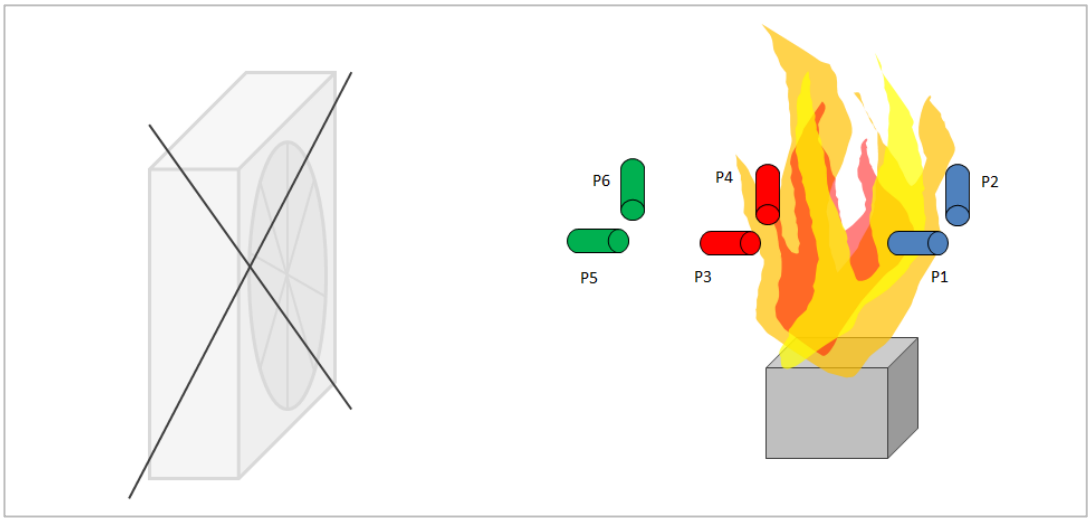

Figure 5.10: Purely buoyant case has no cross flow and is assumed to be immersed in an ambient bulk fluid. Probes 1, 3 and 5 are identical to the previous case however probes 2, 4 and 6 have been added and are aligned to measure (buoyant) vertical flow (downward flow would be recorded as set of negative numbers).

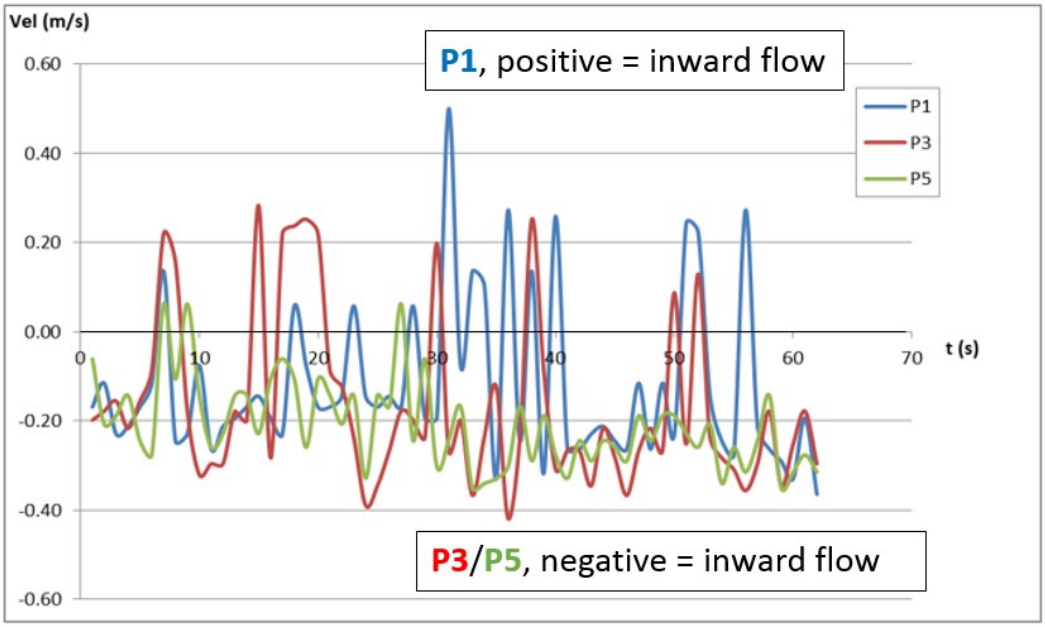

(a)

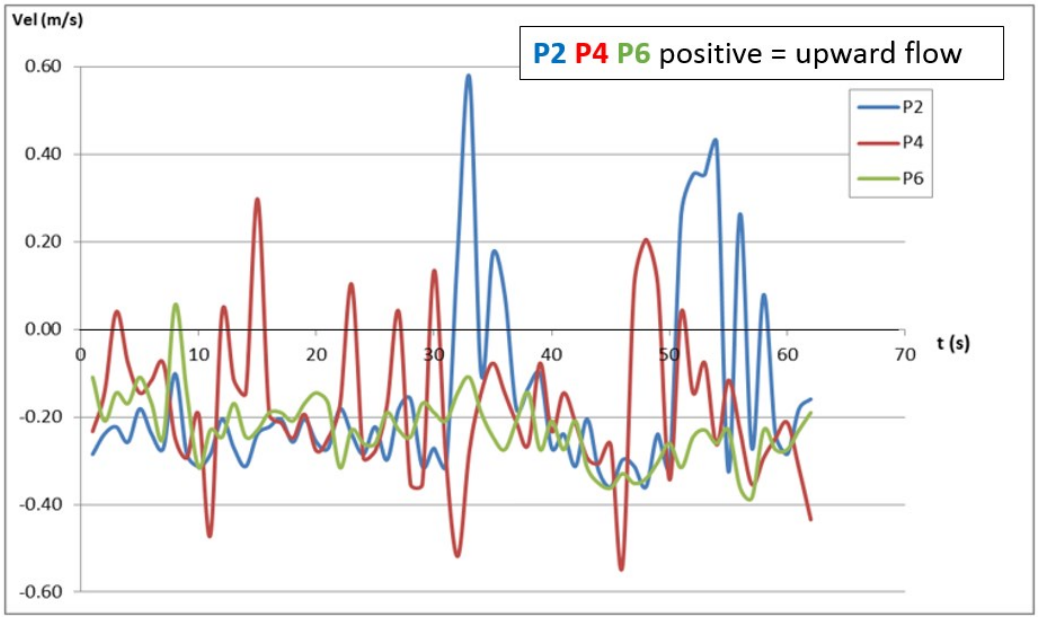

(b)

Figure 5.11: (a) horizontal velocities and (b) buoyant (vertical) velocity readings from the purely-buoyant axis-symmetric case, where Q = 10kW.

Observing figure 5.11 reveals an interesting trait in the data that was not observed in the cross flow cases in section 5.1.1. In numerous instances along the data set, fluctuations and perturbations registered in the data for each horizontal probe can

be seen to be registered simultaneously, to varying degrees, by each of the vertical probes.

While the probe locations used in this section helped to explain the behaviour of the natural fire in-flow during a purely buoyant example, we acquired no meaningful data on the magnitude of the buoyant pressure differential generated at the centreline of the flame. What would be beneficial now would be to consider an example of purely buoyant data at the flame centreline to allow comparison with the fully-buoyant-case literature, and investigate briefly the impact of the addition of different cross flow pressures on the purely buoyant flow.

5.1.3 The Mixed-flow Data (Test 3)

The test was then varied slightly by choosing the following parameters: z = 0.6m, Q = 10/20kW, fan speed = zero (v0), v1 and v2. Most significantly probe locations were changed to investigate pressure data at different locations around and within the flame. Although these locations are physically close to the probe locations from test 1 and test 2, due to the contrast between the intense flow magnitude characteristics at the flame centreline compared with those just outside the flame boundary, these variations to the test set up were considered to be of great worth. The probes are now denoted with the letter "A" to differentiate them from the previous test locations. Figure 5.12 depicts the new locations of pressure probes 1-6 in relation to the burner, fan and flame.

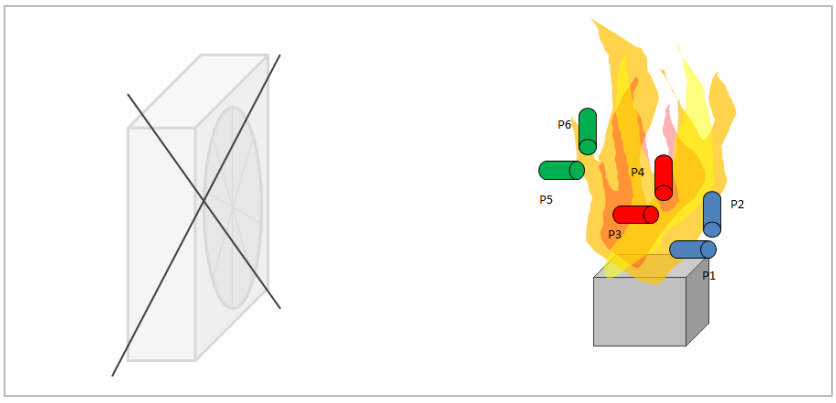

(a)

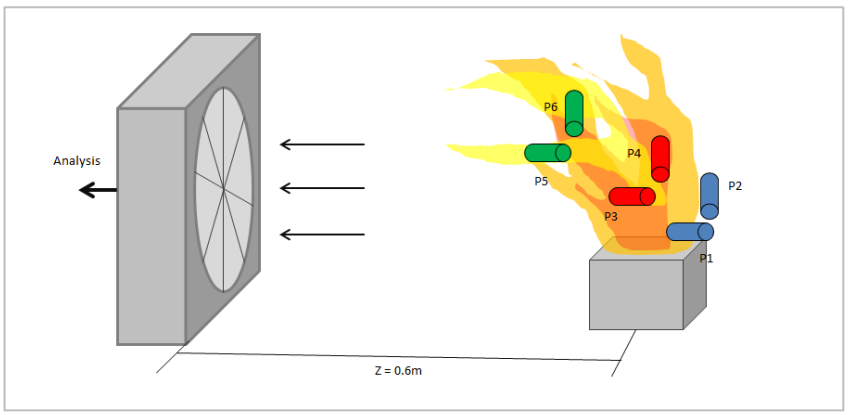

(b)

Figure 5.12: Re-arranged probe locations to acquire further pressure data from critical locations within and around the flame. The buoyant case and a cross flow case are depicted. Again this figure is not to scale and is approximate only.

Probes 1/2 have been relocated to take account of the flow at the leading edge of the flame where a small laminar portion was regularly observed before the onset of turbulence further along the flame length. Probes 3/4 have been relocated to the centreline of the flame in an attempt to acquire the strongest buoyant force magnitude. Probes 5/6 have been relocated to the wind-ward edge of the flame to attempt to acquire meaningful cross flow and buoyant pressure data as the flame is increasing tilted further as the fan speed is increased.

Figure 5.13 displays the pressure reading from the probes in the vertical positions across the test 3 locations. Part (a) shows the data from probe 4A which is located at the approximate centreline of the flame at z = 0.1m, while part (b) shows the data for probes 2 and 6, located at the flame boundary at the leading edge and windward sides of the flame.

During the first and fourth columns in part (a) we can observe what would intuitively have been expected which is a strong and relatively constant buoyant pressure flowing upward at the centreline. Some scatter might be expected here since the probe is submerged in the turbulent, oscillating flame fluid however the regression lines demonstrate a fairly constant upward flow perturbed by natural fluctuation in the flame fluid. The upward buoyant velocities recorded during the 10kW and 20kW v=0 cases appears to be approximately equal suggesting that the additional fuel delivered to the burner during the 20kW cases has the effect of rising a greater distance before undergoing combustion, which will have the effect of lengthening (and potentially widening) the flame. This is a fair assumption since, from this data, at z = 0.1m, it would appear that no noticeable additional upward buoyant pressure is created by the additional fuel/combustion. If anything, the noise is reduced for the v=0 case at 20kW compared to that at 10kW suggesting that as the flame is elongated the upward pressure at z=0 becomes increasingly constant and dominant over lateral turbulent oscillations which are more associated with the intermittent phase of the flame.

As the exhaust fan is engaged buoyant readings can be noticed to reduce for v=1 and further till for v=2. This is expected as the cross flow inertia perturbs the naturally buoyant flow and much greater noise is then introduced into the readings. One might expect the 20kW case to show less of a reduction in buoyant readings as the fan is engaged however in the case of v=1 the 10kW case appears to retain the more strongly buoyant flow.

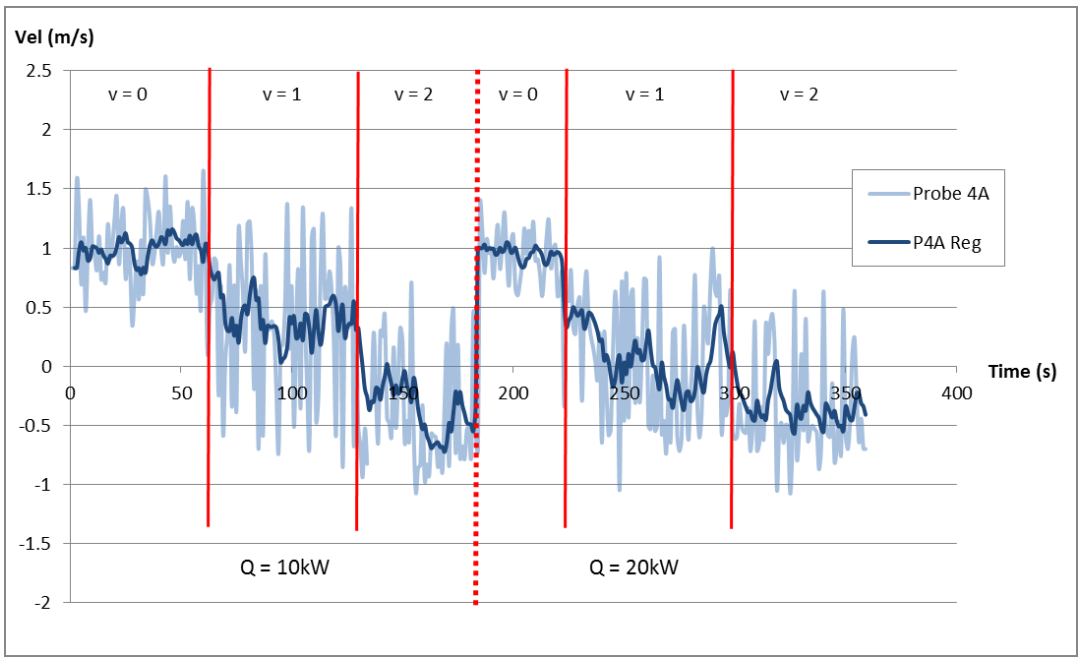

(a)

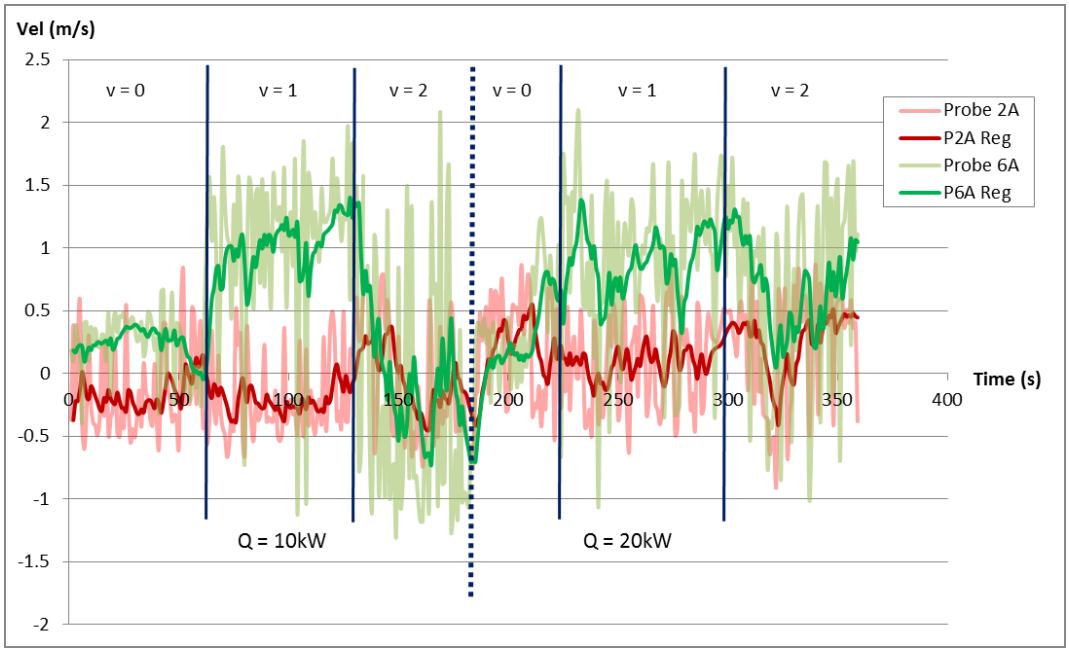

(b)

Figure 5.13: Vertical pressure probe readings for test 3 where (a) is at the flame centreline and in (b) probes 2A and 6A are a few centimetres outside the front and rear flame edge. For clarity of data detail SD and error have been omitted. Those statistical margins are comparable however to those demonstrated in figures 5.8 and 5.9.

The magnitude of the scatter raises uncertainty when comparing these levels, however one explanation may be that which is discussed in Appendix B where in figure B2, the impact of crossflow upon vertically positioned probes is discussed. It is arguable that the cross flow pressure differential created by fan setting v1, since being relatively greater when compared to the 10kW fire over the 20kW fire, was therefore able to exert more effect at the (underside) probe lip and so may in part have contributed to a greater extent to the buoyant flow velocity reading for v=1 at 10kW in figure 5.13 (a) than for 20kW case. As the fan speed is increased to v2 the flame is tilted further toward the fan and the buoyant force can be seen to drop further. With the aid of the regression data lines we can clearly observe explainable trends which are repeated quite noticeably in both the 10kW and 20kW examples.

The data in part (b) tells a different story for probes 2A and 6A. Vertical probe 2A is positioned right at the leading edge of the flame, 0.02m laterally outside the flame boundary, and 0.02m vertically above the flame base, essentially on the cusp of the small laminar portion of the leading edge of the flame. It is not realistic therefore to see negative data for v=0 of the red probe 2A line at Q=10kW, since the upper lip of the probe was more frequently exposed to the flame surface as the initiation of flame oscillations begin in that region. Subsequently, the case of v=0 for Q=20kW shows some expression of fluctuations of buoyant upward pressure as the flame overall volume was increased. The slow increase in buoyant probe 2A data throughout all cases in figure 5.13 is most likely due to the impact, again, of the cross flow pressure leaking into the underside of the vertical probe. As the flame is further tilted in each case and cross flow pressure builds, the buoyant force generated by the small laminar portion of the flame at probe 2A has less and less significance.

As for probe 6A some buoyant pressure readings are apparent for both fire sizes and they tend to increase as the first fan speed (v1) is engaged. Due to the location of this probe it becomes more fully involved with the flame when the flame is slightly tilted which appears to be the best explanation for the increase in buoyant

data during both v1 cases, especially where clear and relatively well-defined large fluctuations in the data occur. Based on the data noise from the previous two tests these characteristics do not appear to be the result of cross flow pressure. For both the Q=10kW and 20kW cases the buoyant pressure then drops at fan speed v2. Due to probe 6A being located at a greater height than the other probes (z=0.2m) the tilt experienced by the flame at v=2 effectively pulls the flame below the location of probe 6A and removes the probe from the full involvement with the flame that it experienced at v=1, thus the buoyant pressure is reduced as the inertia of the mixed flow overcomes the buoyant pressure more significantly. This effect is more pronounced in the 10kW case since the buoyant force of this fire sizes is less than that in Q=20kW which manages to maintain a greater buoyant reading.

Figure 5.14 displays the cross flow pressure data for the same experiment, recorded simultaneously with the buoyant pressure data. Again part (a) articulates the probe (3A) immersed at the flame centreline and part (b) shows data for probes 1A and 5A and the leading edge and rear edge of the flame respectively.

Interestingly, the data from v=1 and v=2 for both fire sizes in (a) suggests that the cross flow pressure generated appears to reach a maximum measured at the central flame volume which is not increased even when the fan speed is turned from v1 up to v2. This highlights the idea that even when the flame is substantially tilted due to cross flow pressure the centreline, relatively near the base, it is proportionally stronger against the cross flow pressure than further downstream in the flame. As energy begins to dissipate the further up the flame the cross flow pressure becomes stronger relatively speaking, and the curved tilt shape of the mixed-flow flame is realised.

Part (b) demonstrates that the horizontal cross flow pressure is increased more greatly at probe 5A due to its proximity to the fan compared to probe 1A. Probe 1A is also relatively well protected in test 3 from the direct cross flow as it is positioned right at the base of the buoyant flame edge.

This rest of the sub-sections of chapter 5 will utilise the raw data discussed over the last few pages and will begin to analyse the flow characteristics of the cases where the buoyant flame is subjected to a horizontal cross flow pressure under a mixed convection paradigm.

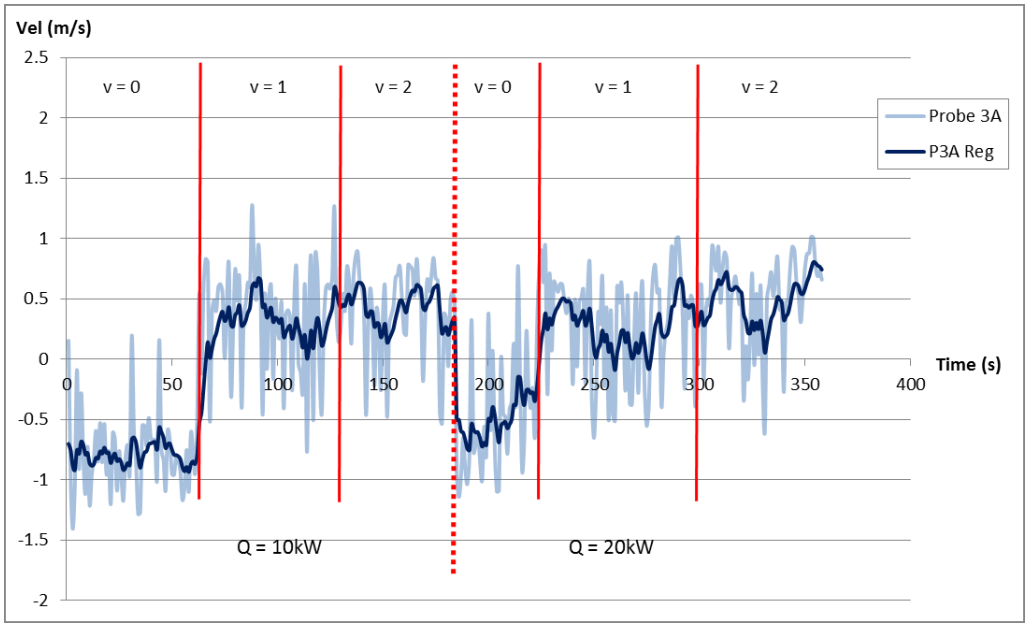

(a)

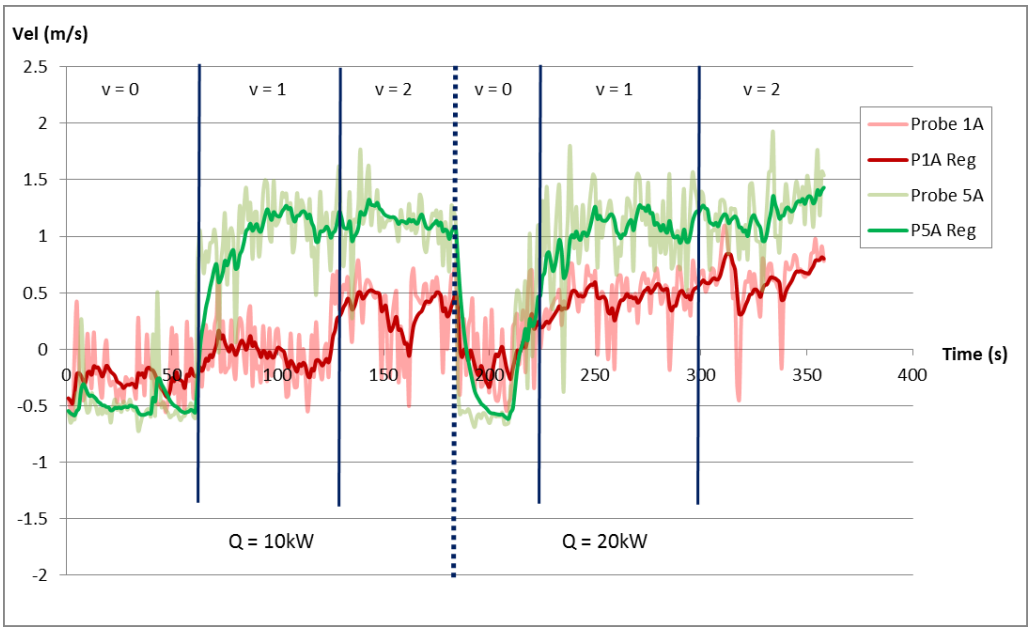

(b)

Figure 5.14: Horizontal pressure probe readings for test 3 where (a) is at the flame centreline and in (b) probes 1A and 5A are a few centimetres outside the front and rear flame edge. For clarity of data detail SD and error have been omitted. Those statistical margins are comparable however to those demonstrated in figures 5.8 and 5.9.

5.1.4 Measurement Data Comparison with Literature

It is necessary to compare the flame centreline and inflow/outflow data recorded here with the corresponding calculated descriptions available in the traditional plume literature. Concerning flame fluid velocity, the centreline velocity equation for the constant flame region of McCaffrey [2-29] shall be compared with data from the 10kW fully-buoyant cases in test 2 and test 3.

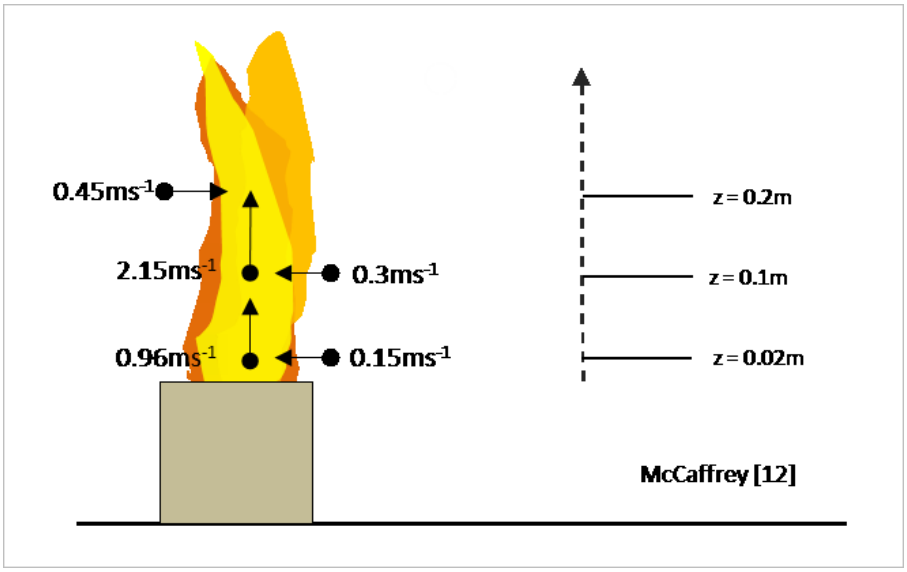

(a)

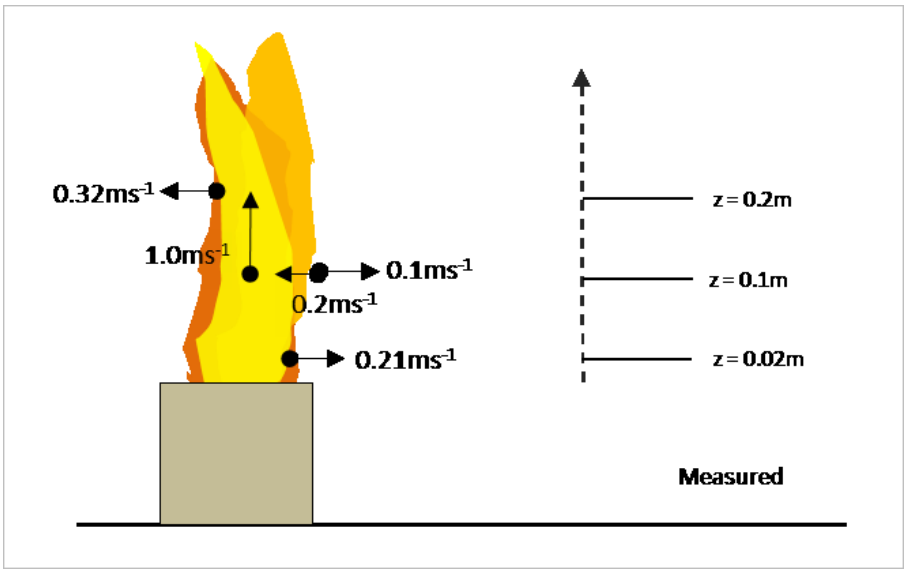

(b)

Figure 5.15: (a) Predicted flame velocities using equation 2-29 compared with (b) measured velocities by pressure probes. Predicted inflow velocities are based on the assumption v=0.15u (equation 2-6)

There is some disparity between measured flame velocities and those predicted by the traditional literature. Buoyant centreline velocity was measured to be around 45% of the predicted value. Furthermore the predicted inflow velocities a few centimetres outside the flame boundary were not practically realised. The pressure probes located in these positions typically recorded velocity data flowing outward from the flame. As discussed previously this is likely due to expansion of the hot gases of the flame and these were noted particularly at 0.02m and 0.2m above the burner surface. At the elevation 0.1m above the burner surface however the flow velocity fluctuated more evenly between and inflow of 0.2m/s and outflow of 0.1m/s. This inflow velocity of 0.2m/s lies between the predicted inflow velocity (0.3m/s) based on calculated vertical centreline velocity, and the predicted inflow velocity (0.15) based upon measured vertical centreline velocity at that elevation.

Equation 2-29 for centreline velocity partially resulted from experimental work in which the fire HRR ranged from 150-600kW on gas burners of ~0.3m^2. By comparison the fire in this case has a HRR of 10kW emanating from a burner source of 0.15m^2. This results in a buoyancy-source description of the McCaffrey fires in the approximate range of $Q^* \approx 0.75 - 3$ which is, on average, an order of magnitude greater than $Q^* \approx 0.14$ which is applicable to the current experiment. Therefore the McCaffrey correlation for centreline velocity in the continuous flame region may not describe so well the gas velocity in the current case.

Velocities inside and around the cross flow flame are analysed with respect to the axis-symmetric literature in detail in chapter 5.3.

5.2 *No Flame* Cross Flow Characterisation

As previously discussed the extraction fan induces a significant negative pressure differential (an area of low pressure) near to the front edge of the fan face which is translated into inertia (dynamic pressure, $0.5\rho u^2$, where ρ=density (air) and u=air flow velocity) as the horizontal forced flow field is created.

Figure 5.16 shows the pressure measured at each probe when no flame is present. This represents the naturally decaying inertia per unit volume of the cross flow with increasing distance from the fan when no additional forces are applied. In each case the blue plot represents the lowest fan speed (v1), the red plot denotes the intermediate fan speed (v2) and the green plot depicts the greatest fan speed (v3).

The simplest trend, and of importance to note for the context of this study, is of the decreasing ΔP with distance from the fan at each fan speed, and the convergence of this data with distance from the fan. It is intuitive to note that the greater fan speeds lose momentum at a greater rate than the lower fan speed and that over a distance of approximately 1.1m, the pressure differential for each fan speed converges substantially.

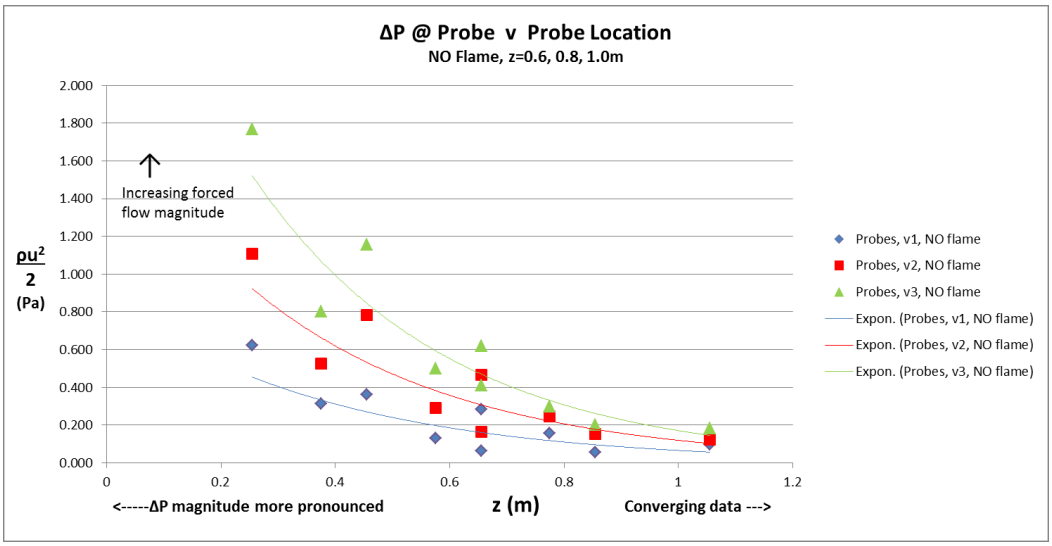

Figure 5.16: ΔP Measurements at Probes (0.6m, 0.8m, 1.0m cases) with NO flame present

Based on the free-cross flow data it is clear that the decrease in inertia with increasing distance from the fan will impart lesser influence upon flame characteristics at greater distance. Similarly, the cross flow dynamic pressure is greater closer to the fan and will have a greater impact on any volume of the flame closer to the fan than any portion of the flame further from the fan. It is reasonable to postulate therefore that the buoyant force of the flame has greater relative strength against the cross flow inertia further from the fan.

This reinforces the intuitive notion that the smoke extraction system is more effective in removing a greater volume of smoke when the fire occurs in closer proximity to the fan. This is of course only in terms of the ability of the fan flow to overcome the buoyant force of the fire plume, as per the experiment scenario, and does not consider the dynamics of a smoke hot layer or collected smoke reservoir.

More specifically it can be inferred that for practical purposes of the experiment design the maximum distance from the fan at which a flame should be evaluated is around 1 metre. Figure 5.16 demonstrates apparent convergence of the decreasing cross flow inertia at this distance which signifies a distance after which the cross flow has little impact upon the ambient fluid, at least in terms of the scale of interest for the experiment. Due to both the magnitude of pressure readings at this location and the physical distance, the fan will have little impact upon the flame beyond this point and certainly in terms of smoke extraction, has negligible effect. These experiment parameters were arrived at by observing the data as the fan-flame distance z, was increased and is verified by the analysis which is presented in the results sections.

It is possible to make a coarse scaling analysis of the horizontal inertia flow field based upon conservation of mass, similarly to the simplified principle adopted for *ideal plume* model.

Stating that the mass flow is equal at any point along the length of the flow field can be represented numerically as:

$$\rho \bar{U} \pi r^2 = constant$$

Equation 5-6

where ρ = air density (presumed constant) [kg.m^{-3}], $\bar{U}$ = average air flow velocity [m.s^{-2}] and r = the radius of the inertial flow field [m]. In this way it is possible to track the evolution of the radius of the flow field beginning at the fan and up to the limits of the experiment range at around 1.1m from the fan where, as described above, the fan-induced pressure differential is barely large enough to affect the fire. This is of course an idealised approach and a number of simplifications must be accepted for this analysis. The flow velocity at the fan edge is averaged by the surface area of the fan opening considering the recorded mass flow rate. The velocities used at each probe point along the length of the flow field are point readings, but are assumed to be an average across the flow field circumferential surface area. This "top hat" velocity contour assumption should be acceptable since it is also used in the fire engineering *ideal plume* derivation. Figure 5.17 depicts the flow field of the fan induced flow.

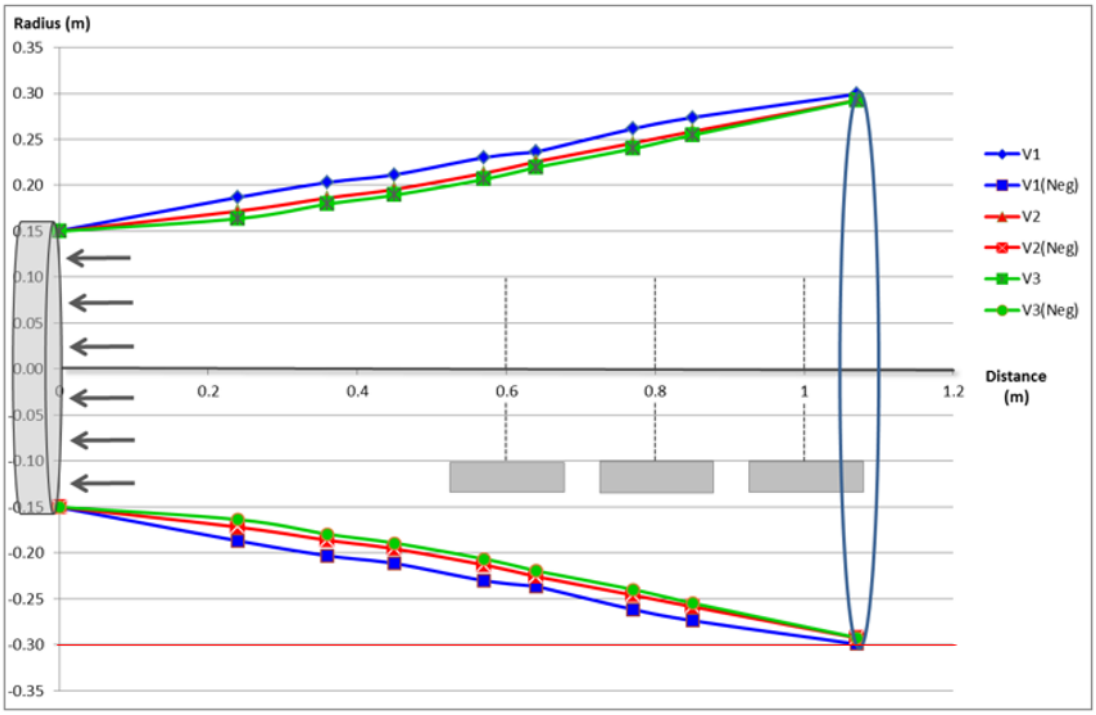

Figure 5.17: From analysing conservation of mass using velocity data from nine locations along the experimental area the flow field cross-sectional area may be approximated for 3 fan speeds where no fire is included. The fan is depicted at x=0 and is 0.3m in diameter. The ground (table top) boundary is highlight by a red line at -0.3m on the y-axis.

A further assumption built into this 'ideal flow field' approach is that the presence of the ground (table top) as a boundary has negligible effect upon the pressure/ propagation in the lower half of the conical flow field. The table top is highlighted in figure 5.17 by the red line at y = -0.3m. The theoretical flow field does not cross the ground boundary until around 1.05m, corresponding with the furthest edge of the largest flame-fan span (z'). This is preferable as there should be almost no opportunity for boundary layer drag to influence the bottom half of main flow field. One result however is that the air entrained into the main flow field from directly beneath is now limited and air must be drawn in across the surface of the table top and then upwards into the flow field. This may have a small impact upon the direction of air flow into the turbulent flow field which appears in the wake of the flame (to the rear of the flame) however this will remain unquantified as the level of instrumentation required to analyse this pattern is not included at present.

In any case, the base of the flame is located 0.2m above the table top boundary and the solid burner casing presents a 0.15m^2 solid blockage in the fan-induced fluid flow path. This is unavoidable and the turbulence caused at the rear of the burner by the burner itself is probably greater than the influence of the table top boundary 0.2m below. Furthermore, the focus of the measurement instrumentation in this work is focused from along the height of the flame in each case which should not be adversely influenced by the table top boundary located beneath the burner.

The experiment arrangement is designed to represent the practical scenario that we want to study, the smoke extraction concept, however the range of fans speeds, inertia of the cross flow in case and the increasing fan-flame distances used represent a set of variable conditions for evaluation so that insight might be gained in to the influence of that extraction system on the behaviour of the flame and the nature of the entrainment.

5.3 Cross Flow Characterisation – 10kW Flame

Figure 5.18 shows the ΔP recorded at each probe when a fire (Q=10kW) is introduced. Probe locations are demonstrated by location along the x-axis, and by noting that the fan is located in each instance at x=0. For each corresponding graph 0.6m, 0.8m and 1.0m corresponds with the centre of the burner, covering the full range of the fan strength where after 1.0m, the induced flow is essentially insignificant in terms of smoke extraction.

The graph scales have been kept constant on 5A-5C to articulate the direct impact of increasing the fan-to-flame distance (z) on local ΔP readings at each probe. The reduction in local pressure readings can clearly be seen between each case z=0.6m, 0.8m and 1.0m where the increase in fan-to-probe distance in each case of 0.2m has a significant effect.

It is also important to note that the clear and general trend of decreasing ΔP measurements with increasing distance from the fan is still firmly apparent. What we can also now postulate is that to the LHS of each graph, where ΔP readings are greater, local flow velocities are likely to be dominated by the inertia of the cross flow. To what extent this is true will be dependent of course upon the size of the fire and the local flow characteristics which will also have great impact upon the angle of flame tilt and the length and shape of each flame. Similarly we might suppose that to the RHS of the data set in each graph, where ΔP measurements are low relative to the LHS and the location along z is aligned with the approximate location of the burner in each case, that the natural buoyant force of the fire will play a greater role in determining local velocities. The relative balance of buoyant-to-inertial forces requires further analysis; however the changing impact of inertial to buoyant forces across the length of the tilted plume will certainly make a contribution to the entrainment flow characteristics and contributes to the resulting boundary layer / transition / plume modes described in [20, 24].

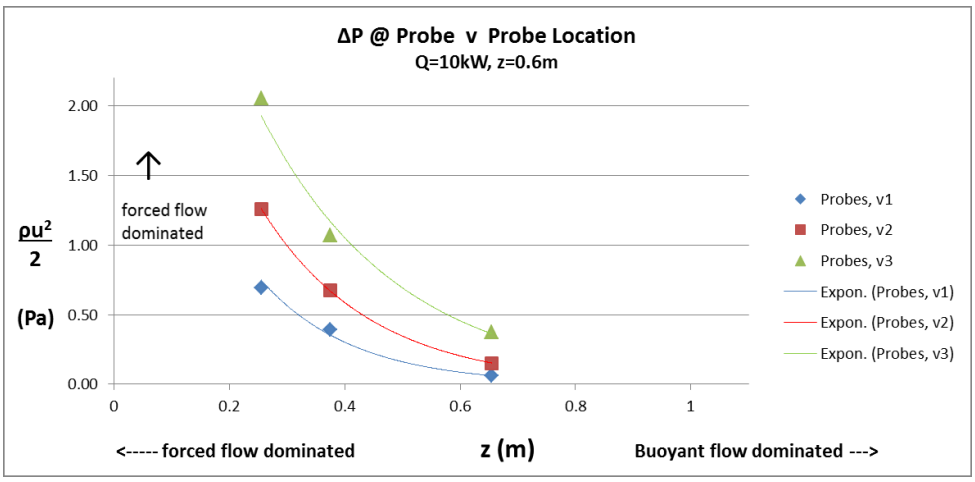

Figure 5.18: ΔP Measurements at Probes, z'=0.6m, Q=10kW (v1, v2, v3)

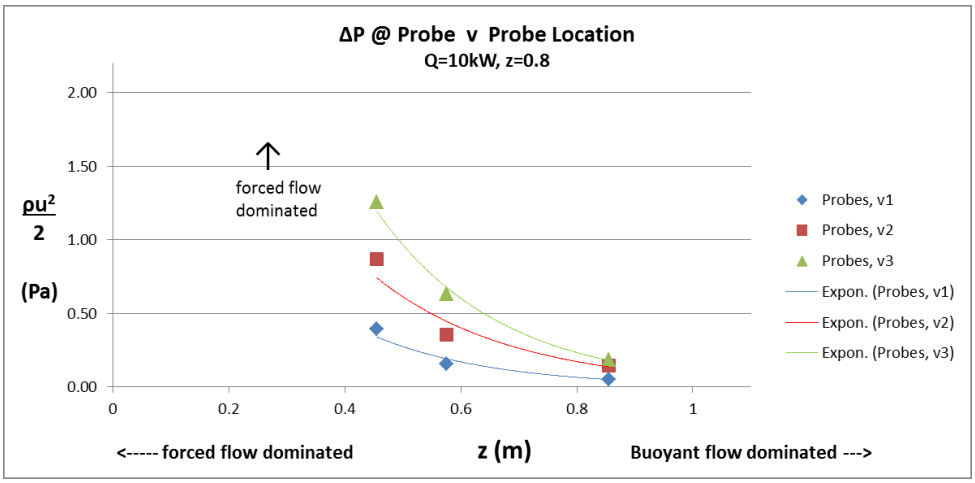

Figure 5.19: ΔP Measurements at Probes, z'=0.8m, Q=10kW (v1, v2, v3)

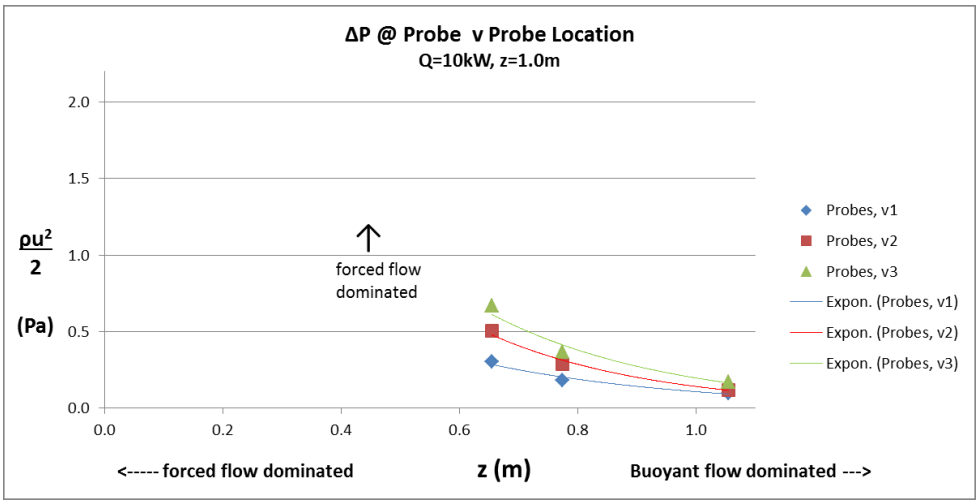

Figure 5.20: ΔP Measurements at Probes, z'=1.0m, Q=10kW (v1, v2, v3)

5.4 Crossflow Characterisation – Impact Upon the Flame

In order to analyse the impact of the addition of a purely buoyant force to the free cross flow the data from figures 5.16 (free cross flow) and figures 5.18 - 5.20 (cross flow where Q=10kW) must be combined. Since the ratio of inertial to buoyant weighting at each probe appears to change with each instance of z' (0.6m, 0.8m, 1.0m) it is necessary to investigate each case separately. It is also convenient for practical purposes so that an adequate resolution for detailed analysis can be achieved. Even though the same general trend of decreasing ΔP measurement with increasing distance from the fan of was noted in the no flame and 10kW flame cases, it is noticeable that the case with the addition of the fire has, as one might expect, discreet nuances that differentiate the tends between the no flame and 10kW cases.

Parts a, b and c of figure 5.21 correspond with those parts from 5.18 - 5.20. The images depicted here are not to scale and flame shapes/angles are meant as purely descriptive tools to tell a qualitative story of the impact of the cross flow and more specifically, the location of the fire along the length of that cross flow, upon the flame structure and global behaviour. The 3 flames in each image correspond with fan speeds 1-3 and the nomenclature is colour-coordinated with the v1-v3 data lines in figure 5.18 - 5.20. Therefore in each case the most severely tilted flame (yellow) is produced at the greatest fan speed (v3, green) and the most upright flame (red) is produced under the lowest fan speed (v1, blue).

The amount by which the flame is tilted away from vertical is affected by its proximity to the fan. At z' = 0.6m the flame most strongly tilted and in the case of the stronger fan speeds (v3 and to a lesser extent v2) the flame typically leans significantly and appears to point toward the fan, signifying the dominance of the cross flow inertia across the entire length of the flame. At the weaker fan speed (v1) the flame leans less and the tip of the flame typically points more upward, signifying a change from the inertial dominance lower in the flame to the relatively stronger buoyant force at the tip. In each of the cases at 0.6m it appears that all or most of the smoke produced at the flame is extracted by the fan.

Moving the flame further from the fan to z′ = 0.8m has the general effect of tilting the flame less at each fan speed. Since the distance from fan to flame is greater, the cross flow ΔP per unit area is reduced so the ability of the forced cross flow to tilt the flame and extract the plume smoke is diminished somewhat. Flame shapes appear generally similar to

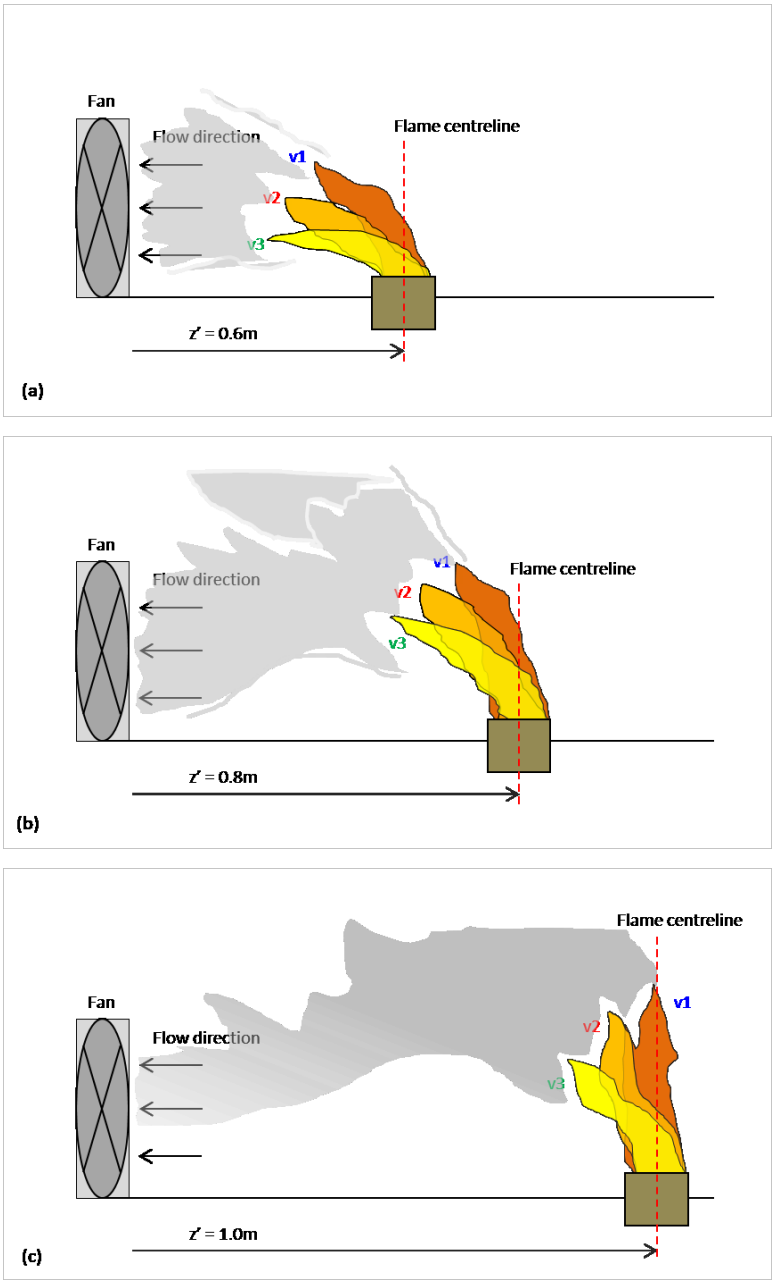

Figure 5.21: Depicts the approximate impact upon flame shape and angle for 3 fan speeds as the distance between the fan and the flame is increased, due to decrease in ΔP per unit area with increasing distance

those witnessed at z′ = 0.6m however all flames tend toward exhibiting more of a buoyant, upward pointing tip (plume mode) due to the increased relative buoyant force experienced at the flame resulting from the reduced cross flow ΔP compared to 0.6m. At this distance some of the smoke is extracted by the fan and some can be seen to evade the fan. Witnessing smoke evading the fan is more noticeable when the flame sporadically shows more erratic behaviour and turbulent movement. It was generally noticed that in the less extreme cases (extreme cases would be the shortest fan to flame distance (0.6m) with highest fan speed (v3) or greatest distance (1.0m) with lowest fan speed (v1)) where the cross flow and buoyant pressure differentials are typically more comparable in magnitude, random fluctuations would be more common since neither force exerts significant dominance to maintain flame structure / shape.

Moving the flame further still from the fan to z′ = 1.0m, flames no longer point toward the fan and in each case are tilted significantly less than the previous two distances of 0.6m and 0.8m. In fact, the difference in apparent tilt angle between the flames for all fan speeds seems less than the difference in tilt angle for the flames at all fan speeds for the shorter distances. This can be confirmed by noticing in figures 5.18 - 5.20 that with increasing distance (across parts a, b and c) the *difference* in ΔP per unit area between each fan speed case diminishes. That is to say that the blue, red and green data lines representing the readings at probes for each fan speed converge with increasing distance from the fan. This can be seen between probes within each part (a, b and c) and when comparing parts a, b and c directly. We can say therefore that that not only does the *impact of the cross flow upon the buoyant flame* decrease with distance, but the *difference* in impact between each strength cross flow (fan speeds v1, v2, v3) also decreases with distance.

In each of the cases depicted in figure 5.21 the smoke detail is intended to qualitatively represent the distribution of smoke between that captured by the exhaust fan and that which escapes upward due to buoyancy. At z′ = 0.6m the

exhaust fan captures most of the smoke, where the chance of smoke escaping increases with slower fan speeds (and reduced cross flow inertia). As the fan to flame distance is increased the quantity of smoke which escapes the fan increases due to the relative increase of the buoyant force compared to the cross flow inertia. The quantity of smoke which is not captured by the fan is tied to the balance of buoyant versus inertial forces at the flame location so each set of variable parameters (fan speed / distance) results in a unique outcome in terms of smoke flow characteristics. In later sections it will be seen that increasing the fire size increases the local buoyant force at the flame enabling an even greater quantity of smoke to escape the exhaust fan.

In each cross flow case the physical nature of the flame also takes on unique tendencies. The fully buoyant flame takes on a shape and volume which is a function of many aspects, but is particularly influenced by the direction and magnitude of the naturally-induced fire flow, from all directions. The rate of delivery of fuel, of oxygen and the surface area of the burner all contribute to the volume of the fully buoyant flame, which remains, from a global point of view, essentially constant. Assuming that the fuel flow rate and the burner diameter remain constant, this means that the inflow of entrained air from all directions 360° around the flame also remains, essentially constant, and more specifically *of equal magnitude* from all directions. Once the cross flow is introduced to the fully buoyant case the variable which begins to evolve is the magnitude of the inflow from each direction.

The images in figures 5.22 – 5.24 highlight examples of the change in the physical structure of the flame once a cross flow is applied and the magnitude of the inward flow toward the flame is severely perturbed, as investigated qualitatively in Chapter 4. The images in figure 5.22 are taken facing the direction of the flow therefore the flame is tilted away from the camera and toward the fan in the distance. It can be seen that with a relatively strong cross flow inertia applied the flame is tilted somewhat significantly toward the fan and the surface area of the flame from a

lateral perspective is now reduced. The three images demonstrate the changeable flame shape whereby the flame was noticed to widen and narrow quite sporadically. This phenomenon was more apparent when the inflow to the fan was perturbed. This happened particularly when these photos were taken and the photographer's body intermittently blocked the flow path. This also explains the angle of the flames in figure 5.22 where they appear to lean to the left. This was not typically observed at other times throughout the experiments.

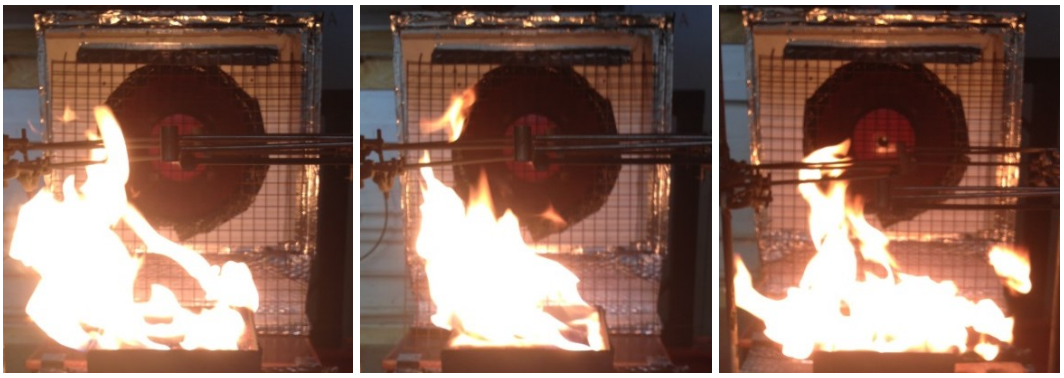

Figure 5.22: Flame tilt toward the exhaust fan. Flame appears tilted to the left due to position of photographer body blocking the inflow (in the direction of the photo)

Figure 5.23 shows an example of the transition between when a vortex begins to evolve near the base of the flame and then roles along the flame length before reaching the intermittent region of the flame body and dissipating outward. One of the interesting points about this sequence is that as the vortex, and in this case the main volume of the flame at that time, moves downstream it is elongated and thinned quite substantially due to the cross flow ΔP created at the flame location. In this sense the vortex does not evolve and roll to its natural (buoyantly-driven) conclusion. This is typically not observed in the purely buoyant case. Again, these figures are only a representative snap-shot and a fuller analysis of the flame structure under cross flow conditions was presented in chapter 4. The important concept to appreciate here is that not only does the creation of an inertial ΔP across the flame alter the apparent angle of the flame but the naturally buoyant structure of the flame fluid flow process is also infracted and a new regime appears. As the flame is moved further from the fan (or the fan speed is reduced) the perturbation to

the fully buoyant regime diminishes until the flame, at around 1m from the fan, appears to lean slightly toward the exhaust fan but generally resembles the structure of the fully buoyant case.

(a) Very low fan velocity, almost fully buoyant flame

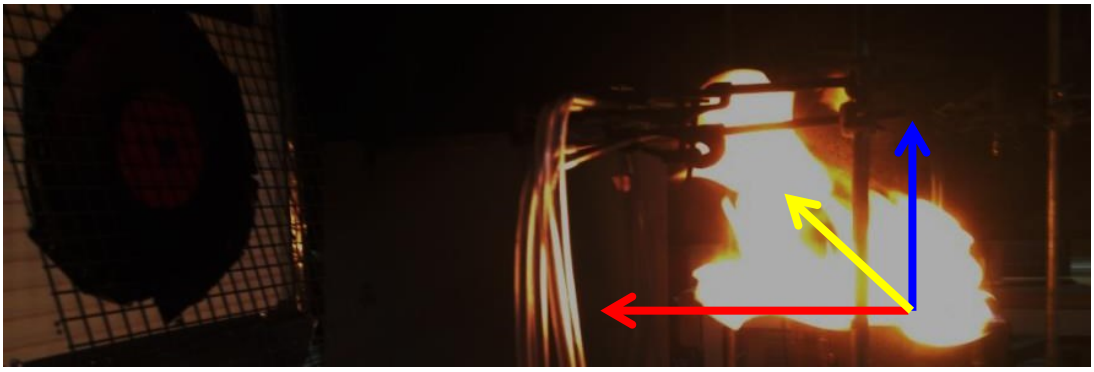

(b) Increasing fan speed and crossflow inertia. Visually the flame is now noticeably influenced by the horizontal pressure but not enough to display a classic tilt. The slight leaning off-centre is intermittent and turbulent

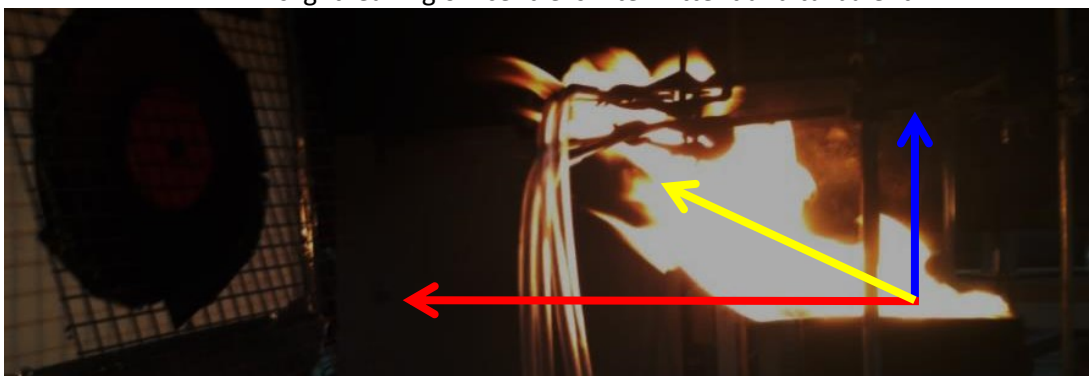

(c) With further increasing cross flow pressure the flame now clearly 'leans' toward the fan (in the direction of the crossflow). This action is again intermittent, but visually more pronounced and the comparatively strong crossflow pressure eventually begins to flatten the flame and random turbulence appears to decrease.

Figure 5.23: Typical examples of increasing crossflow velocity (horizontal pressure). Blue arrow = buoyant force, red arrow = horizontal inertia and yellow arrow = resultant flame angle and apparent length. Qualitative and indicative only.

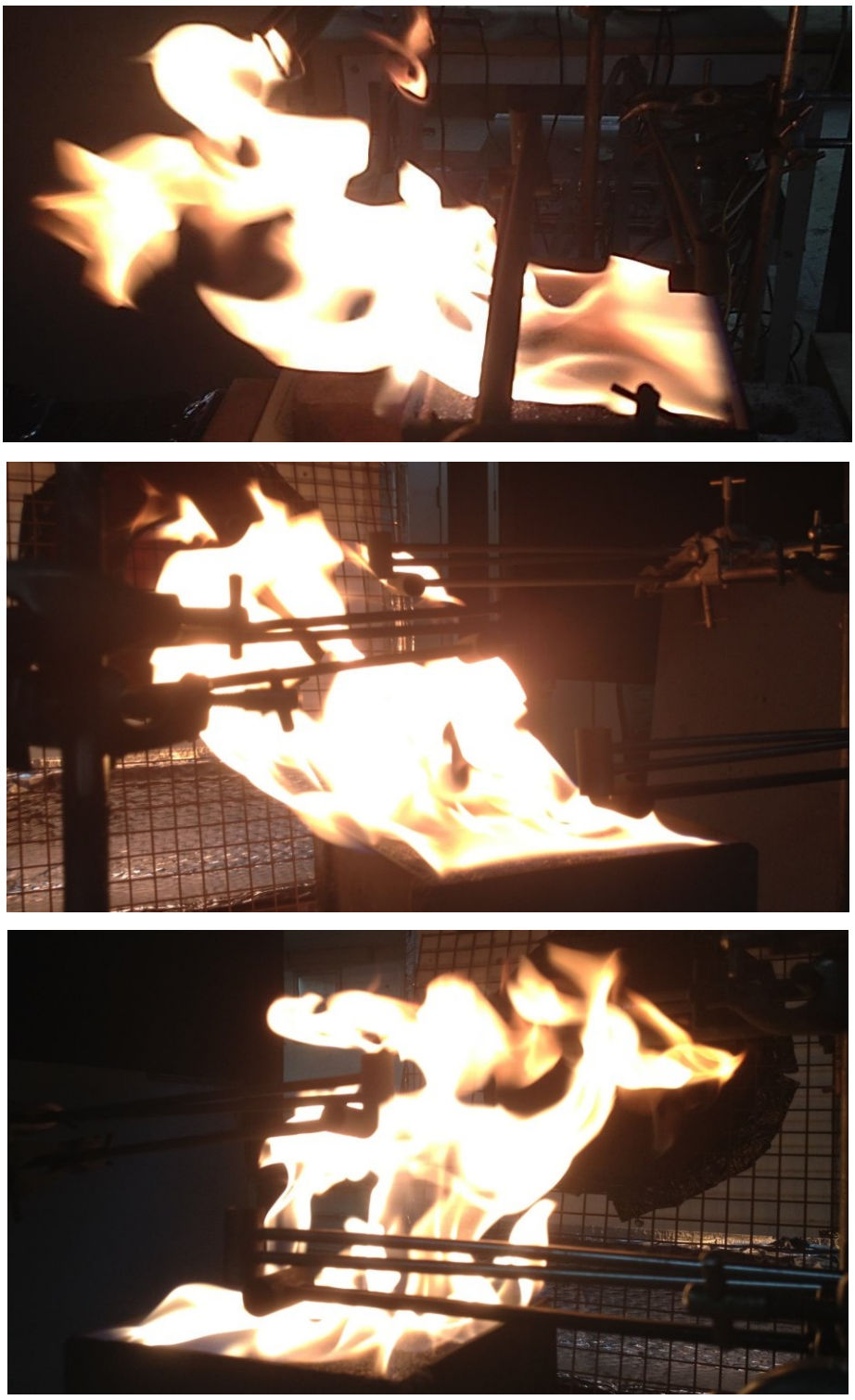

Figure 5.24: Flattened flame sheet from 3 different angles. As the crossflow pressure is increased further still the distinct flattened flame can be seen close to the leading edge of the burner. In this region (red) the crossflow inertia is significantly greater than the buoyant force and almost no fluid rise is apparent. Downstream the comparably greater buoyant force drives the flame fluid vertically (blue) and as the two forces become more comparable a particularly turbulence flow pattern becomes apparent.

Figure 5.24 shows the flattening phenomenon which occurs close to the flame base and begins at the generally laminar initial flame portion at the leading edge of the burner. Since the ΔP of the inflow of bulk fluid into the flame is clearly greater in the direction of the fan the inertia in this location drives the flame fluid (the fuel and the combustion region in general) across the burner with little resistance in the opposing direction. This causes a "flattening" of the flame which is apparent from the base of the flame across the width of the burner (0.15m) before the flame reaches an area with Reynolds number large enough to allow the onset of a somewhat more turbulent flow pattern. As the burner is moved further form the fan the apparent flattened and laminar region beginning at the leading edge decreases in size and at $z' = 1.0$m generally no flattening is apparent.

5.5 ΔP Comparison of 10kW Flame vs NO Flame at z=0.6m

Figure 5.25(A-C) shows a direct comparison of ΔP measurements at each probe for the NO flame and 10kW flame cases for the three fan speeds v1, v2 and v3. In each case the black trend line shows the measured ΔP data for the NO flame case at one fan speed and the coloured trend line shows the measured ΔP data when the flame is present with the same fan speed setting. The guidance notes included on each graph are also colour coded as the inertia/ buoyancy-dominated tendencies are only applicable for the cases where the flame is present (the coloured data set in each case). The guidance notes themselves simply highlight the ideas discussed in the previous pages that close to the fan the inertia of the cross flow will tend to be the dominant force in influencing local velocities and far from the fan the natural buoyancy of the fire plume will likely play an increased role in influencing local velocities. Note then that moving the flame closer to the fan and subsequently increasing the apparent tilt angle decreases the magnitude of the buoyancy in the flame.

Scanning across figure 5.25 (a) through (c) several trends may be seen. Firstly, and perhaps most importantly, the change in ΔP is either positive or negative depending upon which probe the reading corresponds to. That is to say that at probes 3 and 5, both located at the fan side of the flame, the measured ΔP increases when the fire is added into the cross flow, and conversely, the measured ΔP at probe 1 in each case consistently decreases when the flame is added. Certainly, the positive changes in ΔP at probes 3 and 5 are clearly noticeable however the change at probe 1 is more discreet, especially at fan speed v1, however this becomes more pronounced as fan speed is increased.

A second important observation to note is that the increase at probe 3 is consistently greater than the increase at probe 5. This is at first curious perhaps since probe 5 is located closest to the fan and one might expect this to correspond with the greatest ΔP increase when the flame is added.

Due to the typical proximity of probe 3 to the flame – probe 3 is always closer to, or more fully involved in the flame fluid than probe 5, this therefore shows an increase in entrainment flow due to the greater buoyant force at that location.

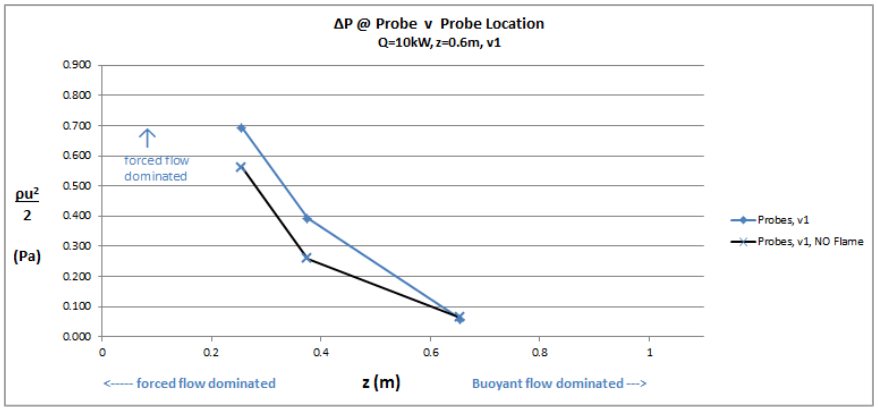

(a)

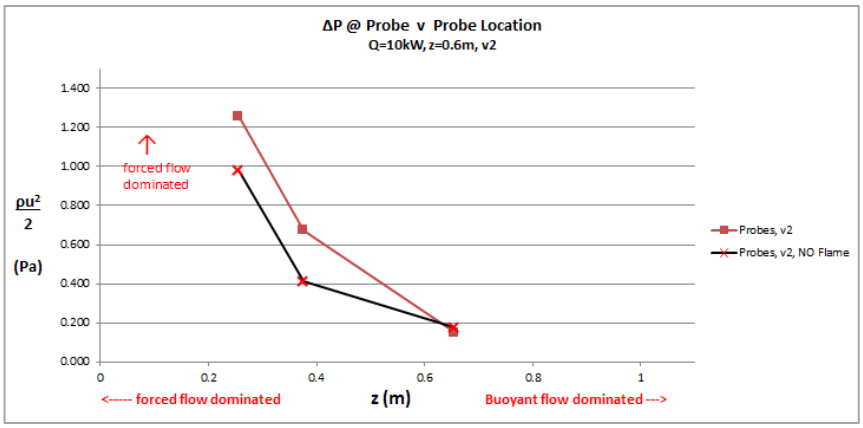

(b)

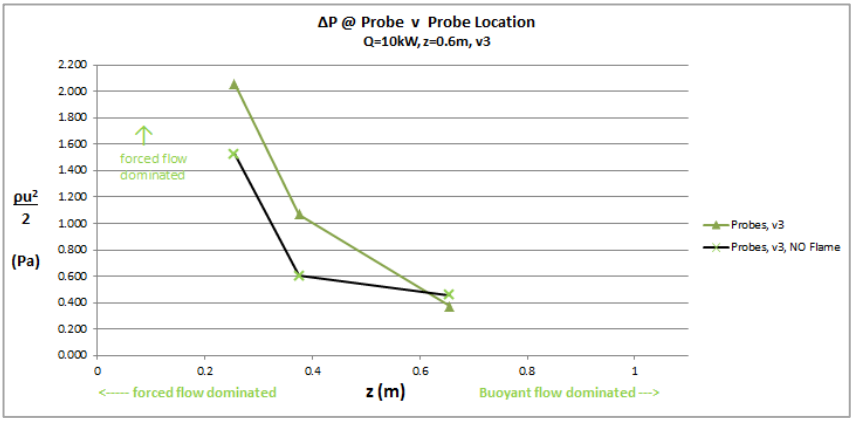

(c)

Figure 5.25: Comparison ΔP Measurements at Probes, z=0.6m for NO Flame and Q=10kW, Fan speed (a) v1, (b) v2, (c) v3.

The characteristic velocities gained from the probe data at each location cannot capture the small scale detail of the fluid flow and rather therefore, the velocity measurements can be used to give a descriptive and qualitative representation of the story across the fire plume as a whole, from a global perspective. To this end figure 5.26 attempts to give a theoretical example of the increase in cross flow velocity recorded at probe 3 following the introduction of the 10kW fire. Consider that probe 3 is located somewhere central to the large dark blue arrows in figure 5.26. These exaggerated arrows then represent the increase in flow velocity once the flame is added to the cross flow as a result of the addition of the buoyant ΔP_B to the cross flow ΔP_f. The impact at the other two probes is not considered in this example. What is also of importance here is the theoretical increase to the surface area of the buoyant flow field when it is perturbed by the cross flow. While the image in figure 5.26 is purely an impression and not quantified in any way, clearly the horizontal inertia of the cross flow has the effect of spreading the smoke and hot gases from the buoyant plume over a greater area than if it were the fully buoyant case. Even if the buoyant plume was tilted and not increased as depicted here, the circumference increases with height so in both cases it is apparent that the flow field of smoke *increases* as it approaches the exhaust fan, in contrast to the fan-induced flow field which *decreases* with increased proximity. It is intuitive to imagine then that cases where the fire is located further from the fan are more prone to creating larger, disjointed smoke plumes implying that the fan will at some point in the scale of severity of cases, not be able to cope with the full extent of the smoke entrainment.

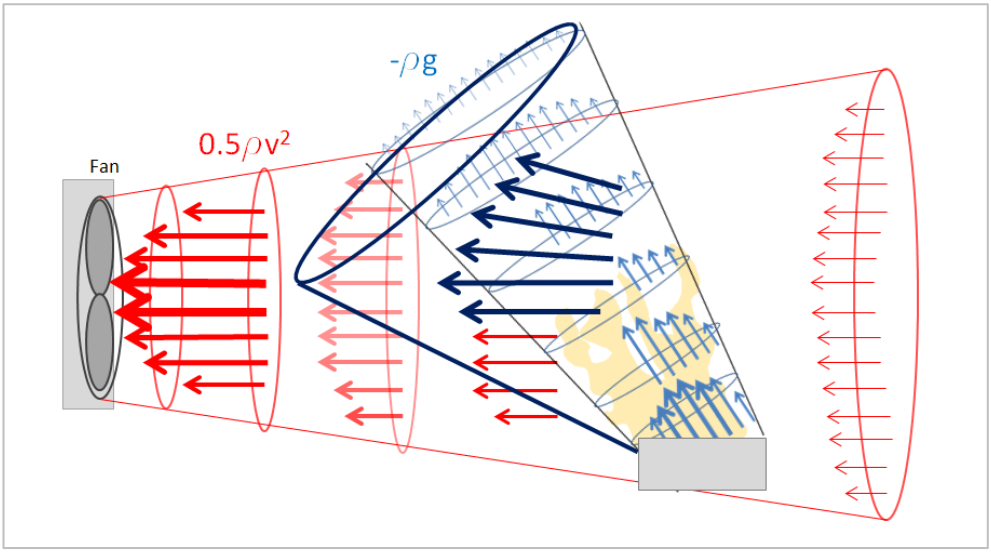

Figure 5.26: Qualitative depiction of smoke flow field increasing as it approaches the fan

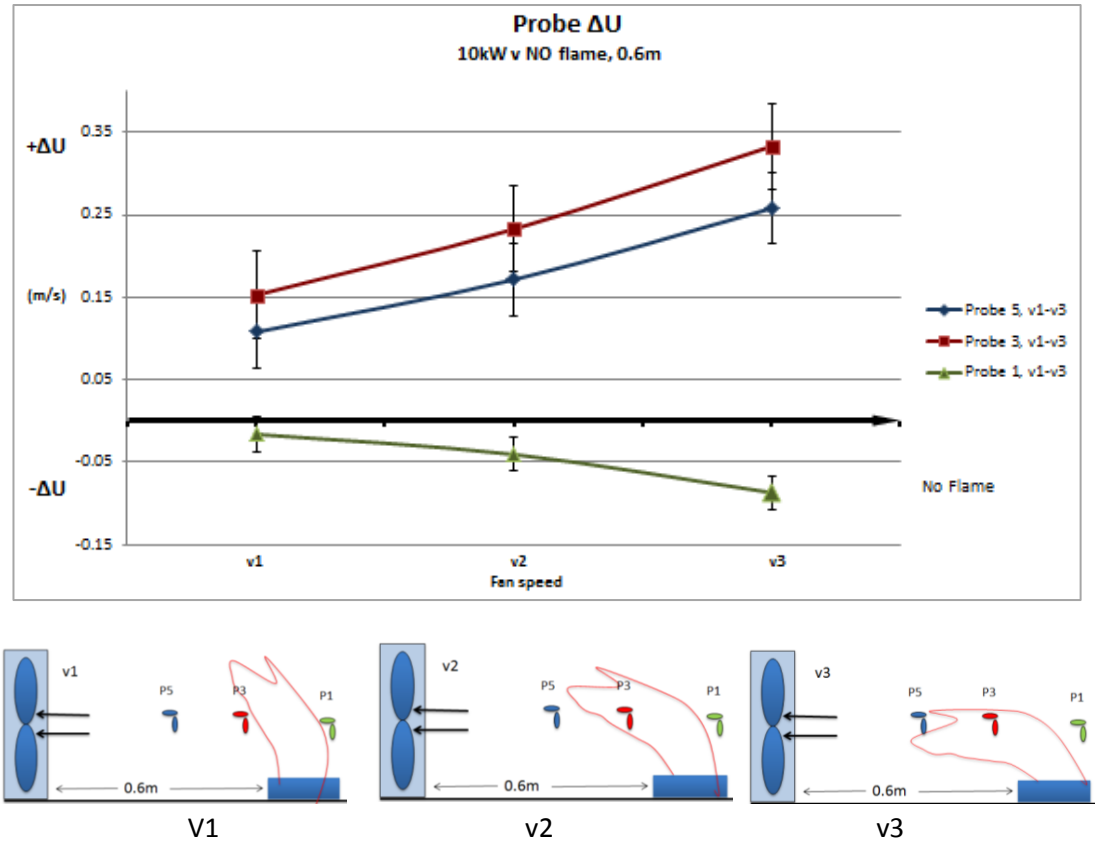

V1 v2 v3

Figure 5.27: Change in velocity at probe with & without flame for each fan speed (v1, v2, v3), standard error from each dataset is demonstrated.

In figure 5.27 the left-most data points are recorded at fan speed = v1, the central data points at v=2 and right-most data points at v=3. The heavy black line marked along the x-axis at y=0 represents the flow velocity in each case (v1, v2, v3) where NO flame is present. The data points therefore demonstrate the difference in velocity measured between the NO flame and 10kW flame cases.

It is immediately apparent that with the increase in fan speed local velocities at each probe are altered. It holds as discussed following figure 5.25 that the velocity change at probes 3 and 5 are positive (velocity increases when flame is added) and the change is negative at probe 1 (local velocity decreases at probe 1 when the flame is added). Further it can be noted that the magnitude of the velocity increase at probe 3 is consistently greater than that at probe 5. These variations are a clear indication that an increase in fan speed, and thus the magnitude of the cross flow inertia, directly influences local velocity measurements and the probe location *relative to the fan* clearly demonstrates an inverse effect on local velocity (increasing distance from fan ~ decreasing velocity). The story of local velocity measurements is more complicated than this however and there are multiple parameters which influence the change in local velocity following the setting of a cross flow speed. The next boundary condition is probe location *relative to the fire*. This is demonstrated in figure 5.27 where the velocity change at each probe following either a different trend (positive [Probe 3, Probe 5] or negative [Probe 1]) or equates to a different magnitude in a similar trend (positive [Probe 3, Probe 5]).

5.5.1 ΔP Change Relative to the Horizontal Flame Length

Change in local velocity at each probe *relative to the fire* can be demonstrated more intuitively by plotting the ΔU trend for each probe across actual probe location. Figure 5.28 shows the change in velocity at each probe with respect to its location relative to the burner. The flame imprint on the graph is for illustration only and to demonstrate the location of the burner within the experiment scheme. The average flame shape will be different for each fan speed and this diagram is not

representative of flame shape. The thumbnails below the main plot in figure 5.28 are indicative of flame shape in each case as the fan speed increases (slightly tilted, moderately tilted, and severely tilted).

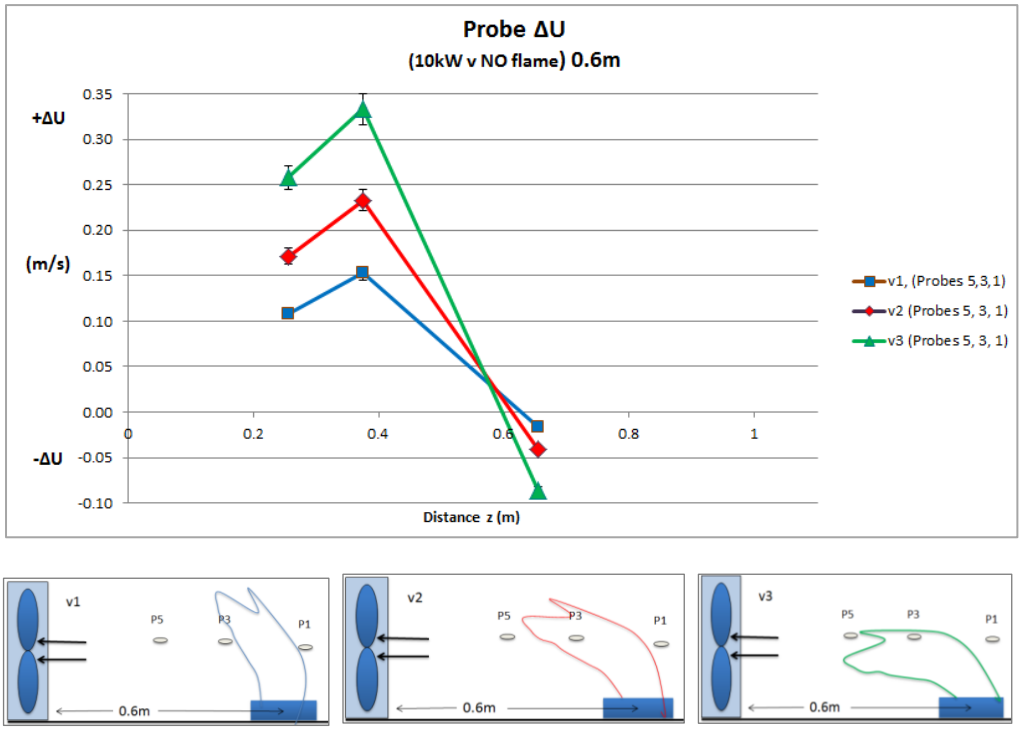

Figure 5.28: Change in velocity at probe with & without flame for each fan speed (v1, v2, v3). Notice the standard error with dataset increases as ΔU is increased.

Figure 5.28 affords the opportunity to picture the ΔU change across an idealised image of the flame length. We can notice the increase in velocity at probe 5, closest to the fan, the greater increase at probe 3, located further from the fan but closer to the rear edge of the flame, and the decrease in local velocity at probe 1, located furthest from the fan, at the leading edge of the flame.

It is clear therefore that the description of the change in local velocity (increase or decrease) differs depending upon which side of the fire the reading is taken from. Considering the location of probe 1 relative to both the fan and fire, we can say that the addition of the fire to the experiment has the impact of decreasing the velocity at this location of this probe. The fire is located directly in the line of sight between probe 1 and the fan. The buoyant fire therefore represents a blockage to the

crossflow when considering any point on the leading side of the fire and the overall effect of adding this heat source is to reduce the cross flow velocities at the leading side to lower than they were when no fire was present. The relative reduction in velocity increases with increasing fan velocity as can be seen where fan speed v3 (green line) results in the greatest decrease to local cross flow velocity at probe 1.

To this end, a study of flame drag coefficient might be possible. Such analysis would further contextualise the impact of the buoyant source within the horizontal inertial flow by describing the drag coefficient as a function of Reynold's number, flame tilt angle and flame roughness. A further study may include this however future work following on from this thesis will seek to utilise an experimental technique with a constant crossflow pressure across the length of the flame, or a blowing wind source, as to better replicate a natural wind profile across the flame length, so further consideration of the flame drag coefficient for the current work will not be investigated further at this point.

Subsequently, probes 3 and 5 should be considered in tandem since they exhibit the same trend in positive velocity change however the addition of the fire clearly has a varying impact upon velocities in around these locations. We can say therefore that velocities on the rear side of the fire are positively affected by the addition of the heat source, increasing local velocities to greater than they were in the purely inertial cross flow when no heat source was present.

5.5.2 Fluid Flow Behaviour at Probes 3 & 5

A description of the fluid flow characteristics around the location of probes 3 and 5 is required. Since thinking of the fire as a blockage to the cross flow it is intuitive to imagine the negative pressure created by the fan flow must evolve as it meets the strongly buoyant fire. This manifests in the main bulk of the fluid which is drawn into the cross flow being drawn from around the sides of the fire, where, just outside the flame boundary, the inflow velocity is assumed to be approximately

only 15% of the centreline velocity. The cross flow, on meeting the buoyant plume, essentially splits when it reaches approximately the leading edge of the fire and is drawn around the outside edges of the flame. From the point of view of the negative pressure created by the fan, this path around the outside of the flame boundary represents the path of least resistance at this location. As the fan speed increases the inertial force increase relative to the buoyant force of the fire and increasingly the flames are tilted further and more of the flame fluid is drawn into the cross flow.

The result is that the fluid flow which is split and drawn around the outer edges of the fire then converges at the rear of the flame where an area of high negative pressure exists, as demonstrated in [26]. The combination of these converging flows appears to result in an area of greatest velocity measurements at the rear edge of the fire.

These flow paths then converge on the fan side of the flame, some way down the length of the tilted flame. This can be seen where P3, which is located immediately on the rear side of the flame and has the greatest increase in local velocity of all the probes when the flame is introduced, for each fan speed. It is located such that it is involved in both the direct fan induced flow (being on the fan-side of the flame, and is also involved with the convergence of the fan flow which was split around the flame and re-joins in this region. The cumulative effect of both these flow fields is an area of greatest local flow velocity and subsequently an area where a large portion of the mixed flow entrainment occurs.

This description of the fluid behaviour in the case where a buoyantly fire is placed in a free cross flow aligns well with the data collected by [26, 35] who showed that the split flow around the flame converges in a series of vortices starting immediately on the rear side of the flame and continuing further downstream with decreasing size/rate.

5.6 Cases of Increased Fire Size, Q=10/20/30kW

The change-in-pressure analysis from section 4.5 is now presented with the addition of data for two larger fire sizes where all variable iterations have been repeated for each (experimental cases 10-27, chapter 3.3.4). The addition in fire size increases the relative buoyant force for each case in relation to the initial 10kW fire size (cases 1-9) and the ΔP data recorded at each probe is first presented together (figure 5.29) and then separately (figure 5.30) to aid further analysis and summary of the changes to the flow data.

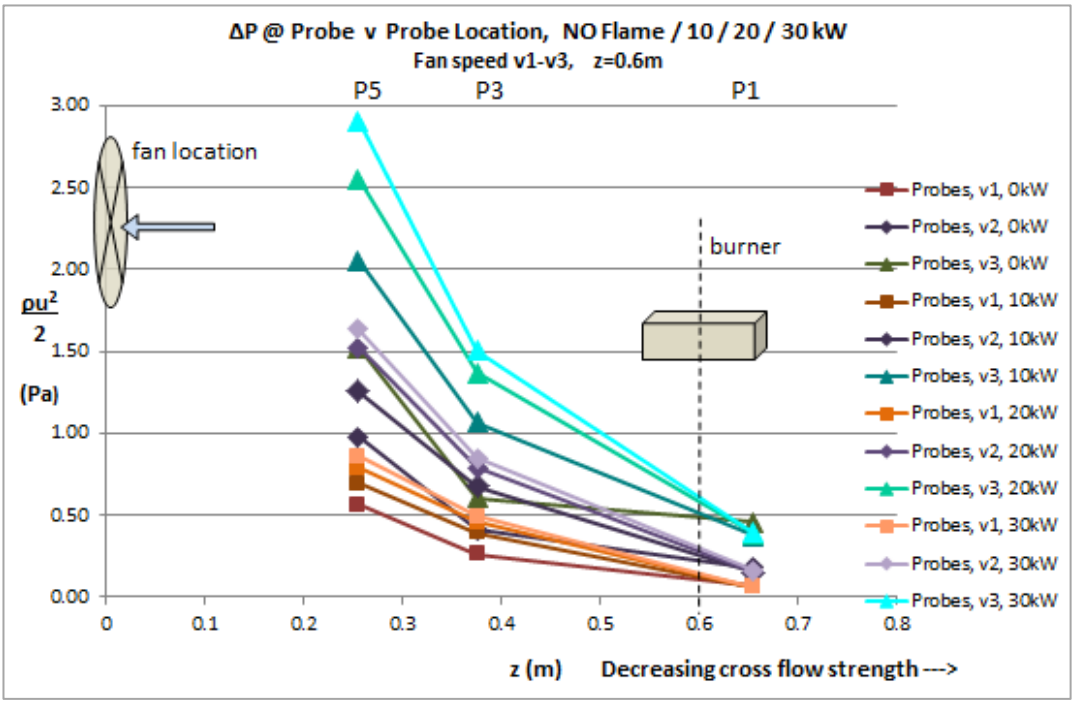

Figure 5.29: ΔP recorded at each pressure probe for all three fire size iterations of the previous section, 10, 20 and 30kW cases at z'=0.6m and for fan speeds v1-3.

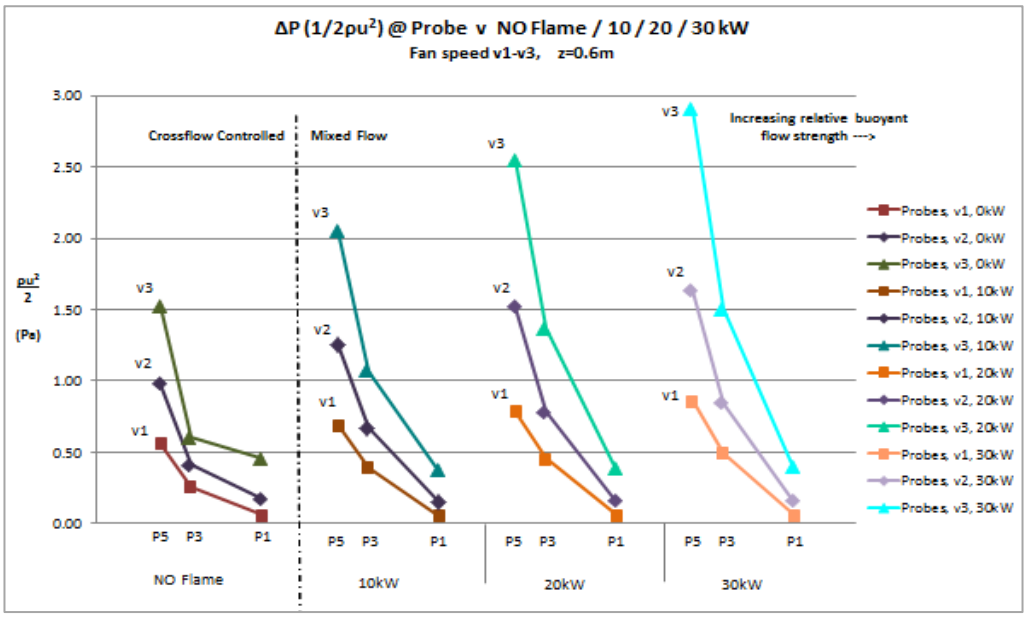

Figure 5.30: Separates the data presented in figure 5.29 by fire size

The following concise summary describes the impact on flow data at each probe as demonstrated in figure 5.30:

Probe 1

- Decrease at probe 1 in each case from no flame case.
- ΔP reading at Probe 1 increases with increasing Q. This is a balance between stronger buoyant force blocking the cross flow path, but also greater naturally-induced entrainment field as a result of the stronger buoyant force.

Probe 3

- ΔP at probe 3 increases in each case with increasing Q
- ΔP increase from NO flame case is consistently larger than probe 5

Probe 5

- ΔP at probe 3 increases in each case with increasing Q
- ΔP increase from NO flame case is consistently less than probe 3

Figure 5.31 demonstrates the ΔP change at each probe for each fire size where graphs are arranged by fan speed (v1, v2, v3) and give a qualitative view of how the pressure readings change over the length of the flame. At each of these cross flow strengths a certain average flame tilt angle is achieved (this is analysed in more detail in chapter 5.8.3). The general trend immediately apparent is that ΔP measurements at each probe increase with increasing Q. What we will see in chapter

5.8.3 is that increasing Q also decreases the degree of flame tilt apparent. That is to say that flame tilt increases with increasing fan speed v, and decreases with increasing fire size Q. The summary points above are more clearly apparent in figure 5.31:

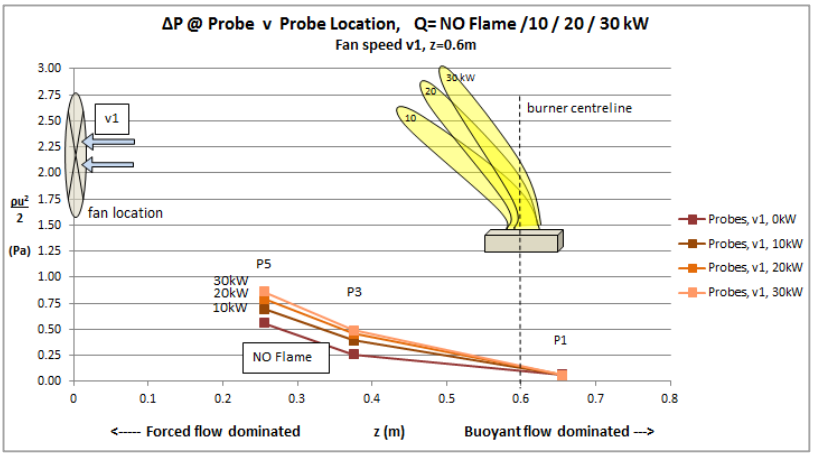

(a)

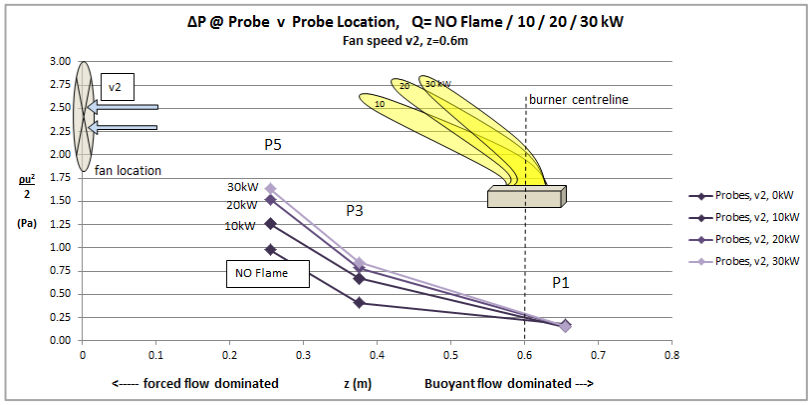

(b)

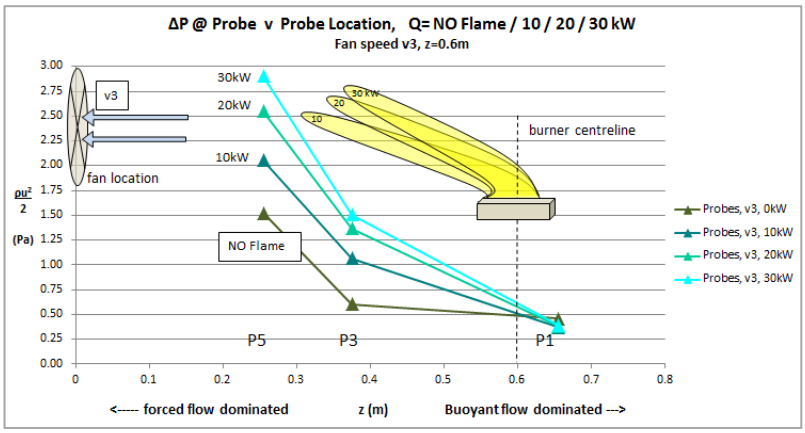

(c)

Figure 5.31: ΔP at each probe location as fire sizes are increased for each fan speed. Probe data are plotted in reference to burner location (fire images are NTS).

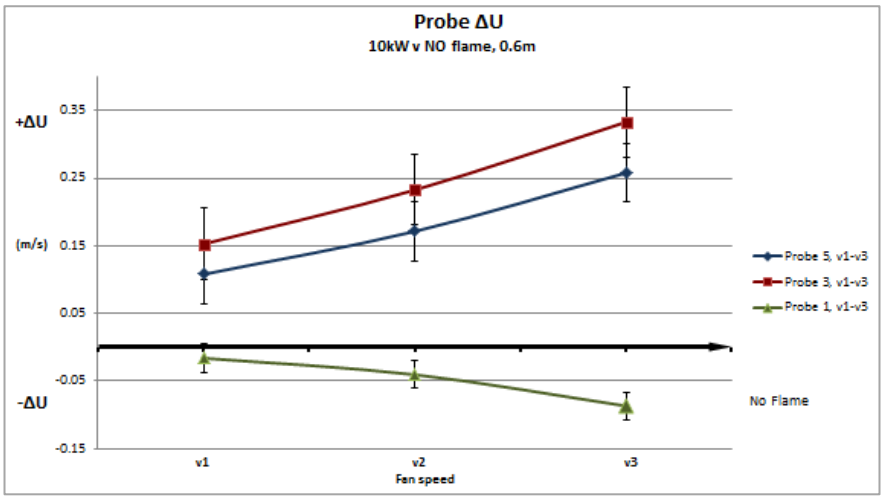

(a)

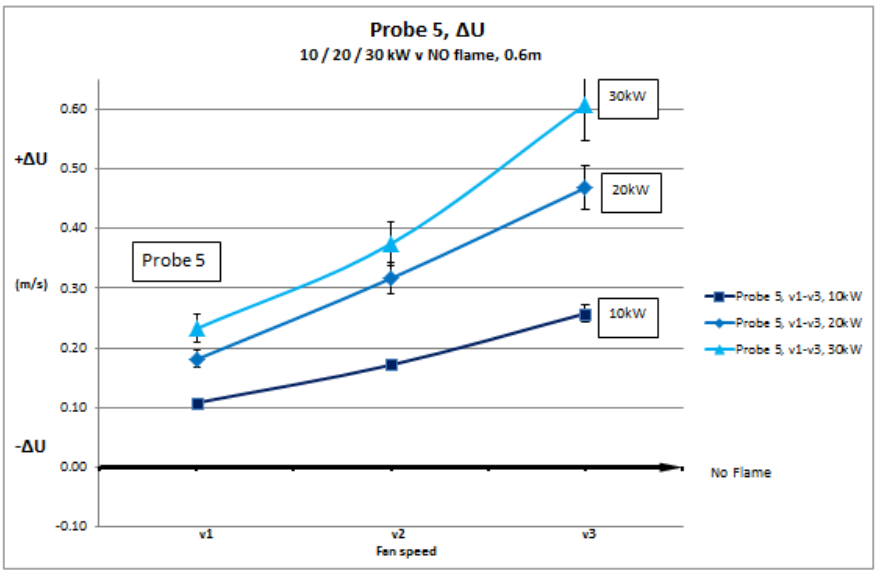

(b)

Figure 5.32 (a) shows change in local velocity, u, at each probe for the initial 10kW fire case as fan speed is increased. For this figure only the cases where z′ = 0.6m are presented here. Results for z′ = 0.8/1.0m demonstrate similar trends. To keep the current discussion concise, further comparative analysis is presented in Appendix C. As noted previously, probe 3 demonstrates the greatest ΔP increase and this increase appears to grow slightly as fan speed is increased. This is most likely due to the changing location of the flame in relation to probe 3 as fan speed is increased and flame tilt becomes more pronounced. This will be discussed in more detail over the following pages.

Figure 5.32 (b, c, and d) demonstrate the Δu at each probe (5, 3, 1) individually across each increasing fire size and as fan speed is increased in each case. Velocity measurements generally, are higher across each fire size and indeed, increase as fire

size increases. This holds true for probe 1 at the leading edge of the burner which is somewhat sheltered from the fan flow by the flame, and both probes 3 and 5 on the rear side of the flame, which are directly exposed to the fan flow. An exception to this trend is at probe 5 when Q is increased to 30kW for fan speeds v2 and v3, although the fact is much more pronounced at v3. In this case velocity measurements at probe 5, on average, are greater than at probe 3.

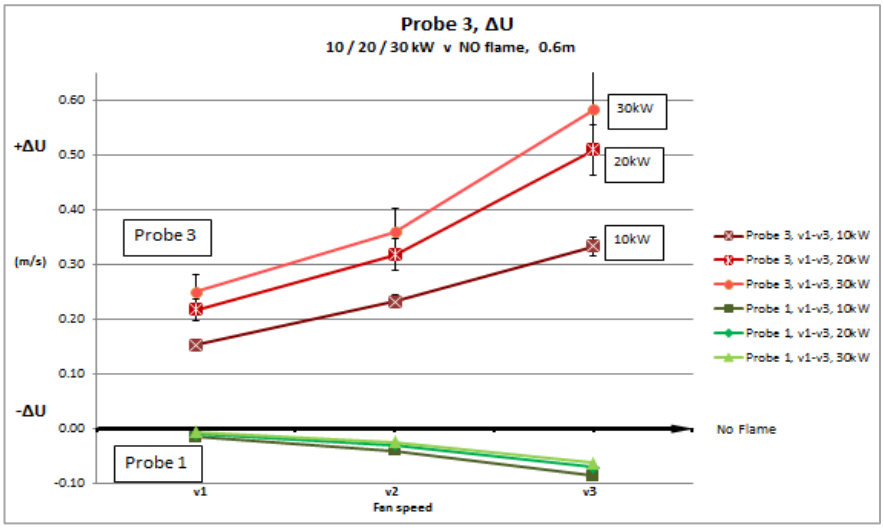

(c)

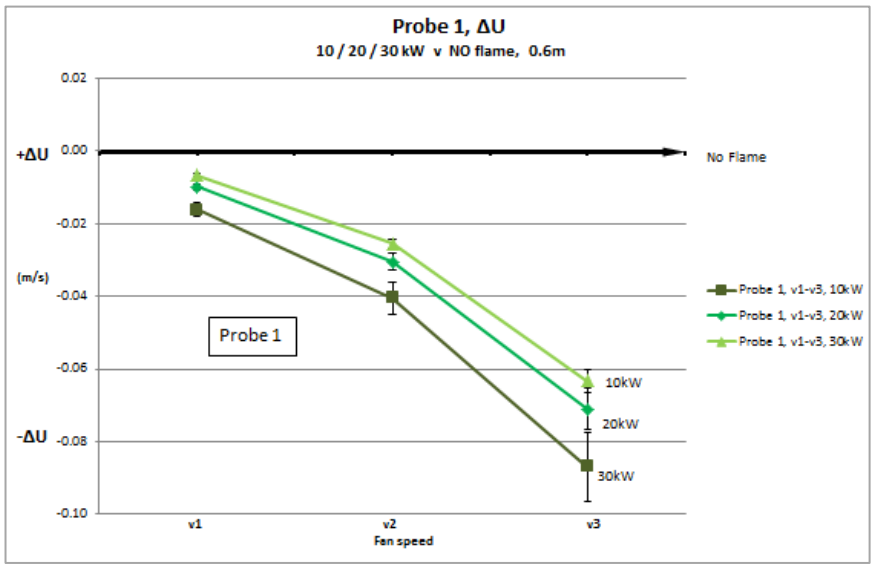

(d)

Figure 5.32: Demonstrates the change in velcoity (Δu) for cases where z' = 0.6m. (a) displays data for each probe (1, 3, 5) for the 10kW case, and (b), (c) and (d) show the Δu at probes 5, 3 and 1 respectively for the three fire sizes 10, 20, 30kW.

It is no coincidence that this exception occurs when the fire size and fan speed variables are at their greatest magnitudes within the experiment boundary conditions. It is intuitive to consider that the increase in the physical flame size (manifested in an increasing flame length with incresing Q), also increases the length over which the split cross flow rejoins at the rear of the flame. When the flame is large enough and is tilted far enough, this turbulent region extends further than before and subsequently involves probe 5 enhancing the increase in velocity measurement recorded at the probe.

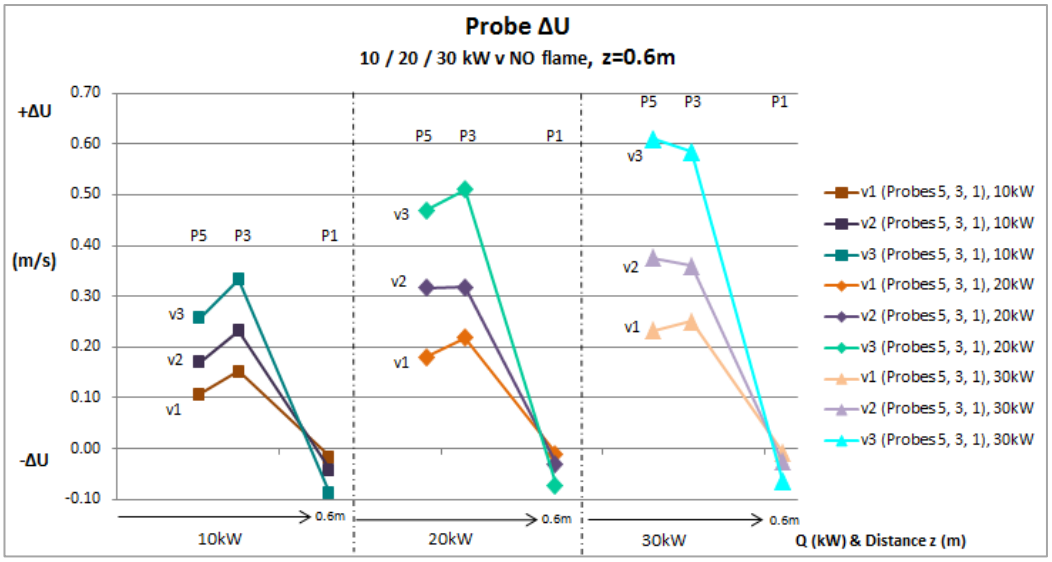

Figure 5.33: Change in velocity at each probe for each fire size and fan speed

Figure 5.33 highlights the trend at probe 1 (decrease in local velocity against the NO flame case – decrease more pronounced with increasinng fan speed) is exhibited across the increased Q cases. The magnitude of the decrease in each instance however can be seen to lessen as Q is increased. The fan speed (and resultant cross flow inertia) is never great enough to tilt the flame so that it is completely horizontal and to such an extent that it no longer acts as some measure of obstruction to the fan-induced cross flow. That is to say that across each Q case and at each fan speed the result is consistently a reduction in local velocity at probe 1 against the NO flame case. As noted however, with increasing Q the magnitude of the reduction in

velocity at probe 1 against the NO flame case reduces [-0.085m/s at Q=10kW vs -0.06 at Q=30kW]. This suggests that if the fire size was increased further, eventually there may be no reduction in local velocity at probe 1 after introducing the fire into the free cross flow. This premise requires a large buoyant force (large fire) in relation to cross flow strength, where the natural inflow created by the large fire is at least equal to the free cross flow in the NO flame case. What this trend does highlight is the increasing magnitude of the natural fire inflow as a result of the increase in fire size and therefore buoyant force. The larger fire attempts to draw air in from 360 degrees at a greater rate than the smaller fire sizes which appears to offset the reduction in cross flow velocity at probe 1 as a result of the flame acting as a blockage to the fan flow. This proposition of this mechanism is supported by consideration of the fact that a larger, more buoyant flame should in theory act as more of a blockage to the cross flow and if we were unaware of the natural fire flow created by the buoyant flame, one might expect the local velocity at probe 1 to reduce further as Q is increased.

Figure 5.34 demonstrates the variation in velocity (ΔU) at each probe across a scaled interpretation of the experiment extents (that is ΔU plotted against probe location relative to the burner – flame images indicative only). The shift toward greater ΔU at probe 5 in the case of Q=30kW / fan speed =v3, can perhaps be more clearly appreciated in this figure (ii-iii) where the dip in the trendline approaching P5 flattens out and the gradient changes so that in the case noted (Q=30kW @ v3) the greater ΔU at probe 5 is clearly evident. We can also appreciate that the case Q=30kW and fan speed v2 also tends toward this result. The combination of largest Q and medium fan speed v2 is enough to extend the rejoining zone so that the difference in magnitude of ΔU at probes 3 and 5 is reduced somewhat, however the magnitude of the buoyant force here keeps the zone from extending fully as far as probe 5. Increasing fan speed to v3 decreases the relative buoyant force (by increasing horizontal inertia) thus further involving probe 5 and extending the rejoining zone further down stream from the flame base.

This case is not fully buoyant since we can see that the relative magnitude of the cross flow inertia has a direct impact upon the fluid behaviour at and around the flame and correspondingly with the increase in the experimental mass flow rate. We can however, draw a comparison with the fully buoyant case whereby an increase to Q in the fully buoyant case results in an increased entrainment rate due to greater fire size and thus greater buoyant flow ΔP in the upward direction. This in turn generates an increased rate of air being entrained through the edges of the fire and plume. By increasing Q in the tilted, not- fully buoyant cases we can infer that not only is the in-flow velocity increased around the plume, bu the turbulent rejoining area is extended further from the flame base which appears to enhance mixing and subsequently, will be demonstrated in section 5 to correlate with increasing experimental mass flow rate.

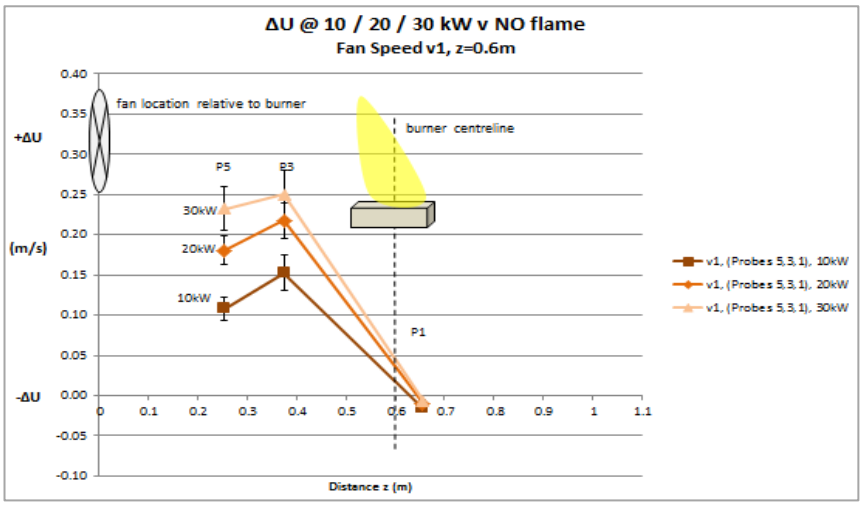

(a)

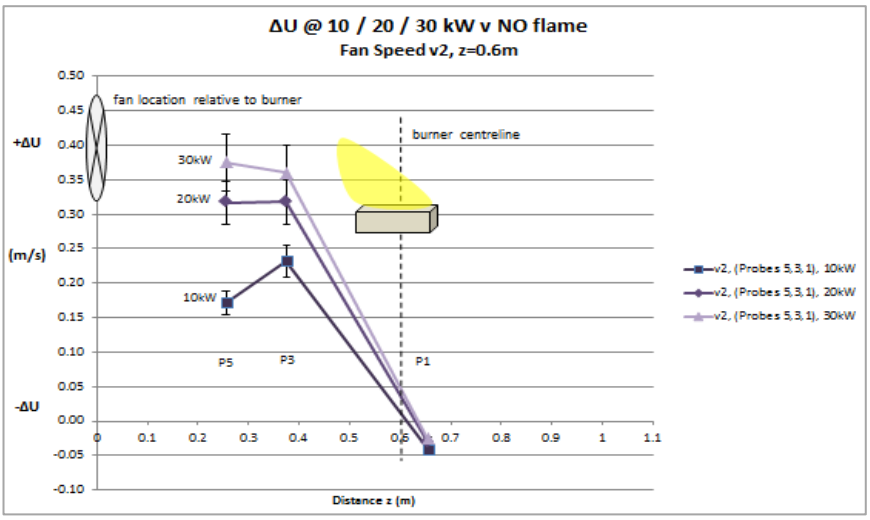

(b)

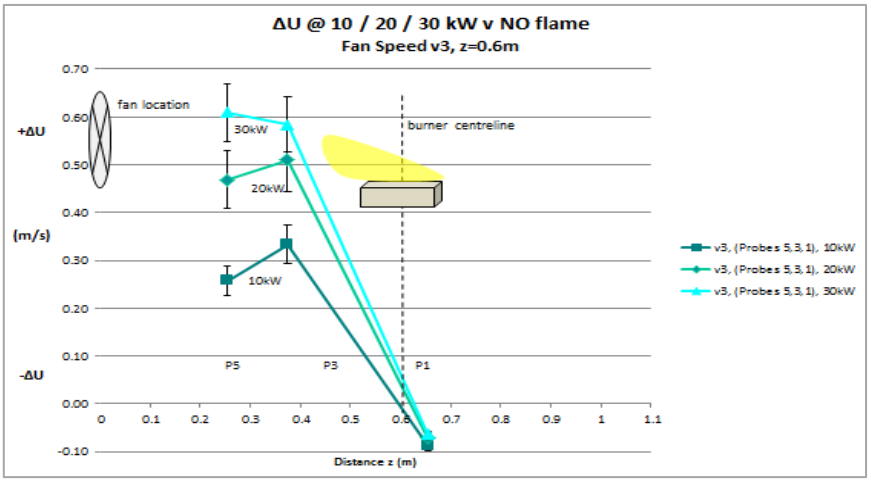

(c)

Figure 5.34: Change in velocity (ΔU) at each probe across a scaled interpretation of the experiment extents, (a) v1, (b) v2 and (c) v3. Flame images are NTS.

5.7 Cases of Increased Entrainment Distance, z' = 0.6/0.8/1.0m

Now that we have looked at flow characteristics around the flame in terms of probe location relative to the flame, and considered the effect of increasing the buoyant force by increasing Q over the set range of cross flow strengths (with the flame a set distance from the fan (z)), it is now desirable to consider the data following a variation of the flame distance from the fan. By increasing z', we are in theory increasing the entrainment distance or "height" z, as imagined through the premise of the ideal plume, however what we are literally doing here is decreasing the impact of the cross flow on the buoyant plume for each set fan speed since ΔP_f, as previously discussed, reduces with increasing distance from the fan. This can be thought of as the similar to the effects of increasing fire size as outlined in the previous chapter 5.6. A short chapter investigating the impact of pressure and velocity change at each probe is presented in Appendix C.

5.8 Mixed Flow Gr/Re^2 Analysis

5.8.1 Context & Discussion

The *relative strength* of the cross flow inertia versus the buoyant force has been referenced heavily throughout the previous sections, and will continue to be referred to throughout the following sections and the discussion about experimental results. In attempting to characterise the behaviour of fluid flow in and around the flame and fire plume for each experimental case, it has been well established that the addition of an induced cross flow to an isolated flame results in a complex set of flow behaviours around the flame which are not included in any of the current fire plume entrainment literature. In fact the only place we can find detailed discussion of the impact of these separate forces in relation to plumes of any kind is in work such as [18] when studying large atmospheric plumes, like those from industrial chimneys and in small scale analyses such as [20, 24]. There are numerous reasons why, despite being informative, the atmospheric plume studies are not applicable to the study of the fire plume for modern infrastructure fire safety engineering. Such non-reactive plumes are generally studied over a much larger scale, often several miles down wind, and upward into the atmosphere. The fire plume presents a fundamentally different paradigm since a relatively large portion of the vertical axis-symmetric fire plume (depending upon the height of the room) is filled by the flaming region, which is comparatively very hot and buoyant, acting as a pump to constantly power the entire fire plume mechanism. There is an argument to be made that farther downstream (several orders of magnitude considering the physical flame size), the smoke plume that results from the fire might be somewhat well described by the atmospheric plume treatment, however since the focus for this study incorporates the "fire" itself, we must find a way to describe and resolve the battle between the cross flow inertia and the strongly buoyant flame and quantify the result. Chapter 2.11 introduced the concept of the Richardson number:

$$\mathrm{Ri} = {}^{Gr}/_{Re^2}$$

Equation 5-7

By using this approach we can ascertain an order of magnitude description of the relative importance of the individual buoyant and inertial flows when these adjacent forces meet over the length of the flame.

The Grashof number is traditionally given by:

$$Gr = \frac{g\beta\Delta T L^3}{\upsilon^2}$$

Equation 5-8

This correlation is driven by both the absolute temperature difference of the fluid in question as well as the length over which the analysis of the force is applicable. For this equation to be suitable it is preferable to have a well-defined change in temperature between each calculation of the Grashof number, or in practical terms, a well-defined temperature difference in each case of increased fire size.

In each case of increased Q, the result is a larger flame volume (and surface area) since the fuel injection rate is increased and the distance over which combustion occurs is elongated as the increased fuel mass requires an equal measure of O_2 for combustion. The larger hot core of the 20kW and 30kW flames is still surrounded by layers of zones of decreasing temperature so the percentage increase in temperature *in relation to the volume of entire flame* varies only slightly. This makes assigning an [increasing] average flame temperature to each increased Q flame difficult and gives an inadequate description of the change in boundaries conditions.

A better articulation then of the increase in buoyant force of each manipulation of Q is to incorporate Q itself, the energy release rate, into the Grashof derivation and substituting temperature variation out.

The heat release rate can be described by:

$$\dot{Q} = \rho A u c_p \Delta T$$

Equation 5-8(a)

Where ρAu gives mass flow (by flow mass density, area and velocity) by with the product of specific heat capacity and temperature difference gives a description of $\dot{Q}$. Rearranging for ΔT:

$$\Delta T = \frac{\dot{Q}}{\rho A u c_p}$$

Equation 5-8(b)

Expanding and multiplying out for area and velocity, and introducing the $sin\theta$ component to account for buoyant vector related to flame tilt gives:

$$Gr = \frac{\dot{Q}_c}{\rho c_p v}\left(\frac{L}{D}\right)^3 . sin\theta$$

Equation 5-9

Equation 5-9 allows the full extent of the increase in energy release rate to be accounted for in the Grashof description. A unique Grashof number will be calculated for each fire size and Gr/Re^2 will be calculated at each pressure probe location.

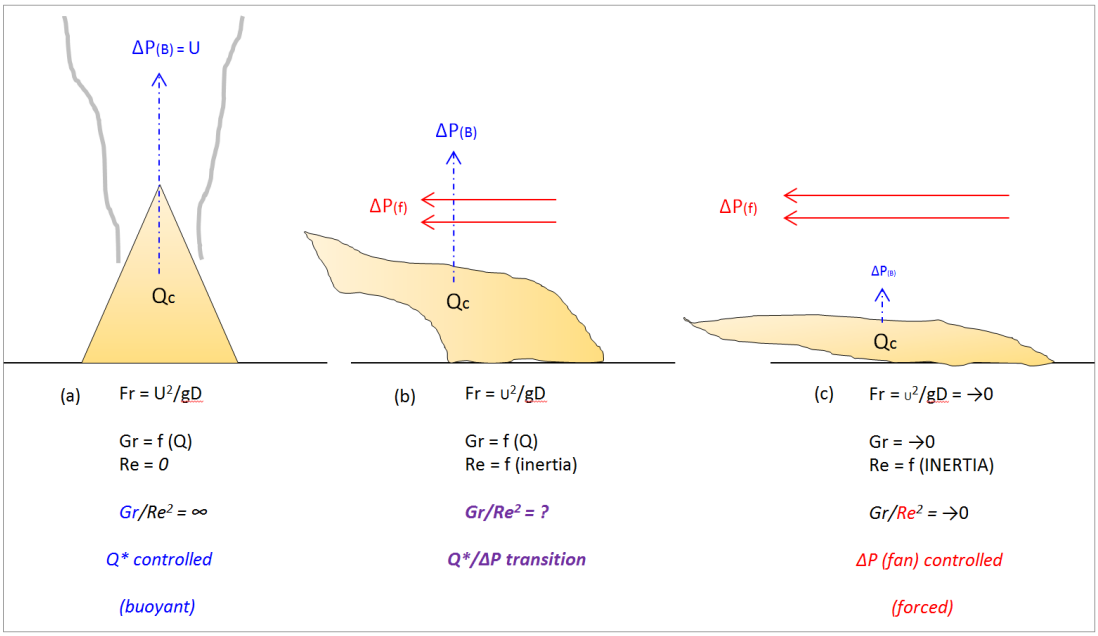

Figure 5.35: Progression from fully buoyant plume (a) to inertia dominated flame (c). The mixed flow case (b) requires an assessment of the balance of buoyant and inertia forces.

Figure 5.35 gives an overview of the different flow regimes inherent in the *fire plume with an increasing cross flow component*. In (a) the fully buoyant case no cross flow is applied. In fact the natural fire flow draws air in from 360° around the plume, equally from all directions, so there is no residual force with any horizontal propagation and the flame and plume is well described as axis-symmetric. For this reason the Reynolds number in this case is 0, or is not applicable and the simplified approach to modelling this plume is a Froude approach. In this Froude balance gravity (g) is tied to the magnitude and propagation of the upward force and the dimension of interest is the diameter (D) of the flame base. Since this case has no cross flow Re is zero and $Ri=Gr/Re^2$ is not applicable. At the other end of the scale the fully tilted case (c) shows a cross flow of magnitude so great that the flame is fully tilted to approximately 90° and the vertical component of the effective buoyant force is essentially zero. At the very small scale buoyancy will persist (otherwise the entire flame volume would stick to the ground) but within the context of the scale of interest here, the buoyant force would be considered to approach zero and the Froude approach is no longer of use. Conversely the cross flow inertia in this case is large and the Gr/Re^2 ratio is, again, not appropriate. Re is calculated with respect to the inertial (fan-induced) flow, measured from the leading edge of the burner downstream, to each lateral probe location.

Case (b) represents the mixed flow case where buoyancy and cross flow inertia are of comparable magnitude and demonstrates the case of interest in this work. In chapter 6.1 an analysis of the experimental mass flow rates, the design mass flow rates, experimental velocity readings and design velocity readings will be used to show which cases can be separated into the 3 categories defined here and those that fall into category (b) the mixed case offer the opportunity for further direct analysis.

In case (b) the Froude approach is applicable but only for a first iteration of the vertical buoyant force. Once the cross flow inertia is added the relative strength of the combined adjacent pressure differentials determines the cumulative effect and

the resultant flow characteristics. For the varying iterations of the mixed case the Gr/Re^2 ratio can be applied and will describe the relative importance of each force over three lengths of interest (bounded by the burner leading edge and each probe location) each mixed case, as demonstrated in figure 5.36. The distance (L) for probe 1 is a nominal distance chosen to represent a length scale which describes the location of the leading edge of the burner. Subsequently the distance (L) corresponding to probes 3 and 5 is also taken from the leading edge since the buoyant upward force theoretically begins at this location and it is important for the relative location of each probe to be taken from the same starting point so that the location of each probe relative to the other probes can be maintained across each calculated Grashof number.

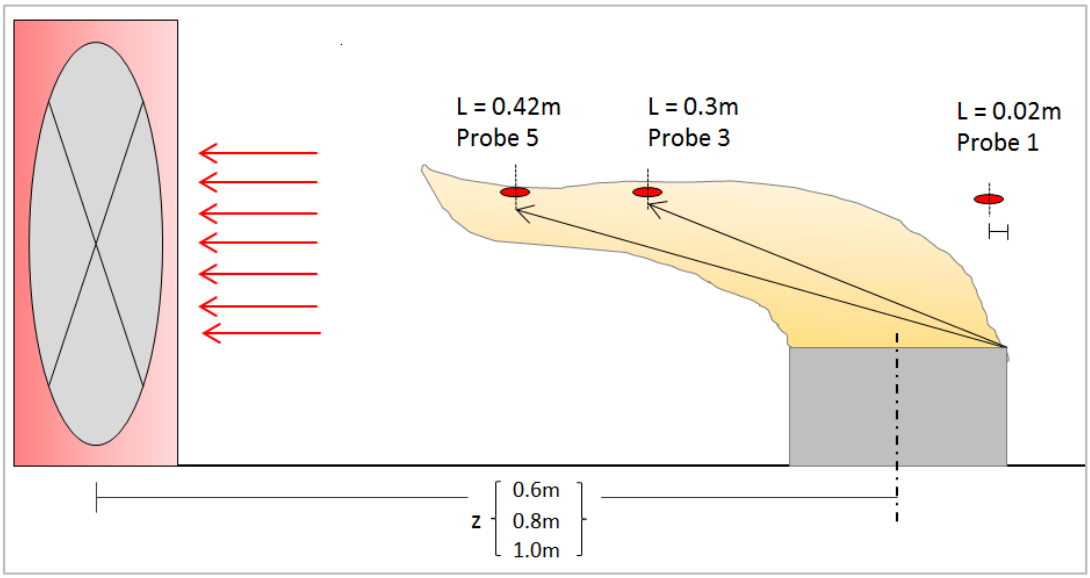

Figure 5.36: Length scales used in calculation of the Grashof number at each probe location are demonstrated. Probes 3 & 5 are measured from the leading edge of the burner, while probe 1 is measured laterally from the leading edge. Probes are located at same locations relative to the burner in each z case, where z is measured from flame centreline to the face of the fan.

5.8.2 An Appropriate Analysis

The Gr/Re^2 analysis is an effective approach to demonstrate the fundamental difference between the traditional axis-symmetric plume model and the mixed-case, where a quantifiable horizontal pressure differential is introduced. Since, for the Q*-

controlled, purely buoyant case the Gr/Re^2 number essentially approaches infinity, the Gr/Re^2 graphs which follow, and are intrinsic in describing the characteristic flow behaviour over the length of the tilted flame, are not possible for the traditional axis-symmetric case. This approach becomes applicable as soon as one is able to define that there is a small, disproportionate in-flow (ΔP) to the flame/ plume. In this circumstance the tilt of the flame may be very small; it may not even affect the entire flame length and specifically this phenomenon was highlighted briefly in [6]. This special mechanism is not the focus of this study and in chapter 6 it will be demonstrated that some of the cases studied in this experiment create these conditions and must be segregated. Since the physical deviation from the axis-symmetric model is quite discreet, the *marginally disproportionate in-flow* case may be better studied with the traditional, axis-symmetric experimental technique [6] where variation in entrainment results may be clearly apparent in the results.

Figure 5.37 shows the inertia and buoyant dominant portions of the wind-blown flame as demonstrated by [24]. Since then, across the length of the flame/ plume both inertia and buoyantly dominant regimes can exist awareness of this is required in order to study the additional impact of the cross flow ΔP with respect to the axis-symmetric case. Since the entrainment mechanism of the purely buoyant fire is relatively well-defined and has been simplified to give quick engineering calculations, and agreement of the results of which with experimental work has previously been demonstrated in the major entrainment literature, it is necessary to attempt to exclude the results data which can be attributed to the buoyancy-dominated region in the mixed case, in far as possible, from the experimental output here.

This is achieved as demonstrated in figure 5.37. Figure 5.37 (a) and (b) are both representative of the outcomes from the experimental work here. Part (a) depicts the instance where the cross flow ΔP is not great enough to overcome the buoyant force over the entire flame length. Even though the cross flow ΔP increases in magnitude closer to the fan, the buoyant flame still rises along the angle which it is tilted to. At

some point along the flame length a great enough height is reaches by the hot gases and they essentially escape the fan flow, creating a sharp rise and a return to a buoyant regime, tending strongly back toward the axis-symmetric entrainment paradigm. By assessing the parameters of each experimental case it will be shown in chapter 6 that this transition from inertia to buoyancy-dominant regimes correlates with a breakdown in the experimental calculation of an increased mass flow rate [against the axis-symmetric case] and an explanation will be given.

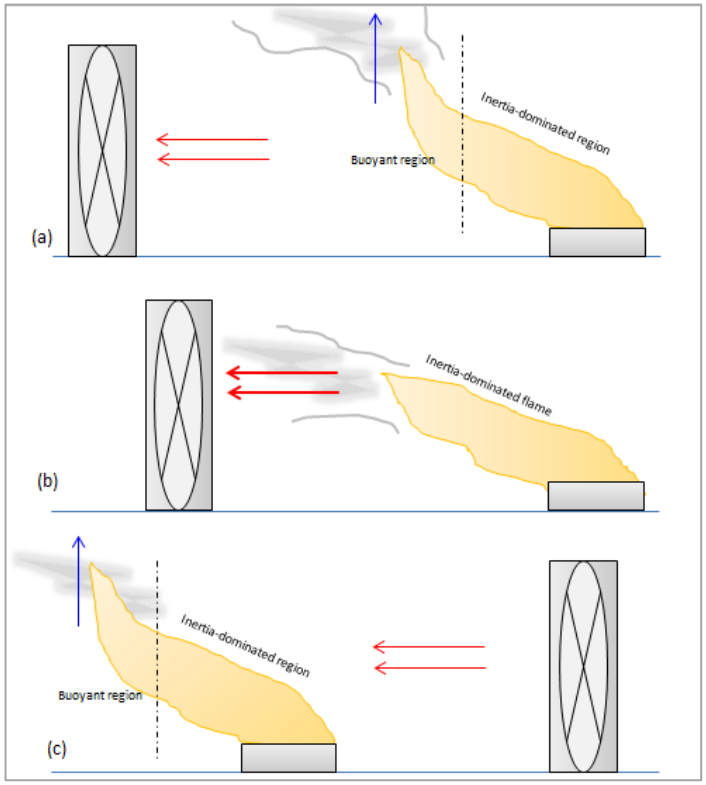

Figure 5.37: Examples of flames demonstrating (a) inertia and buoyant-dominated regions with an aspirated cross flow source, (b) inertia-dominated flame and (c) inertia/buoyant regions where the cross flow is blown rather than aspirated.

Therefore, of greater interest for this work is the inertia-dominant flame as depicted in figure 5.37 (b). As described fully throughout the previous section, this case is achieved by either reducing the distance between fan and flame or increasing the fan speed in order to increase the cross flow pressure differential at the flame

relative to the natural buoyant force. In this way, we can study the balance of forces along the length of the flame when the axis-symmetric paradigm (purely-buoyant) is not applicable to the case and the entire flame is composed only of iterations of the inertia-dominated, tilted flame. It is then not necessary to have to differentiate between the two regimes in figure 5.37 (a) and the problem is simplified.

Briefly, figure 5.37 (c) shows an alternative experiment design in which the fan blows the cross flow across the flame. In this instance it is impossible to achieve a flame with no buoyant region since the cross flow strength decreases with distance from the fan and eventually the buoyant force recovers. In any case, a collection hood design (as per [6]) would be needed to collect the mass of hot gases which specifically requires a return to the buoyant regime in order to acquire a buoyant reservoir of smoke.

These experiments are designed to articulate the relative strength of the inertial and buoyant forces at various locations in and around a fire when the flame is significantly tilted so that a differentiation can be made. This analysis is important because even in the inertia-dominant portion of the flame the buoyant force still plays a major role and similarly in the buoyant-dominant portion of the flame, the cross flow inertia may still be a contributing factor.

5.8.3 Flame Tilt Angle

A more precise description of the Grashof number at any point in time requires that we establish the reduction in buoyant force of the hot gas as a result of the reduced gravitational vector directly involved with the flame fluid flow direction when the flame is tilted away from vertical. This requires that average flame angles are acquired for each of the 27 cases across all Q/z/fan speed variations. Average flame angle images were acquired following the methods described in chapter 3 and the images can be observed in figure 5.48, chapter 5.8.5. The average angles were thus acquired and are displayed in figure 5.38 for all 27 cases.

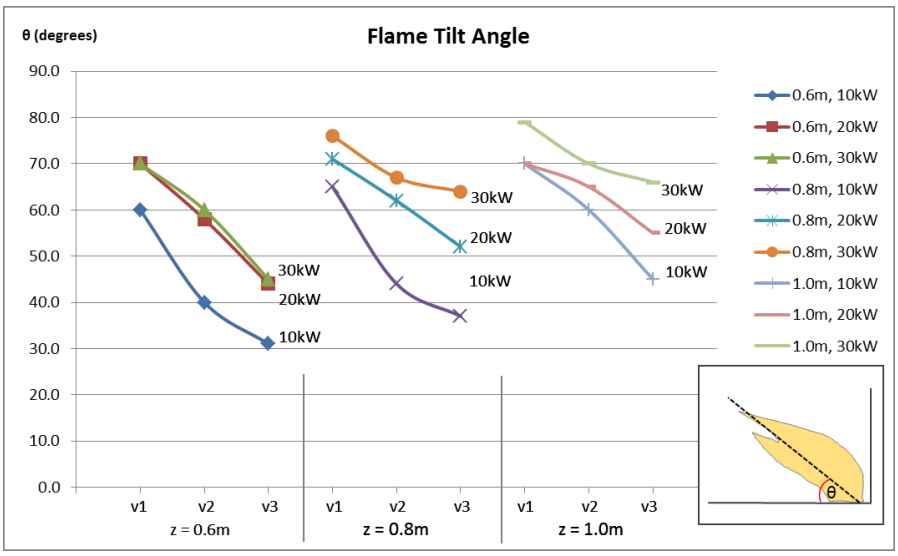

Figure 5.38: Average flame tilt angles for all 27 cases

The most obvious, and expected, trends that are displayed here are of increasingly tilted flames with each increasing fan speed and decreasing tilt when the HRR and increase in fan-flame distance, z, are increased. It can be noted that the trend in each case is variable and trend gradients are not shared from case to case. The possible exception to this is the 20kW and 30kW flames at z = 0.6m where the average flame angle values are almost identical at fan speeds v1 and v2, with only a few degrees tilt separating the data points at v2. This is most likely due to the increase in buoyant force of approximately 50% (20kW/(30kW-20kW)) not being sufficient to significantly overcome the fan-induced inertial cross flow at 0.6m, the closest fan-flame distance investigated. Note that there is significant decrease in tilt angle when the fire size is doubled (10kW→20kW) at z'=0.6m (a larger buoyancy increase relative to the cross flow inertia), and similarly the decrease in tilt is more pronounced at z'=0.8m when the fire size is doubled. The impact of varying fire size is noticeably different at z'=1.0m where the cross flow inertia strength is reduced further, compared to the buoyant force and the cross flow pressure decreases with distance from the fan.

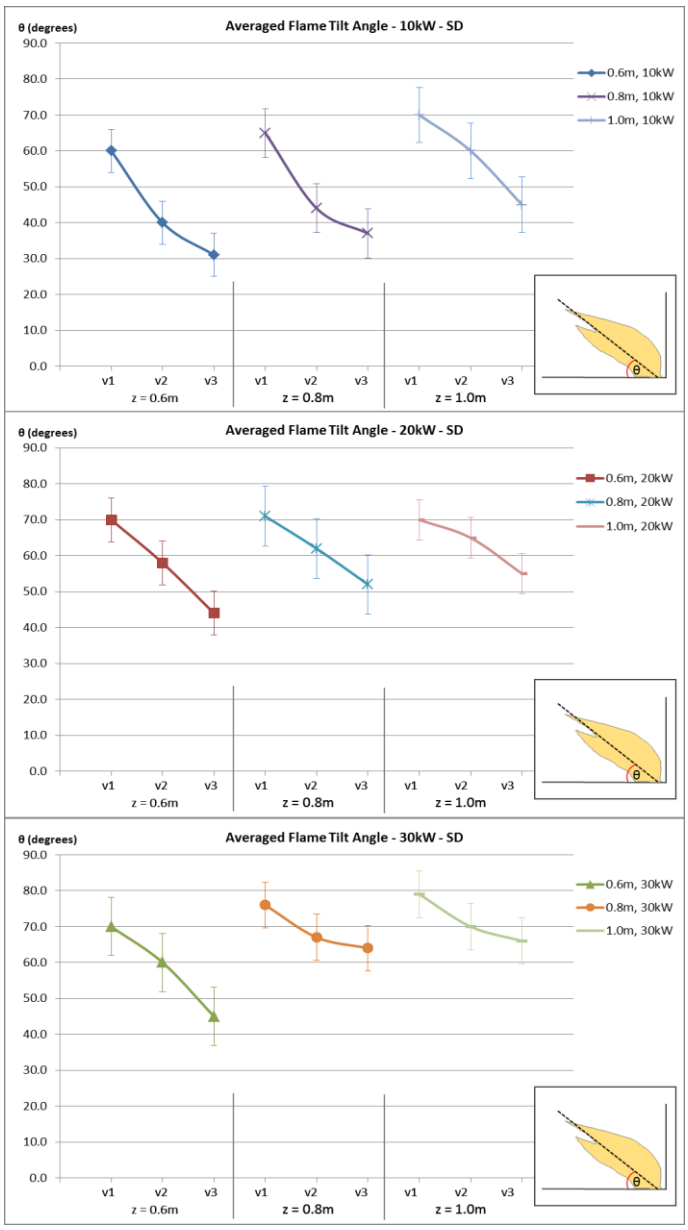

Figure 5.39: Standard deviation of averaged flame angles for each HRR at each distance z

In every case the flame was observed to become more erratic in movement and shape as the cross flow ΔP was increased as a more turbulent environment was created around and across the flame. This postulation is discussed in the following section and was also investigated with reference to flame flicker frequency in chapter 4. Figure 5.39 is important therefore because we can see that across the case-averaged standard deviation range for all averaged flame tilt angles that there is a

general commonality (range: 5.6 - 8.3, median 6.66 – mean 6.87) and no significant outlandish raw data were apparent. In literal terms this suggests that the similarity between 20/30kW cases at z = 0.6m is due to naturally chaotic turbulent flow behaviour and not an unexplained anomaly or undocumented / temporary perturbation of the controlled test conditions. In addition one method of estimating flame tilt angle form the literature was carried out and the results evaluated against the observed experimental data here. Drysdale [40] notes that the correlation developed by the American Gas Association was suggested as likely to be the most accurate of several flame tilt angle correlations developed in the literature, and is given as:

$$cos\theta = d'(u^*)^{e'}$$

Equation 5-10

where d' and e' are empirical constants pertaining to a range of fuels, θ is the tilt angle measured from vertical to the flame centreline and u^* is a dimensionless wind speed written as the ratio of the cross flow velocity (u_w m/s) and a characteristic buoyant velocity (u_c). It follows that u^* and u_c are given by:

$$u^* = u_w/u_c$$

Equation 5-11

$$u_c = (g\dot{m}''D/\rho_a)^{1/3}$$

Equation 5-12

where $\dot{m}$ is the mass burning rate (g/m² s) and D is the burner length (m). The use of the ratio of crossflow velocity to characteristic buoyant velocity for u^* however assumes that the crossflow velocity is the greater of the two and in the limiting case that the characteristic velocity is greater, it is then precluded that in equation 5-10 cosθ = 1 (therefore θ = zero) and the flame is assumed not to tilt. It has been noted in the literature that several plots of $cos\theta$ versus u^* (as components of equation 5-10) show increasing scatter as u^* tends toward unity, as the crossflow velocity decreases with respect to the buoyant velocity. Figure 5.40 shows clearly that equation 5-10 under-predicts the amount the flame is tilted by in almost every case (25 of 27) and

the cases represented by a smaller Gr^*/Re^2 number, the cases which tend toward a more forced-flow dominated regime appear to be better predicted in general. This trend may be evened out however if more data from a larger Gr^*/Re^2 number were gathered.

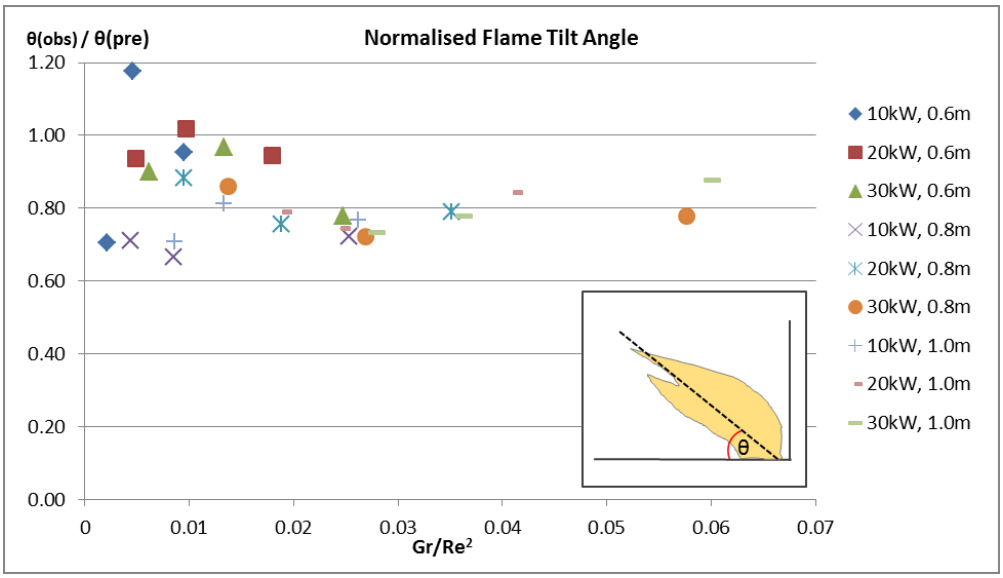

Figure 5.40: Measured flame tilt angle normalised by predicted tilt angle (equation 5-10)

5.8.3.1 Sensitivity to Empirical Flame Tilt Correlation

To this end, a brief analysis of the potential error occurring in the equation 5-10 as a result of the range of empirical constant variation was carried out. Figure 5.41 demonstrates the non-dimensional tilt angle as a function of the average of the range of empirical constants that are given in the literature. The average error was 7% and the size of the potential error appears generally to decrease with increasing Gr/Re^2 (increasingly buoyantly-dominated regime). This is interesting since, as noted previously, predictions made using equation 5-10 in the literature have been noticed to show less reliable results as the flame tends toward being buoyantly dominated.

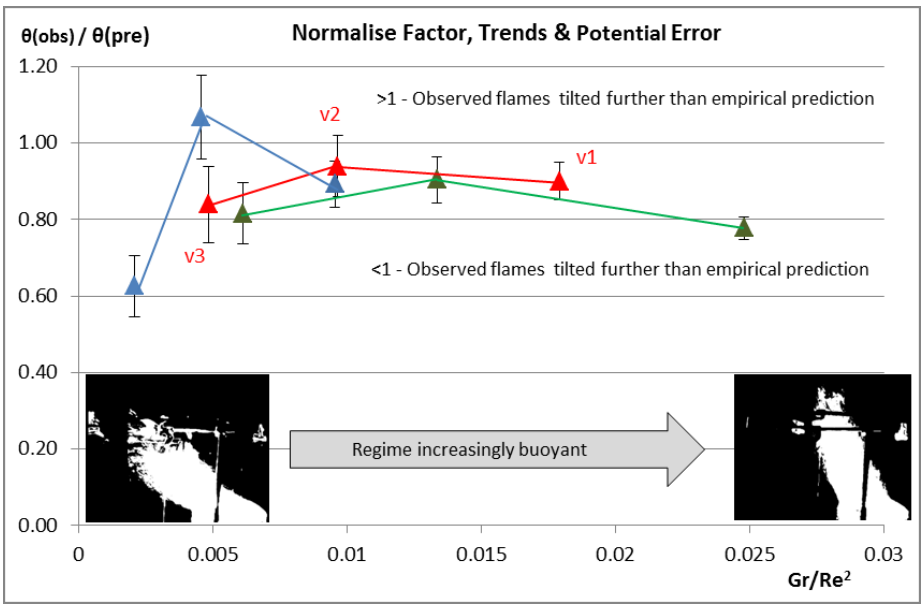

Figure 5.41: Range of error in normalised tilt angle (z=0.6m) as a function of the maximum and minimum value for empirical constants in equation 5-10 (predicted flame correlation).

Since these constants are given following experimental work involving hydrocarbon/LNG pool fires and solid (wood) fuelled fires there is already a question over the direct application of these data to the buoyant gas burner fires created in this work. Despite this of course, figure 5.40 demonstrated fairly acceptable results. Figure 5.41 data contains error bars to indicate the maximum and minimum normalised flame angles possible (utilising the full range of empirical constants for equation 5-10) and the data points themselves represent the average of this range.

It can also be observed that the tilt angle at fan speed = v2 is consistently under-predicted more than v1 and v3, as highlighted by the blue, red and green trend lines in figure 5.41. Finally it is notable that if the largest of the empirical constants of equation 5-10 is used (suggested for LNG fires) then of the 9 cases presented here, 6 are predicted to within 10% by the equation 5-10 correlation and 3 fall lie 10-25% out.

Previously (figure 5.40) we compared observed and predicted tilt angles against Gr^*/Re^2, which is the don-dimensional description of the buoyancy/forced-flow dominant range which is central to this work. The non-dimensional wind velocity u^*

(equation 5-11) is the parameter that plays a similar role in the equation 5-10 flame tilt correlation. In order to approximate the flame tilt angle it is then multiplied by, and raised to the power of, the empirical constants (d' and e') discussed above. It is of interest to note then that these comparable parameters appear to display an almost linear relationship (figure 5.42).

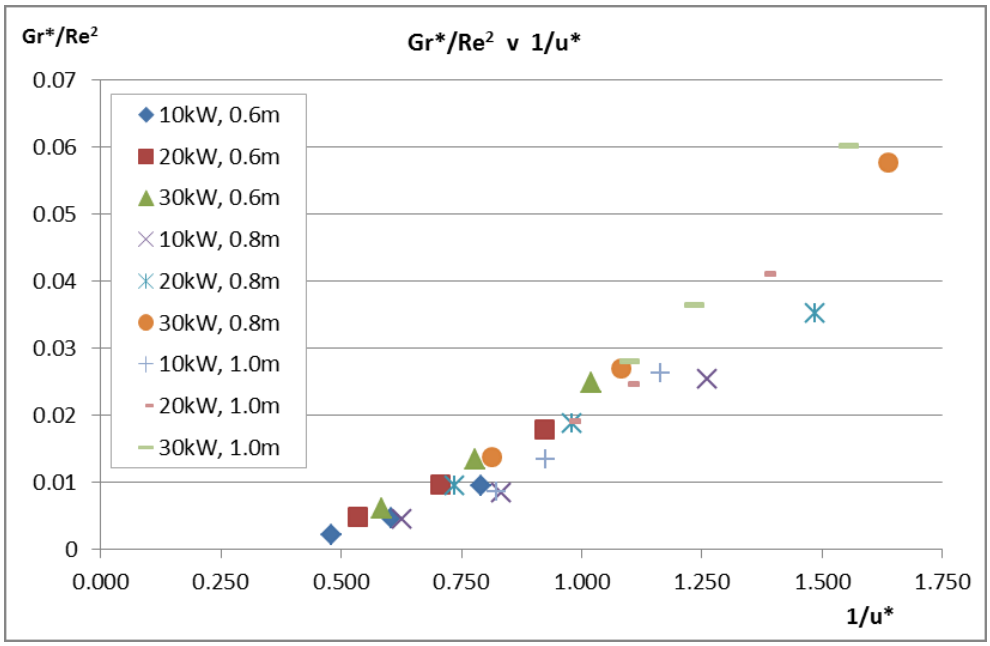

Figure 5.42(a): Gr^*/Re^2 plotted against the inverse of the non-dimensional wind velocity

5.8.4 Flame Length

Across all 27 experimental cases it was observed that only small changes in average flame length could be noticed. Even for the most inertia-dominated cases (10kW, 0.6m, v3) measurable decrease in flame length was small. The measurement of flame length was carried out using the techniques and cut-off thresholds as described in chapter 3.5. Figure 5.43 demonstrates the flame length measurements across all nine cases at z = 0.6m (Q=10/20/30kW x v1/v2/v3). For the no wind cases the flame lengths were consistently found to be essentially indistinguishable from the v1 cases.

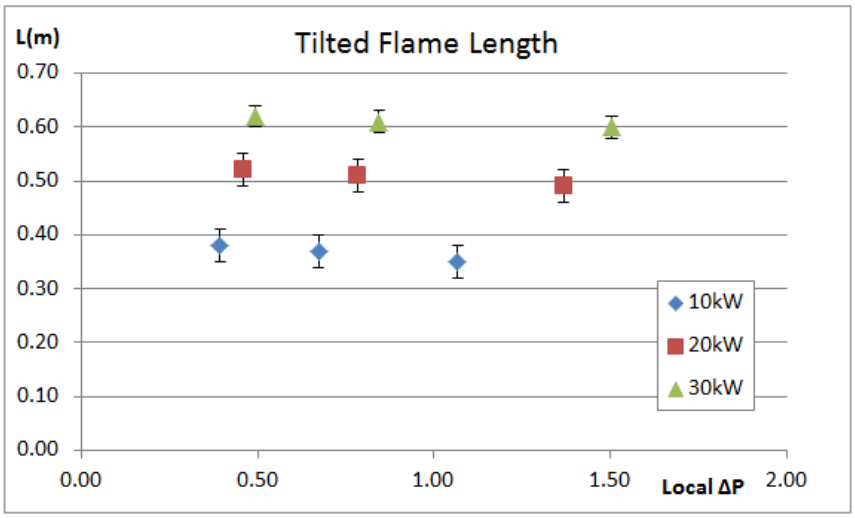

Figure 5.42(b): Tilted flame length v local ΔP (measured at probe 3) for 10/20/30kW fires at z = 0.6m.

It is clear form figure 5.42(b) that the measurable flame length reduction as the comparative crossflow strength is increased is very small and in each case the 'no wind' measured flame length is within the statistical error provided by the range of flame images studied. It is postulated that for these experiments the crossflow inertia was not great enough to create the obvious flame length reduction commonly discussed in literature. The discussion in chapter 4.1.4 highlights that flame flicker frequencies are somewhat perturbed as the crossflow inertia is increased, but that the birth of buoyant pulses culminating into rising vortices appears to continue at the same rate, relatively unaffected, especially very near the

flame base. Is it quite possible that the lack of flame length change witnessed in the experimental cases is due to the location of the fan and the fact that crossflow inertia pressure increases downstream along the flame length. Had the fan been located upstream of the flame the comparatively stronger crossflow inertia would interact at with the flame at the leading edge of the burner, perhaps delivering oxygen at this location more efficiently than in the experiment cases and thus creating an apparent shortening of the flame length.

As a further investigation, after the formal investigation cases, the fan was turned up to maximum flow rate and the images analysed in chapter 3 were recorded. During this case the crossflow velocity (at probe 3) was noted to be around 1.5 times the maximum noted in the most inertia-dominant experimental case (10kW, 0.6m, v3). This further increase resulted in the noticeably reduced flame lengths discussed in chapter 3. Given these outcomes, for the 27 formal experimental cases no clear relationship can be demonstrated between crossflow strength and flame length.

5.8.5 Gr/Re^2 Discussion

In order to fully appreciate the information provided by the application of the Gr/Re^2 equation it is necessary to describe both the buoyancy of the flame and the magnitude of the cross flow by their Grashof and Reynolds regimes respectively, before combining these attributes for the range of mixed-convection cases. Sections 4.8.5.1 and 4.8.5.2 consider how the Grashof number and the Reynolds number change as the experiment parameters are varied.

5.8.5.1 Grashof Number Description of the Buoyant Flow

Figure 5.43 demonstrates the variation in Grashof number across each case where Q and z are varied. The 3 starting points for the data lines along the x axis at y=0 represent the probe 1 location at the leading edge of the burner for z = 0.6m, 0.8m and 1.0m, as denoted along the top of the plot area. The x axis represents the distance from the fan and therefore each of the 3 data points on a single line represents probe 1, 3 and 5. What this graphs demonstrates therefore is the increase in Grashof number as:

1. L_P (the distance from burner leading edge to the probe) increases, noted by following the points along each ascending data line
2. HRR increases (blue to red to green data lines), and
3. As z (the distance from fan-flame) increases (0.6m, 0.8m, 1.0m).

Subsequently, some further trends are apparent here. The increase in Grashof number as fan speed is varied is less pronounced as z is increased. This is a further graphical representation of the concept discussed much earlier that the impact of the fan-induced ΔP decreases with distance from the fan. In fact, at z = 1.0m and Q = 30kW the Grashof number change is almost negligible, demonstrated by the lack of divergence of the green data lines to the top-right of the plot. Compare this to the greater divergence of the green data points at the upper-left side where z=0.6m and the fan-induced ΔP has a greater impact, tilting the flame further, which reduces the Grashof number (as fan speed is increased) by reducing the gravitational component relative to the propagation of the now-tilted flame.

What this means more generally is that for some of these cases the gravitational component which gives buoyancy to the flame and hot smoke is reduced such that it contributes significantly to the resulting smoke from the fire being fully evoked by the fan-induced ΔP and thus captured by the extraction fan, while at the other extreme, the flame is tilted only slightly and the reduction in the opposing flame flow gravitational component is minimal, such that the hot smoke is buoyant enough to overcome the fan-induced ΔP and escape upward, alluding the extraction fan. How each experiment case fits into this scale will be qualified in chapter 6.2.

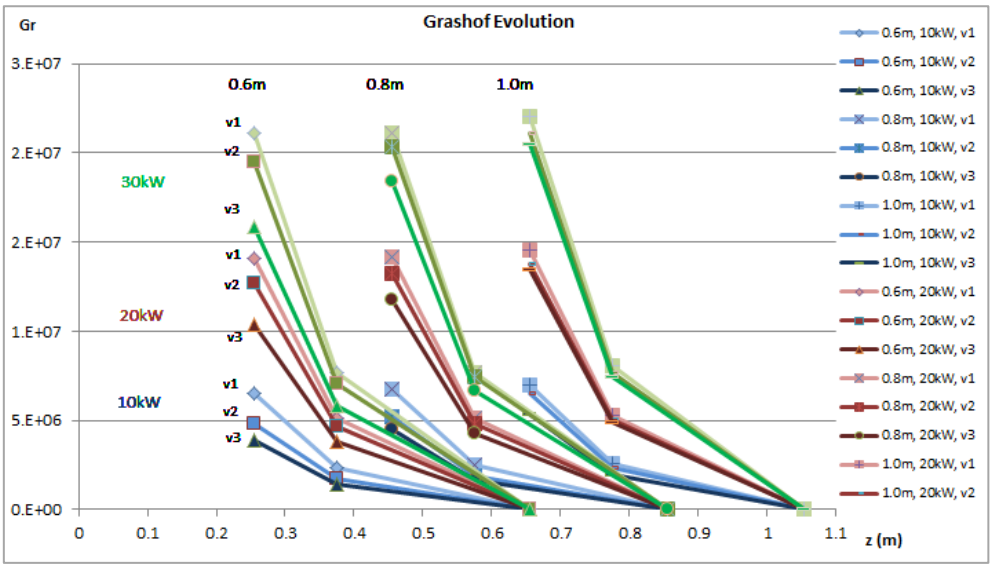

Figure 5.43: demonstrates the range of Grashof numbers as calculated at various locations along the length of the flame.

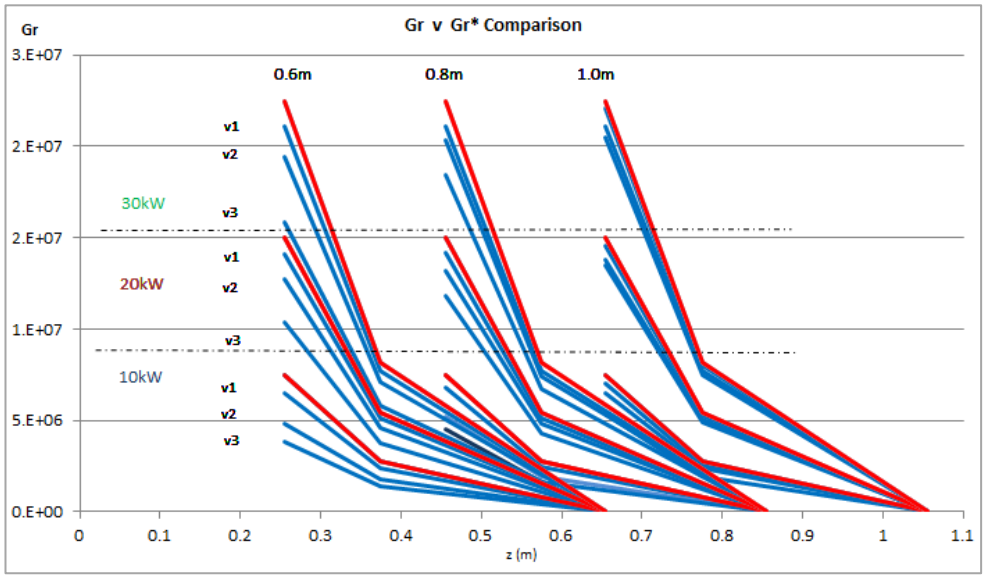

Figure 5.44: The data from figure 5.43 is displayed (blue) against the same data but when the reduction in the Grashof number *as a function of decrease in gravitational magnitude* (resulting from increasing flame tilt angles) is excluded (red) from the Grashof correlation.

In figure 5.44 each red data line represents the 3 blue data lines immediately below it if the reduction in Gr (and hence relative buoyancy) due to the increasing flame tilt angle

were to be excluded from the Grashof calculation. This is purely theoretical but the result is that this graph demonstrates clearly the reduction in buoyancy due specifically to the resultant impact of increasing cross flow ΔP (fan speed) in each case. A flame tilt of approximately 45°, for example, will reduce the gravitational magnitude on the flame propagation by around 30% (since *sin45 = 0.7*). Moreover, the increasing relative impact of the cross flow ΔP as z and HRR are reduced (aligning generally with an increasingly tilted flame) can be seen moving from the data of the upper-right corner to the lower-left corner of the graph as a greater deviation of blue data lines below each red data line is demonstrated. This is a clear visual representation of where along the spectrum of variables the buoyancy produced by the axis-symmetric flame is perturbed to the greatest extent. Clearly this aligns with the smallest z, the smallest HRR and the greatest cross flow ΔP, as represented by the bottom-left area of the graph.

$$Gr^* = \frac{\dot{Q}_c}{\rho c_p \upsilon}\left(\frac{L}{D}\right)^3 . sin\theta$$

(Equation 5-9)

The *Gr** correlation is reproduced here for convenience. It is important to note for this experiment that the parameters on the denominator do not change across experimental cases. That is to say that the buoyancy term $\varrho c_p V$ is not experimentally varied, and the dimension of the burner also remains constant. Given this, it is clear that our non-dimensional measure of *Gr** and its transition is essentially described by the product of the HRR and length scale, both of which are varied in each case. In this correlation Q represents the magnitude of the ΔP (in this convective case provided by buoyancy). We have established, the perturbation of the buoyant flow (ΔP_B) by the cross flow (ΔP_f) manifesting as the subsequently tilted flame, reduces the magnitude of the buoyant flow to some extent in every case, and thus $sin\theta$ is the third important term herein.

5.8.5.2 Reynolds Number Description of the Forced Flow

Just as *Gr* varies with each evolving case of *HRR* and cross flow ΔP_f the *Reynolds* number (Re) is also transitional across each experimental case. The Reynolds number is a common non-dimensional measure used in fluid dynamics to describe the ratio of velocity of a fluid (density x velocity x length scale) to fluid viscosity (v):

$$Re = \frac{\rho v l}{v}$$

Equation 5-13

Essentially we see the Reynolds number get larger as the length scale over which we evaluate is increased (distance from flame leading edge to each probe) and as local cross flow velocity measurements (ΔP) increase, since with increasing length scale and increasing velocity, viscosity in the fluid of observation becomes less important. Further, the increase of either of these parameters is representative of a step toward turbulent flow (or *more* turbulent flow) development. We can make the same observation here as with the *Gr* correlation whereby the (viscosity) term in the denominator is not considered to vary in any case. The same can be said of the density term in the nominator and thus again, the term directly representing ΔP in this correlation and the length scale of observation are the significant terms.

In figure 5.45 probes are numbered and are plotted to scale (where dotted line = burner centreline at z=0.6m/0.8m/1.0m, and x=0 represents the fan location) and fan speed settings are described in each legend. Figure 5.45 quite clearly demonstrates the increase in Re as measurement length scale is increase (moving from probe 1 to probes 3 and 5) and as velocity measurements at each probe increase. This velocity increase in each case is a function of a number of parameter manipulations including decreasing z (moving across data sets from right to left), increasing fan speed setting (blue to red to green, in the left-most data set, for example) and increased HRR. The direct impact of increasing HRR can be seen by comparing the

data across the 3 graphs where Re increases (particularly at probes 3 and 5) as larger HRRs result in slightly greater probe velocity measurements.

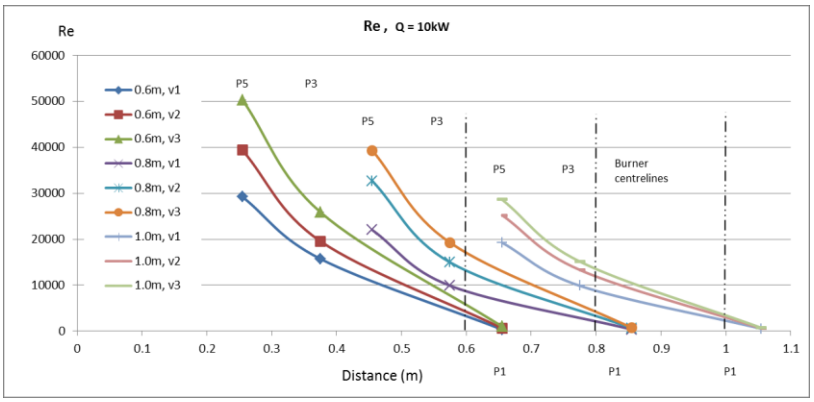

(a)

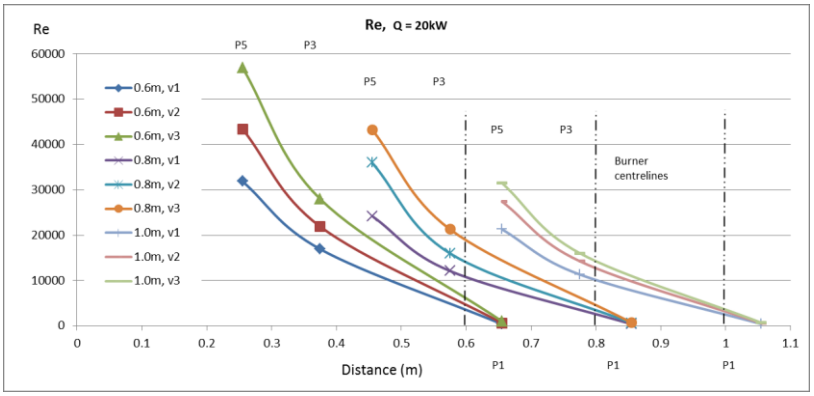

(b)

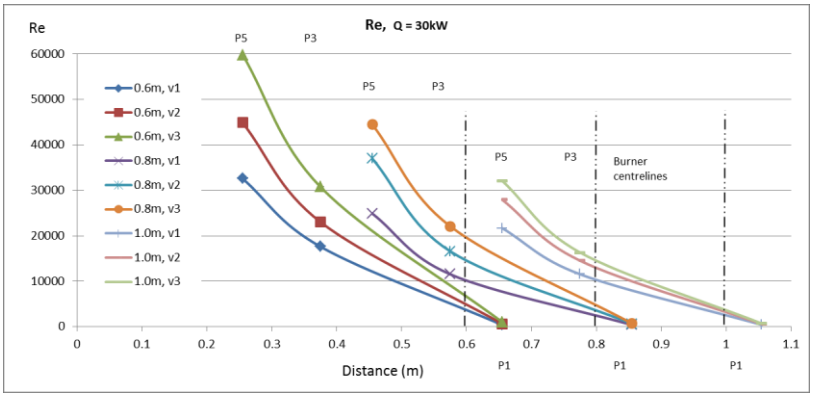

(c)

Figure 5.45: Increase in Re with increasing downstream distance (L along z') for z'=0.6/0.6/1.0m and 10/20/30kW (a-c respectively)

Re variation gradients across each parameter return similar trends, and the detail lies in the nuances of data variation, and the picture the data presents is quite repeatable across each of the experimental cases. This is similarly true with the *Gr*

data in the previous section. It is therefore convenient now to compare the relationship between both parameters over the experimental cases.

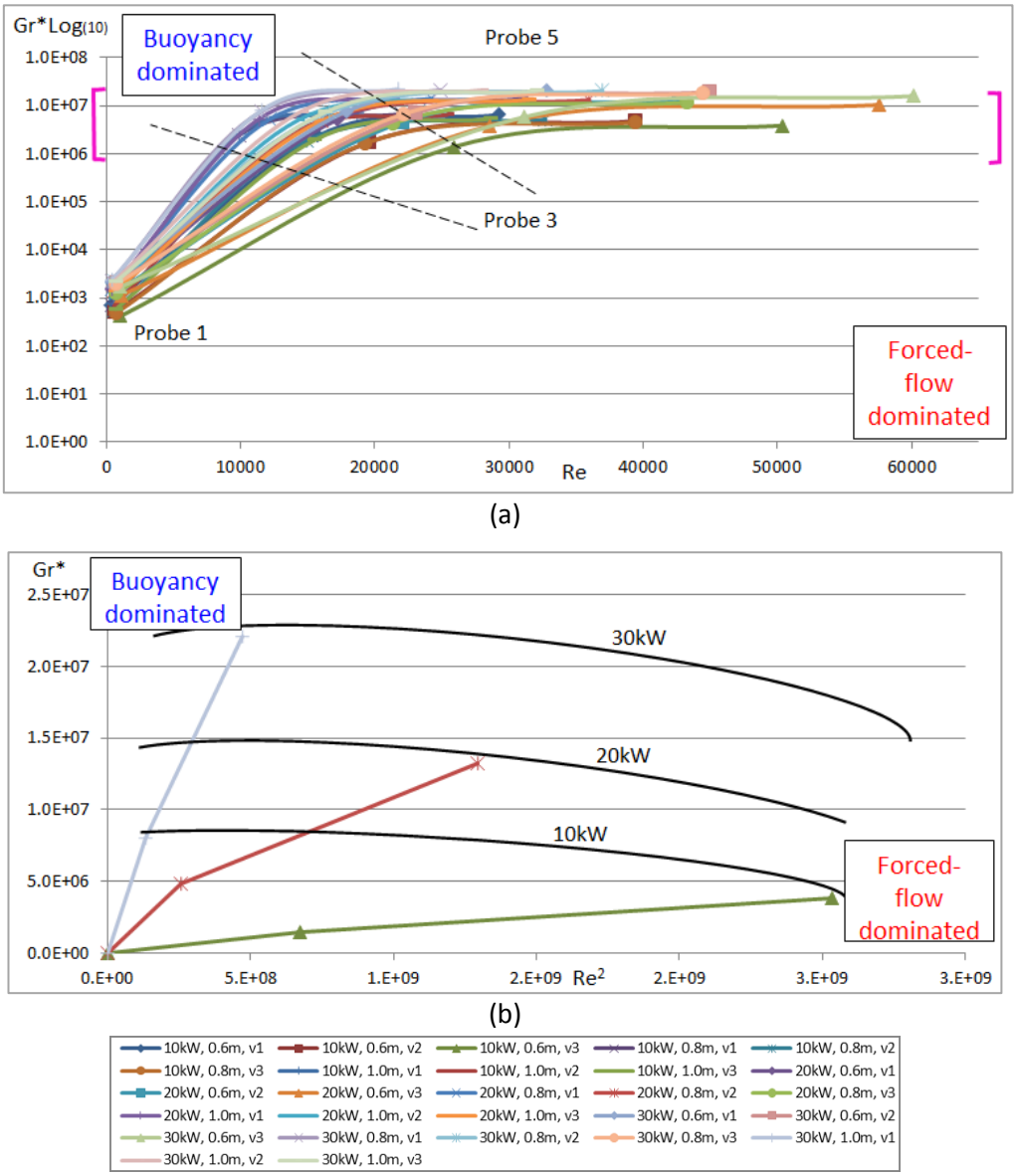

Figure 5.46: Gr* v Re for all cases where (a) Gr*Log(10) demonstrates the full range of Gr development (v1, v2, v3) and (b) zooming in (to the region y= $1x10^6$ through $2.6x10^7$) depicts the variation in data gradient (Gr^*/Re^2) for the region that appears to plateau for the extreme cases from part (a).

Figure 5.46 shows the relationship between Gr and Re variation across all the experimental cases. Part (a) uses a $\log_{(10)}$ scale in order to show the full extent of the Gr range which spans 3 to 4 orders of magnitude from the data at probe 1 to the

data at probe 3 (and can only been observed using a logarithmic scale). No log scale is taken on the Re (x-axis) in order to keep a scale that demonstrates the variation in Re through all the experimental cases. The data at probe 5 causes a clear plateau in all cases to occur after probe 3 (probe 3 data points are approximately located within the dotted lines just before the strong gradient drop-off). Graph (b) zooms in on the purple bracket region of graph (a) for the two extreme cases (most buoyant / most momentum-dominated and the midway case – only 3 cases have been shown for clarity on the graph) Part (b) more clearly demonstrates the relative increase in both the Gr and Re as the variables are manipulated toward the buoyant and inertia dominated cases. The 3 black lines (denoted (10, 20 and 30kW) demonstrate the upper bounds that would be apparent if the rest of the cases were plotted. These lines demonstrate the upper limits categorised by fire size, Q. In (a) it would appear that the trend is for the *Gr* to stop increasing after probes 3, however although from the frame of reference of the entire *Gr* range (a) a plateau occurs for all data lines, we can see in (b) that within this relative plateau, a larger *Gr* corresponds with increased *Q* and a greater initial buoyant force (ΔP_B). Subsequently, when *Q* is increased (where z and fan speed are fixed) flame tilt decreases reducing the significance of the term $sin\theta$ in equation the Gr/Re^2 ratio. These factors culminate in a slightly greater rate of increase of *Gr* at larger values of *Q*. These nuances are small of course when considered in the context of the 3-4 orders of magnitude increase that the *Gr* exhibits between probes 1 to 5.

Figure 5.47 is again a close-up of the purple bracket region of figure 5.46 however this time the *Gr* log scale is plotted. This allows us to see more clearly the three distinct plateaus corresponding to each value of *Q* and the 10/20/30kW titles are located approximately in line with each plateau on the graph.

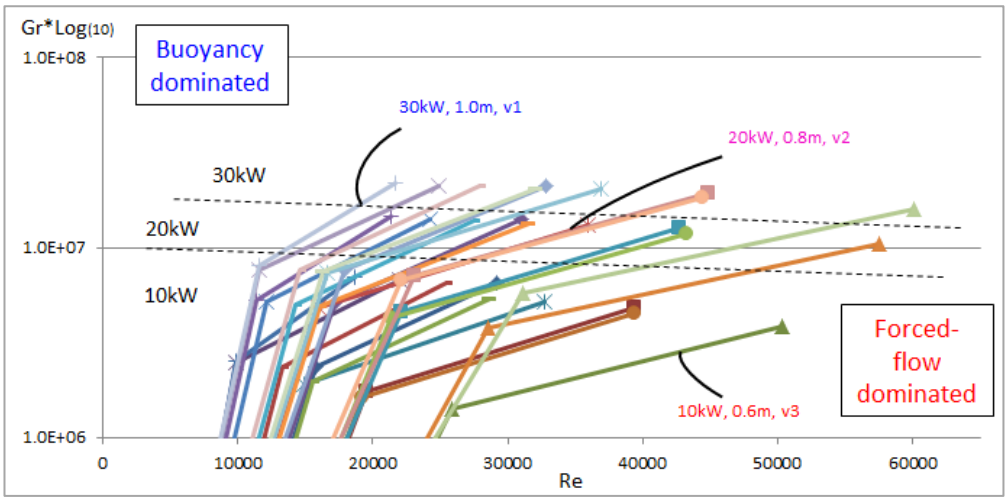

Figure 5.47: Gr* v Re for all cases (close up of figure 5.46) (a) separates the three Gr* plateaus for each fire size (10/20/30kW).

The importance of this graph is that it demonstrates that there is a limiting factor for *Gr* at each Q and in fact this limiting factor is the product of Q and observed length-scale L. Q carries much more significance however since for Gr calculation in these experiments the importance of L is several orders of magnitude less than that of Q. The black dotted lines delineate the limits for Gr at each fire size, Q.

5.8.6 A Gr/Re^2 Description of All Cases

We can now apply a non-dimensional parameter that describes the relative importance of the *Gr* and *Re* across all the experimental mixed-convection cases and as each variable is manipulated.

To this end, figure 5.48 demonstrates plots of Gr/Re^2 against probe location for 3 x *Q*, 3 x *z* and 3 x fan speed variables, 27 cases in all. Averaged flame angle images for each case accompany each graph and are located directly below. A description of the *general* trend of forced flow-dominated to buoyancy-dominated regimes is given by the red-blue trend arrows. These essentially highlight the increase in ΔP_B with increasing *z* and increasing *Q*. Average flame angle and shapes are derived in the procedure outlined in chapter 3.5.

In figure 5.48, each graph demonstrates the impact of the 3 fan speeds and therefore the ΔP_f in each case, differentiated by the blue, red and green data lines. Although fan speed settings (v1, v2 & v3) are identical for each case, ΔP_f recorded at each

probe location is of course dependent upon z as well. Nevertheless the basic principle that increasing ΔP_f for each case decreases the buoyant magnitude of the regime is signified as the data lines on each graph decrease in magnitude from v1 (blue) through v3 (green). Moving left to right across each row of 3 graphs follows the increase in z from 0.6m through 1.0m. This is illustrated graphically where data lines can be seen to increase in magnitude (increasing Gr^*/Re^2) from graph to graph. That is to say that the regime becomes more buoyantly-dominated as z is increased and relative ΔP_f magnitude across the flame reduces as a result. Similarly, moving from top to bottom down each column of 3 graphs demonstrates the increase in data line magnitude from graph to graph as a result of increasing Q from 10kW through 30kW. That is to say that the regime becomes less forced-flow dominated as Q is increased, since the net result is to increase the literal and relative ΔP_B.

All 27 cases presented here may be described as mixed-convection regimes since both natural convection from the fire flow (ΔP_B) and a forced cross flow (ΔP_f) contribute to the fluid flow characteristics of the fire plume, particularly so in and around the flame region. The repetitive trend observed across all data lines tells the story of the relative importance of ΔP_B and ΔP_f in each case and specifically, each data point represents this balance approximately at the location of the corresponding probe. The locations of each probe relative to the flame and to the fan have been outlined previously and to aid qualitative appreciation, the averaged flame images below each graph are sized so that the data points on the graphs correspond with the location directly below on each flame image. Probe 1 is therefore located at the leading edge of the flame (RHS), probe 5 is 0.42m from the burner centre (extreme LHS) and probe 3 is approximately midway (0.32m from burner centre). Probe 1 is distinguishable in nearly all the images, most clearly in the first 3 images. Some artefacts from probes 3 and 5 are present throughout the images. Across all cases 3 statements are true.

In each case:

- Probe 1 returns the smallest value of Gr^*/Re^2
- Probe 3 returns the largest value of Gr^*/Re^2, and
- Probe 5 returns a value for Gr^*/Re^2 somewhere between probes 3 and 5.

This means that ΔP_B is most significant in the region of probe 3, which is located in principle, on the windward side of the flame. Since the value of Q applies to the entire flame, and since the *average* flame shapes result in generally quite constant tilt angles along the entire length of each flame, brief consideration of equation 5-9 (Gr^*) confirms that the only term contributing to the *variation* in magnitude of Gr as defined at each probe in any one flame (at a fixed z), is the length scale (length of observation), which in the case of 5-9 is normalised by the diameter of the burner, all to the 3rd power, $(L/D)^3$. Therefore, Q and $sin\theta$ are constant in the calculation of Gr^* at each of the three probe locations for each individual case. For Gr^* calculation purposes the flame angle is assumed constant over the entire flame length, as per the average flame angle images. By comparison, in the calculation of Re (equation 5-13) both length of observation L, *and* velocity of cross flow, v (measured at each probe), are responsible for the increase or decrease in Re.

On the following pages, since figure 5-48 contains a lot of data, the 10kW, 20kW and 30kW cases have been reproduced in large font, to allow clearer reading of the information contained within.

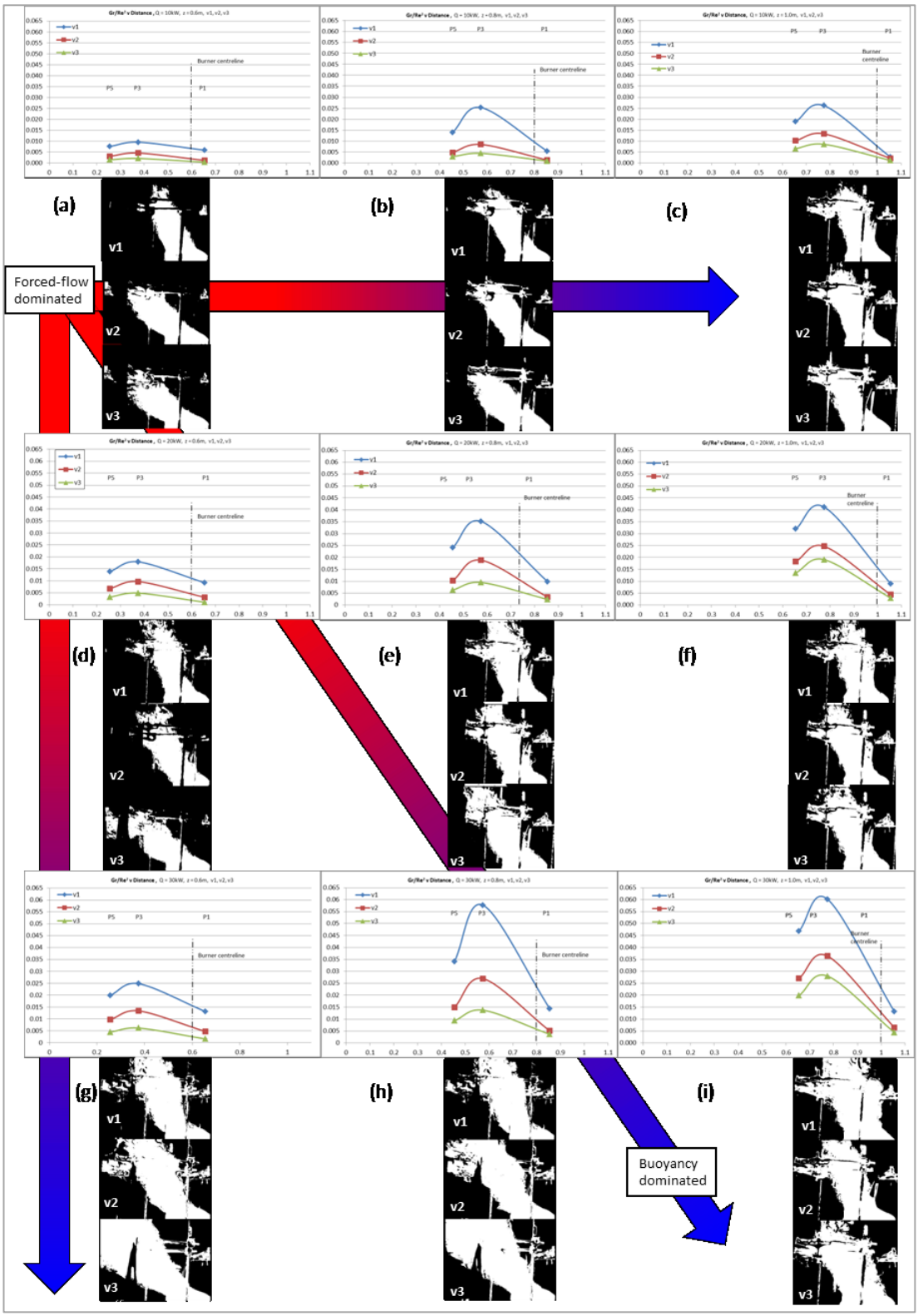

Figure 5.48: Gr*/Re^2 charts varying horizontally in fan-fire distance (z=0.6/0.8/1.0m) and varying vertically in fire size (Q=10/20/30kW).

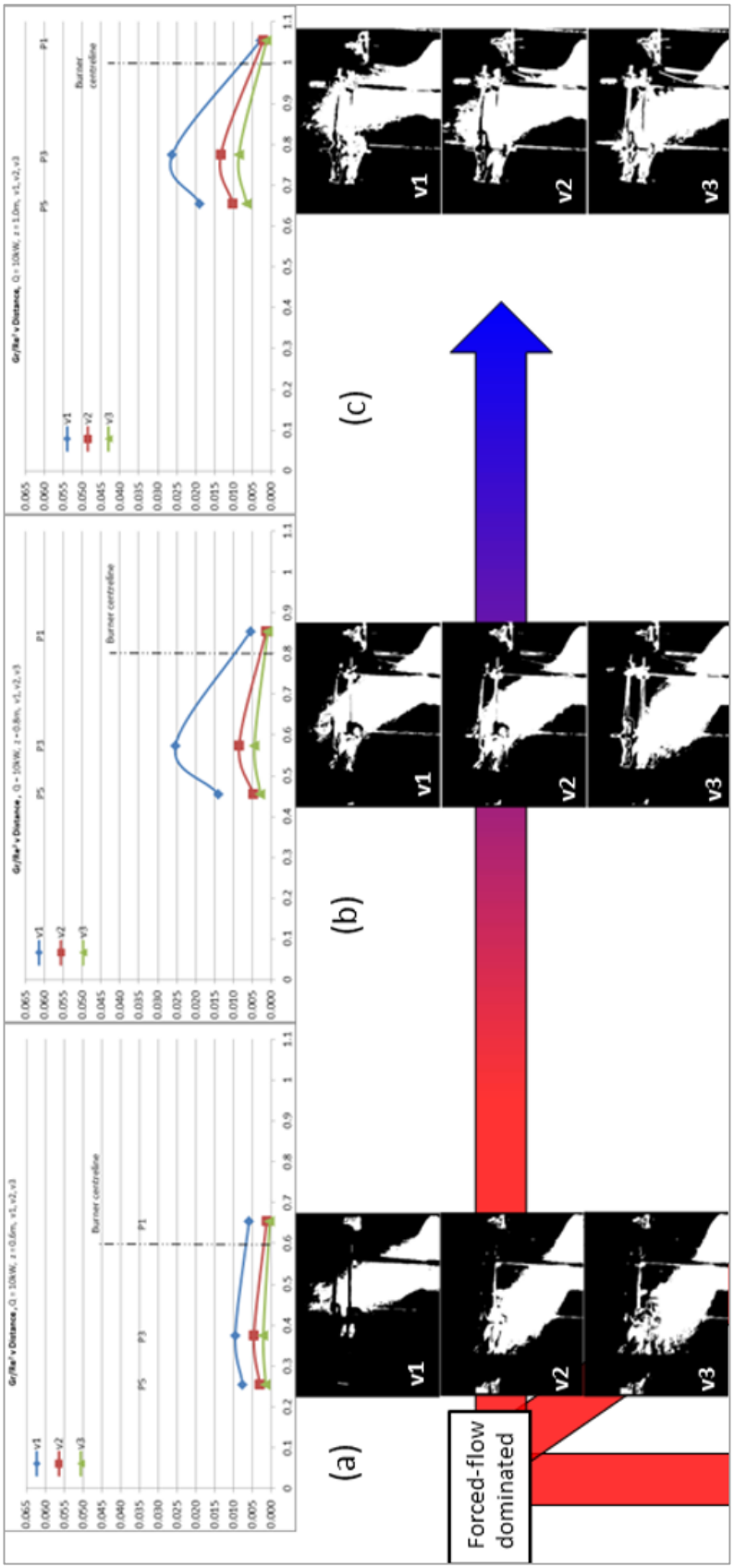

Figure 5-48(a): 10kW cases at 0.6, 0.8 and 1.0m

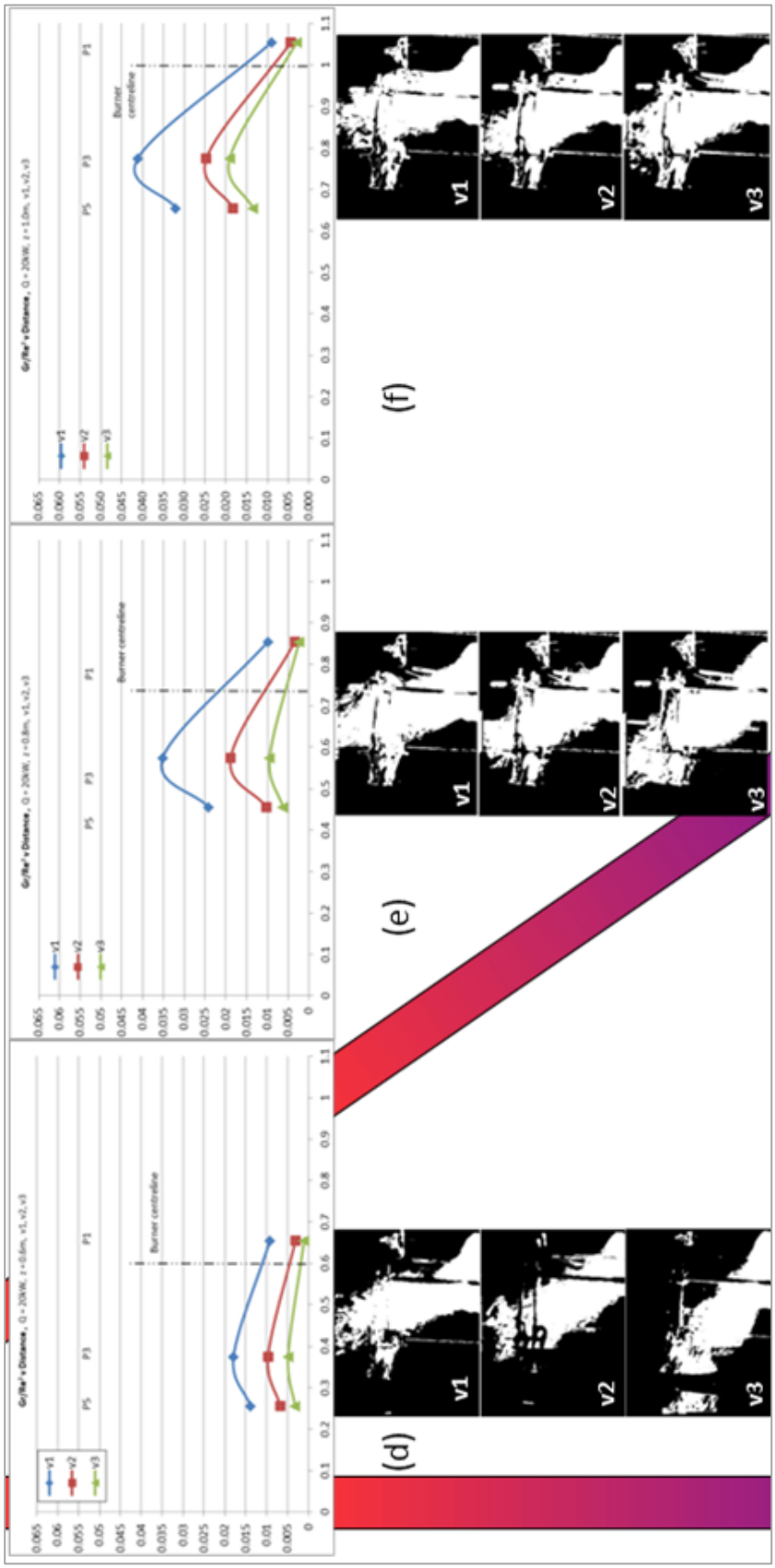

Figure 5-48(b): 20kW cases at 0.6, 0.8 and 1.0m

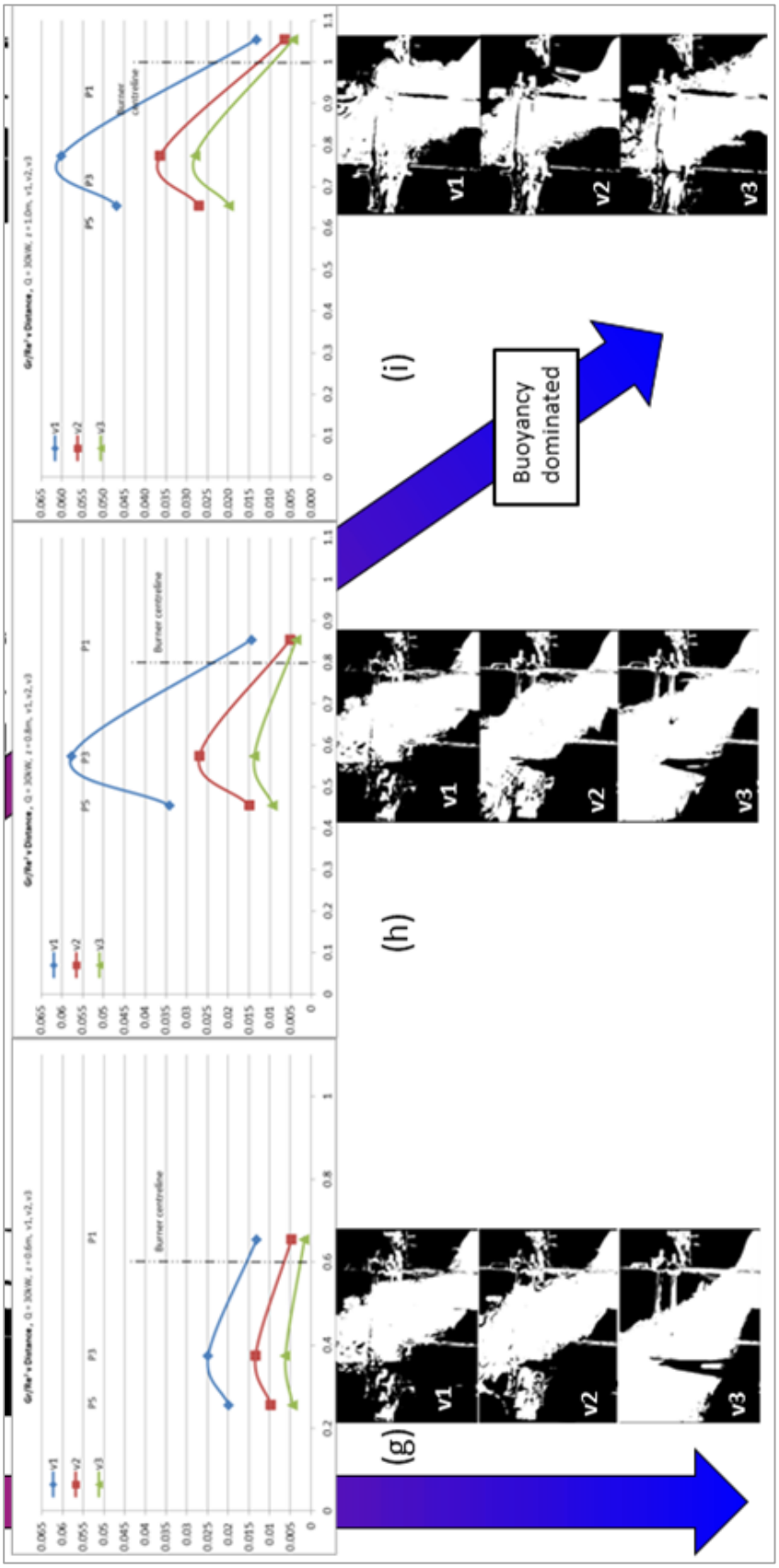

Figure 5-48(c): 30kW cases at 0.6, 0.8 and 1.0m

What this ultimately leads to is the realisation that the maximum potential *Gr** is limited by the maximum observed length scale (in this case, probe 5) and of course, with each increase in ΔP (increasing fan speed v1 through v3) for each flame case, *Gr** is in fact *reduced* since the greater tilt angle results in a decreasing *sinθ*. By contrast, *Re* is not limited by length scale and each increase in fan speed increases the local cross flow velocity. Thus *Re* will increase as long as fan speed can increase. This suggests that between probes 1 and 3 *Gr** increases at a greater rate than *Re*, after probe 3 this rate begins to decrease and at probe 5 *Gr* increase becomes very small, and in fact decreases with each increase in fan speed, while Re continues to increase with each increase in fan speed. This can perhaps be more clearly articulated by figure 5.49 where a close-up has been taken of figure 5.47 (a) for each of the nine 10kW cases.

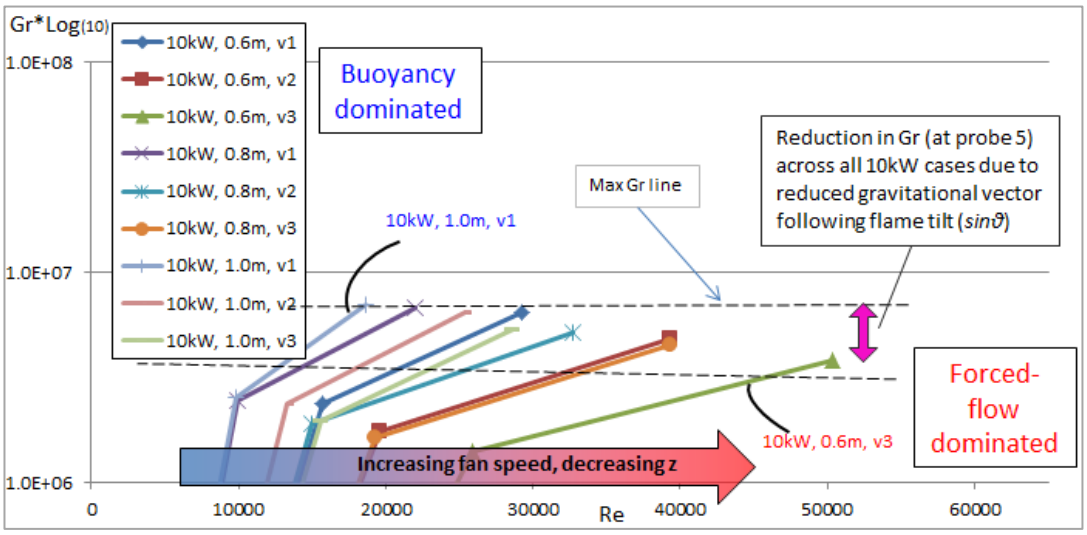

Figure 5.49: Close up of figure 5.47 (a) of the 10kW cases only. Data points that lie within dotted lines correspond to probe 5 for all 9 of the 10kW cases.

An example is made at the probe 5 data points (within the dashed lines) where the upper-most data point (highlighted *10kW, 1.0m, v1*) is limited by *L*=0.42m and the significance of *sinθ* is small. Indeed all data points within the dashed lines are limited by *L*=0.42, but as ΔP_f increases (following the blue-to-red arrow) probe velocity readings increase (net positive effect on *Re*) and flame tilt increases/*sinθ* decreases having a negative effect on *Gr*. As can be seen from referring back to

figure 5.47, the same trends are apparent for 20kW and 30kW cases except at a greater magnitude of *Gr*, where the data lies within y=1x10^{7} through 1x10^{8}.

Referring back to figure 5.48 it is apparent that the data line trend is consistent across all cases. It is necessary to discuss the shape of the data lines further in order to ensure a qualitative understanding is gained and that the data activity can be linked to a literal description of how the flame fluid dynamics are affected. As has been described previously the balance of each of the active terms in the *Gr** and *Re* equations bound and control the relative importance of ΔP_B and ΔP_f in each case. The shift from positive gradient (probe 1 - probe 3) to negative gradient (probe 3 - probe 5), when moving right to left (the direction of forced flow) is quite dramatic. As discussed above the Gr increases only with increasing distance L for each case, whereas Re increases not only with increasing distance but also due to the magnitude of the local velocity measurement. Since ΔP_f becomes stronger closer to the fan, Re at probe 5 is much greater than at probe 3 and the Gr^*/Re^2 value decreases significantly. Figure 5.50 shows the increase in measured cross flow velocity with respect to observed length scale L and in relation to the burner. The increase in velocity that can be seen after probe 3 (moving right to left) and this corresponds directly with the negative gradient occurrence in figure 5.48.

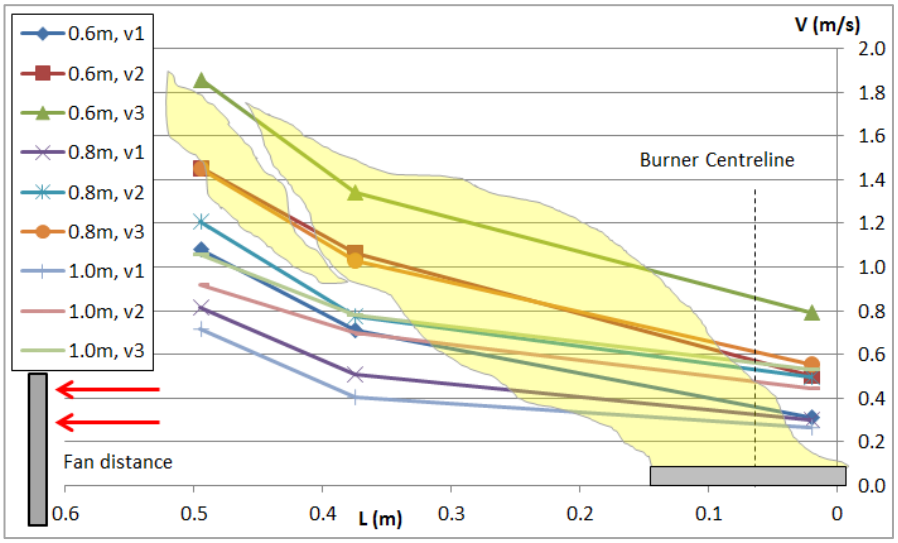

Figure 5.50: Velocity data for all 10kW cases, recorded at probes located 0.02m, 0.375m and 0.495m downwind from the burner leading edge. Velocity readings increase from probe 1 through probe 5. The background flame image is purely an example for spatial context.

Data from all 10kW cases from figure 5.48 have been plotted as a function cross flow velocity in order to view the negative relationship between Gr^*/Re^2 and increasing ΔP_f. In figure 5.51 the middle data point in each data line represents probe 3 and consistently the point along the observed length of the flame that buoyancy is most significant. The larger arch peaks to the top=left of the graph are the more buoyant cases and the flatter data lines to the bottom-right of the graph represent the more forced-flow dominated cases where probe velocity readings were greatest and greater flame tilt is achieved. When plotted in this manner the data clearly demonstrates the negative relationship between Gr^*/Re^2 and ΔP_f. Again 20kW and 30kW cases display similar tends but at higher Gr^*/Re^2 values.

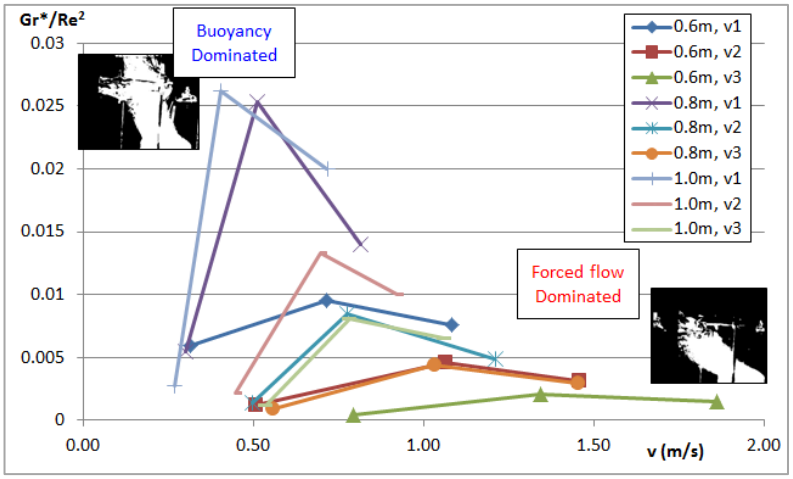

Figure 5.51: Gr^*/Re^2 as a function of measured cross flow velocity for all 10kW cases.

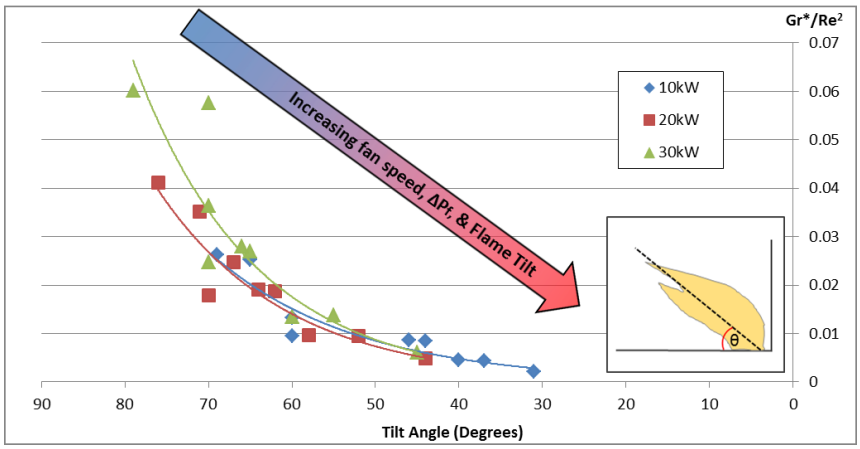

Figure 5.52: Gr^*/Re^2 as a function of flame tilt angle. Data points represent probe 3.

Figure 5.52 demonstrates Gr^*/Re^2 as a function of flame tilt for all 10/20/30kW cases. Exponent trend lines demonstrate the comparative agreement between each Q case. This agreement appears slightly better when ΔP_f is greater. As an average over the flame length the data points are all representative of probe 3, since this probe is most involved with the flame over time and is less affected by the cross flow extremities at the leading edge of the burner (probe 1) and near the fan (probe 5). The negative relationship between flame tilt and Gr^*/Re^2 follows quite well the trend apparent in figure 5.51, since the relationship between tilt angle and cross flow velocity is quite well-defined. (This is described as a negative relationship since the tilt angle is measured from horizontal, so that the angle of interest *decreases* with a *more* tilted flame).

The following is a brief summary of the overarching principles discussed in chapter 5.8.

Cases are increasingly *Buoyancy-dominated* where:

- Gr^*/Re^2 increases with increasing **Q**
- Gr^*/Re^2 increases with increasing **z**
- Increasing Gr^*/Re^2 characterised by **less tilted flame**

Cases are increasingly *Forced flow*-dominated where:

- Gr^*/Re^2 decreases with increasing $\mathbf{\Delta P_f}$
- Gr^*/Re^2 decreases with decreasing **z**
- Decreasing Gr^*/Re^2 characterised by **more tilted flame**

Typically across the length of any individual flame:

Increasingly Buoyancy-dominated

- Gr^*/Re^2 increases with observed length, L, below L=0.375m (probe 3)

Increasingly Forced Flow-dominated

- Gr^*/Re^2 decreases with observed length, L, above L=0.375m (probe 3)

6 Review of Results

6.1 Mass Flow Analysis

The design mass flow rate is based upon equations 2-24 (Cetegen/Zukoski) and 2-25 (Heskestad) which increases with increasing fire size by Q to the 1/3 power, and increases with height above the fuel bed by z to the 5/3 power. The Heskestad derivation suggests that mass flow rate increases with these variables to the same powers but as a function of an additional (Q and z related) variable. Therefore as we gradually increase these variables, fire size Q, which represents an increase in the relative strength of the buoyant force, and distance z, which also effectively increases the strength of the buoyant flow (as cross flow inertia ΔP_f diminishes) the design mass flow rates $\dot{m}_{a(Zuk)}$ and $\dot{m}_{a(Hesk)}$, which are both based upon the buoyant force alone, tend to increase toward, and subsequently surpass the experimental (measured) mass flow rates ($\dot{m}_e$). The practical outcome of this balance change is that the exhaust fan at constant speed will not be able to cope after a certain point when the fire size is increased or when concerned with the quantity of smoke ascertained at a greater measure of z (corresponding to a greater fan to flame distance, z'). This is similar to the idea first discussed with figure 5.26 in which depicts the mass of smoke increasing as it approaches the exhaust fan making it impossible for the fan to cope with the total volume of smoke resulting from the mixed flows. This principle is visualised in figure 6.1 which depicts an idealised schematic. Evaluation of the measured mass flow rates against the design mass flow rates given by the Zukoski and Heskestad approaches is important because the comparison demonstrates clearly the limits of applicability of these industry standard correlations when the main plume dynamics variables are manipulated by a relatively small amount.

As the smoke plume increases in theoretical circumference as it approaches the fan it will increase out with the cross-sectional area of the fan flow and will also increase irregularly due to the mixing with the forced fan flow. The entrainment which occurs at the volume of the smoke plume which eludes the exhaust fan flow and

rises above it cannot be accounted for by consideration of the fan mass flow rate and this makes it impossible to truly characterise all facets of the entrainment regimes which are created from the mixed interaction. This is investigated further in chapter 6.4.

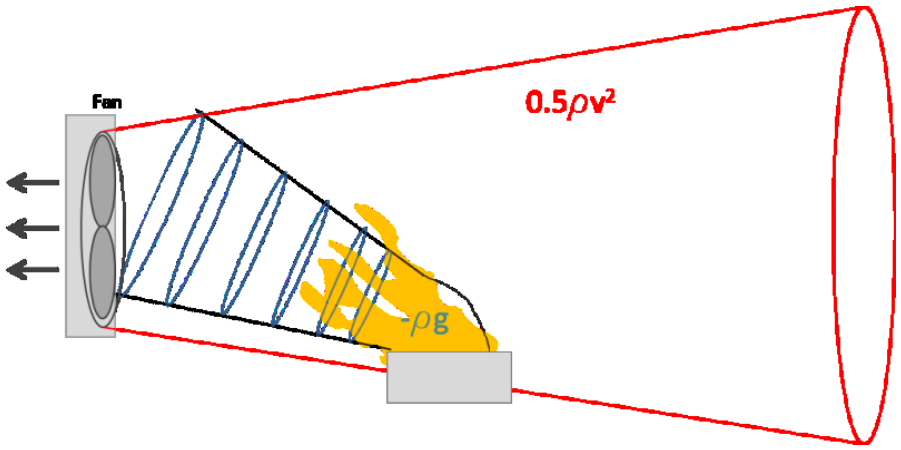

(a)

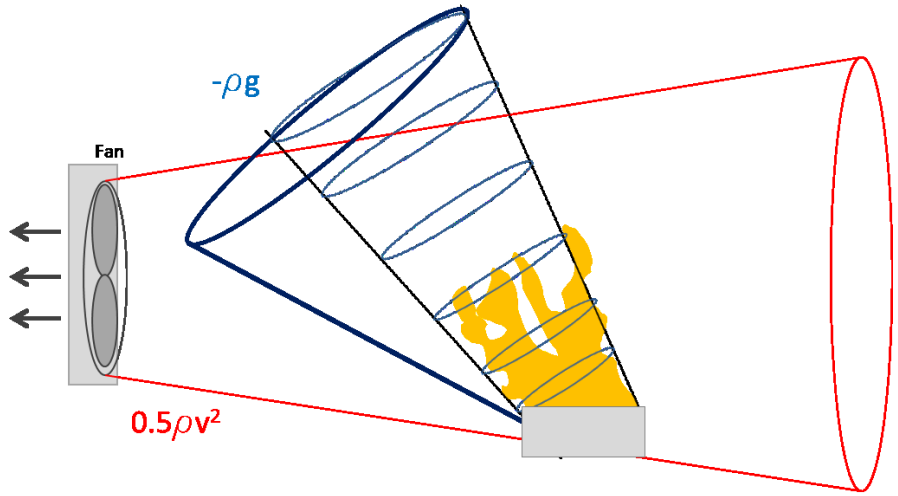

(b)

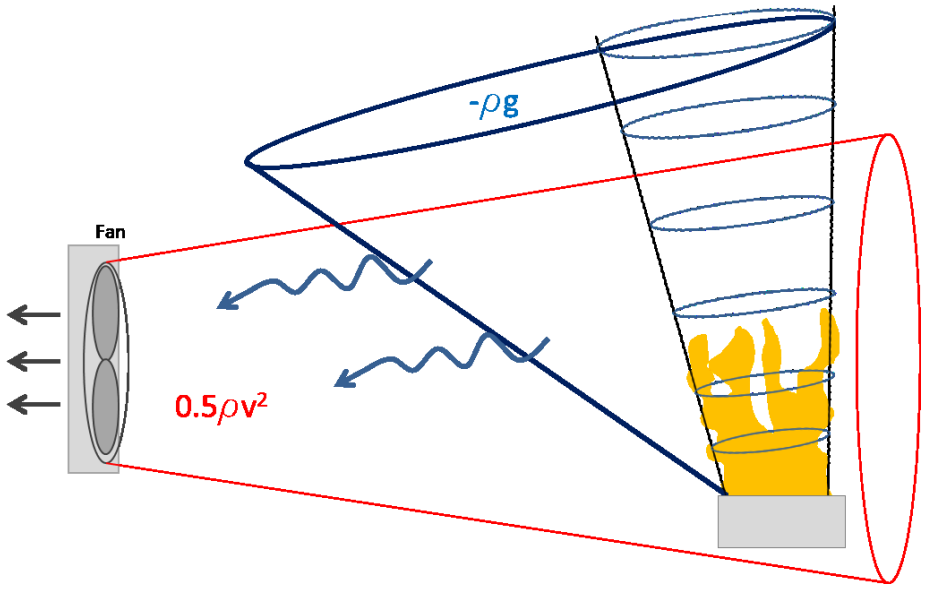

(c)

Figure 6.1: Idealised interaction of buoyant plume and forced cross flow where (a) represents z' = 0.6m, (b) represents z' = 0.8m and (c) represents z' = 1.0m. Flow field vectors have been removed (as per figure 5.26) for clarity.

Figure 6.1 offers a qualitative and simplified outline of the principle whereby some of the mass of the buoyant smoke plume escapes the exhaust fan flow. This is partly a function of z (and z') where further from the fan (z') the forced flow is weaker and cannot overcome the buoyant strength of the fire hot gases (parts b & c), or farther along the smoke plume (z) where the circumferential area is large (part c) and cannot be contained by the exhaust fan flow. Conversely it can be seen in (a) that close to the fan, where flame tilt it greater, the resultant buoyancy is reduced and most, if not all of the smoke from the fire is captured by the exhaust fan flow.

The following investigations aim to describe with a quantitative approach the theories discussed here by analysing the experiment data and comparing the measured exhaust fan mass flow rates against the traditional plume entrainment correlations for each specific case.

Figure 6.2 details the experimental (measured) mass flow rate ($\dot{m}_e$) as well as the design mass flow rates following Zukoski and Heskestad. The experimental (measured) mass flow ($\dot{m}_e$) corresponds directly to fan speed, therefore in these experiments the experimental mass flow rate does not change with respect to variation in flame size (Q) or distance (z). This explains why the experimental mass flow data points on the graphs in figure 6.2 do not vary for each Q case, and similarly do not vary across each graph for z=0.6m, 0.8m and 1.0m. Instead experimental mass flow rates increase only with increasing fan speed (v1, v2, v3) in every case.

Figure 6.3 shows the change (positive or negative) in mass flow rate between the design and experimental mass flow rates. In order to give some clearer context to the magnitude of change, figure 6.4 presents the experiment mass flow normalised by the design mass flows $\dot{m}_{a(Zuk)}$ and $\dot{m}_{a(Hesk)}$. For each case where $\dot{m}_e/\dot{m}_a > 1$ the extraction fan is considered to acquire all of the smoke from the fire plume and the mass flow rate is subsequently greater than the design mass flow rate given by the use of the axis-symmetric entrainment correlations $\dot{m}_{a(Zuk)}$ and $\dot{m}_{a(Hesk)}$. The amount by which the measured mass flow rate is greater than the design rates increases with increasing fan speed, ΔP and therefore, flame tilt.

We can say that in these instances the plume environment tends toward being *forced-flow dominated*. At z=0.6m only 1 of the 9 configurations does not tend toward a forced flow-dominated regime. Intuitively this is the case with the larger fire size (30kW) and lowest fan speed - resulting in the weakest cross flow ΔP_f pitted against the most strongly buoyantly driven fire case.

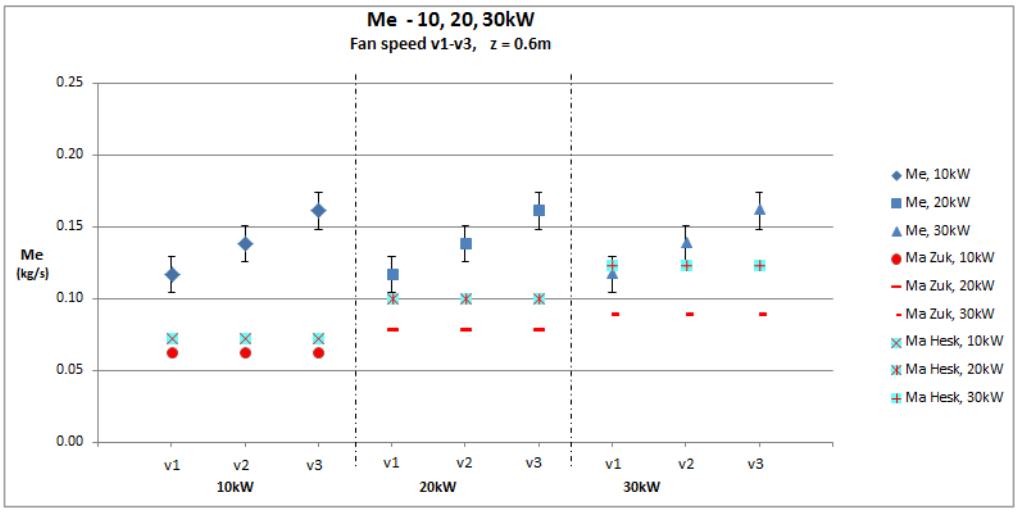

(a)

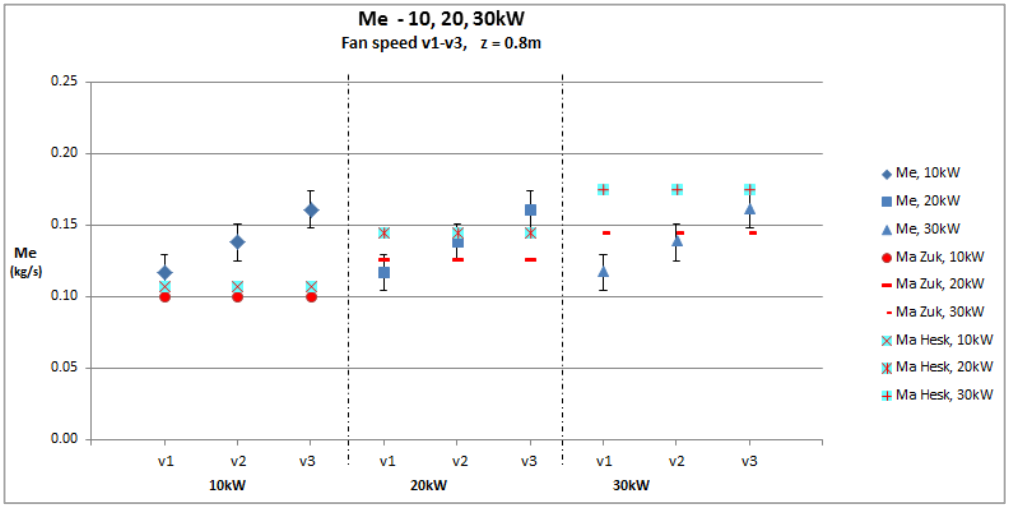

(b)

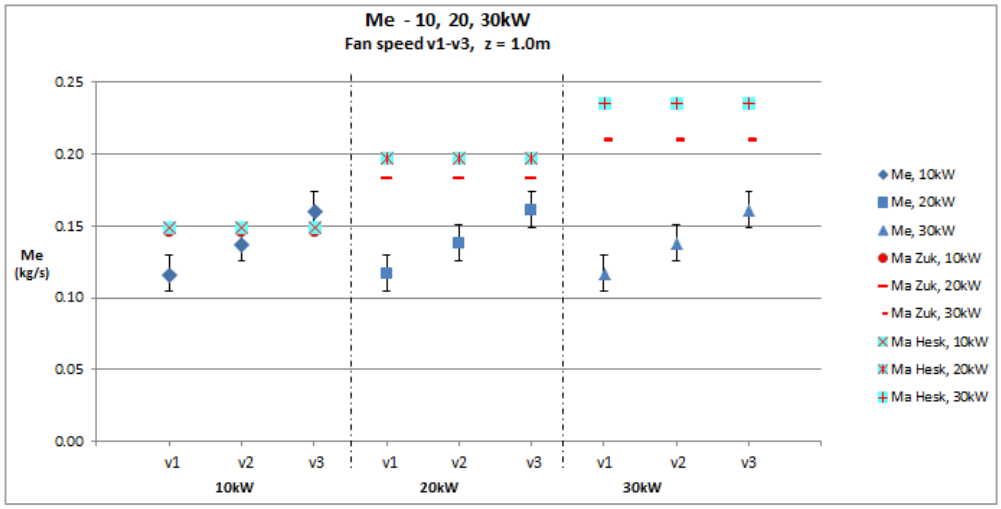

(c)

Figure 6.2: Measured (experiment) mass flow rate (showing potential error) and design mass flow rates for all 27 cases. z'= (a)0.6m, (b) 0.8m and (c) 1.0m.

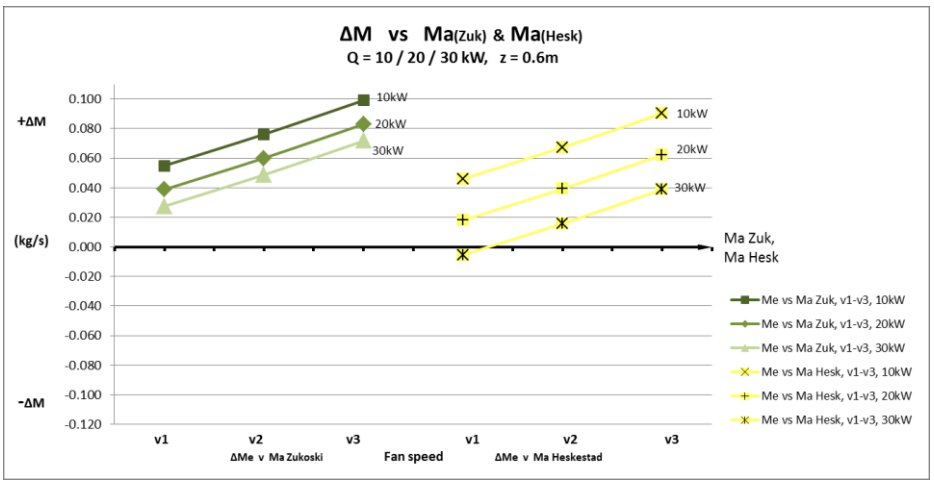

(a)

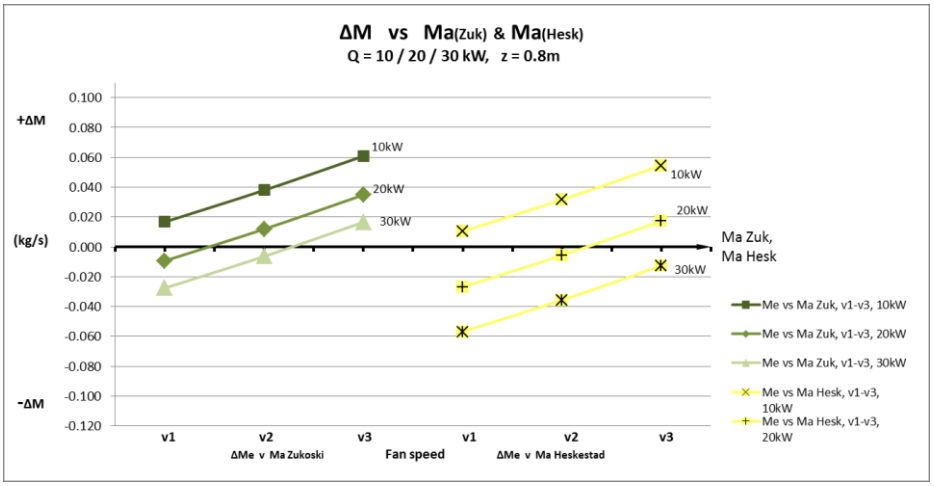

(b)

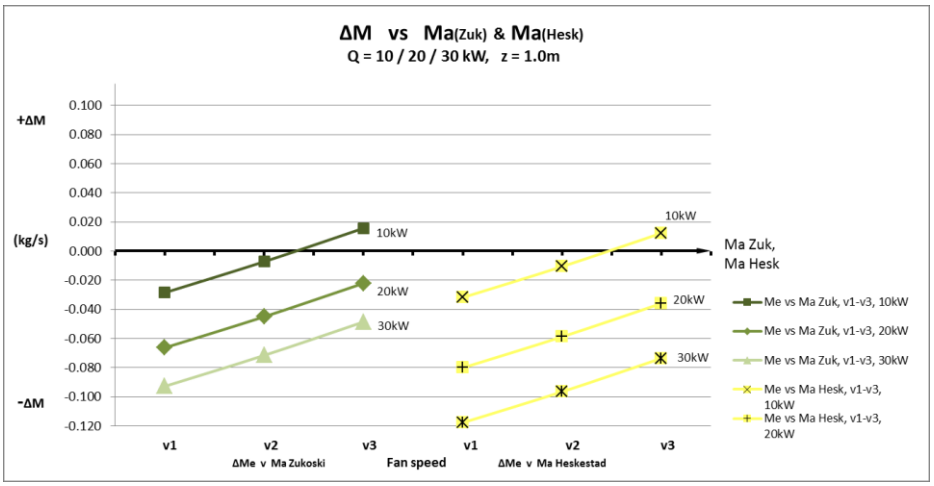

(c)

Figure 6.3: Change in mass flow rate between experimental rate and design mass flow rates, at (a) z=0.6m, (b) z=0.8m and (c) z=1.0m. The transition from positive to negative change on the mass flow rate can be seen across a-c whereby the increase in z affects the design mass flow correlations but not the experimental mass flow readings.

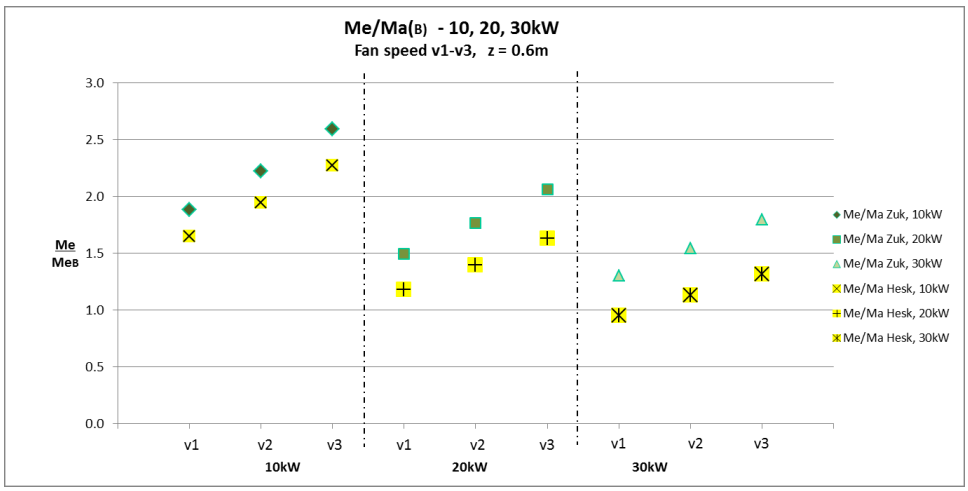

(a)

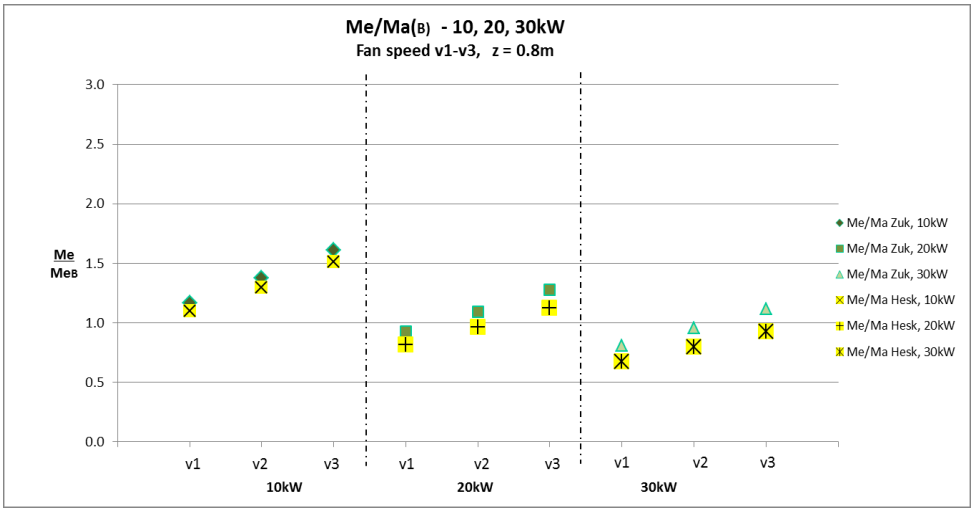

(b)

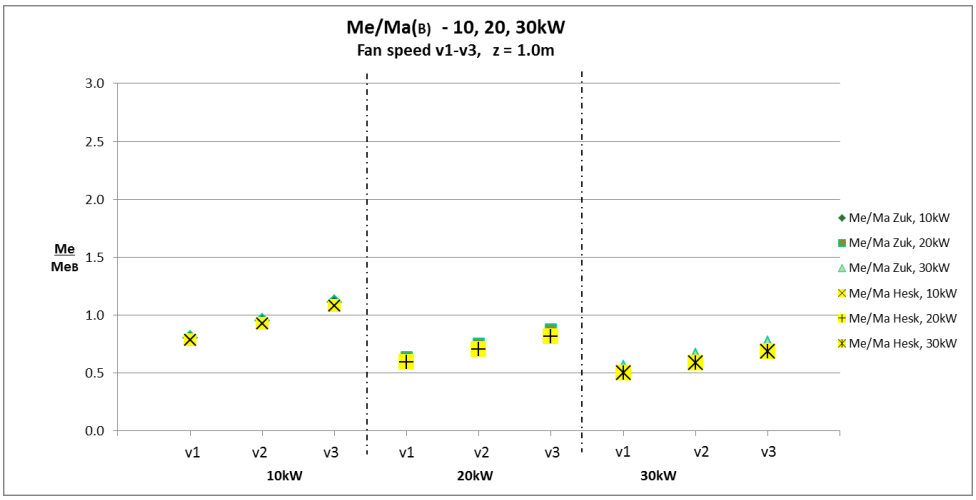

(c)

Figure 6.4: Measured (experiment) mass flow normalised by design mass flow rates

At z=0.8m the normalised mass flow rates reduce across every case since the design correlation mass flow rates $\dot{m}_a$ are increased due to the increase in z while the experiment mass flow rates are not. At z=0.8m almost half of the normalised mass flow rates tend toward a forced flow-dominated regime and intuitively, the tipping point occurs around the middle fire size (Q=20kW) and medium fan speed (v2).

At z=1.0m only two cases remain forced-flow dominated and as expected this is true of the case with the smallest fire size (Q=10kW) coupled with the fastest fan speed (v3) and strongest cross flow ΔP_f.

For those cases where $\dot{m}_e/\dot{m}_a < 1$ we suppose that the buoyant force is of such magnitude that it partially overcomes the induced cross flow and not all the plume smoke is captured by the fan. These cases are increasingly buoyancy-dominated as more smoke escapes the fan flow. In the extreme cases - the traditional axis-symmetric plume is completely buoyant and the fully tilted plume (where the flame is tilted to approximately 90°- parallel with the ground - and the effect of buoyancy is effectively ceased (buoyancy will still be apparent/ persist at a much smaller scale)) is considered completely forced flow-dominated. All the intermediate cases described by the experiment demonstrate an intermediate regime, a mixed flow where both buoyancy and forced-flow inertia are important, but to varying degrees. For the cases where $\dot{m}_e/\dot{m}_a < 1$ the forced-flow still has an impact upon the flame since a tilt angle is apparent and thus deviation from the axis-symmetric model is achieved, however due to the nature of the set-up of the experiment quantification of the impact of this smaller deviation from the axis-symmetric ideal entrainment rate is unattainable.

What we can say however is that since, within certain boundaries, mass flow tends to increase with increased flame tilt angle we know that these buoyancy-dominated cases are most likely to exhibit a mass flow rate greater than that of the completely buoyant axis-symmetric case. Since the experiment is designed to isolate and quantify, specifically, the mass flow rate resulting from the flame that tends toward being forced flow-dominated, data from those flames which exhibit a significant

buoyancy-dominated portion are difficult to directly compare with the data from those which do not.

In every instance the trend persists that increasing ΔP_f has the effect of increasing the experiment mass flow rate. For the buoyancy-dominated cases it is realistic to postulate that the total mass flow rate is a combination of the mass entrained as described by the design correlation rate plus an additional entrained portion influenced by the cross flow pressure. These cases where ΔP_f makes only a small contribution to the mixed flow mirrors the reports in [6] whereby small disturbances to the ambient plume environment were noticed to result in up to a 50% increase in smoke layer depth during the axis-symmetric plume entrainment experiments. In those instances the ΔP_f and the Re that describes the cross flow magnitudes remained small and unquantified despite the noticeable significance of their impact upon the smoke flow volume.

6.2 Identifying Inertia and Buoyancy-dominated Cases

Figure 6.5 reproduces the information of figure 5.48 however the data demonstrated in figure 6.4 has been applied where red sections correspond with $\dot{m}_e/\dot{m}_a > 1$ and blue sections represent cases in which $\dot{m}_e/\dot{m}_a < 1$. Generally speaking red sections therefore represent inertia-dominated cases and blue corresponds with buoyancy-dominated cases. The average Gr/Re^2 ratios for each individual case is displayed in the white bars and correspond with the average flame angle images (denoted v1, v2, v3) for each case immediately below. In each graph the blue data line corresponds with the v1 flame image (the lowest fan speed in each instance) and the left-most (and largest) Gr/Re^2 number. The red data line represents the v2 image and the middle Gr/Re^2 number and the green data line corresponds with the v3 image (greatest fan speed) and right hand side (and lowest) Gr/Re^2 number.

The application of red/blue (inertia/buoyancy-dominated) colour scheme demonstrates the intuitive notion that with increasing distance from the fan and increasing fire size, the regime becomes more buoyancy-dominated (corresponding with higher peaks in the graph data) and a greater portion of the plume smoke escapes the draw of the extraction fan. In practical terms this increases the smoke hazard in the fire room of origin as well as within the extraction system. In theoretical terms figure 6.6 demonstrates that the inertia-dominated cases typically correspond with those instances where the terms in the Gr and Re correlations result in a steeper increase in Re number across each case. Furthermore, in those cases marked in red ($\dot{m}_e/\dot{m}_a > 1$), we can say that the fan flow rate alone, (which includes some portion of smoke depending on the case) is greater than the buoyant entrainment that would be predicted by the design calculations for the fully-buoyant case.

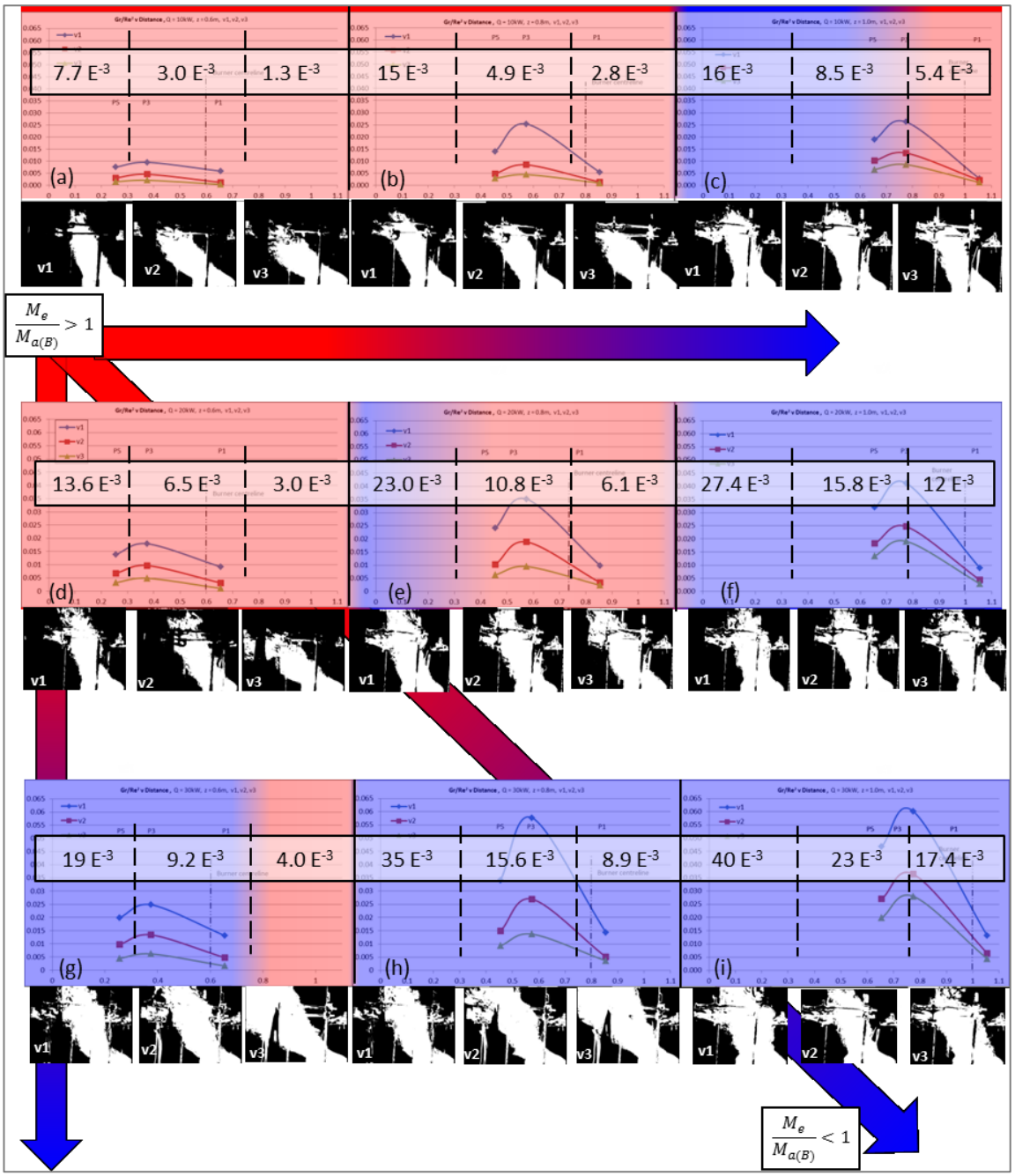

Figure 6.5: This figure reproduces the Gr/Re^2 charts of figure 5.48, however the relationship between non-dimensionalised mass flow rates depicted in figure 6.4 and Gr/Re^2 characteristics of each case have been highlighted where for *red* charts: $\dot{m}e/\dot{m}a > 1$ and are typically forced-flow dominated and for *blue* charts: $\dot{m}e/\dot{m}a < 1$ and are typically buoyancy-dominated.

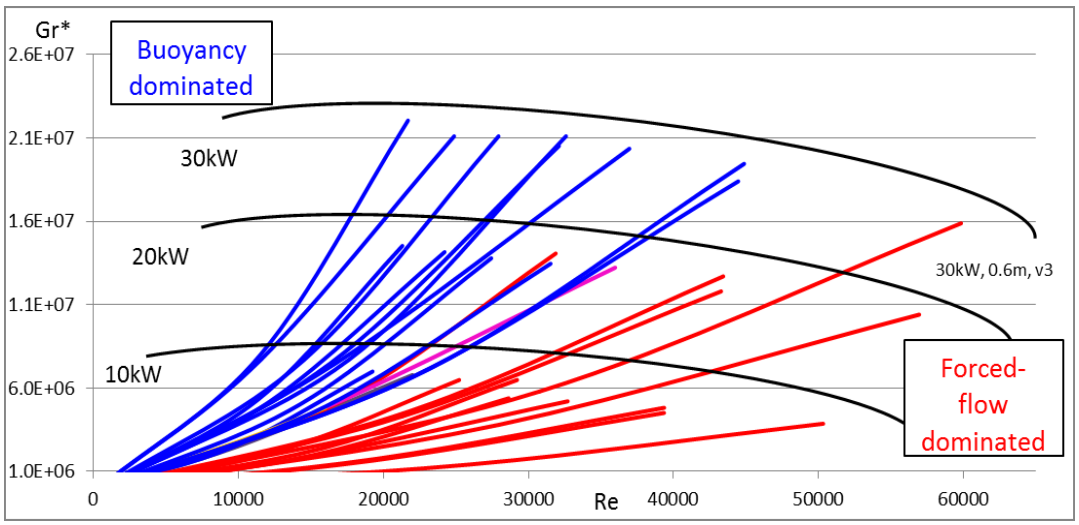

Figure 6.6: Gr* v Re for all cases where (a) depicts the variation in data gradient for the region that appears to plateau (v2, v3) in figure part.

Since the experiment fan extraction rate is set (v1, v2, v3) for each of the 9 main cases and Gr/Re^2 varies due to the evolution of ΔP_f as a function of Q and z, demonstrating the changing Gr/Re^2 number is best done when graphed against the normalised mass flow rate and when considering the data in a range of groupings. Figure 6.7 part (a) demonstrates the expected negative correlation between Gr/Re^2 and normalised mass flow as mass flow increases and is grouped by the 9 governing cases where in each Q and z are fixed and fan speed is increased (v1, v2, v3). Each data set therefore has 3 data points corresponding to fan speeds v1-v3 and as discussed in detail previously, as fan speed is increased Gr/Re^2 decreases and $\dot{m}_e/\dot{m}_a$ increases. There are a range of gradients across each data group which reflect the impact of the cross flow ΔP_f at the flame as a function of the distance from the fan and the size of the fire, Q. Despite the overlapping data points when the entire data is considered, which is a function of the impact of the many variable combinations across all cases, in general the closer the flame is to the fan (small z), smaller the fire size (Q), and the greater the cross flow inertia (ΔP_f), the more pronounced the impact upon the flame becomes and the greater the deviation (in terms of tilt angle and global fluid flow) from the ambient design fire case, the greater the proportion of the smoke plume is captured by the fan. In part (b) the data is identified by each

measure of z (0.6m, 0.8m & 1.0m). In this graph the trend suggested above that $\dot{m}_e/\dot{m}_a$ increases as z is decreased is further demonstrated. Even though there is some overlap in mass flow rate across data from each measure of z, the same clear trend exists for each z group. We can also notice more clearly the trend that the smaller the Gr^*/Re^2 number the more sharply the mass flow rate increases. This is of course related to the increase in ΔPf which is experienced by the flame closer to the fan however this is only partially responsible for the data trend since Q also plays a significant role in determining how much of the resultant smoke and hot gases escape the extraction fan.

An interesting point to observe is that the chosen method for normalising the mass flow has a direct impact upon the geography of the data for the z= 0.6/0.8/1,0m groups. We have established that the general trend, including the gradient nuances for each z group are confidently repeated however notice that most of the data at z=1.0m corresponds with $\dot{m}_e/\dot{m}_a$ <1, z=0.8m typically lies around $\dot{m}_e/\dot{m}_a = 1$ (slightly favouring $\dot{m}_e/\dot{m}_a$ >1) and data for z=0.6m lies well into $\dot{m}_e/\dot{m}_a$ >1 (actually reaching $\dot{m}_e/\dot{m}_a$ >2.5). As alluded to in the previous section Me is set by the experiment extraction fan speeds (v1, v2, v3) however in the calculation of $\dot{m}_a$ increasing Q and z actively increase the mass flow rate (to the power of 1/3 and 5/3 respectively) which creates the differentiation that can be clearly articulated by figure 6.7 (b) when the two mass flow parameters are directly compared. Since the ratio of these mass flows decrease this suggests that the extraction fan acquires smaller and smaller portions of the total smoke produced as the fire grows in size, or the consideration of mass flow rate is stipulated at greater heights (z) along the axis-symmetric plume. At the data point where $\dot{m}_e/\dot{m}_a = 0.6$ then, ~40% of the smoke produced by the fire is not acquired by the experimental extract fan however this mass is not unaccounted for in practical terms since this smoke will still be present in the room of origin of the fire.

Of primary interest are the cases which present with inertia-dominated (red) sections in figure 6.5 and therefore $\dot{m}_e/\dot{m}_a$ >1 in figure 6.7. By logical reasoning we can consider that the larger the fire the higher the velocity and mass of entrained air

and therefore the greater the volume of resultant smoke produced. It follows then that by increasing the velocity (and therefore the ΔP_f) of air flowing across the plume the result is a greater volume of smoke measured at some length downstream in the plume. If we make the assumption that the extraction rate of the fan is equal to the 'smoke' produced then all the red cases in figure 6.5 are of particular importance. In each of the instances where v1 is red (Q=10kw at z=0.6/0.8m, and Q=20kW at z=0.6m, noted as (a), (b) and (d) in figure 6.5) and thus inertia-dominated, the application of the weakest fan setting has already produced a pressure differential, normal to the propagation of the axis-symmetric plume, great enough to noticeably enhance the volume of resultant smoke. Working on this hypothesis these settings produce an increased smoke mass flow rate of approximately 150-185% at z=0.6m and roughly 120% at z=0.8m when compared with the design rate. The simple systematic approach of further increasing the normal pressure differential (ΔP_f) by increasing the fan speed to v2 further enhances the increase in normalised smoke mass flow to 170%-220% at z=0.6m and 140% at z=0.8m of that of the design rate. Finally, in these 3 particular instances (Q=10kw at z=0.6/0.8m, and Q=20kW at z=0.6m) a third increase in smoke mass flow rate is achieved by again increasing the pressure differential normal to the flame and plume flow resulting in a maximum increase of approximately 260% against the design mass flow rate at z=0.6m.

For the other experimental cases in which red inertia-dominated instances are included along with blue buoyancy-dominated instances (Q=10kW and z=1.0m, Q=20kW and z=0.8m, Q=30kW and z=0.6m, denoted (c), (e) and (g) respectively in figure 6.5) these cases present the same notion that increasing the cross flow pressure differential to a particular degree will increase the smoke mass flow rate. The difference for these cases compared to the fully inertia-dominated cases described above, is that the forced-flow pressure differential normal to the plume is smaller *relative* to the fire size (Q) either because Q has been increased or because of the impact of increasing distance (z), in the (blue) buoyancy-dominated instances. In these cases the full plume smoke flow was not captured by the lower fan speed

setting and either v2 or v3 were required in order to increase ΔP_f to a great enough magnitude in order to demonstrate the increase in smoke mass flow over the comparable design flow rate.

In all cases the velocity of the air flowing around the plume (and *in the direction of plume propagation* in the context of the tilted plume) is greater than that of the axis-symmetric case. This concept is quantified and investigated in chapter 6.3. Due to the terms Q and z which are the only likely variables of any significant scale in the design mass flow rate correlations and which are not accounted for in terms of volumetric flow rate of the experiment extraction fan, the various examples are produced whereby increasing fan speed from v1-v3 either further enhances the increase of the normalised mass flow rate (all red instances in figure 6.5) or overcomes the larger fire size/increased z (blue/red instances in figure 6.5) to demonstrate an increased mass flow rate in terms of the context of the experiment data. Cases (f), (h) and (i) of figure 6.5 are those whereby the combination of larger Q and the greater measures of z are not overcome by the increasing cross flow pressure differential and Gr/Re^2 remains suitably high to maintain that the extraction fan captures only a small portion of the increased smoke mass.

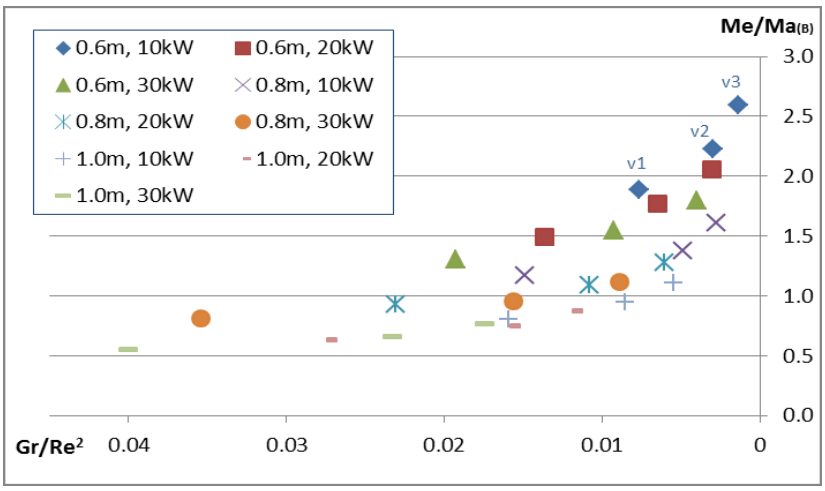

(a)

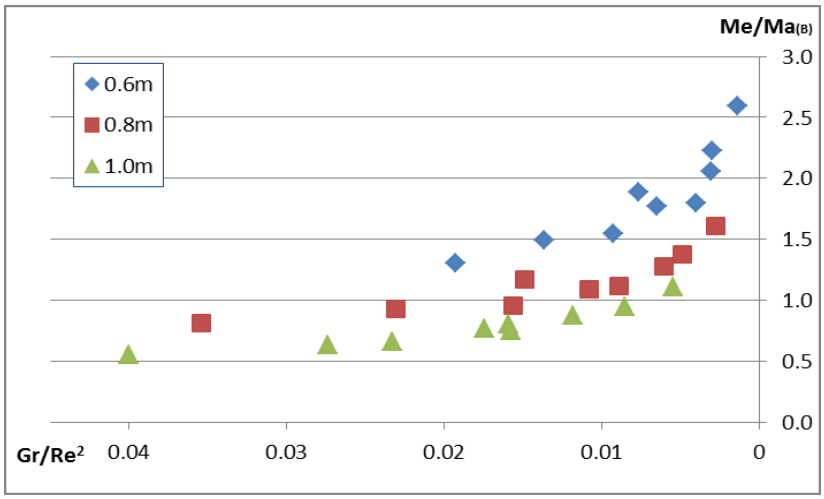

(b)

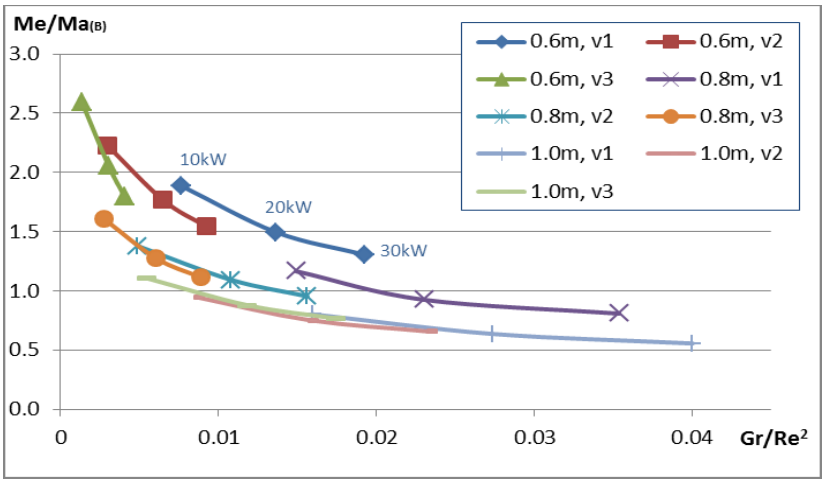

(c)

Figure 6.7: shows the relationship between Gr/Re^2 number and the normalised mass flow rate ($\dot{m}e/\dot{m}a$) distinguished by (a) each inference of Q and z, (b) distance from flame to fan z, and (c) increasing Q for each case of constant z and fan speed.

Figure 6.7 part (c) highlights the decrease in normalised mass flow rate with each case of increased fire size Q. This graph is interesting because it helps to articulate to impact of the combination of the pressure differential ΔP_f with reference to fire size Q, the mass flow v Gr/Re^2 data. A clear comparison is that of the green (0.6m, v3) data lines and the blue (0.6m, v1) data lines. Because the v3 fan speed (0.6m, v3, green) creates the greater ΔP_f at the flame, the increases in Q are less significant in terms of increasing the Gr/Re^2, and by comparison the v1 fan speed (0.6m, v1, blue) creates a weaker ΔP_f at the flame and thus the increase in Q is more pronounced effecting a greater rise in Gr/Re^2, reflecting the comparatively greater buoyant force component in this case. The (red) 0.6m, v2 data can be seen to fit approximately between these data lines since relatively speaking, an intermediate ΔP_f is created by fan speed v2. Similar but less pronounced trends can be observed for the z=0.8m and z=1.0m data.

6.3 Air-flow Around the Plume

Local [horizontal] velocity readings at each probe, normalised by ideal plume centreline velocities (based on the Zukoski correlation), are plotted in figure 6.8. This set of graphs is particularly interesting because of the large number of nuances which contribute to the data plot. These details must be discussed in order to appreciate the results.

Firstly, local velocities at each probe location in the case of the design plume correlations (that is the idealised plume as described by simplified correlations derived from first principle reasoning) will vary greatly depending upon the location of each probe in relation to the flame. For example once the flame is tilted across the experiment runs, we will assume probe 3 represents a centreline location within the flame/ plume and an approximate centreline gas velocity can be found using equation 2-29.

It is discussed in chapter 5 that for each tilted flame case the flame volume is erratic and is not constant. In most instances probe 3 is engulfed for a significant portion of the test despite the variation in flame tilt angle for each fan speed/ Q configuration. It is therefore a necessary but acceptable simplification to consider probe 3 to represent the centreline velocity across the mixed-flow cases. The ΔP readings from probe 3 are nuanced by the fact that they are orientated to read the pressure differential along the horizontal axis and the buoyant flow of the flame is essentially, or at least initially, purely vertical. As the flame is tilted part of the buoyant flow contributes to the horizontal flow field and some does not. The greater the flame tilt angle (and the relative cross flow ΔP) the greater the reduction in the vertical buoyant vector. For all cases therefore, apart from, perhaps the most tilted cases, the entirety of the combined (vertical buoyant and horizontal inertia) flows, which is greater than the sum of its constituents, is not completely transmitted to the pressure probe. For probe 3, and to an increasing extent probe 5 then, mixed flow ΔP graphs (including figure 6.8) will slightly underestimate the true velocity of the combined mixed flow field for most of the tilted cases. This applies certainly at least, to all of the cases which were highlighted in figure 6.4 as being applicable to the *forced-flow dominated* experiment set-up. This is important to note because the combined mixed-flow field in the tilted cases is the ΔP of interest for comparison with the purely buoyant vertical flow of the ideal plume case.

The same story can be applied to the case of probe 5, but generally to a lesser extent. Further nuance comes in here because fewer cases involve the flame being tilted far enough to fully engulf probe 5 compared to probe 3 since a greater degree of tilt and more specifically, a longer flame, are required to do so. Probe 5 is also located closest to the fan so will naturally be affected by the cross flow inertia to a greater extent than probe 3 for the same fan speed. This contrast in mechanisms affecting the average ΔP_f recorded at probes 3 and 5 is demonstrated in figure 6.8 where a greater increase at probe 5 is apparent compared to the increase at probe 3 against the design pressure differential (ΔP_1). This balance is due to the varying influence of each of the mechanisms discussed above. A further nuance here is that since

buoyant flow velocity in the ideal plume decreases with height, the denominator for $\Delta P/\Delta P_1$ *probe 5* favours an increase over that at probe 3.

It can be observed that the normalised ΔP decreases across each graph with increasing z. It is necessary to consider here the same dynamic as was discussed previously when analysing the normalised mass flow rates. Since for the ideal plume (buoyant) ΔP_B increases proportionally with increasing Q and the vast majority of the buoyant flow contributes to the calculated centreline velocity, the calculated ΔP_1 increases at a greater rate than measured ΔP_f. It was demonstrated in chapter 5 that an increase in Q does have some impact upon measured ΔP_f at each probe (enhancing ΔP_f somewhat) however since in the tilted cases only part of the buoyant flow contributes to the horizontal inertia component, measured ΔP_f does not increase with increasing Q as strongly as ΔP_1. The effect is that $\Delta P/\Delta P_1$ appears to fall below unity in most of the nine cases across all probes at some point. This is indicative of the horizontal flow only and should be considered with this in mind.

$\Delta P/\Delta P_1$ at probe 1 in each case appears exaggerated and is so due to the location of the probe in relation to the flame. Probe 1 is located at the edge of the flame/ plume and the horizontal ΔP at this location in the ideal plume case is not well described by the centreline velocity. Instead, first principle analyses tend to approximate the horizontal inflow velocity toward/ into the plume edge at around 15% of the vertical centreline velocity at the same height (z) above the fuel source. Since the probe 1 location does not change (approximately) relative to the leading edge of the flame during the axis-symmetric case and only by a small distance in the most tilted cases, the assumption of inflow at this location during the fully-buoyant case in the horizontal plane of 15% of the calculated centreline velocity is appropriate and is adopted for ΔP_1. The *increase* in velocity and thus ΔP_f at this location between the ideal and experimental cases is much greater than the increase observed at the locations of probe 3 and probe 5, which, due to their involvement with the flame in many of the tilted cases (as described previously) have adopted 100% axis-symmetric centreline velocity in the configuration of ΔP_1.

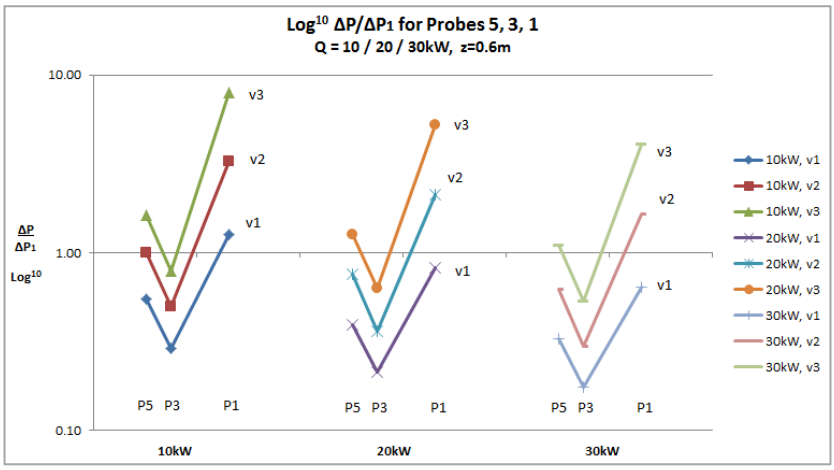

(a)

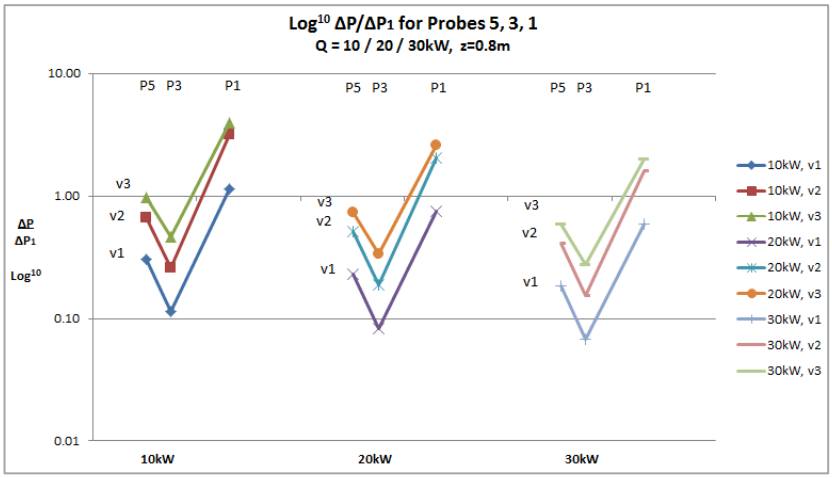

(b)

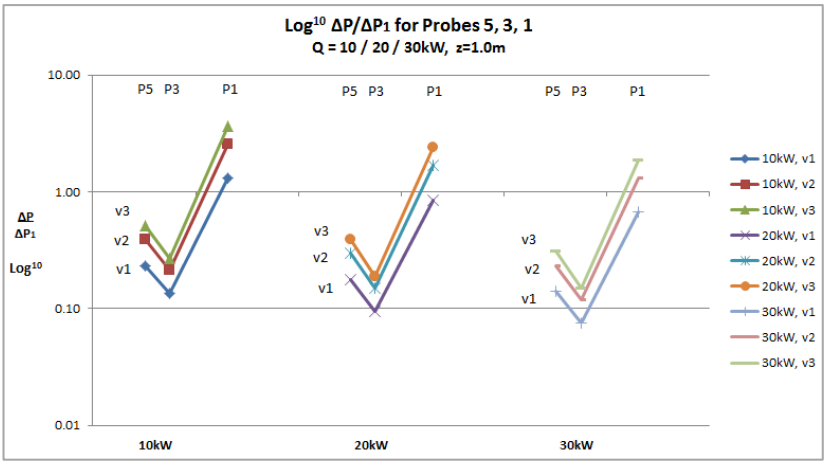

(c)

Figure 6.8: Differential pressure at each probe location for each cross flow case normalised by the fully-buoyant case. Fully-buoyant case pressure at probes 3 and 5 is based upon centreline velocity calculation (Ma*Zuk*) however at probe 1 the 15%-centreline velocity assumption is made for the fully-buoyant case since this location is at the outer edge just outside the flame boundary and is not well-described by the centreline pressure.

Figure 6.8 demonstrates approximately how the differential pressure at the leading and rear sides of the flame boundary change once the cross flow is added to the axis-symmetric case. Aside from the various descriptions above of the reasons why the graph data appears as it does, it is important to recall that one of the results of increasing Q in the axis-symmetric case and therefore the centreline velocity, is that the velocity of entrained air along the length of the plume under consideration is also increased. So to describe the story of increasing entrainment it is necessary to think about the problem from a global perspective, so to speak, encompassing the behaviour of the bulk fluid which is set in motion by the mechanics of the fire plume and as it becomes part of the plume structure itself. So even though the nuance of the negative pressure cross flow exists as a result of the aspirated fan set-up, the results across the width of the plume region, still afford an approximate inquiry into the nature of the changing fluid behaviour inside and around the plume region.

Crucially, what we can derive from this discussion is that in the cross flow case, it is no longer the size of the fire Q, and the apparent centreline velocity that controls the entrainment rate (or velocity) of air into the plume. This is reflective of the core theory outlined previously which is that the buoyant force of the flame and plume is no longer the sole force responsible for the description of the entrainment rate of the fire plume. The cross flow, regardless of its origin (aspirated fan/natural wind/perturbed fire wind), affects the entrainment velocity at the edge of the plume to a certain extent, and the interaction of the same cross flow with the flame region subsequently affects this boundary region further. It is perhaps intuitive then to imagine that the entrainment velocity of air at the leading edge of the tilted plume is affected by two separate but related mechanisms. Consider again figure 6.8 where the normalised pressure differential at probe 3 (the probe most commonly engulfed by the tilted flame – and therefore considered to represent an approximation of centreline data) is below unity. This is in part a function of the data chosen for

comparison (described in previous paragraphs) but also due to the complex and turbulent mixing of the cross flow fluid with the flame fluid. The physics in this region cannot be defined in great detail due to relatively sparse resolution of probes in the experimental set-up, nevertheless an approximate insight is sufficient to gain an understanding of the global phenomena occurring. It can be seen that although the pressure differential at the approximate plume centreline may not increase much, or at all in the presence of a relatively weak cross flow, the pressure differential at the leading edge of the flame can simultaneously be seen to approach an order of magnitude increase over that of the axis-symmetric case. The phenomenon is the result, as discussed above, of both the pressure created by the cross flow at that location, but also by the negative pressure gradient created by the hot flaming region, drawing air in to fuel the combustion process. Moving from left to right across figure 6.8 part (a), one can see that the relative increase in pressure differential at the leading edge decreases with increasing Q, since the velocities at the leading edge in the axis-symmetric case would have been greater to begin with, meaning that the portion of the increase assigned to the cross flow alone are relatively smaller with increasing fire size. To imagine a much larger fire and weaker cross flow, it is intuitive to realise that the increase in pressure differential at the leading edge in such a case would be small when considering the reduced relative magnitude of the cross flow. The same trend can be observed when moving across parts (a)-(c) where the relative magnitude of the cross flow reduces as the distance z between flame and fan is increased.

This discussion can be articulated visually in a series of graphs plotting $\dot{m}_e/\dot{m}_a$ against the average ΔP_f for all 27 cases. Again, considering the fan extraction rate to equate to the smoke mass flow for the inertia-dominated cases and to equate to part of the smoke mass flow for the buoyancy-dominated cases figure 6.9 demonstrates again the increase in mass flow and how it can be tied to an increase in the velocity and pressure differential across the fire plume in all cross flow cases. In this instance ΔP_f has been averaged across each of the probes, where the variation in ΔP_f at each

probe location was demonstrated in figure 6.8. Moving from a-c (z=0.6m - z=1.0m) shows again that the rate of increase in mass flow is more pronounced as z is decreased since the average ΔP_f diminishes with growing z. Furthermore the magnitude of $\dot{m}e$ can be observed to lessen as Q is increased, since the relative average ΔP_f is smaller when ΔP_B is increased, as discussed in the previous paragraphs in some detail. Within figure 6.9, $\dot{m}_e$ is again normalised by both equation 2-24 (Zukoski) and equation 2-25 (Heskestad). The normalised mass flow results given by the Heskestad ratio are marginally lower than those of the Zukoski ratio since the Heskestad correlation places slightly more significance on Q and Z than Zukoski and so the fact that Q and z variables do not affect the experiment extraction rates (v1, v2, v3) is further exaggerated by the comparison of these results.

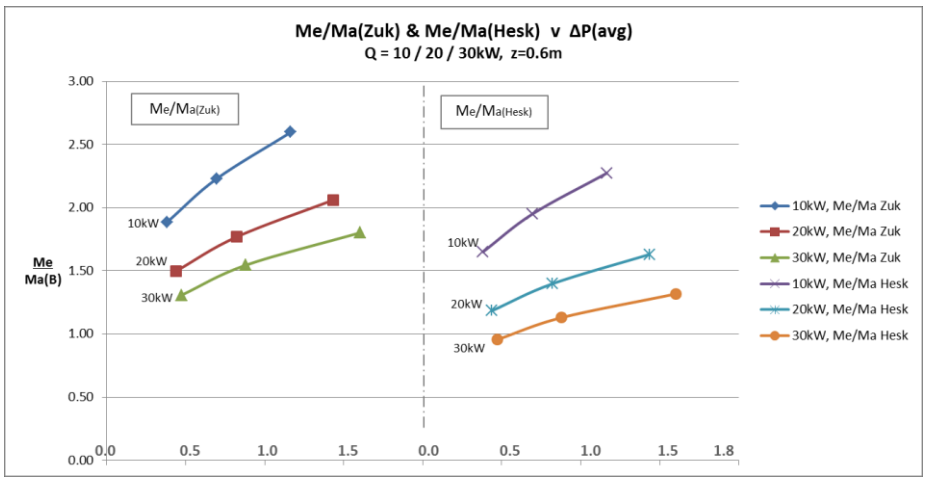

(a)

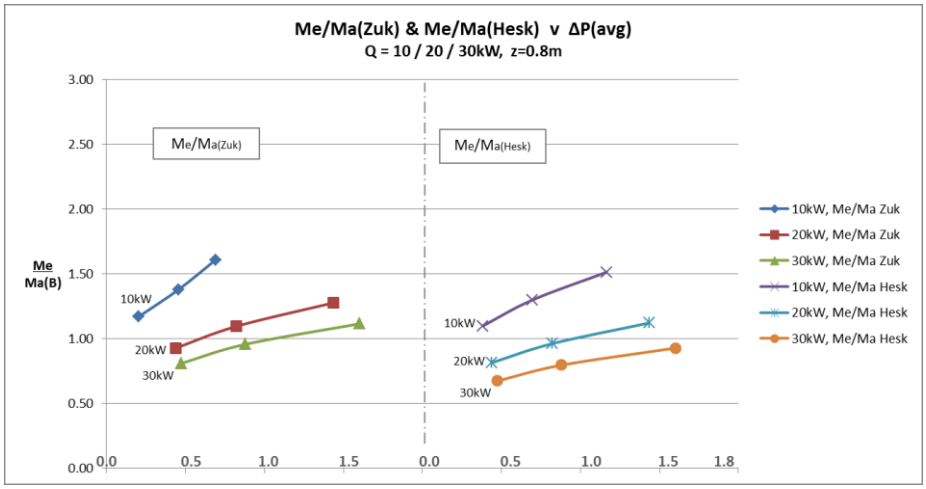

(b)

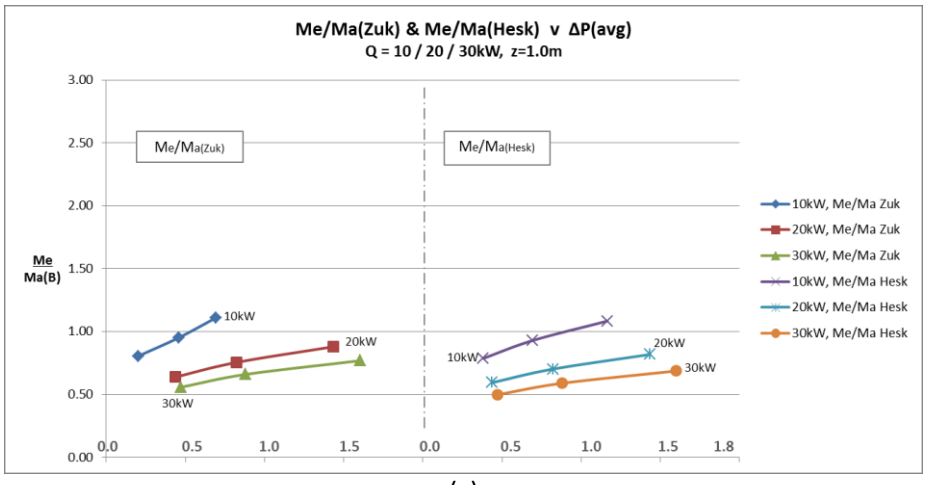

(c)

Figure 6.9: Normalised mass flow rates plotted against crossflow differential pressure demonstrating a positive relationship

6.4 Experimental Scenarios & Practical Implications

The aim of section 5.4 is to describe the data from section 4 and sections 5.1 - 5.3 in terms of the entrainment regimes that are produced across the 27 experimental cases and their theoretical application to the fire engineering approach.

Four cases of interest are defined that cover the range out mixed-convection cases; two extreme instances, the fully-buoyant regime and the inertia-dominated regime, and two intermediate examples, where buoyancy and forced-flow are both important. Each regime is depicted visually, qualitatively described and quantitatively investigated where practical.

In order for this to be possible the O_2 depletion data (figure 6.10) recorded in the exhaust hood calorimeter is presented for the relevant cases. The potential error in this data has been discussed previously and the apparent scatter in some of the data is commented upon in the following pages.

The analyses over the coming pages is semi-quantitative, however as well as the O_2 data, is also based upon data captured by the pressure probes, hood flow-rate readings, and from visual observation during the experiments, which is documented on both the IR camera and video-camera. The video camera data, and some of the physical flames characteristics which arise in this section are discussed in greater detail throughout section 6. Therefore, although general in some places, the analysis is considered to be of great worth, especially since such an investigation currently appears absent in the fire engineering literature.

The main goal of this section is to describe how the data from the previous sections can be utilised by the fire engineer in a practical sense.

Figure 6.10 demonstrates the reduction in O_2 as read by the hood calorimeter across each of the cases studied throughout the rest of the chapter. These include an inertia-dominated case where essentially all the smoke from the fire is captured by the fan, and two intermediate cases, one which tends toward inertia-dominance and

a second which tends toward buoyancy dominance. Preceding these cases, the theoretical fully-buoyant case is discussed.

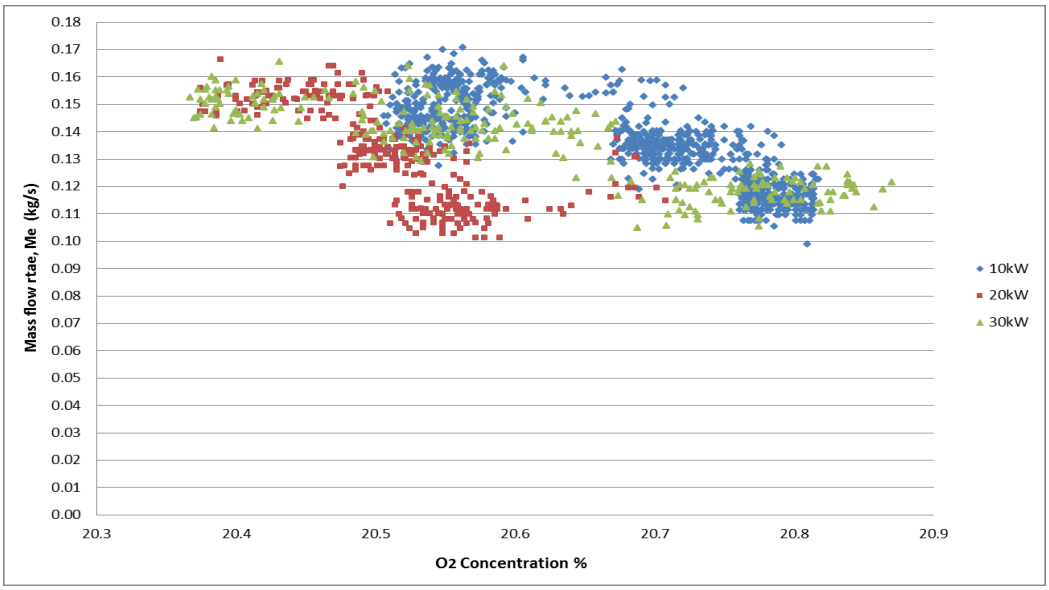

Figure 6.10: Hood calorimeter O_2 depletion data for the 3 example cases.

The graph above is quite complex and requires discussion upon all of the variables affecting each experimental case. For example, the 10kW fire data above shows three distinct clumps of data points, each corresponding to increasing fan speeds as the data moves from right to left. When the fire size is doubled to 20kW, the corresponding data shows a very similar pattern (in red) but with the data appearing further to the LHS, depicting a greater drop in O2 concentration at each data clump (at each fan speed). This is intuitive since the larger fire size should produce a greater mass of smoke and O2 concentration would be expected to be less, compared directly with the smaller fire size (10kW).

Less intuitive is the 30kW data (green) following a further increase in fire size. What we see here is that firstly there is a greater data spread, and the same well-defined clumps of data points do not appear. Despite the increase in smoke which would follow an increase in the fire size, the O_2 concentration for fan speed 1 appears

greater than that in the 20kW case (bottom right of graph data), and in fact is better aligned with that of the 10kW v1 case. This is most likely because of the greater buoyant force generated by the 30kW fire resulting in a greater portion of the smoke from this fire evading the fan which results in a less of an apparent O_2 concentration drop in the hood readings. As the fan speed is increased a greater portion of the 30kW fire smoke is captured by the fan and the data O_2 concentration is now aligned with (slightly less than) the 20kW concentration (top left of graph data).

The outcome of this brief discussion is that individual cases must be analysed in order to understand the O_2 concentration reading for each case and give a fuller picture to the entrainment story in each case. This is presented throughout the rest of the chapter.

6.4.1 Fully Buoyant Regime – The Traditional Plume Model

The fully buoyant case results in an axis-symmetric plume and equal in-flow velocities from all directions around 360 degrees where the plume velocity and entrainment velocities are driven by the buoyant force alone.

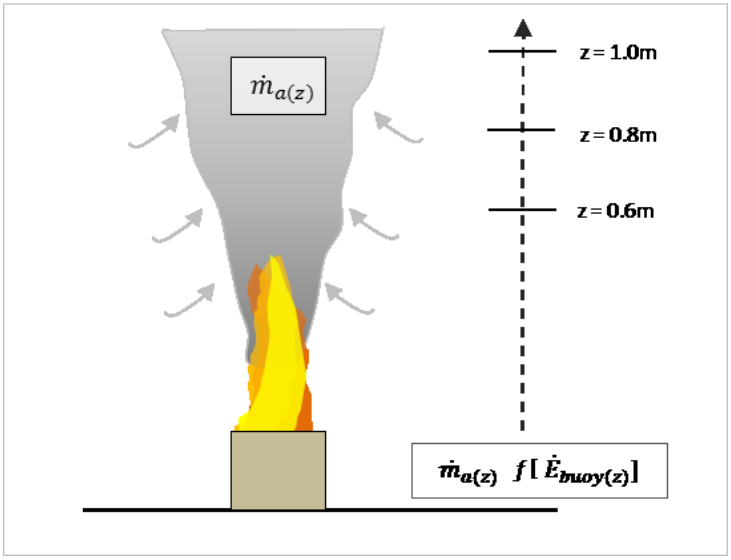

Fig 6.11: Fully buoyant plume entrainment

Entrainment in the fully buoyant (axis-symmetric) case is a function of the plume flow velocities which are generated by the pressure gradient resulting from the fire source alone. Gr/Re^2 for this regime leans to infinity since there is no forced horizontal flow. The equations presented in section 2.3 describe the ideal plume dimensional analysis which approximates the mass entrained along the plume body between the base and some height of interest. The plume mass flow rate is proportional to the distance along the z-axis which is of interest. For the fully-buoyant case therefore we can say that the mass flow $\dot{m}_a$ at some height z, is a function of the products of combustion $\emptyset$ from the fire size Q and the entrainment $\dot{E}$ due to the buoyant force along the same elevation on the axis z:

$$\dot{m}_{a(z)} = \emptyset_Q + [\dot{E}_{buoy(z)}]$$

Equation 6-1

For the purpose of this analysis it is helpful to think about a mass of combustion products being produced at the flame and that as they rise along the flame and beyond the combustion products are then mixed with more and more fresh air which is entrained through the sides of the plume which forms as a result of this buoyantly driven process. This rising, evolving mixture constitutes the fully-buoyant design mass flow $\dot{m}_{a(z)}$. In the case of the axis-symmetric, fully-buoyant plume the *total* mass flow for this scenario is equal to the mass flow of the buoyant plume:

$$\dot{m}_T = \dot{m}_a$$

Equation 6-2

6.4.2 Inertia-Dominated Regime

The inertia-dominated case is at the other end of the spectrum from the fully-buoyant case. There are steps to get from the buoyant case to the inertia-dominated case (intermediate cases) however it is preferable to outline the fully-buoyant/inertia-dominated cases first since they are more well-defined than the intermediate cases and set the boundaries within which the intermediate cases can be described. The experimental conditions which embody the inertia-dominated regime in the truest sense is that of the minimum z′ (0.6m) and minimum HRR (10kW) since in this case the forced-flow pressure gradient (stream-wise) induced at the location of the fire is the greatest in all the test cases and the buoyant pressure gradient (cross-stream) force is least, since this is the smallest fire size investigated. Gr/Re^2 was also the smallest compared with all cases at 1.3×10^{-3}.

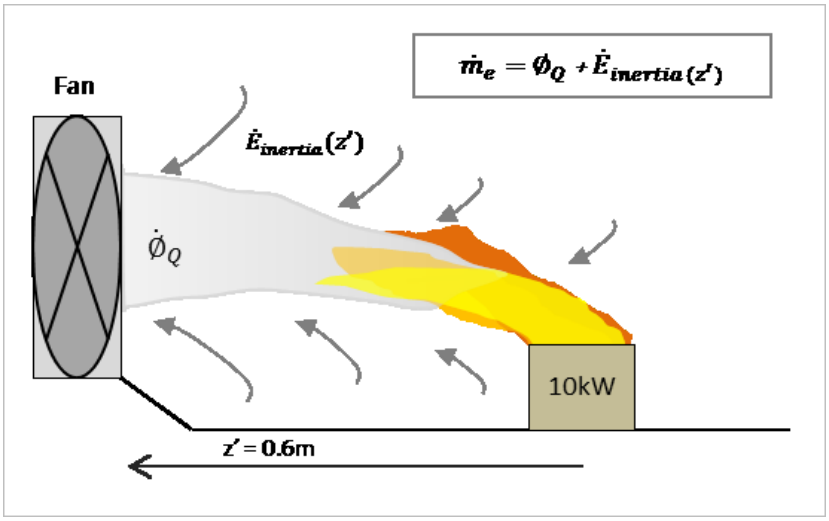

Figure 6.12: Inertia-dominated regime

In the inertia-dominated regime we will make the reasonable assumption that all smoke produced by the fire is captured in the exhaust fan flow. This was observed visually during experiments certainly, for the sake of discussion, for experimental *case 3*. In this case the flame was tilted to an average (horizontal-to-centreline) angle in the range of 30-35°. In this case, with the introduction of the exhaust fan we can introduce the mass flow captured by the fan, $\dot{m}_e$.

In section 5.1 the mass flow by the fan was normalised by the purely-buoyant plume mass flow, calculated for the same elevation, z, as was mirrored by the fan-to-flame distance z'. It is important to note that even though these distances are physically equal z is exactly vertical and is driven by the buoyant force and z' is considered horizontal and is driven initially by the fan-induced (horizontal) forced flow.

For experimental *case 3* the normalised entrainment rate, $\dot{m}_{e(z')}/\dot{m}_{a(z)}$ was averaged at around 2.5 suggesting that the mass of fluid captured by the exhaust fan was ~250% of that expected to be produced for the same downstream distance in the fully-buoyant case. The design mass flow rate in the fully-buoyant case is in the region of 0.065kg/s (Eq. 2-1) and the mass flow exhausted by the fan was averaged at 0.16kg/s. Clearly then, if we consider the mass exhausted by the fan to constitute

the mass of smoke produced due to the global processes then there is a stark increase in smoke mass. The critical factor, for life safety especially, is that the mass of smoke is substantially more dilute – if the species fraction is 1.0 for the fully-buoyant design case then has now been reduced to around 0.4.

There is an obvious trade-off in smoke density when the mass is increased. This analysis is simplified of course since one of the bounding parameters is that the fuel mass introduction rate is constant and cannot be influenced by any of the phenomena associated with the tilted flame environment such as higher O_2 delivery rate or increase heat flux to the fuel bed by the tilted flame.

In the instance of this extreme regime (again, best characterised by case 3) a quite general quantitative analysis can be applied. From figure 6.12 the oxygen depletion measured in the calorimeter hood flow during this case can be taken as 0.0045 (where no oxygen depletion would give 0.21). By noting that each kilogram of oxygen produces approximately 13,100kJ of energy (typically +/-5% error) [33] this can be introduced with the O_2 reduction fraction and the mass flow rate to estimate the HRR whereby:

$$\dot{Q} = 0.0045\%\ (O_2)\ \times 0.16 kgs^{-1}\ \times 13{,}100\ kJ = \sim 9.4 kW$$

Equation 6-3

This figure is a good approximation of the 10kW fire size as measured by the controlled propane fuel injection rate of 0.216g/s, considering the potential +/-10% error introduced in the hood calorimetry measurement. This interrogation of the O_2 content and exhaust fan flow rate is of course representative of the *increased mass/diluted smoke* flow which is the experimental output. To underline the issue, we can introduce the alternative figures that have been garnered so far. Since we know that the design mass flow rate ($\dot{m}_{a(z)}$) constitutes only 40% of the exhausted smoke flow ($\dot{m}_{e(z')}/\dot{m}_{a(z)} = 2.5$) and therefore the oxygen depletion factor has been reduced by a factor of 2.5, equation 6-3 can be rewritten inserting the mass flow the for the buoyant case:

$$\dot{Q} = (0.0045\%\ O_2\ \times 2.5)\ \times \left(0.16 kg s^{-1}\ \times \frac{1}{2.5}\right) \times 13{,}100\ kJ = \sim 9.4 kW$$

Equation 6-4

Although this is simply the introduction of a factor and its inverse, it completes the circle to demonstrate that the products of combustion have been captured by the exhaust fan forced flow and mixed with fresh air which is entrained as a function of the horizontal flow over the length z'. This concept is important when moving on to attempt to characterised some less well-defined intermediate regimes and can be described in s short description by:

$$\dot{m}_T = \dot{m}_e = \emptyset_Q + \dot{E}_{inertia\,(z')}$$

Equation 6-5

Where $\dot{m}_T$= total smoke mass flow, $\dot{m}_e$ = the mass flow captured by the exhaust fan over to the length scale z', and $\dot{E}_{inertia\,(z')}$ = the entrainment of additional fresh air over the length z' as a result of the forced flow.

Furthermore the mass of fresh air entrained is a function specifically, of the local velocities within and around, as well as the diameter of, the horizontal flow field and is *indicative* of the impact had the fan been located upstream and pushed a forced flow across the flame. Although the local velocities within and around the horizontal plume are a function of the fan strength the magnitude of these velocities is integral in the story of the increased smoke mass $\dot{m}_e$ captured by the exhaust fan.

6.4.3 Intermediate Regime 1 (Inertia-controlled)

In the inertia-dominated case of section 5.4.2 the differential pressure gradient induced by the exhaust fan causing the forced cross flow was significantly greater than the vertical pressure differential resulting in the buoyant flow - approaching an order of magnitude averaged over the experimental length, z'. The experimental parameters which we can alter along the spectrum moving from the inertia-

dominated regime to the fully-buoyant regimes are primarily, the fan speed and the fire size Q. Subsequently the fan-to-flame distance (z′) may be altered. Increasing z' is comparable to increasing the relative buoyant force at the flame and decreasing z' is comparable to increasing the relative forced flow at the flame. The benefit of altering z' therefore is to manipulate the buoyant design mass flow $\dot{m}_a$ with respect to height (z), since in terms of cross flow experiment data, increasing the HRR manifests only in a reduction in O2 depletion following hood readings. In the fully-buoyant case the entrainment rate increases as the HRR is increased. Relying on O_2 measurements is problematic however since increasing the HRR in the experiment brings a further level of complexity to the entrainment story. This further complexity is demonstrated as we consider two iterations of the transitional regime between the well-defined inertia-dominated and fully-buoyant cases.

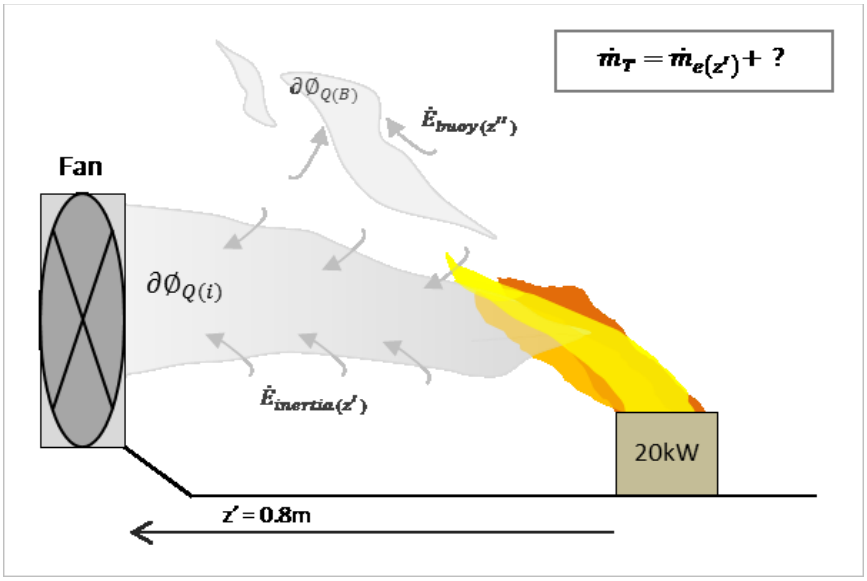

Figure 6.12: Intermediate regime 1 of 2

In the first intermediate case the HRR has been increased to 20kW and the fan-to-flame length z′ has been increased to 0.8m. These variations coincide with the median of the range of the variables – 0.8m is the intermediate option for length z' and 20kW is the same for fire size. The ratio $\dot{m}_{e(z')}/\dot{m}_{a(z)} = 1.0$ when averaged for this case which can be rewritten simply as $\dot{m}_{e(z')} = \dot{m}_{a(z)}$; the exhausted mass flow rate by the fan for z' is equal to the design mass flow at the equivalent height z. It

could be very simply approximated then that the entire smoke mass is captured by the fan and the buoyant and tilted cases are equal in product. This would be a poor approximation however - one of the benefits of formulating the Gr^*/Re^2 comparison for all cases is that intuition can be gained as to the buoyant magnitude of each individual fire case, in context with all other cases. For the current $\dot{m}_{e(z')} = \dot{m}_{a(z)}$ case Gr^*/Re^2 gives 10.8 x 10^{-3} and a horizontal-to-centreline tilt angle of around 60-65 degrees. In terms of the Gr^*/Re^2 ratio this case lies around half way along the inertia-dominated half of the scale. These characteristics demonstrate an increase in the buoyant magnitude of the fire against the previous inertia-dominated case (section 5.4.2) and so it can be inferred that a portion of the smoke in the $\dot{m}_{e(z')} = \dot{m}_{a(z)}$ case escapes the exhaust flow. O_2 depletion data can be analysed to corroborate this assertion. Depletion levels for this case average around 0.0049% reduction from ambient, which is very similar to the readings for the inertia-dominated case. Combined with the fan flow rate and energy per kilogram of oxygen consumed, following the premise of equation 6-3 gives an assumed HRR based on the exhausted smoke of ~8.73kW. This is just under half (~43%) of the actual 20kW HRR provided by the controlled burner in this case which means that since $\dot{m}_{e(z')} = \dot{m}_{a(z)}$, just over half (~57%) of the combustion products can be assumed to escape the fan flow. To simplify the discussion this can be referred to as a 50/50 split. Since the fan flow approximately equals the fully-buoyant design smoke mass flow rate we can say that half of the combustion product has been exhausted and twice the fresh air of the design rate has been entrained, thus approximately halving the concentration of the exhausted smoke compared with the fully-buoyant design case. The other half of the combustion products eludes the fan flow due to the magnitude of the buoyant force at the fire. The entrainment rate for the escaping smoke remains unquantified however this can be assumed in the best-case scenario to be similar to the entrainment rate of the fully-buoyant case following the axis-symmetric paradigm however given the inherent turbulence likely at the edge of the crossflow boundary and the residual stream-wise momentum it is more likely that the escaping smoke will also mix with air at a greater rate than the design rate

would suggest. This can be underlined by recalling the comments in [6] and [12] that "small disturbances" equated to significant increases in entrainment rate while measuring that of the design mass flow rate that is the baseline in this investigation. Due to the relative buoyancy of the fire in this case and the implication that this has as to whether combustion products remain within the exhaust fan flow or escape it, there are therefore two separate mechanisms that contribute to the overall entrainment story for this scenario. It can be described then that the total smoke mass flow rate ($\dot{m}_T$) in this case is given by the exhaust fan flow rate $\left(\dot{m}_{e(z')}\right)$ which includes a portion of the combustion products with respect to the inertia flow $\partial\emptyset_{Q(i)}$, and is roughly equivalent [in mass] to the design mass flow rate $\left(\dot{m}_{a(z)}\right)$, plus the additional air entrained above the fan flow field $\left(\dot{E}_{buoy(z'')}\right)$ which is a function of the quantity of the combustion product which evades the fan flow due to buoyancy $\partial\emptyset_{Q(B)}$. In the case of the entrained mass above the fan flow field (due to the buoyancy) the length scale z'' refers to a third axis which is of importance. Much of the combustion product which rises above the fan flow field due to buoyancy does so at some distance downstream of the flame. This suggests that the combustion product rising above the fan flow field have already been mixed with some mass of fresh air within the fan flow field and then rise above where entrainment and mixing continues but under a regime that probably resembles the buoyant entrainment rather than the forced flow entrainment below. It is important to note that this portion of combustion product has a very complex and changing entrainment journey. Before escaping the forced flow field it is contained within the inertial and then the transitional portion of the fire plume - akin to the boundary layer/transitional/plume modes described by in [24]. This complicates any approximation of the entrainment rate for the combustion product that escapes the fan flow, however at the very least we can denote the related length scale individually as z''. This discussion becomes more apparent in the second intermediate case that follows where it is visually represented with a diagram and a qualitative equation which is then demonstrated with a quantitative example.

6.4.4 Intermediate Regime 2 (Buoyancy-controlled)

The second intermediate case can be thought of as an enhanced version of intermediate case 1. The same processes play out in this instance however with the forced flow rate decrease to fan speed v1, an increased fan-to-flame distance (z'=1.0m) and HRR increased by 50% to 30kW, the buoyant force relative to the fan forced flow is now substantially increased. Subsequently a greater mass of smoke evades the exhaust fan. Due to the manipulation of the parameters described above the ratio $\dot{m}_{e(z')}/\dot{m}_{a(z)}$ now equals 0.5 signalling that the fan can only exhaust half of the smoke produced by the design flow rate.

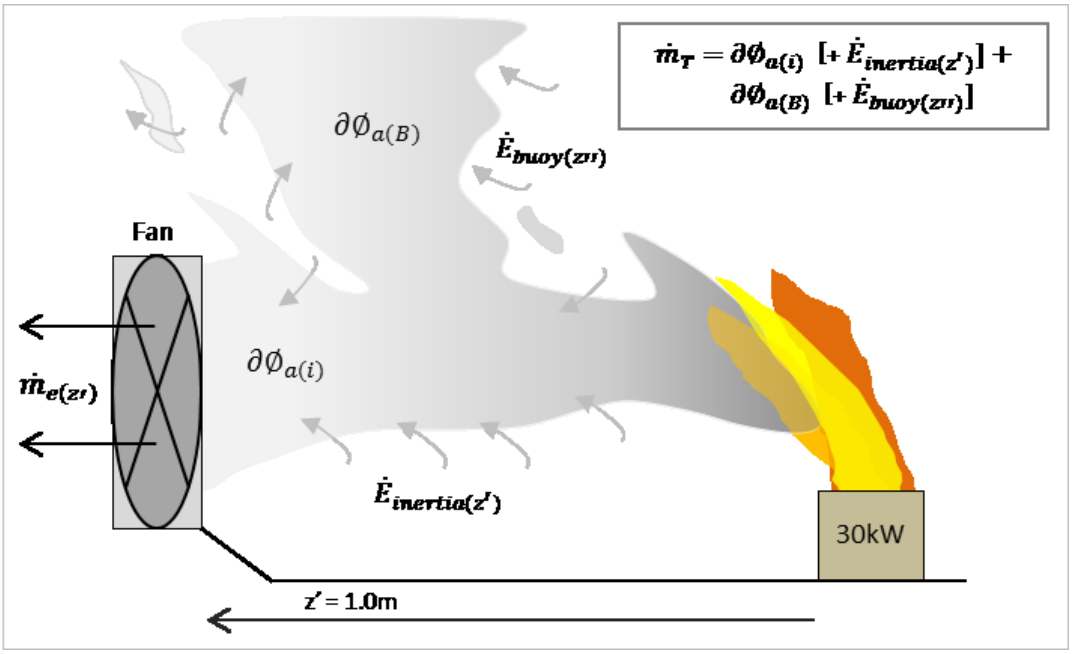

Figure 6.14: Intermediate regime 2 of 2

Figure 6.14 depicts this scenario whereby a portion of the combustion product ($\partial\phi_{a(i)}$) is captured by the fan flow after entraining air as a result of the horizontal forced flow ($\dot{E}_{inertia(z')}$), with the remaining portion of the combustion products ($\partial\phi_{a(B)}$) escaping the forced flow due to buoyancy and mixing with air at a rate ($\dot{E}_{buoy(z'')}$) approximately equal to or greater than that expected in the fully-buoyant case above the horizontal flow field. The total smoke mass flow rate for such a scenario, and applicable to all intermediate cases, can be written as:

$$\dot{m}_T = \left[\partial \emptyset_{a(i)} + \left(\dot{E}_{inertia(z')}\right] + \left[\partial \emptyset_{a(B)} + \left(\dot{E}_{buoy(z'')}\right]\right.$$

Equation 6-6

O2 depletion measurements for the 30kW fire cases typically present with greater scatter than the 10-20kW cases and the Gr/Re^2 for this case is 40 x 10^{-3}. In this second intermediate example (experiment case 27) the scatter is well pronounced and gives an O_2 depletion range of 0.05 - 0.2% corresponding with HRR based upon O_2 measurements of 3.1 - 4.6kW, well below the actual 30kW fire size based upon fuel injection rate. O_2 depletion measurements in the range of 1% would be expected if measured for $\dot{m}_{a(z)}$ - the fully-buoyant case - with the current fire size (30kW) and z (1.0m) therefore since the fan flow $\dot{m}_{e(z')}$ equals approximately half of the design mass flow $\dot{m}_{a(z)}$, it is reasonable to assume that around 1/8 of the combustion products are captured by the fan exhaust flow and the other 7/8 evade the forced flow due to buoyancy.

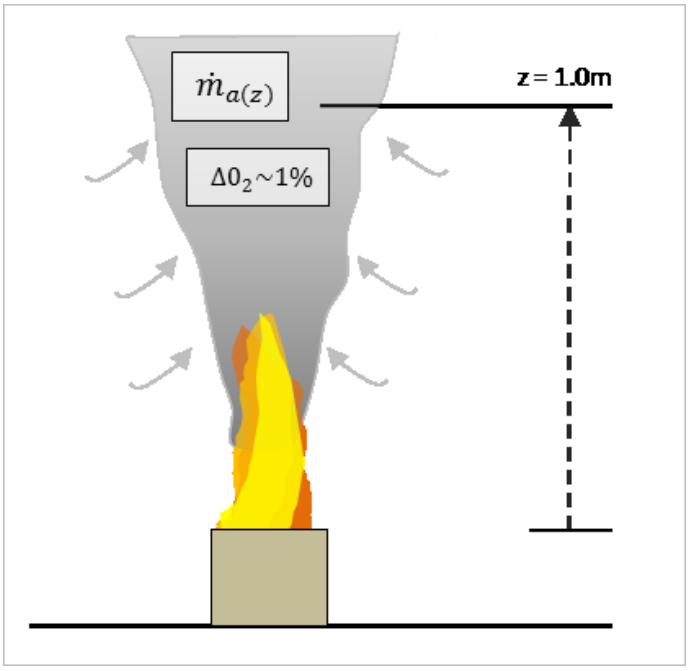

(a)

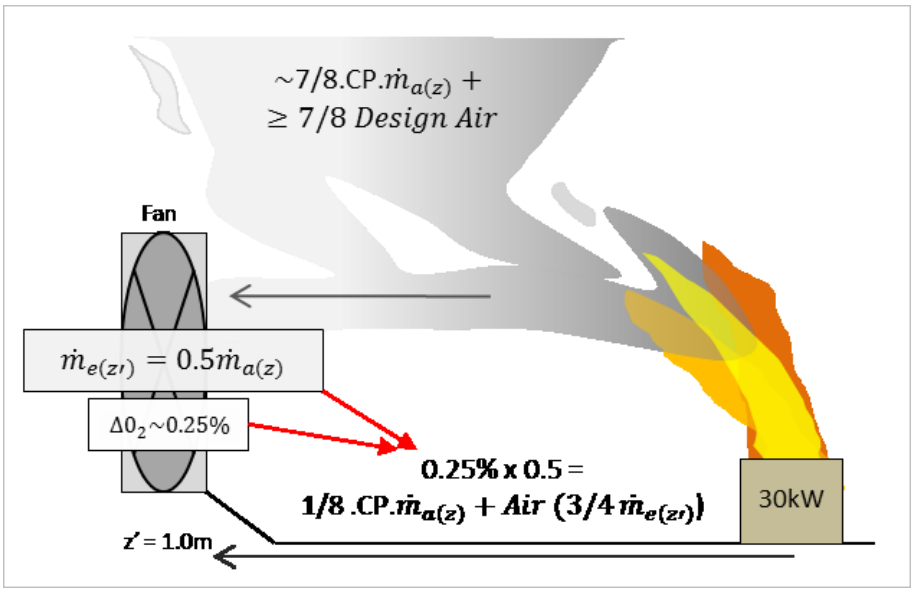

(b)

Figure 6.15: Intermediate 2 example case outlined with a course numerical model inserted – based upon flow rate and O_2 depletion measurements.

The portion of combustion product captured by the fan therefore mixes with additional fresh air and contributes to around 4 times the mass of smoke that 1/8 combustion product would have in the design mass flow rate but is of course diluted to around 1/4 the concentration. As for the 7/8 combustion product (the

majority of the smoke) that rises above the forced flow field; the best case scenario is as in the previous case that this portion entrains air as per the design mass flow rate. As discussed however this mixing is likely to be enhanced by turbulence and residual stream-wise momentum. This description of the flow behaviour for this case is depicted in figure 6.15 where it is helpful to think of the fan flow as made up of 1/4 by combustion products mixed with air at the concentration that would be expected in the fully-buoyant case, and the other 3/4 additional fresh air due to the nature of the forced flow field pressure. The remaining 7/8 of the combustion products are depicted to rise due to buoyancy and mix with fresh air as described above.

6.4.4.1 Additional Buoyant Flow Postulation

One further detail of interest is the physical impact that increasing the relative buoyant force with respect to the forced flow force has upon the behaviour of the buoyant combustion gases. In section 6 the need arises to for a brief discussion about the physical nature of the flame under the influence of a cross flow concerning the waves of buoyant pressure which correlate with the rising vortex structures of the flame. Subsequently the increased scatter noted in the O_2 depletion data for experiment case 27 - where the buoyant force is more comparable to the forced flow than was the case in the inertia-dominated case or even intermediate case 1, could be argued to align with the following postulation. What was not depicted in figure 6.15 was the buoyant gases that escaped the forced flow field immediately at the location of the flame due to intermittent waves of clear buoyant force dominance over that of the constant forced flow pressure. It is likely that, in combination with the downstream buoyant flow described for intermediate case 2, a portion of the escaping combustion gases rise immediately above the flame and entrain air at a rate more closely aligned with that of the fully-buoyant case. This is merely a nuance to the already unquantified buoyant entrainment portion of the overall entrainment story for each cross flow case, but it is important to note since

the qualitative analysis is of great importance in this investigation overall. Figure 6.16 outlines this idea.

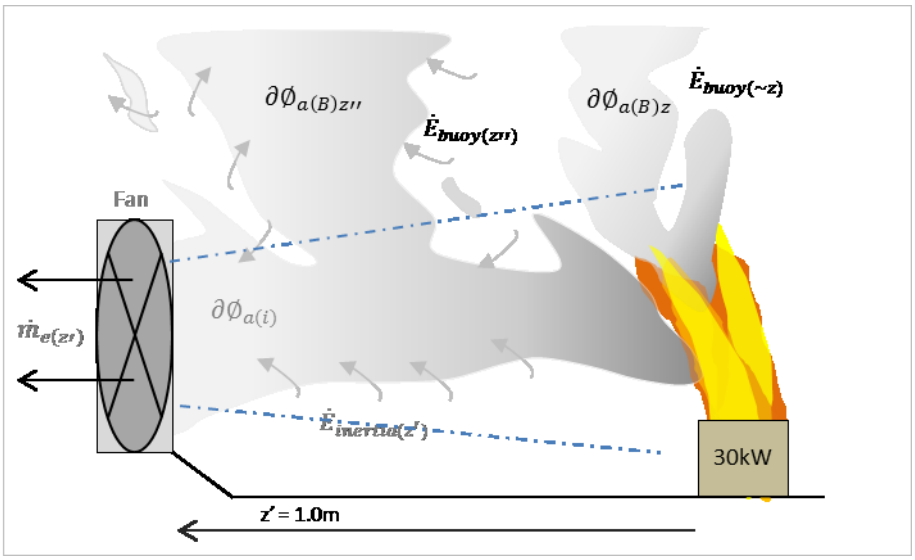

Figure example 6.16: The two extreme descriptions of buoyant entrainment in a mixed convection case where the buoyancy force tends toward dominance.

In figure 6.16 the two yellow flames represent the relatively large range of flame tilt angle prevalent when the fire size is large compared to the forced cross flow force. The flame angle averaging data and images from chapter 5 highlight this phenomenon well. When the flame tends toward vertical, sometimes corresponding with large, rising vortex structures, puffs of combustion product ($\partial\emptyset_{a(B)z}$) can escape essentially vertically upward (as if along the fully-buoyant *z-axis*), evading the forced flow field and entraining fresh air at a rate ($\dot{E}_{buoy(\sim z)}$) possibly similar to that in the fully-buoyant case along axis z. During forced flow-dominated moments the combustion product is swept downstream in the forced flow and is separated as some escapes upward ($\partial\emptyset_{a(B)z''}$) due to inherent buoyancy as previously discussed. The path of this portion is marked z'' to denote the journey of combustion product and gases across boundary layer, transitional and plume modes. Equation 6-6 can be rewritten to include this nuance as:

$$\dot{m}_T = \left[\partial\emptyset_{a(i)} + \dot{E}_{inertia(z')}\right] + \left[\partial\emptyset_{a(B)z} + \dot{E}_{buoy(\sim z)}\right] + \left[\partial\emptyset_{a(B)z''} + \dot{E}_{buoy(z'')}\right]$$

Equation 6-7

6.4.5 Experimental Scenarios Summary

Section 5.4 has been used to define 4 overall entrainment scenarios:

- Fully-buoyant
- Intermediate (roughly-evenly split)
- Intermediate (strongly buoyantly)
- Inertia-dominated.

The intermediate scenarios follow the same logic, as previously discussed, however the $\dot{m}_e/\dot{m}_a$ range is great, spanning between the two extreme cases and therefore deserves more detailed consideration, hence the inclusion of two intermediate scenarios.

What can be discerned from the results data in sections 4 and 5.1 - 5.3, and the qualitative descriptions of these data throughout section 5.4 is that the smoke mass flow rate - when inertia is strictly dominant - is controlled by the fan flow rate and the induced velocities of that flow, and the composition of the smoke is, in addition, a function of the HRR of the fire.

When buoyancy and inertia are comparable the smoke mass flow is partially a function of the fan flow rate/velocities but also an unknown entrainment rate outside of (literally, above) the fan flow. The quantity of combustion product that contributes to each mechanism is a function of the HRR in terms of particulate mass produced and residual buoyant force which, when pitted against the forced flow, governs the escaping smoke mass. The buoyant combustion products and the entrainment involving them may be subject to two similar systems, depending upon the physical characteristics of the flame.

Importantly, the Gr/Re^2 ratio has been a central theme throughout the results presentation and its importance can be further demonstrated here since it would be helpful to characterise all 27 of the main experimental cases within the context of the extreme and intermediate cases discussed throughout section 5.4. Because of the nature of the interdependent nature of the variables (HRR, z, fan speed) cases 1-27 do not rank in that order in terms of the Gr*/Re2 classification. A scale can be produced for all cases, with an overarching Gr^*/Re^2 classification. Here the cases discussed in section 5.4 are used as an example:

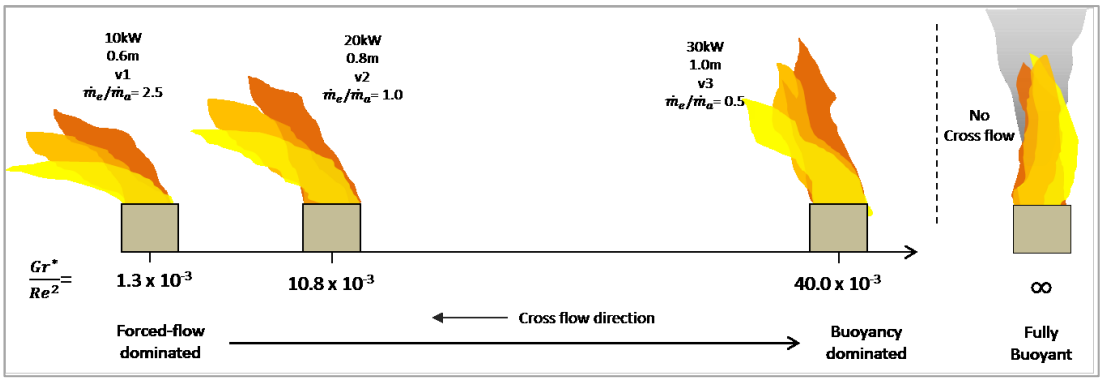

Figure 6.17: Location on the Gr^*/Re^2 scale of the four cases from section 5.4

In future it may be worthwhile for estimating total smoke mass flow from cross flow fire scenarios to assign a *first principle* or *mass balance* approach in describing the entrainment resulting from each of the processes defined within the four scenarios (inertial, fully-buoyant, 2 x intermediate cases). In order to do this the overall entrainment regime would need to be identified. This can be done by defining the expected mixed convection regime in terms of a Gr^*/Re^2 number along the forced-flow / buoyancy-dominated scale based upon knowledge of a design fire size and expected cross flow magnitudes (differential pressures), in a similar way that design fires are inserted into fire engineering designs while *assuming ambient* atmospheres. This does however, in the short term, require detailed investigations into each and all of the stages of entrainment outlined across all of the cross flow cases.

7 Discussion and Conclusions

In the closing section the analyses results, observations and theories derived throughout the preceding chapters will be noted in point form for a concise summary and followed by a closing discussion adding depth to the conclusions by presenting their worth in terms of a practical industry context.

7.1 A Summary of Conclusions

Concerning smoke mass flow from fire plumes subjected to a range of perpendicular forced flows, observations and analyses may be concluded as follows:

- **The smoke mass flow rate is found to increase with decreasing Gr/Re^2**
- **A decreasing Gr/Re^2 is indicative of increasingly important forced cross flow and decreasing relative buoyant force**
- A decreasing Gr/Re^2 also generally indicates a more tilted flame shape
- Exhaust fan capacity-to-design mass flow ratio ($\dot{m}_e/\dot{m}_a$) ranged from 2.5 – 0.5
- When $\dot{m}_e/\dot{m}_a$ is large (2.5), the exhaust fan flow is responsible for 100% of the smoke mass flow, and the mass flow rate is therefore controlled by the fan flow
- When $\dot{m}_e/\dot{m}_a$ is small (0.5) the fan has the potential flow rate required to capture 50% of that of the design smoke mass flow ($\dot{m}_a$). The fraction of $\dot{m}_a$ that the fan captures is then a function of HRR and fan-to-flame distance z'.
- There is a strong loss in exhaust fan smoke capture as z' is increased since this act increases $\dot{m}_a$ and has the simultaneous effect of decreasing forced flow pressure at the flame and increasing the relative importance of buoyancy
- This was reflected in the analysis where across the range of cases:
  When $\dot{m}_e/\dot{m}_a$ = 2.5, exhaust fan captured 100% combustion product, plus air
  When $\dot{m}_e/\dot{m}_a$ = 1.0, exhaust fan captured ~50% combustion product, plus air
  When $\dot{m}_e/\dot{m}_a$ = 0.5, exhaust fan captured ~13% combustion product, plus air

- Depending on case boundary conditions - HRR, z', fan speed - a certain portion of the fire combustion product may be captured by the fan flow and a portion may escape the fan flow due to buoyancy

Different entrainment rates are appropriate depending upon the flow regime of the combustion product (smoke):

- Combustion product captured by the exhaust fan entrains air at a rate proportional to the fan flow rate, and has been quantified with examples in Section 6
- Combustion product escaping the fan flow downwind of the flame may entrain air overall at a rate greater than $\dot{m}_a$ due to time spent in the forced flow field and increased turbulence at the boundary of the forced flow field. This rate requires quantification
- Combustion product escaping the fan flow directly above the flame may entrain air overall at a rate similar to that of $\dot{m}_a$ due to an essentially upward propagation. Increased turbulence compared to the fully-buoyant case may increase entrainment as per [6, 12, 19]. Decreased buoyancy due to a large portion of the hot gases being transported downwind may decrease the entrainment rate. The rate for such combustion product portions requires quantification
- There is therefore increasing uncertainty in these entrainment rate postulations as the flame cases become more buoyantly-dominated and more combustion product escapes the fan flow. Nevertheless the Gr/Re^2 ratio can provide definition of a scale on which to appropriate each case by accounting for the relative importance of the buoyant and forced flows at the flame location in each instance. This could be used to classify a known chosen fire size / cross flow velocity combination as tending toward being forced-flow dominated and therefore with a relatively well-defined resultant mass flow rate, or tending toward being buoyancy-dominated, and to what

extent, as the mass flow rate transitions closer to the magnitude of a fully-buoyant case.

Concerning fluid flow characteristics around fire plumes subjected to a range of perpendicular forced flows, observations and analyses may be concluded as follows:

- Cross flow fire plume is no longer driven solely by HRR (buoyancy). On this basis alone the traditional calculations are no longer appropriate. This is emphasized by the observation of an order of magnitude increase in the velocity of inflow air at the leading edge of the flame during cross flow conditions compared to the design inflow velocity based on axis-symmetric mass balance calculations.
- **Fire in cross flow has fundamentally altered characteristic fluid flow dynamics at and around the flame compared with the fully-buoyant case (increased velocity, turbulent wake to rear of flame)**
- **In the cross flow case plume velocity and inflow velocities are no longer solely a function of buoyancy**
- Entrainment flow, which is equal from all directions in the axis-symmetric case, is overwhelmingly a function of the forced flow direction
- Entrainment velocities around the cross flow plume are strongly dependent upon cross flow velocity. This becomes even more pertinent as the forced flow velocity is increased, highlighting further divergence from the naturally buoyant entrainment velocities directly tied to buoyant force in the axis-symmetric case
- The inflow of air comes predominantly from one direction (the direction of forced flow propagation). The flame therefore begins to act as a blockage for the forced flow and the air that is not immediately entrained in to flame fluid is diverted above and around the flame. This is in great contrast to the circumferentially equal axis-symmetric inflow
- Free crossflow velocities are increased substantially to the rear of the flame (downwind of the burner) following the addition of the flame to the free

cross flow. This aligns with the findings of [26] and [35] that a negative pressure wake is induced at the immediate rear of the flame invoking greater local flow velocities with a stream-wise propagation

- Velocities measured with pressure probes located inside the cross flow flame fluid tend to show an increase against free cross flow velocities at the same location demonstrating the increase to the stream-wise velocity of a flow field due to the addition of a cross-stream buoyant force
- Measured flame tilt angle was typically within 20% of that predicted, however significant erratic movement of the flame, especially when buoyant and inertial-forces are comparable suggests that flame tilt correlation should be used as an indication only. Time-averaged flame angle images suggest that flame may spend only a small amount of time at the average angle
- Cumulative buoyant force, characterised by Gr, increased over the length of the flame. This was true for the vertical and tilted flame. This is suggested by the Gr derivation and the behaviour of the tilted flame in exhibiting a vertical, strongly buoyant portion downstream, despite the incremental increase in forced-flow pressure as one moves downstream

Specifically, within the near-field flame region, numerous observations of worth may be summarised as follows:

- Visual observation using video stills and Fourier Transform investigation based upon pressure probe data in and around the flame suggest that vortex generation is similar in frequency for comparable cross flow and axis-symmetric cases.
- Increased turbulence, less well-defined vortex structures and shorter vortex lifespans (in terms of time and distance) are evident with increasing cross flow velocity. These are underscored by an increasing range of contributing hydrodynamic pressure frequencies with which the pressure probes are subjected to as turbulent flame fluid movement increases.

- Given both the small variation in vortex frequency and the increase in mass flow rate with increasing cross flow pressure, the importance of diffusive entrainment in the near-field is supposed to increase dramatically and the previously dominant entrainment mechanism of engulfment by rising vortex structures is supposed to contribute less to the total near-field entrainment rate.
- Downstream, when the cross flow flame tends toward becoming buoyantly-dominated, a strict directional change is often noted in the flame shape and propagation, resembling the structure characterised by [24] as the boundary layer, transitional and plume modes. Vertical tendencies occurring in the flame typically correspond with rising buoyant vortex structures.
- In cases that tend toward inertia-dominance the upright flame tip characterising the plume mode is observed less and instead a more substantially tilted flame (which appears close to horizontal at times) occasionally breaks from the cross flow pressure field and momentarily stands upright (corresponding with rising vortex) before quickly returning to the strongly tilted position.
- Near the burner, with increasing forced flow dominance, the luminous flame sheet appears to be weighted toward the leading edge of the burner where the oxygen delivery rate is greatest. To the rear of the burner little luminosity is apparent by comparison, presumably demonstrating the comparatively small mass of oxygen inflow in the wake region at the rear edge of the burner. This observation is indicative of the increased entrainment velocity unevenly distributed around the circumference of the flame boundary.
- Following on from this an unstable tilted laminar region is observed at the leading edge (tilted, across the burner surface) which regularly births the early stage fluid dynamics of developing vortex structures. As vortex rings are born in the fully-buoyant case they are a function of the shear stress at the flame / bulk boundary and are driven solely by the buoyant force of the fire. In the strongly tilt case the laminar region is almost horizontal and

intermittent buoyant waves occasionally breach the laminar surface rising vertically, a few centimetres. The vortex eddy motion then appears to develop in the stream-wise direction (almost horizontal) driven mainly by the horizontal forced flow, before the vortex enters the transitional and then plume modes of the flame where its motion appears eventually vertical and buoyantly driven. In the most strongly of forced flow cases the vortex never attains vertical propagation and dissipates rapidly along the severely tilted flame direction.

Areas of interest concerning future research include:

- Extensively variable noise data is generated in pressure probe readings depending upon probe location at/in/around the flame/plume. With low momentum flow data frequencies and wave amplitudes can be correlated between probes. At greater pressure (flow velocity) the inherent turbulence is beyond the capability of the probes to acutely define. General pressure trends as variables are manipulated are always clear however. High resolution data capture mechanism such as particle image velocimetry (PIV) may be of great worth particularly in and around the flame near-field and for the complex fluid flow in the negative pressure wake to the rear of the flame.
- A second collection hood to capture the buoyant smoke that escapes the fan flow would be beneficial. Once examples of this escapee entrainment flow are quantified, they can be combined with the exhaust fan flow smoke as an indication of total smoke mass flow. This data can then be compared with a "pushed" flow regime for comparison.
- Entrainment in the continuous flame region in cross flow conditions is an area ripe for study. The increased inflow velocity in this region due to a forced cross flow affects the importance of the gulping entrainment of rising toroidal vortex rings, compared with the fully-buoyant case. The importance of this particular area might be emphasized when scaled up to the wildland

fire case where the near-field flame region is significant in relation to total flame height / physical fire size.

- Finally, placing the cross flow case in the context of a compartment, similarly to [19] is crucial. With further quantified results from tests in the vein of that in this work, compartment effects can be more precisely understood. Work is currently underway at University of Edinburgh that may potentially allow such compartment-based, cross flow entrainment data.

7.2 Closing Discussion

Fires subjected to a forced cross flow present a transitional regime in terms of flow characteristics, velocities and natural/forced pressure gradients responsible for driving the flow and subsequent corresponding entrainment rates. The fact that perturbations to the natural fire in-flow can substantially increase the apparent entrainment rate through enhanced mixing has been documented only briefly within reactive plume entrainment literature and approximations of the magnitude of such increases are not accompanied by focused-investigation to characterise the inherent dynamics.

The addition of a perpendicular forced horizontal flow (20, 24, 39], or even a unidirectional in-flow which is driven by the buoyant mechanism [19], physically alters the axis along which the plume propagates and entrains, and a paradigm shift away from the Gaussian profile assumption occurs. When the flame and plume are tilted sufficiently the buoyant force, which drives the stream-wise flow in the axis-symmetric case, begins to act increasingly as a cross-stream force with two particular outcomes. The buoyant cross-stream force enhances the velocity of the forced flow which had resulted in the tilted plume propagation in the first instance, and subsequently when great enough, the buoyant cross-stream force is responsible for driving the downstream flame and combustion product upward and in the current experimental set-up, out of the horizontal flow field. This results in two

specific entrainment mechanisms; forced flow entrainment - a function of cross flow strength and flow-field diameter, and a pseudo-buoyant entrainment mechanism, perhaps resembling the fully-buoyant case but greatly perturbed, at the cross flow field upper boundary at least, by turbulence. When the increase in fire plume entrainment has been noted in the past, the entrainment measurement approaches were fixed around the buoyant entrainment mechanism and any enhanced entrainment processes were not deconstructed and described separately from the overarching axis-symmetric fully-buoyant paradigm.

This is to be expected since the fully-buoyant entrainment mechanism was the focus in the case of [6] and [12]. In the case of [19], entrainment at the flame, along the 'vertical' plume and along the ceiling hot-layer, all contributed to the *total* entrainment rate as articulated at the smoke out-flow at the compartment opening. Following these works little has been done to characterise and quantify the fundamental impact of the forced flow upon the mechanics of fire plume entrainment. The non-reacting atmospheric plume analogy is not suitable since the entrainment rate, although altered due to the mixed flow regime, does not describe the important nuance introduced by a hot, reacting source at the scale of interest for a fire in a modern building compartment or infrastructural setting. The requirement therefore was to characterise first a physical description of the fire plume under a perpendicular mixed convection case, and subsequently to gather meaningful data of the deconstructed entrainment processes.

Probably most cross flow cases in reality are pushed flows rather than pulled, nevertheless, the pulled flow provides the opportunity to separate the flow regimes since the inertia-driven portion comes to a well-defined and quantifiable end in the exhaust fan collection hood. The pushed flow results in the entire forced, transitional and buoyant entrainment flows being combined, and quantifiable only if the entire smoke mass is realised in the eventual buoyant plume portion, and collected in a traditional hood giving one global mass flow result. We can see from the experiment results that the inertia entrainment (boundary layer mode) and

perturbed buoyant entrainment (plume mode), as well as the transitional regime present starkly different rates of mass flow ($\dot{m}_e/\dot{m}_a$ = 2.5 in case 1, for example, relating only to forced flow entrainment, and $\dot{m}_e/\dot{m}_a$ = 0.5 in case 27). It is therefore imperative that the mixed convection entrainment story be broken down into entrainment components, each component qualified and quantified, in to provide a fundamental understanding of what general physical processes and flow dynamics are responsible for the increase in entrainment rate in a range of cross flow cases.

The cross flow (the pressure differential applied perpendicular to the natural fire plume propagation) is problematic for the fire engineer since it adds another unknown to the design scenario which the performance-based fire engineering approach is based upon. A design fire would now have to be coupled with a design forced-flow, or likely a range of forced flows. A realistic approach would be to approximate what the worst case magnitude of cross flow velocity would be coupled with the design fire in terms of smoke production – comprised of mass flow rate and smoke optical density. On one hand an increased smoke mass flow rate is undesirable since a greater volume can reach ever further and could impact more people, or inhibit more paths to safety. On the other hand a diluted smoke mass loses buoyancy - perhaps through 60% dilution as per experiment case 1. Stratified and low hanging smoke are problematic for a smoke management system based upon a large, strongly buoyant, and "worst case" (in terms of unwanted heat transfer) design fire. The question of redundancy in plume calculations for a tall space (such as an atrium, auditorium or a shopping mall) comes into question when the smoke is diluted through increased fresh air entrainment and, moreover, is directed horizontally away from the source, destroying the buoyantly-driven, hot rising plume model, and scattering cooler smoke over a large area at low elevation. An adjacent area may well be presumed to be 'safe' under the design fire scenario where combustion products rise vertically upward toward roof mounted extraction fans. Many petrochemical processing plants and offshore oil & gas installations rely, in certain hazardous-classified areas, on fire detection by heat and/or smoke

detection, mounted at elevation, in environments where strong winds are commonplace.

The exhaust fan (*pull*-design) allows an understanding and gives some intuition of smoke mass flow for practical design scenarios in industrial settings also. Tunnel and car park smoke control systems utilise longitudinal fan systems which invoke strong horizontal pressures and tunnels themselves can invoke strong natural through flow depend on design and location. Turbine enclosures and forced-flow ventilated hazardous-area halls on petrochemical sites often utilise high air-change rates, induced by powerful positive or negative ventilation systems to minimise the chance of hazardous gas clouds forming following accidental leaks.

Throughout the many potential cross flow fire scenarios imaginable, positive and negative pressure systems are valid, from mechanical extract to natural wind flow. The benefit of this work is in the deconstruction and identification of mixed convection components. A positive (pushed) forced flow scenario is likely to include the forced flow-dominated, transitional and buoyant entrainment modes and a negative (pulled) cross flow scenario is likely to exhibit a forced flow-dominated mode with varying levels of buoyant entrainment depending upon the boundary conditions of the precise scenario, as outlined extensively within this work. The exhaust fan scenario recreates the forced flow-dominated portion of the cross flow fire case and makes quantification of this mechanism possible.

Following further quantification of transitional and buoyant entrainment in the cross flow fire case, a scale based upon Gr/Re^2 could be defined (a more rigorous version of the example presented in chapter 6.4.5) whereby the extent of forced-flow and buoyant entrainment regimes can be approximated based upon the balance of buoyant and forced flow pressure in any fire-cross flow case. Critical cross flow velocities corresponding with a range of fire sizes should be established. These parameters could offer a first approximation of the increase in smoke mass flow rate against the design mass flow rate from the literature, by accounting for the

buoyancy *and* inertia-driven entrainment mechanisms which occur in mixed convection fire plume entrainment.

References

1. Morton, B.R., Taylor, G., and Turner, J.S., *Turbulent gravitational convection from maintained and instantaneous sources,* Proceedings of the Royal Society A, Mathematical, Physical and Engineering Sciences, 1956; 234(1196):1-23.

2. Schmidt, W., *Turbulente ausbreitung eines stromes erhitzter luft,* Journal of Applied Mathematics and Mechanics/Zeitschrift fuer Angewandte Mathematik und Mechanik, 1941; 21(5):265-278.

3. Yih, C.S. (1951) *In proceedings of the 1st U.S. National Congress applied mechanics,* American Society of mechanical Engineering, New York.

4. Rouse, H., Yih, C.S., and Humphreys, H.W., *Gravitational convection from a boundary source,* Tellus, 1952; 4(3):201-210.

5. Taylor, G. (1946) *Dynamics of a mass of hot gas rising in air.* Oak Ridge, Tennessee.

6. Cetegen, B.M., Zukoski, E.E., and Kubota, T. (1982) *Entrainment and flame geometry of fire plumes,* California Institute of Technology, Guggenheim Jet Propulsion Centre, Pasadena, CA. NBS-GCR-82-402.

7. Heskestad, G., *Fire plume air entrainment according to two competing assumptions,* Twenty-First Symposium (International) on Combustion, 1986;21(1):111-120.

8. Dritselis, C.D., Latridis, A.J., Sarris, I.E., and Vlachos, N.S., *Buoyancy-assisted mixed convection in a vertical channel with spatially periodic wall temperature,* International Journal of Thermal Sciences, 2013;65:28-38.

9. Zukoski, E.E., *Mass flux in fire plumes,* Fire Safety Science, 1994;4:137-147.

10. Thomas, P.H., Hinkley, P.L. and Theobald, C.R. (1963) *Investigations into the flow of hot gas in roof venting.* H.M. Stationery Office, Great Britain.

11. Morton, B.R., *Modelling fire plumes,* Tenth Symposium (International) on Combustion, 1965;10(1):973-982.

12. McCaffrey, B.J., and Cox, G. (1982) *Entrainment and heat flux of buoyant diffusion flames,* U.S. Department of Commerce, National Bureau of Standards, Washington, DC. NBSIR 82-2473.

13. Hasemi, Y., and Nishihata, M., *Deterministic properties of turbulent diffusion flames from low Q* fires,* Fire Science and Technology, 1987;7(2):27-34.

14. Tokunaga, T., Sakai, T., Kawagoe, K., Tanaka, T., and Hasemi Y., *Mass flow rate formula for the upward current above diffusion flames,* Fire Science and Technology, 1982;2(2):117-125.

15. Delichatsios, M.A., *Air entrainment into buoyant jet flames and pool fires,* Combustion and Flame, 1987;70(1):33-46.

16. Zhou, X.C., and Gore, J.P., *Air entrainment flow field induced by a pool fire,* Combustion and Flame, 1995;100(1-2):52-60.

17. Zhou, X.C., Gore, J.P., and Baum, H.R., *Measurements and prediction of air entrainment rates of pool fires,* Twenty-Sixth Symposium (International) on Combustion, 1996;26(1):1453-1459.

18. Hoult, D.P., and Weil, J.C., *Turbulent plume in a laminar cross flow,* Atmospheric Environment (1967), 1972;6(8):513-530.

19. Quintiere, J.G., Rinkinen, W.J., and Jones, W.W., *The effect of room openings on fire plume entrainment,* Combustion Science and Technology, 1981;26(5-6):193-201.

20. Torero, J.L., Bonneau, L., Most, J.M., and Joulain, P., *The effect of gravity on a laminar diffusion flame established over a horizontal flat plate,* Twenty-Fifth Symposium (International) on Combustion, 1994;25(1):1701-1709.

21. Brahmi, L., Vietoris, T., Rouvreau, S., Joulain, P., David, L., and Torero, J.L., *Microgravity laminar diffusion flame in a perpendicular fuel and oxidiser stream configuration,* The American Institute of Aeronautics and Astronauts (AIAA) Journal, 2005;43(8):1725-1733.

22. Audouin, L., Kolb, G., Torero, J.L., and Most, J.M., *Average centreline temperatures of a buoyant pool fire obtained by image processing of video recordings,* Fire Safety Journal, 1995;24(2):167-187.

23. Torero, J.L., Bonneau, L., Most, J.M., and Joulain, P., *On the geometry of laminar diffusion flames established over a flat plate burner,* Advances in Space Research, 1995;16(7):149-152.

24. Apte, V.B., Bilger, R.W., Green, A.R., and Quintiere, J.G., *Wind-aided turbulent flame spread and burning over large-scale horizontal PMMA surfaces,* Combustion and Flame, 1991;85(1-2):169-184.

25. Apte, V.B., and Bilger, R.W. (1987) *Measurement and control of air flow in the fire gallery at Londonderry occupational safety centre,* Mechanical Engineering Department, Sydney University, Australia. Contract Report F-15.

26. Nmira, F., Consalvi, J.L, Boulet, P., and Porterie, B., *Numerical study of wind effects on the characteristics of flames from non-propagating vegetation fires,* Fire Safety Journal, 2010;45(2):129-141.

27. Quintiere, J., *Some factors influencing fire spread over room linings and in the ASTM E-84 tunnel test,* Fire and Materials, 1985;9(2):65-74.

28. Knusden, J.G., and Katz, D.L. (1958) *Fluid dynamics and heat transfer.* McGraw-Hill Book Company, Inc., New York.

29. Lavid, M., and Berlad, A.L., *Gravitational effects on chemically reacting laminar boundary layer flows over a horizontal flat plate,* Symposium (International) on Combustion, 1977;16(1):1557-1568.

30. Lavid, M. (1974) *Buoyancy effects on chemically reacting boundary layer flows,* Thesis (PhD), State University of New York at Stony Brook.

31. Chen, T.N., and Toong, T.Y., *Progress in astronautics and aeronautics,* Heterogeneous Combustion, 1964;15:643.

32. Waldman, C.H. (1969) *Theoretical studies of diffusion flame structure,* Thesis (PhD), Department of Aerospace and Mechanical Sciences, Princeton University.

33. Krier, H., and Kerzner, H., *Analysis of the chemically reacting laminar boundary layer during hybrid combustion,* The American Institute of Aeronautics and Astronauts (AIAA) Journal, 1973;11(12):1691-1698.

34. Krishnamurthy, L., and Williams, F.A., *Kinetics and Regression,* Society for Industrial and Applied Mathematics, 1971;20(4):590-611.

35. Kolb G. (1996) *Etude d'une flamme non premelangee caracteristique d'un incendie en presence d'un ecoulement force,* Thesis (PhD), manuscript – unpublished), Faculté des Sciences Fondamentales et Appliquées, Universite de Poitiers.

36. Incropera, F.P., and DeWitt, D.P. (1990) *Introduction to heat transfer,* 2nd Edition, John Wiley and Sons, New York.

37. Raju, M.S., Liu, X.Q., and Law, C.K., *A formulation of combined forced and free convection past horizontal and vertical surfaces,* International Journal of Heat and Mass Transfer, 1984;27(12):2215-2224.

38. Sparrow, E.M., and Minkowycz, W.J., *Buoyancy effects on horizontal boundary-layer flow and heat transfer,* International Journal of Heat and Mass Transfer, 1962;5(6):505-511.

39. Leal, L.G., *Combined forced and free convection heat transfer from a horizontal flat plate,* Journal of Applied Mathematics and Physics, 1973;24(1):20-42.

40. Drysdale, D. (2011) *An introduction to fire dynamics,* 3rd Edition, John Wiley and Sons Ltd, Chichester, West Sussex, United Kingdom.

41. Karlsson, B., and Quintiere, J.G. (2000) *Enclosure fire dynamics,* CRC Press, London.

42. Thomas, P.H., Webster, C.T., and Raftery, M.M, *Some experiments on buoyant diffusion flames,* Combustion and Flame, 1961;5:359-367.

43. Thomas, P.H., Baldwin, R., and Heselden, A.J.M., *Buoyant diffusion flames: some measurements of air entrainment, heat transfer, and flame merging,* Tenth Symposium (International) on Combustion, 1965;10(1):983-996.

44. Yokoi, S. (1960) *Study on the prevention of fire spread caused by hot upward current,* The Building Research Institute, Ministry of Construction, Report No. 34, Japan.

45. Steward, F.R., *Prediction of the height of turbulent diffusion buoyant flames,* Combustion Science and Technology, 1970;2(4):203-212.

46. Cetegen, B.M., and Dong, Y., *Experiments on the instability modes of buoyant diffusion flames and effects of ambient atmosphere on the instabilities,* Experiments in Fluids, 2000;28(6):546-558.

47. Cetegen, B.M., *A phenomenological model of near-field fire entrainment,* Fire Safety Journal, 1998;31(4):299-312.

48. Luo, K.H., *Instabilities, entrainment and mixing in reacting plumes,* European Journal of Mechanics – B/Fluids, 2004;23(3):443-460.

49. Cetegen, B.M., and Ahmed, T.A., *Experiments on the periodic instability of buoyant plumes abd pool fires,* Combustion and Flame, 1993;93(1-2):157-184.

50. Pagni, P., *Pool vortex shedding frequencies,* Applied Mechanics Review, 1990;43(8);153-170.

51. Becker, H.A., and Liang, D., *Soot emission, thermal radiation, and laminar instability of acetylene diffusion flames,* Combustion and Flame, 1983;52:247-256.

52. Hamins, A., Yang, J.C., and Kashiwagi, T., *An experimental investigation of the pulsation frequency of flames,* Twenty-Fourth Symposium (International) on Combustion, 1992;24(1):1695-1702.

53. Zukoski, E.E., Cetegen, B.M., and Kubota, T., *Visible structure of buoyant diffusion flames,* Twentieth Symposium (International) on Combustion, 1985;20(1):361-366.

54. Zukoski, E.E., Kubota, T., and Cetegen, B., *Entrainment in the near-field of a fire plume, California Institute of Technology,* Daniel and Florence Guggenheim Jet Propulsion Centre, 1981.

55. Zukoski, E.E. (1995) *Properties of fire plumes,* In: Combustion Fundamentals of Fire, Academic Press Ltd, 101-219. ISBN 0121942309.

56. Malalasekera, W.M.G., Versteeg, H.K., and Gilchrist, K., *A review of research and an experimental study on the pulsation of buoyant diffusion flames and pool fires,* Fire and Materials, 1996;20(6):261-271.

57. McCaffrey, B.J. (1979) *Purely buoyant diffusion flames: some experimental results,* Centre for Fire Research, National Engineering Laboratory, National Bureau of Standards, Washington, D.C. NBSIR 79-1910.

58. Cox, G. (1995) *Basic considerations, in combustion fundamentals of fire,* Academic Press Ltd, London.

59. Zukoski, E.E., Kubota, T., and Cetegen, B., *Entrainment in fire plumes,* Fire Safety Journal, 1981;3(3):107-121.

60. Heskestad, G., *Luminous heights of turbulent diffusion flames,* Fire Safety Journal, 1983;5(2):103-108.

61. Thomas, P.H., *The size of flames from natural fires,* Symposium (International) on Combustion, 1963;9(1):844-859.

62. Heskestad, G., *Peak gas velocities and flame heights of buoyancy-controlled turbulent diffusion flames,* Eighteenth Symposium (International) on Combustion, 1981;18(1):951-960.

63. Thomas P H and Pickard R W. (1962) *Fire spread in forests and heathland materials,* Her Majesty's Stationary Office, London.

64. Pitts, W.M., *Wind effects on fires,* Progress in Energy and Combustion Science, 1991;17(2):83-134.

65. Nelson Jr, R.M., and Adkins, C.W., *Flame characteristics of wind-driven surface fires,* Canadian Journal of Forest Research, 1986;16(6):1293-1300.

66. Fang, J.B. (1969) *An investigation of the effects of controlled wind on the rate of flame spread,* Thesis (PhD), University of New Brunswick.

67. Welker, J.R., and Sliepcevich, C.M., *Bending of wind-blown flames from liquid pools,* Fire Technology, 1966;2(2):127-135.

68. Rios, J. (1966) *Interaction effects of wind-blown proximate flames from burning woods cribs,* Thesis (PhD), the University of Oklahoma.

69. Putnam, A.A., *A model study of wind-blown free-burning fires,* Tenth Symposium (International) on Combustion, 1965;10(1):1039-1046.

70. Cooper, L.Y., *Some factors affecting the design of a calorimeter hood and exhaust,* Journal of Fire Protection Engineering, 1994;6(3):99-112.

71. Klote, J.H., and Milke, J.A. (2002) *Principles of Smoke Management,* ASHRAE, Atlanta.

72. MathWorks. MatLab (2016). http://uk.mathworks.com/products/matlab/

73. Cowlard, A. (2009) *Sensor and Model integration for the Rapid Prediction of Concurrent Flow Flame Spread,* Thesis (PhD), University of Edinburgh.

74. Woodrow, M., Bisby, L., and Torero, J.L., *A nascent educational framework for fire safety engineering.* Fire Safety Journal, 2013;58:180-194.

75. Devenish, B.J., Rooney, G.G., Webster, H.N., and Thomson, D.J., *The entrainment rate for buoyant plumes in a crossflow.* Boundary-Layer Meteorology, 2010;134(3):411-439.

76. Netterville, D.D.J., *Plume rise, entrainment and dispersion in turbulent winds.* Atmospheric Environment, 1990;24(5):1061-1081.

77. Digidesign Pro Tools (2016). www.digidesign.com

78. Subbarao, E.R., and Cantwell, B.J., *Investigation of a co-flowing buoyant jet: experiments on the effect of Reynolds number and Richardson number,* Journal of Fluid Mechanics, 1992;245:69-90.

Appendix A:

Bi-directional pressure probe calibration method

The units tested for calibration were mounted 140mm from the end of a wind tunnel with the head aligned perpendicular to the flow direction and was calibrated against a laser Doppler anemometer. When stabilised conditions were observed, the measurement conditions were recorded. The air velocity was adjusted to the next condition, and once steady state conditions were achieved, the results were again recorded, this procedure being repeated until the calibration was complete. The results are derived from the average of at least l0 readings. The air velocity and unit-being-tested ΔP readings are referenced to standard conditions of 1013 mbar and 20°C = l.205kg/m^3.

Calibration Results

Air Velocity* (m/s)	Air Density (kg/m^3)	UUT ΔP (Pa)	Pitot Constant (K)	Pitot Constant (γ)	Pitot Constant (M)
0.30	1.170	0.06	0.925	0.962	1.055
0.59	1.170	0.23	0.896	0.947	1.072
0.96	1.170	0.66	0.841	0.917	1.107
2.02	1.170	2.94	0.836	0.914	1.110
3.00	1.171	6.47	0.838	0.916	1.108
3.96	1.171	10.91	0.865	0.930	1.090

Air Temperature during test : 27.8 - 28.1 °C
Atmospheric Pressure during test : 1011.0 - 1011.1 mbarA
Relative Humidity during test : 35.1 - 35.5 % RH

Figure A1: Example of pressure probe laboratory calibration results

The uncertainty of the above velocity measurements under laboratory conditions is +/- 1.0% + 0.lm/s + instrument resolution.

The uncertainty of the above air density measurements under laboratory conditions is + 0.15%.

The uncertainty of the above pressure measurements under laboratory conditions is +/-0.3% + 0.6 Pa.

Appendix B:

Discussion on the suitability of pressure probes based on simultaneous occurrence of pressure waves in the data

We can see in figure B1 that when each of the corresponding probes from each location (1/2, 3/4, 5/6) are compared that each pair of probes exhibits very similar data trends and many of the turbulent fluctuations resulting in seemingly-sporadic peaks are closely, and sometimes precisely, observed in the data from both probes. This highlights two points of interest. Firstly, across each vertical probe, where there appears to be a particular vertical flow trend (either downward or buoyantly upward) this is generally attributed to the horizontal fire flow-induced pressure gradient. For example at probe 6 the negative buoyant trend (and the small buoyant peaks near the LHS of the data set) correlate well with the horizontal inward flow at this location suggesting that the inward flow is also being read to an extent by the vertical probe. A depiction of this is given in figure B2.

Similarly part (b) shows that the observable trend is similar for probes 3 and 4 and a small number of positive fluctuations match precisely (positive for probe 3 relates to momentary pressure wave outward from the flame and for probe 4 this relates to an upward [buoyant] pressure wave). Again, fluctuations at probes ¾ are more pronounced than those at probes 5/6 due to greater proximity to the flame. A great similarity is also shared by probes 1/2 where the readings appear approximately constant with two large perturbations in the middle and toward the end of the data set. Horizontal probe 1 demonstrates small fluctuations in the first half of the data set between positive and negative flow directions, which might be assumed to be the balance between inward fire-induced flow, and hot expanding gases away from the flame. The large fluctuations suggest flows upward and inward with respect to the fire.

Secondly, the similarity observed here demonstrates that at the relatively low velocities achieved with the purely buoyant fire and no cross flow, the pressure probes are sensitive enough to detect small fluctuations in pressure that are observable in the data over and above the level of noise present in the data. As was demonstrated by the data in section 6.1.1 this detail appears to be lost when the cross flow pressure differential is added to the scenario. Even though the pressure differential at probe 1/2 location appears to remain fairly constant or even drop slightly once the fan is switched on, a general increase in turbulent flow all around the flame (affecting the way passing air packets interact with the edges of the probes) must be assumed to contribute significantly to the loss of this detail. This highlights the importance of being able to regress the noisy cross flow case data and rely on clearly observable pressure differential trends at each probe location to build the story of each case.

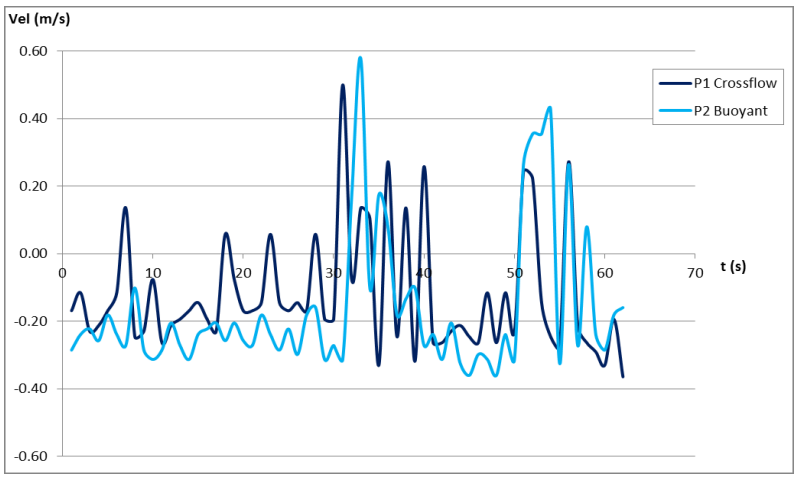

(a)

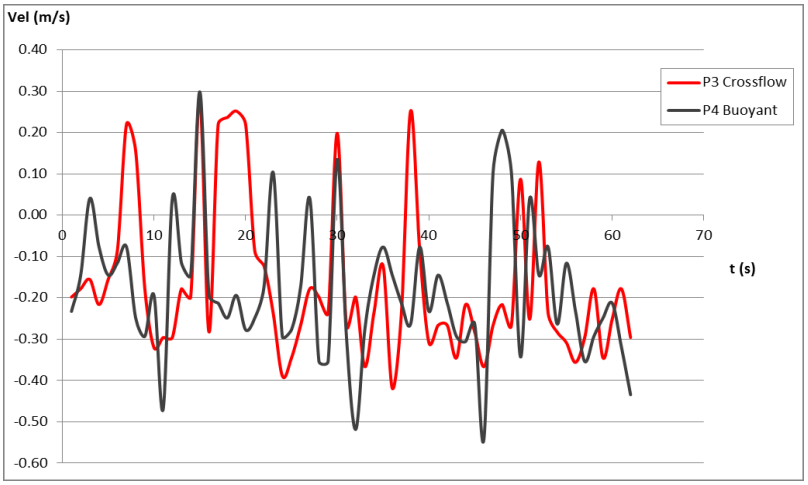

(b)

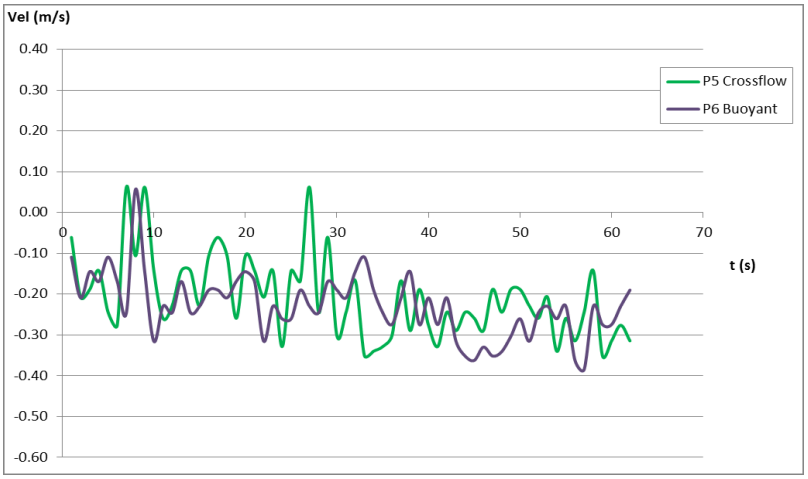

(c)

Figure B1: For each of the probe pairs (vertical/horizontal) pressure patterns can occasionally be observed to align very well demonstrating the scale of sensitivity of the perpendicularly aligned probe pairs

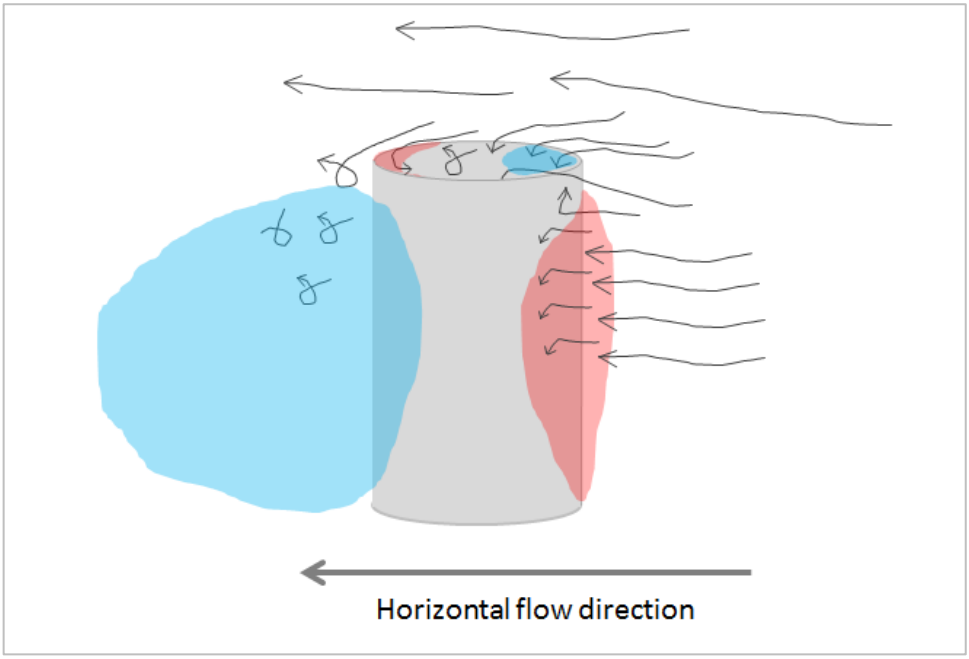

Figure B2: Example of the behaviour of a portion of a horizontal cross at the lip edge of a vertically aligned pressure probe resulting in negative readings which subsequently correspond with the horizontal readings in the same instance. This effect can occur equally at the underside of the probe, simultaneously. Red regions represent areas of high pressure due to contact with the perpendicular flow field and blue regions represent areas of low pressure where vortex streets may be generated as a result of the viscosity and horizontal flow magnitude.

Appendix C:

Impact of increasing z' upon pressure and velocity at probe locations

In terms of the *ideal* entrainment method, increasing z effectively increases the *surface area of interest* at the plume edge through which air is entrained and typically as z is increased, so the ideal entrainment rate increases proportionally. It is somewhat more difficult to demonstrate this proportionality for the mixed flow case since the effective mass flow rate (the extraction fan mass flow rate) is fixed by fan speed, regardless of the measure of z. Instead then we will consider how, in terms of these experiments, moving the flame further from the fan effectively increases the portion of entrained air which is as a result of the natural buoyant force against the fan-induced cross flow. We can then consider what this means for the interpretation of the mass flow results for each flame-fan configuration.

Figure C1 gives an overview of the decreasing ΔP_f magnitude with distance from the fan for each fan speed, each Q, and at each probe. The flame centrelines for z=0.6, 0.8 and 1.0m are marked on the graph for clarity and while the data lines are quite busy and often overlap, the general trend is quite clear. Simply, what this demonstrates is the *decrease in crossflow strength with distance*, and when we consider the flame located at each measure of z, we can describe this instead in terms of what is happening at the flame in each case. The further the flame is moved away from the fan the more buoyantly dominated the mixed flow flame becomes and at a certain point far enough from the fan the flame will in tend toward the ideal, fully-buoyant model. It is this *transition* from the inertia-dominated flame close to the fan, to the buoyantly-dominated flame far from the fan that is of interest in order to understand which of these cases can be directly analysed by the experiment set-up and which are more suited to a purely qualitative description.

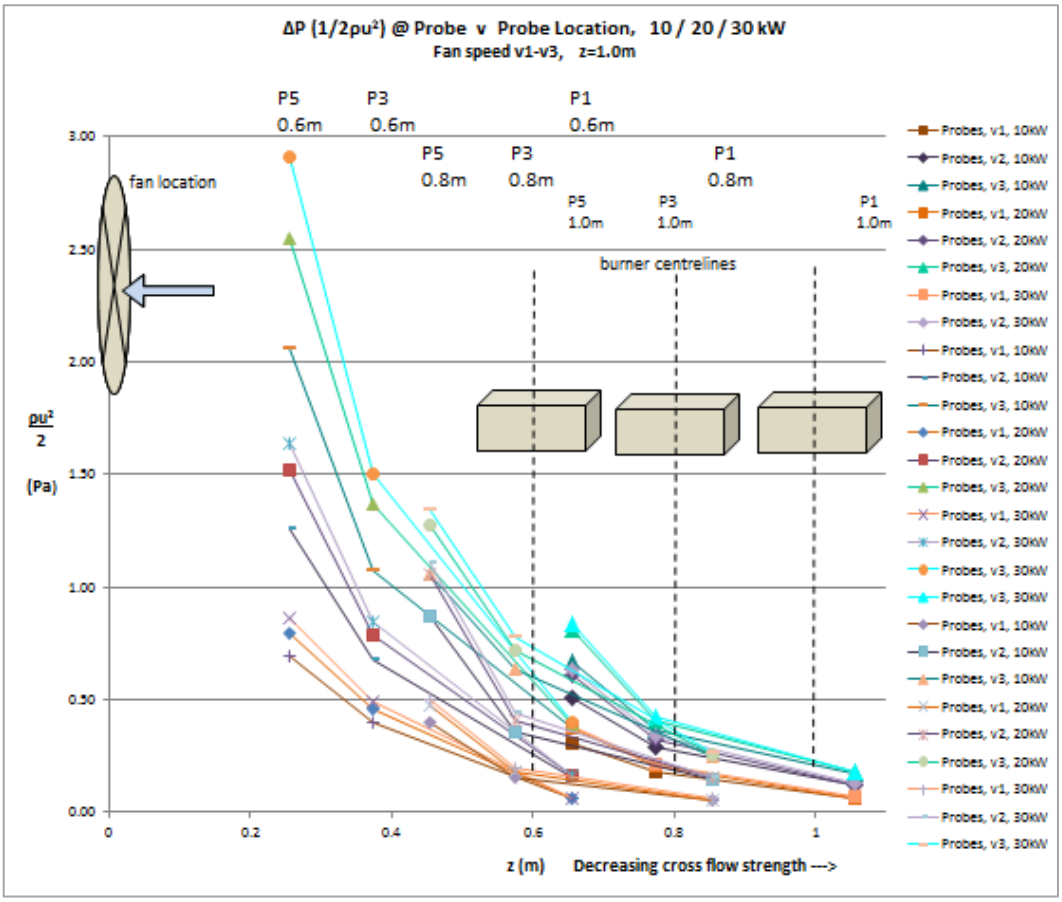

Figure C1: Overview of the decreasing ΔP_f magnitude with distance from the fan for each fan speed, each Q, and at each probe

Figure C2 breaks down the data from figure C1 by distance z'=0.6, 0.8 and 1.0m. Probes 5, 3 and 1 are spaced accurately on the graphs relative to each other, as they would appear on the experiment set-up. Maintaining the ΔP_f scale across the graphs demonstrates the reduction in ΔP for each fire size at each distance increment. Graph (a) demonstrates most clearly the increase in local velocities as Q is increased. By comparing with (b) and (c) it can be seen that the increase in ΔP as Q is increased is diminished as distance, z is increased. It is intuitive to note that the ΔP recorded at each probe as z is increased reduces, to varying extents depending upon the relative strength of Q. It can also be observed that the reduction in ΔP (most notably at probe 3 and probe 5) with increasing z is greatest for the larger fire sizes.

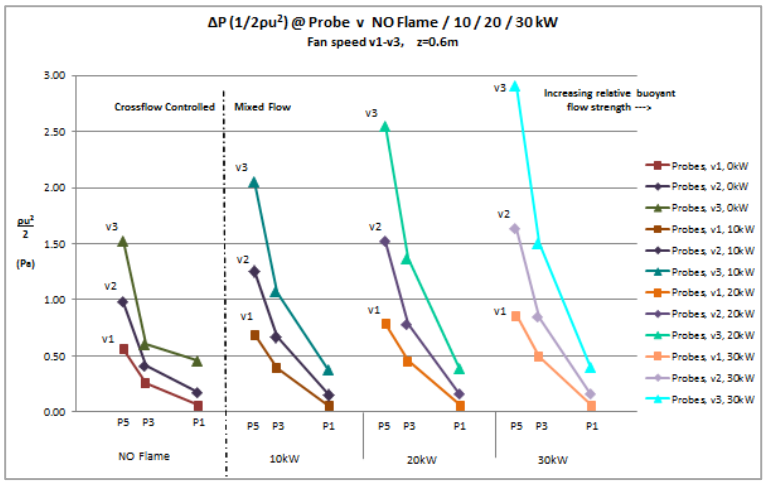

(a)

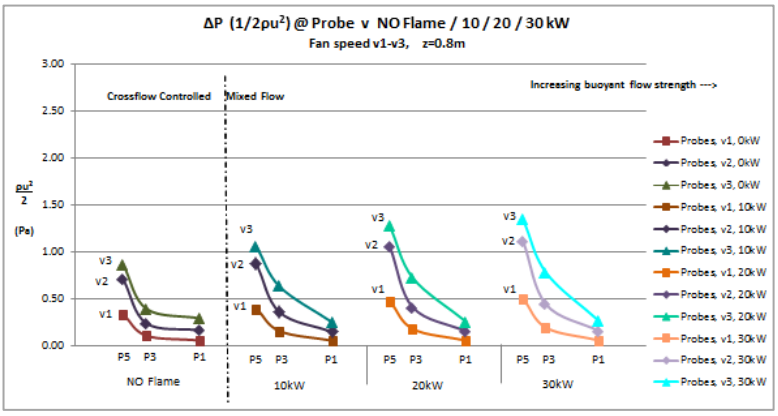

(b)

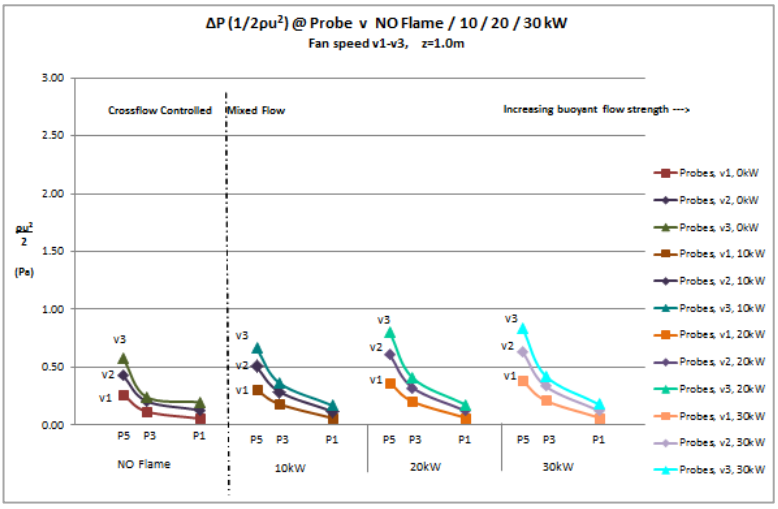

(c)

Figure C2: Break down of the data from figure C1 by distance z'=0.6, 0.8 and 1.0m. Probes 5, 3 and 1 are spaced accurately on the graphs relative to each other, as they would appear on the experiment set-up.

This is because the enhancement to local velocities (again most pertinently to probe 3 and probe 5) with increasing fire size is reliant upon the flame being significantly tilted toward these probes (and most pertinently this concerns probe 5). At the greatest distance from the fan (z=1.0m) the impact of the cross flow has become so low that the flame is not tilted far enough to significantly involve probe 5. Since the largest fire size (Q=30kW) had the greatest enhancement on the NO flame cross flow once the flame was added, the greatest reduction in ΔP due to increasing z is observed where Q=30kW.

Figures C3-C5 break down the data of figure C2 by distance, z and by fan speed (v1, v2, v3) in order to visualise the direct impact of increasing z in each instance. Approximate flame diagrams have again been included to help visualise what the data lines translate into in terms of flame behaviour as the balance of buoyant and forced flows changes from case to case. Data lines are also coloured coordinated with the previous two figures for reference. The 30kW flame can be seen to stand the closest to vertical in each case since this largest fire size has the greatest buoyant force. Since the 10kW flame has less buoyant force by comparison the cross flow ΔP effect is greater on this flame and a greater tilt is achieved. This trend can be seen across each distance of z where the ΔP readings, despite maintaining a similar trend, decrease with increased z. How the data trend lines correspond to flame behaviour can be visualised approximately as the flame images further from the fan in each graph are shown to be tilted less by the cross flow and increasingly stand closer to vertical as z increases. This describes the effect on the flame shape as the fire itself tends toward being buoyantly-dominated.

Part of the interest in the dominant-flow transition demonstrated across these graphs is that at some mid-way point the flow characteristics change. As we move the flame further from the fan there is a critical point where the flame ceases to be forced-flow dominated (where the flame and hot gases are overwhelmingly part of the fan flow downstream), and begins to be increasingly better described as buoyancy-dominated (where, despite the impact of the cross flow ΔP on the overall

flame angle, at some distance along the length of the tilted flame the buoyant force overcomes the cross flow inertia and the flame and some of the hot gases escape the fan flow, rising upward). A general analysis of this transitional regime was presented in chapter 6.4.

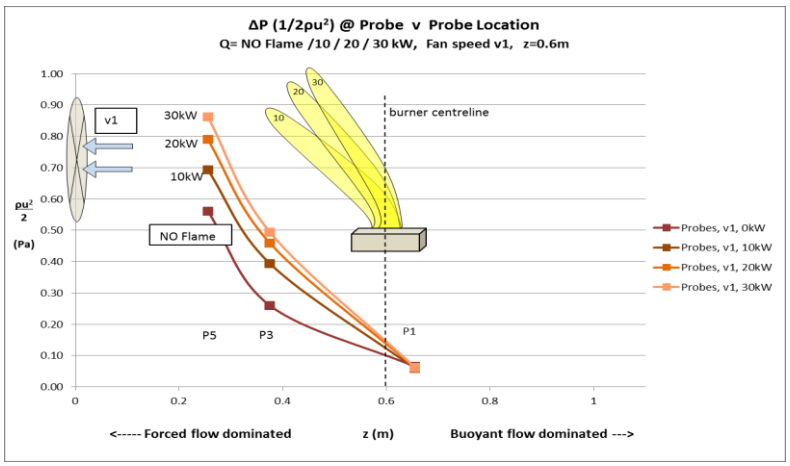

(a)

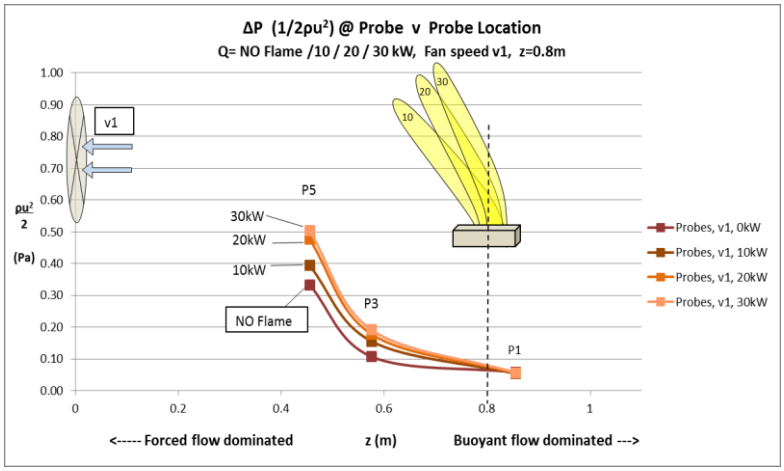

(b)

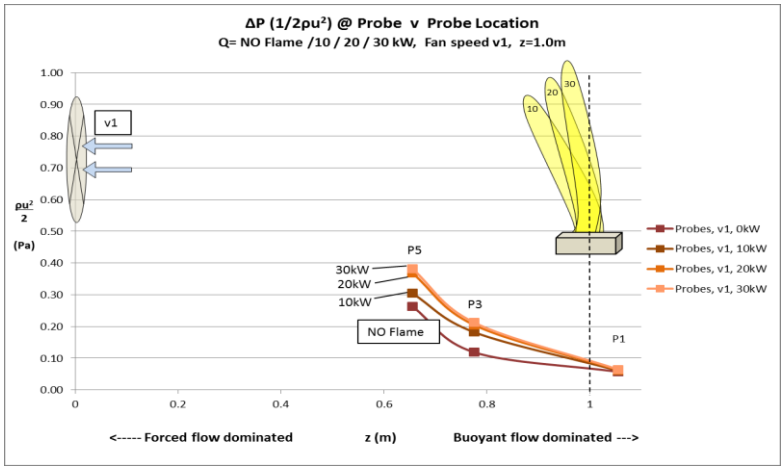

(c)

Figure C3: Break down the data of figure C2 by distance, z' (fan speed v1) in order to visualise the direct impact of increasing z' in each instance

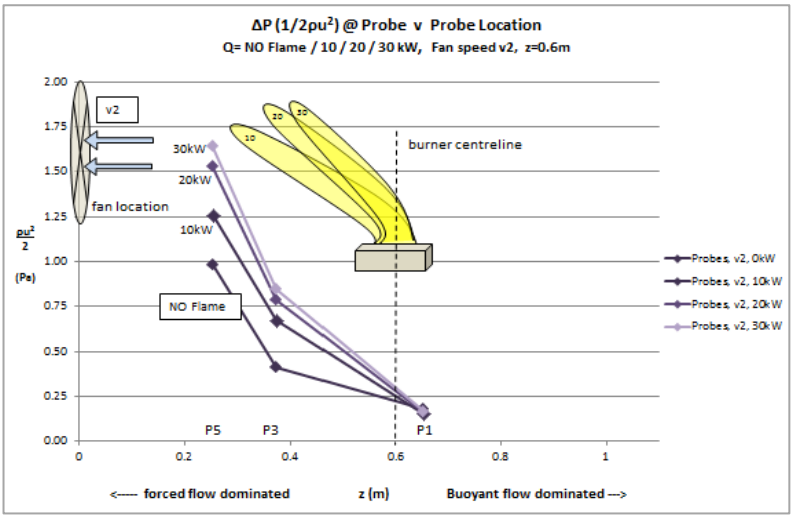

(a)

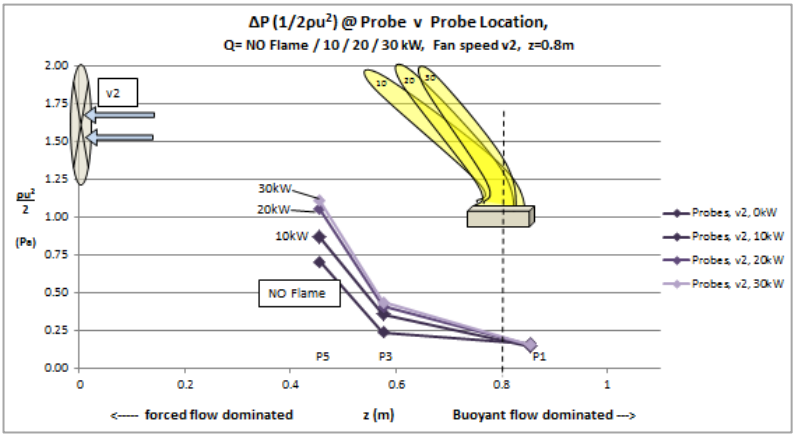

(b)

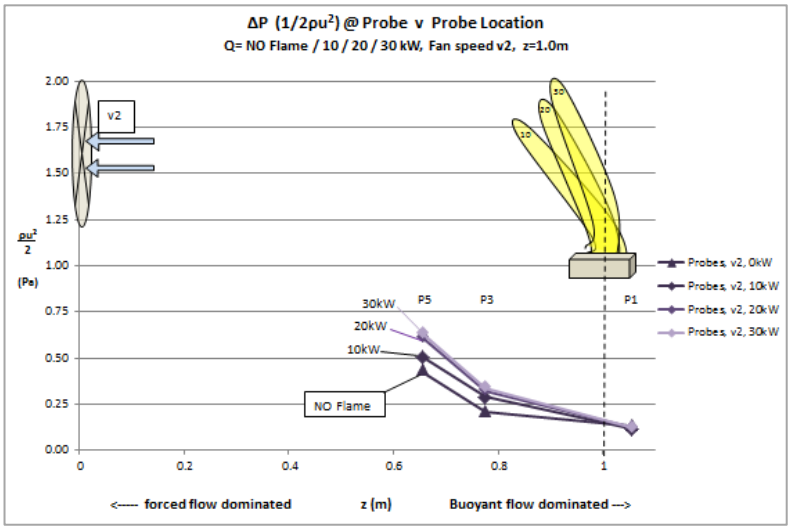

(c)

Figure C4: Break down the data of figure C2 by distance, z' (fan speed v2) in order to visualise the direct impact of increasing z' in each instance

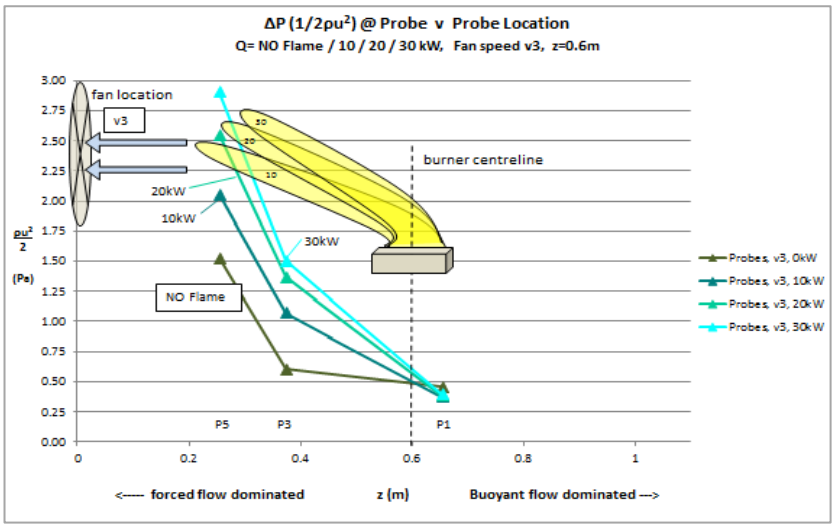

(a)

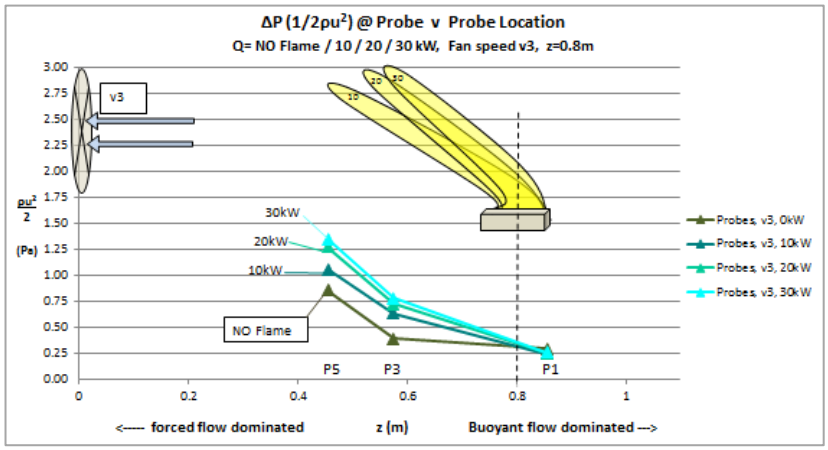

(b)

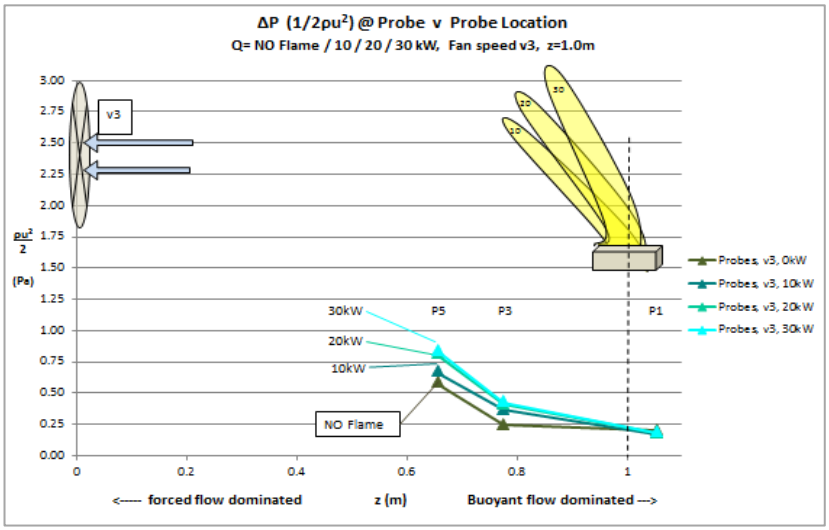

(c)

Figure C5: Break down the data of figure C2 by distance, z' (fan speed v3) in order to visualise the direct impact of increasing z' in each instance

Figures C6-C8 more clearly demonstrate the difference in pressure recorded at each probe for each fan speed, Q and increasing z.

The general trend apparent across all nine cases is that ΔP decreases with increasing z and the magnitude of the increase of ΔP with increasing Q diminishes with distance. This is because (a) since the strength of the cross flow decreases with distance, direct impact is lost form the pressure probes (1, 3, 5) which are aligned in the horizontal plane, and (b) since the flame becomes less tilted with distance as cross flow ΔP diminishes, the buoyant force (which is initially vertical) and makes up some portion of the resultant mixed flow is also lost, or at least reduced in the pressure probe reading. The other trend, which was discussed previously, is that as Q is increased in each case for probes 5 and 3 for 10, 20 and 30kW, the change in velocity reading (ΔU) from the no-flame boundary condition also increases due to the greater velocities generated by the more buoyant, larger fire sizes. The same phenomenon is observed at probe 1 where the increase in local velocity as a result of the increase in Q works against the drop in velocity which resulted from the flame blocking the aspirated flow velocities at probe 1 at the leading edge of the flame when the flame was introduced into the no-flame cross flow case.

Figure C9 rearranges the data of figure C6-C8 to appear with relevance to their location relative to the flame and within the experimental set up. This figure gives a global view of all cases and the impact of increasing Q can be compared directly for each measure of z. Subsequently figures C10-C12 break down this data in better detail, highlighting the approximate location of the flame and the fan in each case and are organised across each figure by extraction fan speed v1, v2, v3 and within each figure by increasing z. Flame images set within each graph demonstrate the typical impact that manipulating each variable has upon the tilt angle of the flame. An aspect of the qualitative results that this highlights is that the numerous experimental cases, with differing combinations of z, Q and fan speed result in a mixture of flame tilt angles which do not change linearly with the order of the

experiment cases. Differentiating and organising these results is focused upon in the results section.

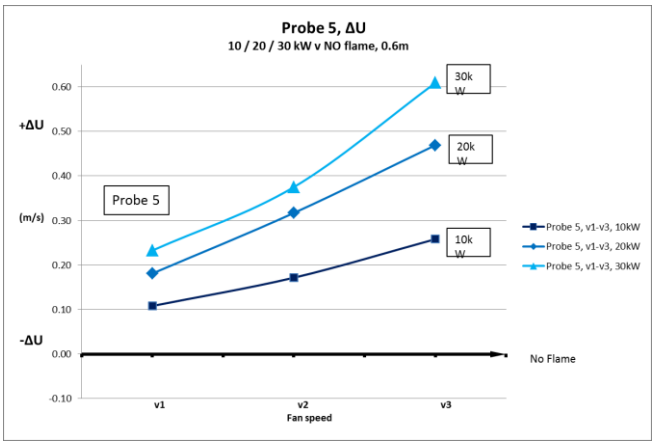

(a)

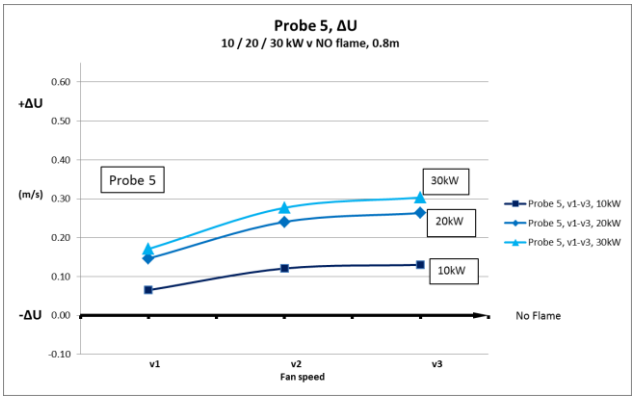

(b)

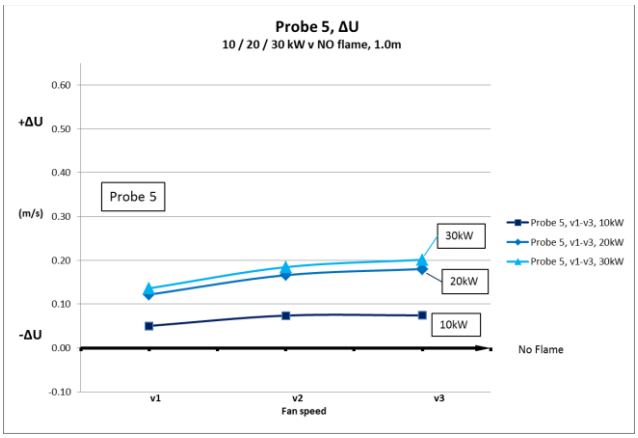

(c)

Figure C6: Change in velocity (Δu) at probe 5 for 10/20/30kW cases at z'= (a)0.6m, (b) 0.8m and (c) 1.0m, for the three fan speeds versus the no flame case

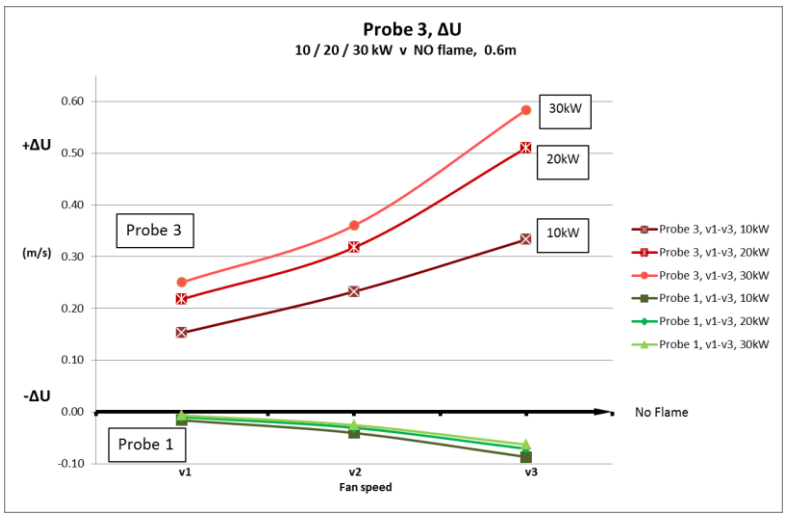

(a)

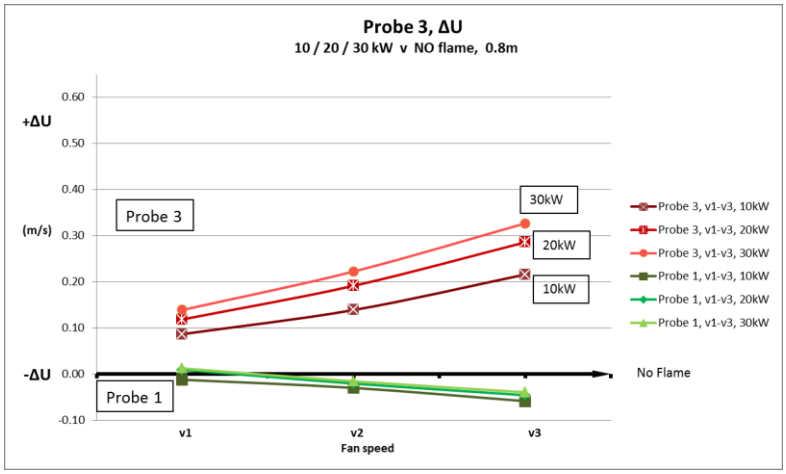

(b)

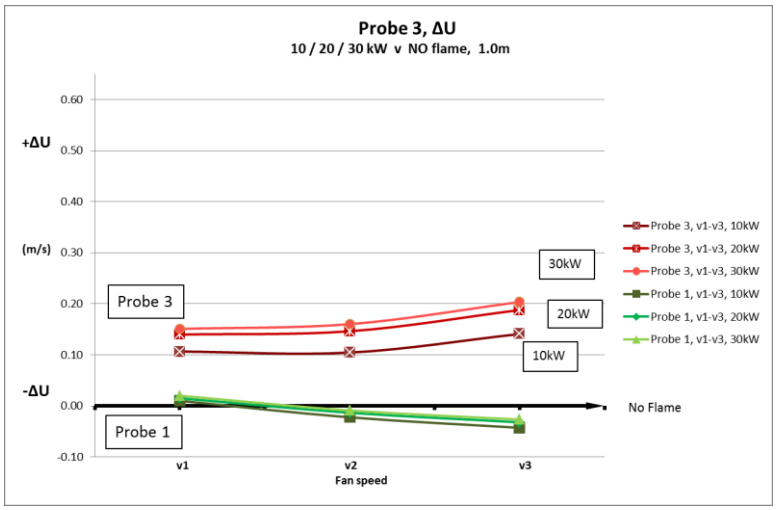

(c)

Figure C7: Change in velocity (Δu) at probe 3 (and probe 1 for context) for 10/20/30kW cases at z'= (a)0.6m, (b) 0.8m and (c) 1.0m, for the three fan speeds versus the no flame case

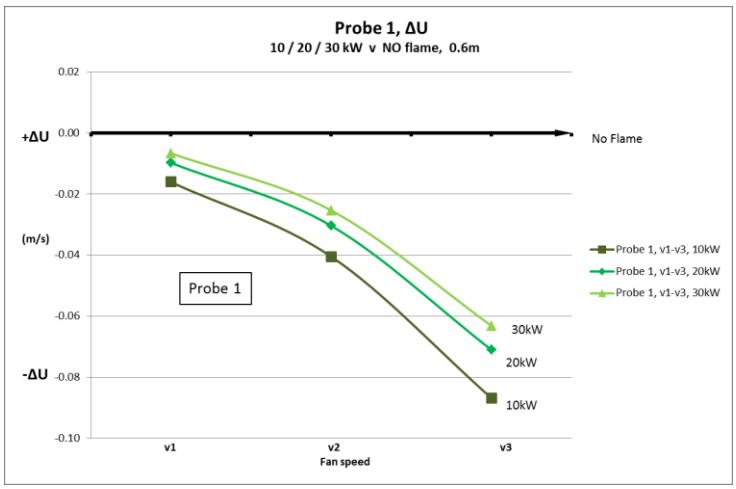

(a)

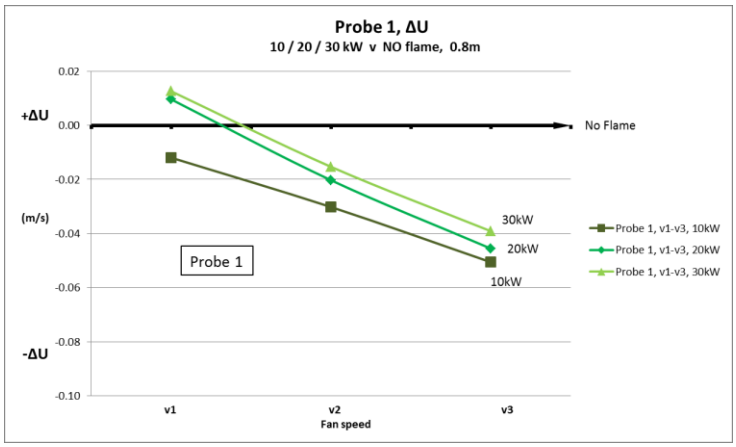

(b)

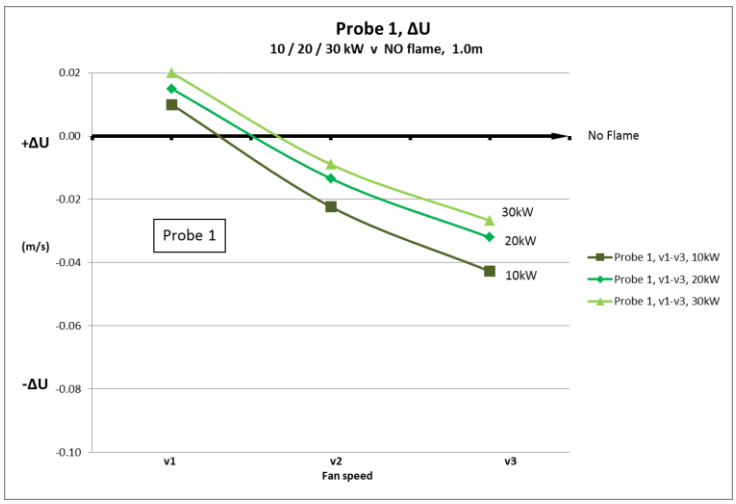

(c)

Figure C8: Change in velocity (Δu) at probe 1 for 10/20/30kW cases at z'= (a)0.6m, (b) 0.8m and (c) 1.0m, for the three fan speeds versus the no flame case

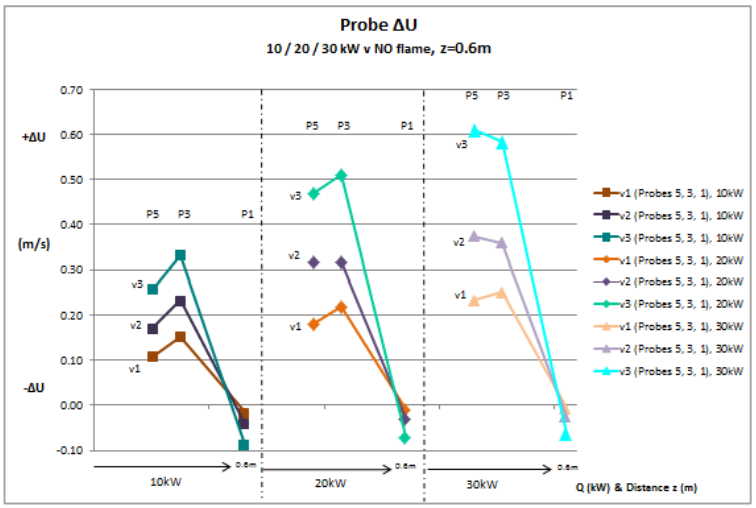

(a)

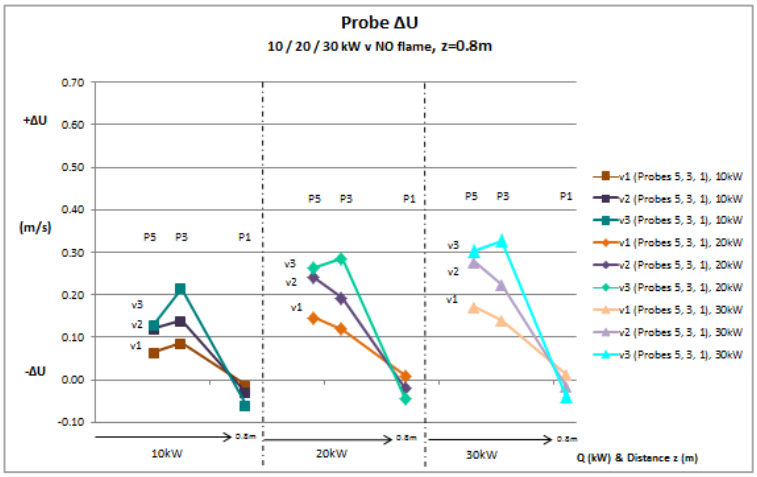

(b)

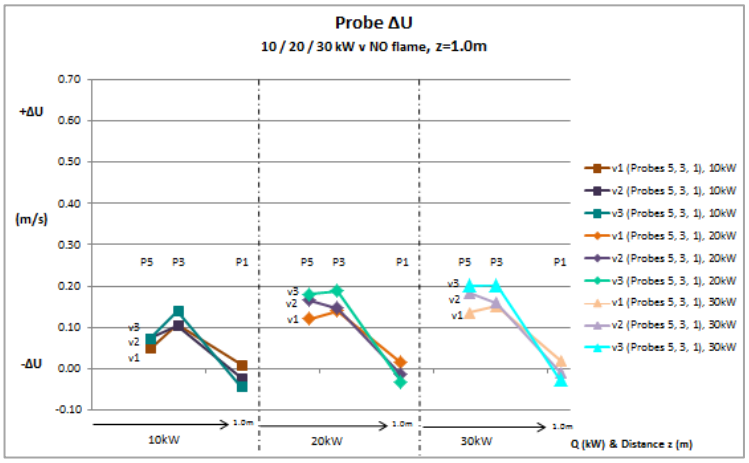

(c)

Figure C9: Rearranges the data of figures C6-C8 to appear with relevance to probe location relative to the burner and other probes

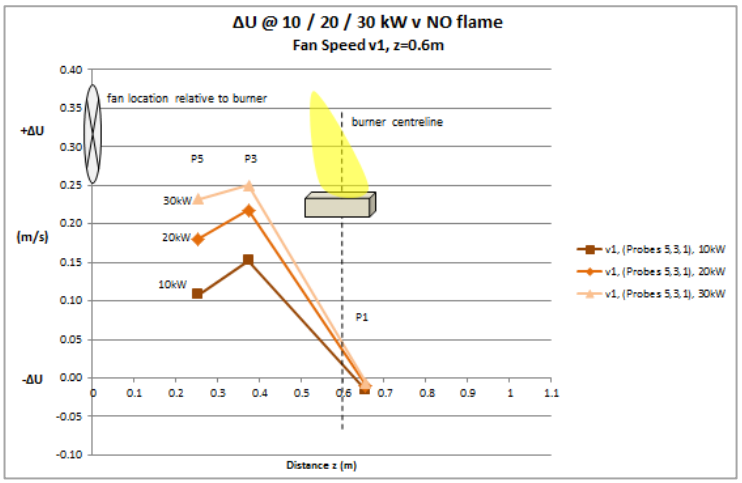

(a)

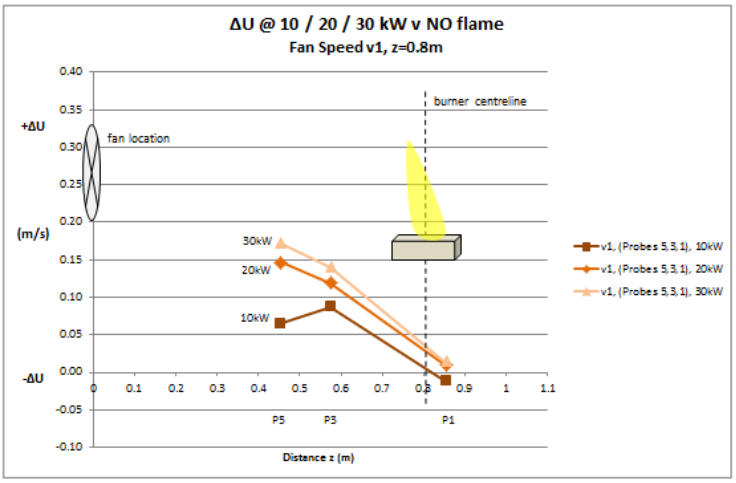

(b)

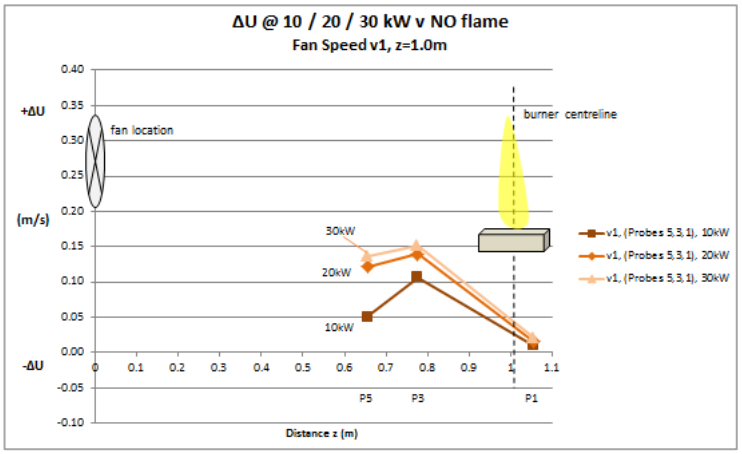

(c)

Figure C10: breaks down data of figure C9 for velocity change data at each probe location relative to burner for fire sizes 10/20/30kW, z'=0.6/0.8/1,0m, for fan speed v1

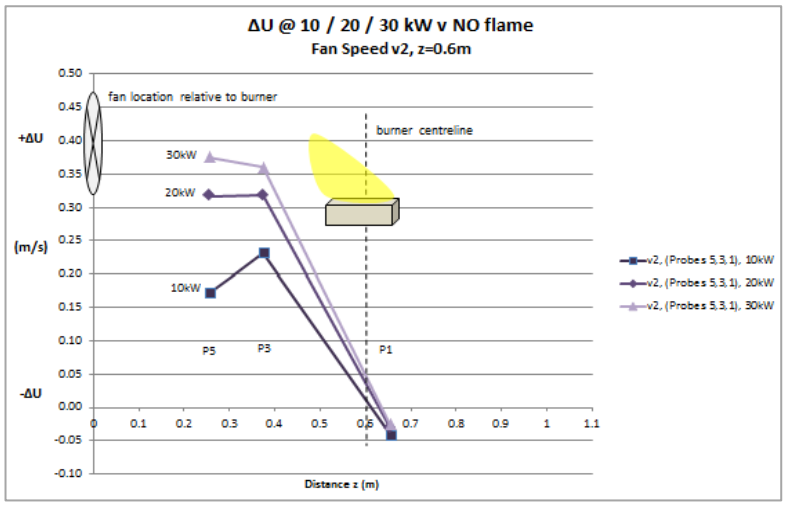

(a)

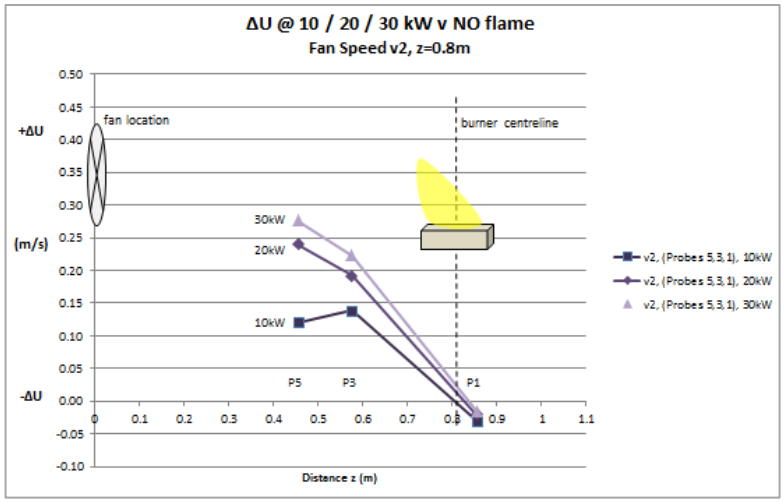

(b)

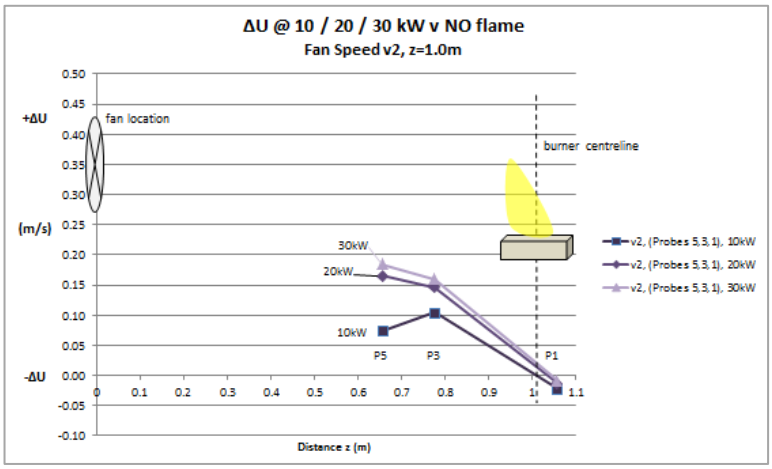

(c)

Figure C11: breaks down data of figure C9 for velocity change data at each probe location relative to burner for fire sizes 10/20/30kW, z'=0.6/0.8/1,0m, for fan speed v2

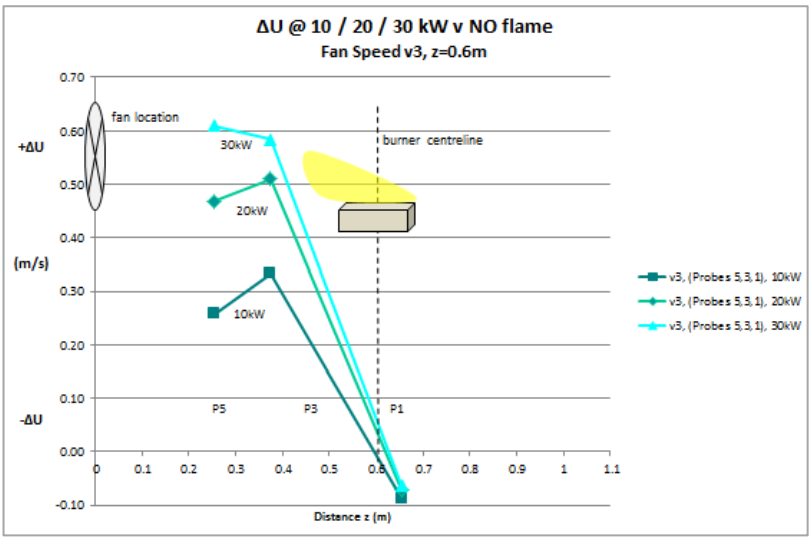

(a)

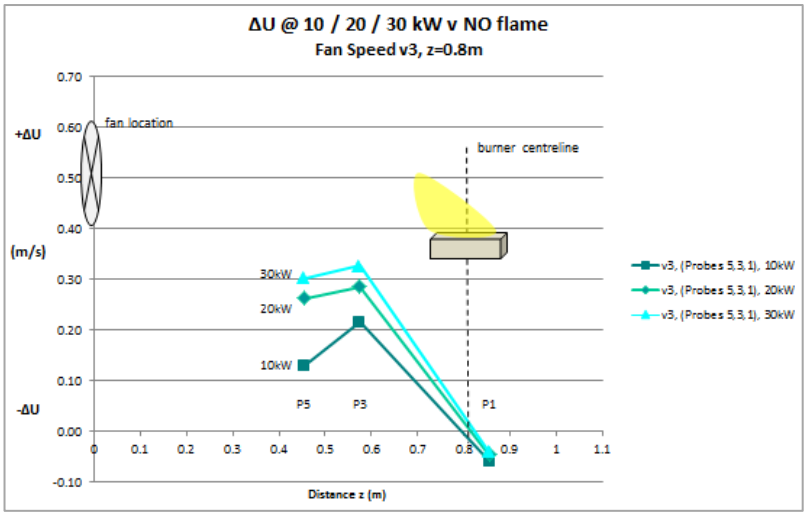

(b)

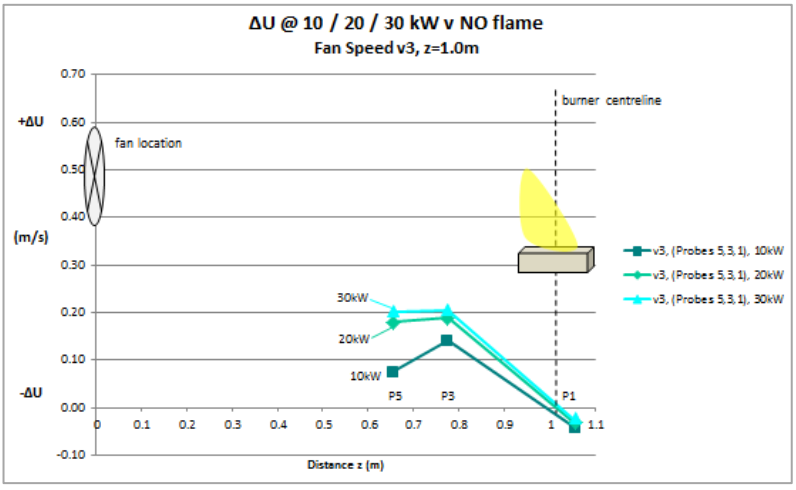

(c)

Figure C12: breaks down data of figure C9 for velocity change data at each probe location relative to burner for fire sizes 10/20/30kW, z'=0.6/0.8/1,0m, for fan speed v3

Appendix D:

Further Fourier analysis
(test 1 pressure probe locations/data)

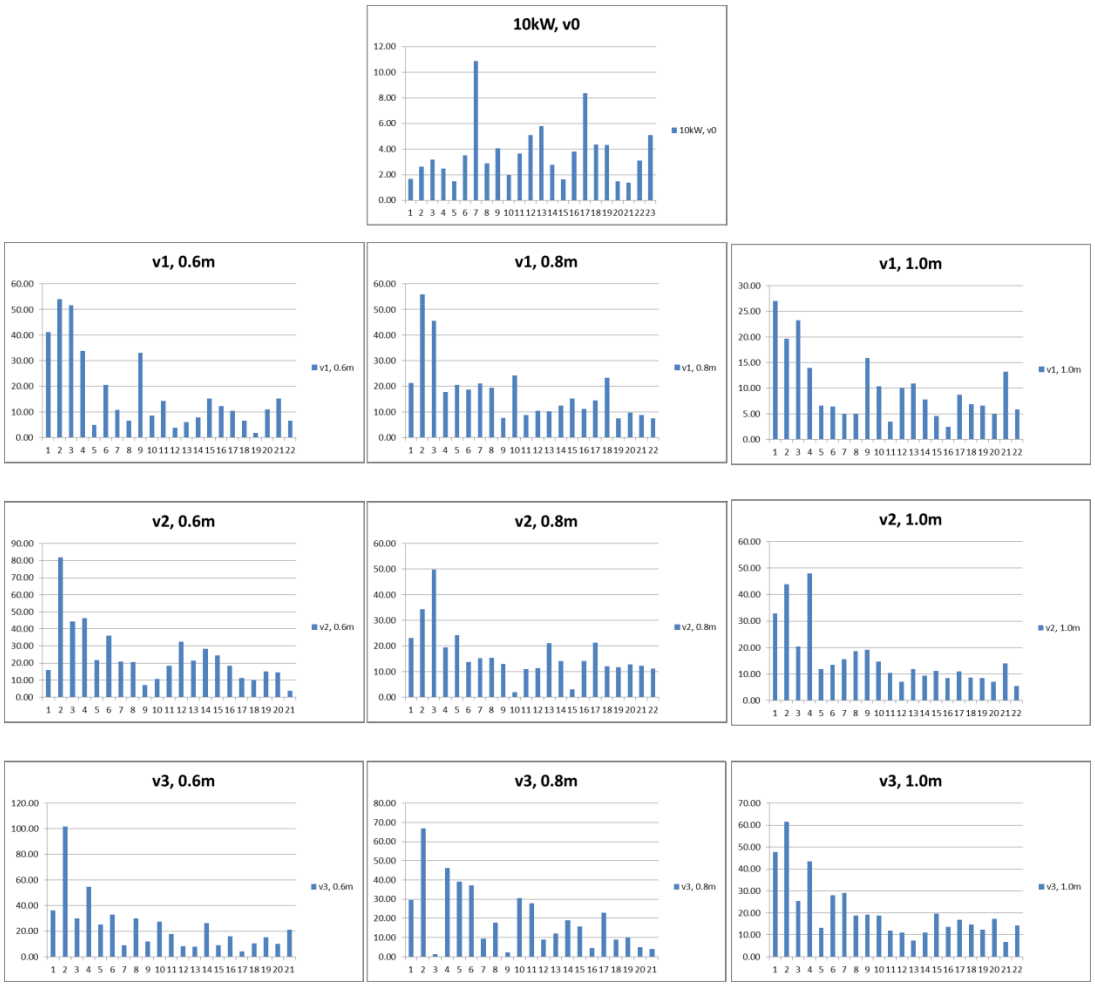

Figure D1: Fast Fourier Transform of pressure probe data from Test 1

Figure D1: Fast Fourier Transform (FFT) complimentary to the analysis presented in chapter 4.1.4 however this analysis uses the probe data from probes located at test 1 locations, which are typically located around the flame rather than involved within it. The location of the probes is less important since probe location appears to have an impact upon the frequency results for the fully-buoyant case, which clearly

depicts 7Hz as a primary contributor here in contrast to 2-3Hz in chapter 4. Of more importance is the clear variation in frequency component contribution once the cross flow is applied to the flame. In each case presented above for z'=0.6/0.8/1.0m and fan speed v1-v3 for each distance the cross flow typically has the impact of generating a more turbulent and complicated fluid flow pattern in and around the flame. This is characterised by the addition of some significant contribution by numerous frequency data in all 9 cross flow cases above. Practically, this suggests more turbulent mixing which promotes entrainment and as discussed throughout chapter 4 in particular, diminishes the importance of vortex engulfment of fresh air in the entrainment mechanism and promotes entrainment by diffusion due to the increased turbulence and greater air velocities around and in the general direction of flame / plume flow.